Modulation of electronic and magnetic properties of nanostructures on a monolayer of MoS_2/Au(111)

Investigated by STM/AFM

Dissertation

zur Erlangung des Grades eines
Doktors der Naturwissenschaften

am Fachbereich Physik
der Freien Universität Berlin

vorgelegt von
Sergey Trishin

Berlin, 2023

Contents

Contents   **v**

List of Abbreviations

AFM	atomic force microscopy
AM	amplitude modulation
ARPES	angle-resolved photoemission spectroscopy
CBM	conduction band minimum
CPD	contact potential difference
DoS	density of states
DFT	density functional theory
FM	frequency modulation
Ethyl-DADQ	ethyl-diaminodicyanoquinone
HOMO	highest occupied molecular orbital
IETS	inelastic electron tunnelling spectroscopy
LCPD	local contact potential difference
LEED	low energy electron diffraction
LUMO	lowest unoccupied molecular orbital
MIM	metal-insulator-metal
MoS_2	molybdenum disulfide
nc	noncontact
RKKY	Ruderman-Kittel-Kasuya-Yosida
STM	scanning tunnelling microscopy
STS	scanning tunnelling spectroscopy
TMDC	transition metal dichalcogenide
VBM	valence band maximum

Abstract

Fundamental electronic and magnetic properties of single atoms and molecules depend crucially on their immediate environment. Understanding its exact influence allows for the manipulation and thus tailoring of said properties. In this thesis, we investigate four different nanostructures on a monolayer of $MoS_2/Au(111)$ by means of scanning tunnelling microscopy (STM) and atomic force microscopy (AFM).

First, single sulfur vacancies in the MoS_2 layer were investigated. Here, the missing sulfur atoms are imaged with a three-fold symmetric shape in the STM topographies. Several defect related in-gap states were observed by scanning tunnelling spectroscopy (STS), most prominently a sharp resonance at zero bias. We identified it as a Kondo resonance by temperature and magnetic field dependent measurements. For defects located in regions of the MoS_2, where the underlying Au(111) was missing, the Kondo resonance was absent, probably due to a different charge state of the defect.

We then investigated the magnetic properties of single iron atoms on the MoS_2 monolayer. We found that the exact position of the atoms in the moiré superstructure, which forms due to the lattice missmatch of the MoS_2 and the underlying Au(111), has a crucial impact on those properties. Atoms on the moiré minimum exhibit an inelastic excitation, which is a signature of a spin-flip excitation and atoms on the moiré maximum show a Kondo resonance, which is a sign of increased spin screening by the substrate electrons. The transition between those two observed features was continuous along the moiré structure. We explain these changes by a local variation of the density of states along the moiré modulation.

An impact of the moiré was also observed on single manganese atoms: they exhibit a Kondo resonance in the weak coupling regime, with the amplitude varying along the moiré. We were able to manipulate single manganese atoms into dimers and found three distinct regimes of interatomic exchange coupling, depending on their atom separation. We focused on the dimers with the closest spacing of one atomic lattice site. They show a direct exchange coupling, which leads to a singlet ground state. The excitation energy from the ground state to the excited triplet state also varies along the moiré structure. In a model calculation we establish that the hybridisation of manganese d-levels with substrate electrons leads to a renormalisation of the singlet-triplet excitation energy. A comparison of experimental values and theoretical prediction suggests that several conduction channels are involved in the renormalisation.

Finally, the high-dipole molecule Ethyl-DADQ was investigated. Pre-characterisations on a bare Au(111) substrate show that the molecular dipole is preserved and that the molecules cause a local lowering of the work function of the substrate. The investigations on MoS_2 allow for a better energy resolution, which helps to resolve several vibronic sidebands of the positive ion resonance. Their intensities vary depending on the electrostatic environment of the molecule, suggesting a partial damping of some vibrational modes.

Kurzfassung

Wesentliche elektronische und magnetische Eigenschaften von einzelnen Atomen und Molekülen hängen von ihrer unmittelbaren Umgebung ab. Den direkten Einfluss dieser zu verstehen erlaubt die Kontrolle und Manipulation dieser Eigenschaften. In dieser Arbeit untersuchen wir vier verschiedene Nanostrukturen auf einer Monolage MoS_2 /Au(111) mit Rastertunnel (RTM)- und Rasterkraftmikroskopie.

Als erstes schauen wir auf einzelne Schwefelfehlstellen in der MoS_2 Monolage. Wir haben die Fehlstellen als dreizählig symmetrische Form in den RTM Topographien abgebildet. Mehrere Zustände dieser Defekte konnten in der Bandlücke mit Rastertunnelspektroskopie nachgewiesen werden, darunter auch ein Zustand am Ferminiveau. Dieser konnte mit Hilfe von temperatur- und magnetfeldabhängigen Messungen einer Kondo Resonanz zugewiesen werden. In Defekten im MoS_2, wo das darunterliegende Au(111) fehlt, war dieser Zustand nicht ausgeprägt, was für einen anderen Ladungszustand des Defektes sprechen kann.

Infolge haben wir die magnetischen Eigenschaften von einzelnen Eisenatomen untersucht. Diese Eigenschaften hängen sehr stark von der Position der Atome in der Moiré-Struktur ab, die sich aufgrund eines Unterschiedes in den Gitterkonstanten der MoS_2 Schicht und der Au(111) Oberfläche bildet. Atome im Minimum der Moiré-Struktur zeigen inelastische Spin-Flip-Anregungen, und Atome im Maximum der Struktur zeigen eine Kondo Resonanz, die auf eine Abschirmung des Spins durch Substratelektronen hinweist. Der Übergang zwischen diesen beiden Phänomenen erfolgt kontinuierlich über der Moiré-Struktur. Wir erklären den Unterschied mit einer sich über der Moiré-Ordnung ändernden lokalen Zustandsdichte.

Die Moiré-Struktur beeinflusst auch die Spektren von einzelnen Manganatomen: diese zeigen eine Kondo Resonanz im schwach gekoppelten Regime, deren Amplitude sich entlang des Moiré-Musters ändert. Wir konnten einzelne Atome zu Dimeren manipulieren und fanden drei verschiedene Kopplungsregime, die sich mit dem Abstand der Atome zueinander verändern. Wir haben uns auf Dimere konzentriert, deren Atome eine atomare Gitterkonstante entfernt waren. Diese sind mittels einer direkten Austauschwechselwirkung gekoppelt und haben einen Singlet Grundzustand. Die Anregungsenergie vom Grundzustand in den Tripletzustand ändert sich je nach der Position in der Moiré-Struktur. In einer störungstheoretischen Rechnung fanden wir, dass die Hybridisierung der Mangan d-Niveaus mit Substratzuständen zu einer Renormalisierung der Anregungsenergie führen kann. Ein Vergleich zwischen den theoretisch erwarteten und experimentellen Werten deutet darauf hin, dass mehrere Elektronenkanäle an der Renormierung beteiligt sind.

Zum Schluss haben wir das Ethyl-DADQ Molekül untersucht, welches ein hohes Dipolmoment aufweist. Erste Charakterisierungen auf einer Au(111) Oberfläche zeigen, dass der Dipol erhalten bleibt und die Moleküle die Austrittsarbeit des Substrates lokal absenken. Die Messungen auf dem MoS_2 ermöglichten es vibronische Anregungen der positiven Ionenresonanz aufzulösen. Die Intensität derer ist sehr sensitiv auf die unmittelbare elektrostatische Umgebung der Moleküle, was auf eine teilweise Dämpfung einzelner Vibrationen hindeutet.

1 Introduction

A little bit more than 40 years ago the field of nanotechnology was rapidly pushed by the invention of the scanning tunnelling microscope [1, 2] and the atomic force microscope [3], shortly after. The scanning tunnelling microscope actually allowed the imaging and manipulation of single atoms and molecules, which properties were not easily accessible beforehand. Up to date, the high interest in the field is still present: As an example, the 2016 Nobel price in chemistry was awarded for works on molecular machines.

In general, the interest of fabricating functional units on the atomic scale is given, as they could end up more efficient than current devices [4, 5]. Several different approaches have been made to realise some proof-of-principle nanodevices. For example, the energy-level alignment of atoms and molecules on surfaces can be tuned by an applied gate voltage, such that they exhibit a transistor-like behaviour [6, 7]. Also conformational changes on the nanoscale can be used to obtain functionality: a rearrangement of single atoms at the contact point of metallic atomic-scale contacts allows it to be operated as a two-terminal switch [8]. A nanostructure, which can store 1 kilobyte of data [9], was demonstrated. For this, the authors rearranged individual vacancies in a chlorine-layer on a Cu(100) substrate with the tip of a scanning tunnelling microscope. In this experiment an information density of 502 terabits per square inch was achieved, which is significantly higher than in conventional hard disk drives. Intriguingly, this memory was found to be stable at temperatures of $77\,K$. Other examples make use of purely spin-based effects: structures, which could perform logic operation were constructed out of two chains of magnetic atoms, which were coupled via a substrate mediated exchange coupling [10]. Here, the distance between the individual magnetic atoms plays a crucial role for their exact coupling mechanism. For application, stability of the magnetic quantum states is required. It can be achieved for example by properly tailoring the immediate vicinity of the nanostructure [11] or an exchange bias field introduced by a magnetic atom on the tip of a scanning tunnelling microscope [12]. Another frequently used path towards longer lifetimes is introducing a decoupling layer between magnetic atoms and the metal substrates [13, 14].

In this thesis, we will investigate fundamental properties of single magnetic atoms and high-dipole molecules on a monolayer of molybdenum disulfide grown on a Au(111) substrate. The MoS_2 acts as a decoupling layer in this system. In chapters 2 and 3 we will lay the foundations for the experimental results, by describing the working principle of a scanning tunnelling microscope and atomic force microscope, the substrates used in the experiment, as well as typical phenomenons in single atom magnetism on surfaces.

In chapter 4 we will describe single sulfur vacancies in the MoS_2 layer. Intrinsic and extrinsic defects both contribute crucially to the properties of the TMDC layer [15]. As these parameters are also impacted on a local scale, a detailed knowledge of the altered electronic structure is necessary to differ between the properties of defects and adsorbates. We were able to controllably manipulate the defect concentration and found evidence that

the defects are actually charged. Therefore the defects host an unpaired electron, which can then exchange interact with the substrate electrons, resulting in the formation of a many-body state around the Fermi level.

Chapter 5 is dedicated to the study of single iron atoms on MoS_2. This research topic is intriguing in two ways: first, MoS_2 was reported to be a very efficient decoupling layer, possibly allowing for very long lifetimes of magnetic states. Moreover, magnetic atoms were predicted to cause a spin-splitting of the valence band of the MoS_2 [16,17]. For this, larger magnetic structures have to be built. As a first step towards this, the properties of single atoms have to be understood. We have found that single iron atoms show different magnetic fingerprints, ranging from spin-excitations to exchange-interactions with the substrate electrons. These interactions vary depending on the position of the atoms in the moiré superstructure.

We follow up on this by presenting our results on single manganese atoms and dimers in chapter 6. Manganese has a half-integer spin in gas phase and thus is predestined for slightly different magnetic interactions. Moreover, manganese atoms were frequently observed to couple via exchange coupling, making them an ideal system to investigate the aforementioned nanostructures. We predominantly studied manganese dimers. The distance between the individual atoms plays a crucial role on the strength of their exchange coupling. We found that atoms, which were separated by one atomic lattice site show a direct exchange coupling and form a non-magnetic ground state. Surprisingly, the energy spacing between the singlet ground state and the triplet excited state was found to vary across the moiré, which we explained by renormalisation processes, stemming from exchange interactions with the substrate electrons.

In chapter 7, we study single Ethyl-DADQ molecules on Au(111) and MoS_2. Here, we do not focus on magnetic, but rather electric properties of the molecule. Molecules with a high-dipole moment can be in principle interesting for application in molecular electronics and are thus of general interest. We find that the Ethyl-DADQ molecules on Au(111) exhibit a sizable dipole moment and locally lower the work function of the metal. On MoS_2 the molecules exhibit much lesser hybridisation with the substrate, allowing for a more detailed study of their electronic states. We see a large contribution of vibrational excitations to their spectra, which vary across the molecules and with their electronic environment. We suspect that the locally varying electrostatic potential around the molecules leads to a partial damping of certain vibrations.

2 Fundamentals of scanning probe methods

There are several techniques established to investigate fundamental properties of surfaces. Diffraction techniques, performed with X-rays or low energy electrons (LEED) for example, give insight into structural properties of materials. With angle-resolved photoemission spectroscopy (ARPES) one can even reveal a big part of the band structure of a material. All the above mentioned techniques average over a big portion of the substrate and portray the reciprocal space. Consequently, these techniques demand clean and uniformly grown samples to produce consistent results.

A complementary local technique was introduced by Binning and Rohrer in 1982 [1, 2] with the invention of scanning tunnelling microscopy (STM). It allows the investigation of structures on the atomic scale and provides information in real space. The first experiments were performed on metals and semiconductors in ambient conditions. Soon after they were carried on in vacuum chambers, which improved the stability of the measurements and lead to cleaner substrates. This allowed the detection of finer contrasts, as the spin-polarisation of the substrate [18]. Besides the structural information, one can also obtain insights into the electronic structure of the substrate via scanning tunnelling spectroscopy (STS). For instance, this allows for the detection of electronic band gaps of semiconducting materials [19–21] or the surface states of metallic substrates [22–24]. When performed at ultra-low temperatures, it can be used to investigate the fundamental properties of impurities or defects. Some of these properties can be detected by inelastic electron tunnelling spectroscopy (IETS), which are most commonly intramolecular vibrations [25] or spin-flip excitation of magnetic atoms [26].

However, the drawback of STM is that it only works for conducting substrates. Non-conducting substrates can be imaged by atomic force microscopy (AFM) with a similar resolution. It relies on a tip which is placed on a cantilever, oscillating at a high frequency. The forces between the tip and the investigated substrate have a direct impact on the oscillation frequency and can therefore be mapped out. Both techniques, STM and AFM, can be performed at the same time with a suitable probe design.

In this chapter we will introduce the theoretical background of the techniques mentioned above. First, we will have a look at the working principle of STM and derive the tunnelling current and matrix element. Second, we will turn our attention to STS and IETS and describe the measurement procedure in more detail. Afterwards we will introduce the basics of AFM and explain how one can learn about local structural and electronic properties with this technique. Finally, we will introduce our experimental setup and the substrates used in this thesis.

2.1 Working principle of the scanning tunnelling microscope

The working principle of a scanning tunnelling microscope is illustrated in figure 2.1: a conducting tip is brought into close vicinity of a conducting sample without touching it. Classically, no current flow is allowed. However, due to the quantum nature of electrons, a current can flow at very small tip-sample distances. To actually measure an effective current, a bias voltage has to be applied between tip and sample. The high spatial resolution of STM stems from the exponential dependence of the tunnelling current on the tip-sample distance. We will show this relation explicitly in section 2.3. To illustrate this, a change of $1\,\text{Å}$ results in a change of the tunnelling current of one order of magnitude. This high sensitivity requires a very precise control of the tip-sample distance, which is achieved by piezoelectric actuators for both the lateral and vertical movement of the tip. Hereby, two main imaging modes are used, which are illustrated in figure 2.2.

In a) the constant-current mode is shown. Here a feedback loop, controlled by a proportional-integral controller, adjusts the tip height such that the tunnelling current stays constant. The variations of the tip height are hereby recorded and directly converted into a topography.

The other mode used is called constant-height mode and is illustrated in figure 2.2 b). Here, the feedback-loop is switched off and the tip height is kept constant. As a result the tunnelling current is the measurement parameter, which changes laterally and can be converted into a topography. Though this technique is not limited by the bandwidth of the feedback loop and can therefore scan areas quicker, it has several flaws. It requires very flat surfaces to avoid tip crashes, which usually enforces smaller scan areas. Also it demands the tip height to stay constant over the time of the scan, which usually is challenging due to external factors as drift, mechanical vibrations and creep of the piezos. If not otherwise specified, STM topographies presented in this thesis were recorded in the constant-current mode.

In the next chapter we derive the relation between the tunnelling current and the tip-sample distance explicitly and discuss, which assumptions can be made to simplify it.

2.2 Tunnelling between two electrodes: the Bardeen approach

The tunnelling effect has been used in experiments already before the invention of STM, for example in studies of metal-insulator-metal (MIM) junctions [28]. For such junction geometries the tunnelling current has already been theoretically derived [29, 30]. We first sketch this derivation and later on modify it for the case of STM. In general the rate of electron transfer between two electrodes from a state ψ_v at an energy E_{ψ_v} to a state ψ_w at an energy E_{ψ_w} can be determined by Fermi's golden rule as :

$$w = \frac{2\pi}{\hbar}|M|^2\delta(E_{\psi_v} - E_{\psi_w}). \tag{2.1}$$

Here, δ is the delta function, which ensures the conservation of energy and makes sure that tunnelling can only take place for states at the same energy level, and M is the tunnelling
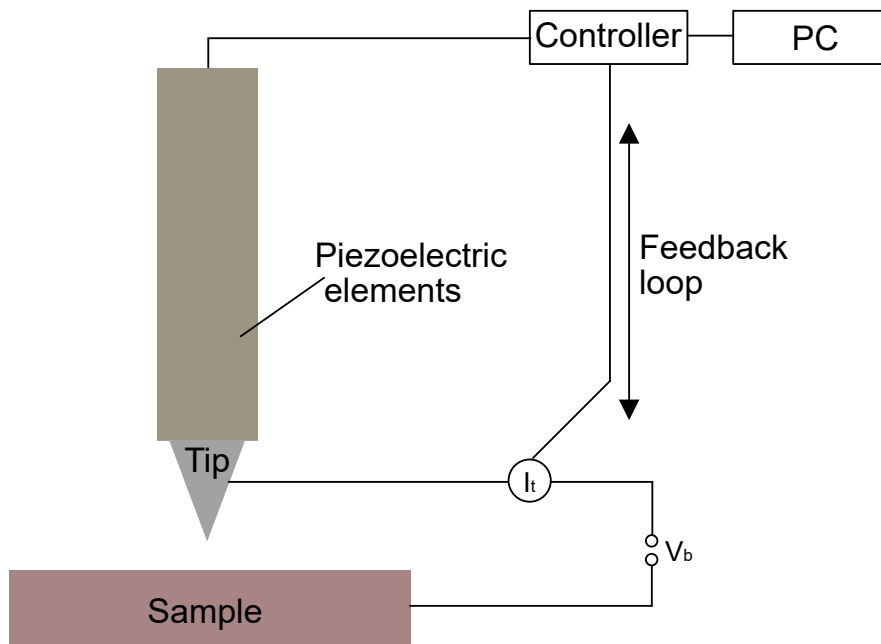
Figure 2.1: Basic working principle of the scanning tunnelling microscope. The tip movement is controlled by piezoelectric elements to allow for precise movements on the atomic scale. For electrons to tunnel from the tip to the sample or vice versa, a bias voltage V_b has to be applied. The effective tip-sample distance depends on the setpoint current I_t, which is regulated by a controller via a feedback-loop. Adapted from [27].
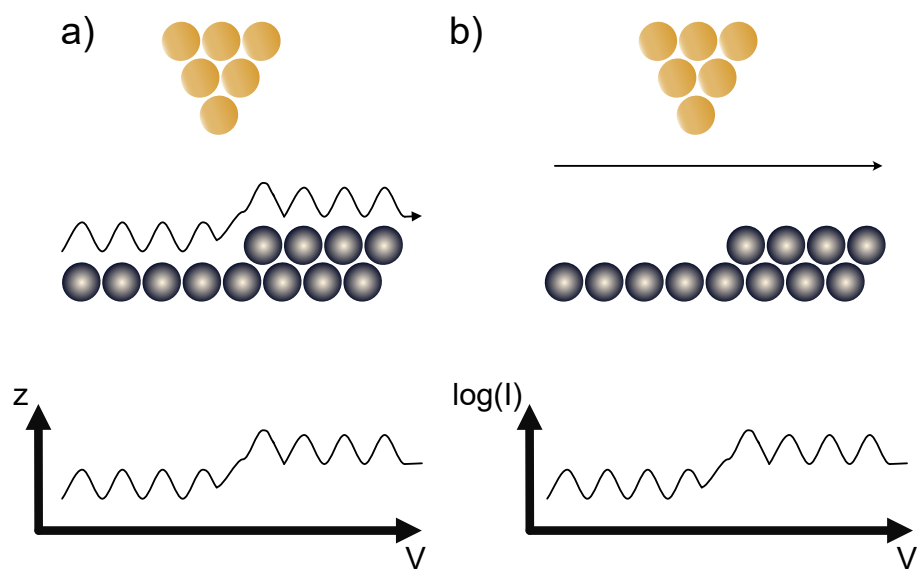
Figure 2.2: Imaging modes in scanning tunnelling microscopy. a) Constant-current mode: a feedback loop keeps the tunnelling current constant, the main measurement parameter here is the tip height z. b) Constant-height mode: the feedback loop is switched off here, resulting in a constant tip height. Here, one measures the tunnelling current I. Adapted from [27].

matrix element. To go from the rate to an actual tunnelling current one has to sum up over all states, relevant in the tunnelling process. One arrives at:

$$I = \frac{2\pi}{\hbar} \sum_{\psi_v, \psi_w} f(E_{\psi_v})[1 - f(\psi_v + eV)]|M|^2 \delta(E_{\psi_v} - E_{\psi_w}). \tag{2.2}$$

Here, $f(x)$ is the Fermi distribution function and V the applied bias voltage. We want to clarify two things at this point: first, tunnelling can take place in both directions, the total current is just the sum of them. Moreover, for metal-insulator-metal junctions the net current will be zero, if the junction is not biased. One can see this conceptually in figure 2.3 a). With an applied bias, an effective tunnel current can flow from one electrode to the other, in this illustrated case from the tip to the sample. The electrons at the Fermi energy contribute the most to the net current, which is indicated by the length of the arrow, even though all states between 0 and eV contribute. If no bias was applied, the Fermi levels of both electrodes would be aligned and no net current would flow.

We can replace the sum in equation 2.2 by an integral if we use the density of states $\rho_{S,T}(E)$ for both electrodes at an energy E. Here, we chose the indices such that they will be already convenient when we talk about the STM junction. We arrive at:

$$I = \frac{2\pi}{\hbar} \int_{-\infty}^{\infty} f(E_{\psi_v} + \epsilon)[1 - f(E_{\psi_w} + eV + \epsilon)]\rho_S(E_{\psi_v} + \epsilon)\rho_T(E_{\psi_v} + eV + \epsilon)|M|^2 d\epsilon. \tag{2.3}$$

One can simplify this expression by taking into account the experimentally plausible limit of small temperatures. Then the Fermi distribution function can be written as just a step-function giving:

$$I = \frac{2\pi}{\hbar} \int_{0}^{eV} \rho_S(E_F + \epsilon)\rho_T(E_F - eV + \epsilon)|M|^2 d\epsilon. \tag{2.4}$$

At this point, the expression only depends on the respective density of states of the two electrodes and the tunnelling matrix element. For latter the first attempt to calculate it was made by Bardeen [29]. He showed that it can be written as:

$$M_{vw} = \frac{\hbar^2}{2m} \int d\vec{S}(\Psi_w^* \vec{\nabla} \Psi_v - \Psi_v \vec{\nabla} \Psi_w^*). \tag{2.5}$$

One can directly see that the matrix element depends only on the overlap of the two wave functions at a chosen integration surface $d\vec{S}$. Bardeen moreover assumed that M does not change significantly at small energies. Then equation 2.4 only depends on the density of states of the two electrodes. However, to obtain quantitative results it is necessary to explicitly calculate the tunnelling matrix element. For STM, this was first done by Tersoff and Hamann in 1983 [31]. In the next subsection we sketch the steps of their derivation.

2.3 The Tersoff-Hamann approach: using s-wave tips

Tersoff and Hamann specified the approach Bardeen used for a STM junction. They assumed the junction geometry illustrated in figure 2.3 b): a tip and a sample are separated by a
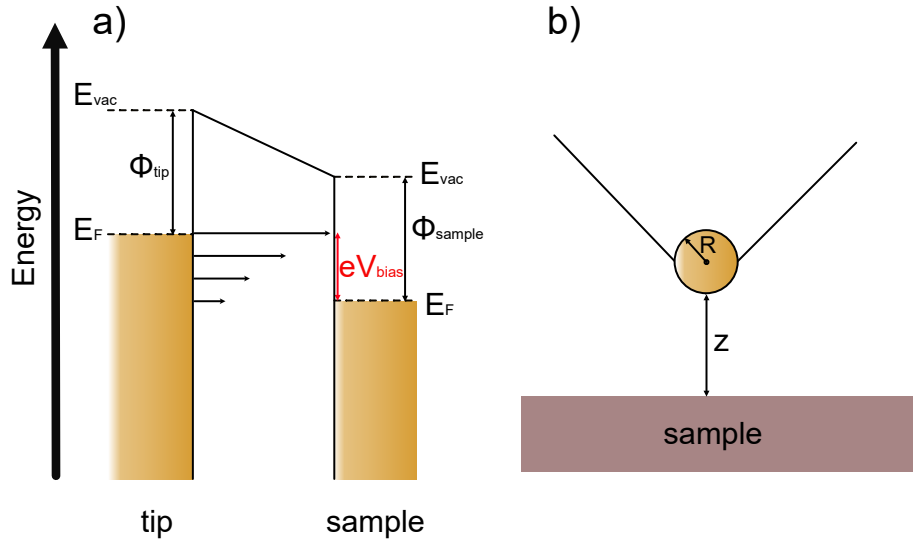
Figure 2.3: Tunnelling in a STM junction. a) Energy-level diagram of the tunnelling process. When the junction is biased a net current can flow, which is illustrated by the black arrows. b) Illustration of the junction geometry in the Tersoff-Hamann model. Adapted from [31].

distance z. They modelled the tip as a s-wave like wavefunction with radius R. The sample wave function was modelled as a decaying Bloch wave:

$$\phi_S = \Omega_S^{-\frac{1}{2}} \sum_G a_G \exp[-(k^2 + |\vec{k_\parallel} + \vec{G}|^2)^{\frac{1}{2}} z] * \exp[i(\vec{k_\parallel} + \vec{G}) * \vec{x}],$$

$$\phi_T = \Omega_T^{-\frac{1}{2}} c_t k R e^{kR} (k|\vec{r} - \vec{r_0}|)^{-1} \exp(-k|\vec{r} - \vec{r_0}|).$$

(2.6)

Here, Ω is the sample/probe volume, k is the inverse decay length of the wave function in vacuum, φ is the materials work function, which is assumed to be equal for sample and probe, $\vec{k_\parallel}$ is the surface Bloch vector of the state and $\vec{G}$ is the reciprocal lattice vector. R in the second part of equation 2.6 is the radius of the tip's curvature as shown in figure 2.3 b) and c_t a normalization factor. They then used this wave functions to explicitly calculate the matrix element given by equation 2.5. Plugging the result in equation 2.2 gives:

$$I = \frac{32\pi^3}{\hbar} e^2 V \varphi^2 D_t(E_F) R^2 k^{-4} \exp(2kR) \sum_S |\psi_S(\vec{r_0})|^2 \delta(E_S - E_F).$$

(2.7)

Here, D_t is the density of states per unit volume of the probe and $\vec{r_0}$ the position of the center of the tip's curvature. Looking at equation 2.7, we see that there is only one parameter, which depends on the tip-sample distance: $|\psi_S(\vec{r_0})|^2$, which scales with $\approx exp[-2k(R + d)]$. This term gives rise to the previously mentioned exponential dependence of the tunnelling current on the tip-sample distance and is ultimately responsible for the high spatial resolution in STM. Note however, that Tersoff and Hamann evaluated the matrix element for tips with s-wave character. In our experiments we used tips, which

apexes were covered in gold. For gold tips the assumption is valid, as their most extended and therefore most dominant orbital is the 6s-orbital. However the STM topographies must always be critically analysed, as picking up impurities form the substrate may alter the character of the tunnelling orbital. Then other matrix elements have to be used in order to evaluate the tunnelling current [30]. Sometimes the usage of different tunnelling orbitals can even enhance the imaging resolution [32].

As seen in equation 2.3 the tunnelling current depends not only on the tip-sample distance, but also on the density of states of the sample. Therefore the current is always a convolution between topography and electronic structure and has to be evaluated carefully. Nevertheless this implies that with STM one can access the actual density of states of the sample and learn about its electronic properties by probing it at different energies. This technique is referred to as scanning tunnelling spectroscopy and will be discussed in the following section.

2.4 Scanning tunnelling spectroscopy

Usually, one is interested in the DoS at a specific energy and not at the integral over all energies, as written in equation 2.3. To eliminate the integral one can therefore form the derivative with respect to the voltage and arrives at:

$$
\begin{aligned}
\frac{dI}{dV}(V) &\approx \rho_T(E_F)\rho_S(E_{F+eV})|M_{vw}|^2 \\
&+ \int_0^{eV} \rho_S(E_F + \epsilon)\rho_T(E_F - eV + \epsilon)\frac{d|M_{vw}|^2}{dV}d\epsilon \\
&- \int_0^{eV} \rho_S(E_F + \epsilon)\frac{d\rho_T(E_F - eV + \epsilon)}{dV}|M_{vw}|^2 d\epsilon
\end{aligned}
\tag{2.8}
$$

This expression can be significantly simplified by making a couple of assumptions. First, as already stated above, for small bias voltages and constant tip-sample distances the matrix element $|M_{vw}|^2$ can be considered as constant, which drops the second term in equation 2.8. Moreover, for metallic tips the DoS ρ_t can usually be considered constant as well around the Fermi energy. Experimentally this property is also very easy to check and enforce. As a consequence, the third term in equation 2.8 also vanishes. Therefore only the first one remains:

$$
\frac{dI}{dV}(V) \approx \rho_T(E_F)\rho_S(E_{F+eV})|M_{vw}|^2 \approx \rho_S(E_{F+eV})
\tag{2.9}
$$

From equation 2.9 it follows immediately that the differential conductance is directly proportional to the DoS of the sample. Besides recording dI/dV spectra, sometimes also $\frac{dz}{dV}$ spectra are recorded. Now we want to briefly discuss the ups ans downs of the respective measurement modes:

In the **constant-height mode** (dI/dV), the tip is placed at a fixed height above the sample. This preadjusted height will be called setpoint in the course of this thesis. After the tip is set, the bias voltage is ramped in the desired range and the corresponding current is recorded.
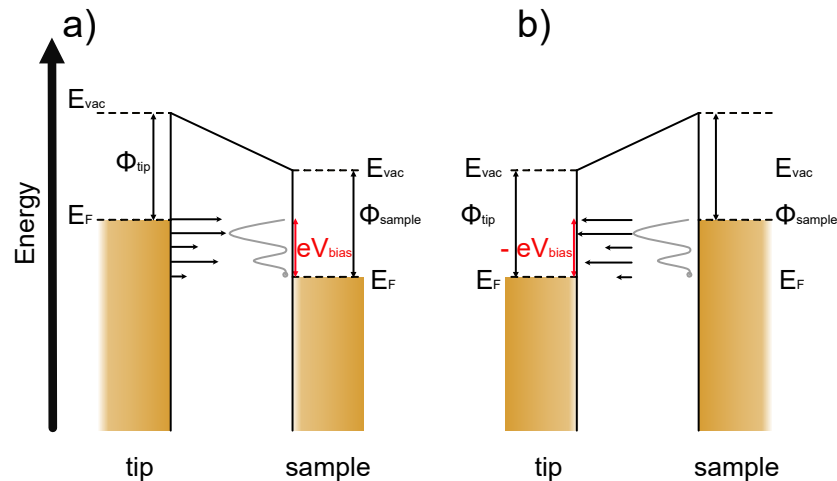
Figure 2.4: Energy level diagram while tunnelling into or from substrate states. a) When a positive bias is applied, electrons from the tip tunnel into empty substrate states. The tunnelling probability depends on the density of states of the substrate, which is indicated with the differing length of the arrows. b) The opposite case to a), here electrons from occupied substrate states tunnel into the tip. Adapted from [27].

This measurement mode is usually only applicable in a small voltage range, as the current can get very large at high bias voltages and lead to an instability of the junction. Setting a low current setpoint at higher voltages would in contrast lead to a very tiny signal at low bias voltages.

In the **constant-current mode**(dz/dV) the tip-sample height is adjusted during the voltage sweep to keep the tunnelling current constant. This method is therefore more applicable at higher bias voltages. However, the assumption of a constant tunnelling matrix element is not valid anymore for a varying tip-sample distance, which can lead to varying intensities and peak positions in comparison to the dI/dV mode. In addition, at very low bias the tip has to be brought very close to the substrate to still allow a sizeable current. Latest at zero bias this will usually lead to an indention of the tip into the substrate.

In conclusion, none of the two methods described is straight forwardly superior compared to the other. Using both and comparing the results can also beneficial, as they can provide complementary information [33, 34]. Often STS is used to record so called dI/dV maps. Here, besides the topography also the differential conductance is recorded for every pixel of the image, giving rise to a 2D image of the DoS. The scanning speed has to be chosen sufficiently low to allow that. Still, forming the derivative for every pixel would take a very long time. A much more convenient method is to record the signal with a so-called lock-in amplifier, which directly acquires the dI/dV signal and on top significantly lowers the signal-to-noise ratio. In the next subsection we want to describe its working principle in more detail.

2.5 The lock-in amplifier

Lock-in amplifiers are used not only in STM, but for various experimental methods. They can extract signals, which are thousands of times smaller than the background noise [35, 36]. Figure 2.5 a) shows the general working scheme of a lock-in amplifier. First, a reference signal is added on top of a physical quantity of interest (in STM, the modulation is usually applied to the bias voltage). This reference signal can come directly from the lock-in, for example as a sinusoidal or can be provided by external sources, as for example a chopper unit in optical experiments. After passing the STM junction and the I/V converter the output voltage arrives at a phase sensitive detection unit, where it is evaluated in comparison to the original reference signal. As the signal afterwards goes through a low-pass filter, only components with no explicit frequency dependence pass the filter. We now show in more detail how this mathematically works for the tunnelling current in STS.

We already stated that the modulation is applied to the bias voltage in STM. The current is proportional to the voltage via equation 2.4, only that now the integration goes until $eV + eV_{ac}$. V_{ac} is the modulation voltage, which writes as $V_{ac} = V_{mod}sin(\omega_{mod}t)$. For small modulation voltages and a fixed value of V we can expand the current in a Taylor series. It gives:

$$I(V + V_{ac} \propto I(V) + \frac{dI}{dV}V_{mod}sin(\omega_{mod}t) + \frac{d^2I}{dV^2}V_{mod}^2sin^2(\omega_{mod}t) + ... \qquad (2.10)$$

The first term in equation 2.10 is just the dc tunnelling current, but as one can directly see, the second and third term are proportional to the derivative and the second derivative of the tunnelling current with respect to the voltage. As we know from equation 2.9, this gives us then a direct way to access the DoS. As mentioned above, in the lock-in amplifier the input signal is finally mixed with the carried on reference signal $V_{ref}sin(\omega_{ref}t + \phi_{ref})$. It follows that:

$$I_{out} \propto I(V)V_{ref}sin(\omega_{ref}t + \phi_{ref})$$
$$+\frac{1}{2}\frac{dI}{dV}V_{mod}V_{ref}cos((\omega_{mod} - \omega_{ref})t + (\phi_{mod} + \phi_{ref})) \qquad (2.11)$$
$$-\frac{1}{2}\frac{dI}{dV}V_{mod}V_{ref}cos((\omega_{mod} - \omega_{ref})t + (\phi_{mod} + \phi_{ref})).$$

Here, $\phi_{mod,ref}$ are the phases of the respective signals. The signal now passes the low-pass filter, which cancels out all the components, which are time dependent. Therefore only parts of the response signal, which match the frequency of the reference ($\omega_{mod} = \omega_{ref}$), are carried on by the lock-in amplifier, eliminating a lot of arbitrary, time-dependent noise. Therefore also the choice of the modulation frequency plays a role: it should be an uneven number, to avoid picking up electrical noise. In the previous subsection we also motivated the usage of the lock-in amplifier to record dI/dV maps. For this purpose the modulation frequency has to be chosen high enough to not coincide with the feedback loop. With the resolution and speed of the lock-in amplifier it is even possible to adjust the feedback loop on the output signal of the lock-in. This corresponds to constant DoS maps and has been shown to give the most accurate iso contours for three dimensional molecules as C_{60} [37].
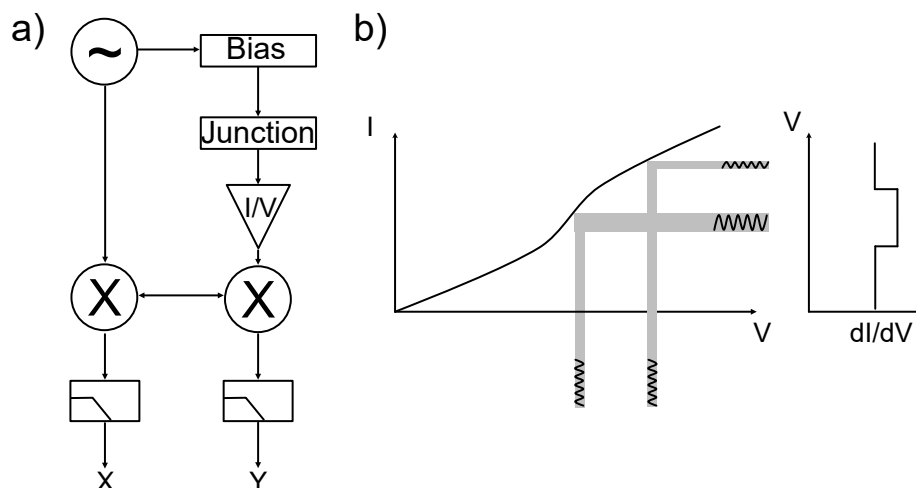
Figure 2.5: The lock-in amplifier in STS. a) Schematics of the signal processing with a lock-in amplifier. For more details see the text. Adapted from [35]. b) Sampling the I-V curve with the modulated bias voltage. A larger slope in the I-V curve leads to a larger lock-in signal, which is proportional to the differential conductance, as shown in equation 2.10. Adapted from [38].

Figure 2.5 b) shows how the additional modulated voltage V_{ac} affects the signal: parts of the I-V curve with a higher slope lead to a larger response signal then the ones with a smaller slope. Also, as we have seen form equation 2.10 the response signal is directly proportional to the modulation amplitude. One might be therefore inclined to use high modulation amplitudes to maximise the signal. However, for spectral features with a small intrinsic line width a too high modulation amplitude could lead to a smearing out of the feature. This is especially relevant for features at low energies, like spin-excitations and vibrations. They arise from inelastic electron tunnelling processes, which will be explained in the next subsection.

2.6 Inelastic electron tunnelling

Until now, we only described elastic tunnelling processes. An example is illustrated in figure 2.6 a): if the applied bias voltage aligns with a state (e.g. a molecular orbital, an electronic band, etc.) the measured conductance increases. Obviously, the slope of the I-V curve increases in this area of interest. In the differential conductance this tunnelling process results in a peak.

The mechanism for inelastic tunnelling is different, as shown in figure 2.6 b). Here, after a certain threshold voltage is matched or surpassed ($eV \geq e\hbar\omega$) an electron can tunnel inelastically into the continuum by exciting a vibration [25,39] or spin excitation [26]. This opens an additional tunnelling channel besides the elastic one, which leads to a permanent increase in the conductance and a step in the dI/dV curve. The intensity of this signal varies very much depending on the type of excitation. For vibrations they are usually not

exceeding a tenth of the conductance of the elastic channel [40], except if they are adsorbed on a decoupling layer [41]. This relatively small change in conductance results from a decreased probability for elastic tunnelling, when a vibration is excited. Therefore these two contributions counteract each other [40]. Moreover, after adsorption on a surface, some vibrational modes might be suppressed and therefore not detectable with inelastic electron tunnelling spectroscopy (IETS), depending on the adsorption geometry [42, 43].

In contrast, the excitation probability for spin-flip excitation is usually higher [26]. Recently changes in the differential conductance of over 100 % have been observed [44, 45]. The higher achievable excitation probabilities stem from an increased coupling strength of electrons to spins in comparison to vibrons. However, not every magnetic atom or molecule actually shows spin-flip excitations. In section 3 we will discuss the requirements for this in more detail.

A combination of elastic and inelastic processes is also possible, as shown in figure 2.6 c). Here an electron can tunnel into a vibronic state, which is a vibrational mode of an excited electronic state. Then beside the resonance several side peaks of energy spacings according to the vibrational energy can be seen. These side peaks can be of similar intensity as the resonance of the electronic state [43] or even surpass it, as we will see in section 7.

IETS has been used to identify different isomers, which were not distinguishable by their STM topography [25]. Another way to learn about the structural properties of molecules is to perform atomic force microscopy (AFM). We want to introduce this technique in the next section.

2.7 Atomic force microscopy

Since STM is restricted to conducting surfaces, it is natural that attempts have been made to find techniques to also image insulating surfaces. Not long after the invention of STM, atomic force microscopy was introduced [3]. Here, the probe is mounted to an oscillating cantilever, which is externally driven into resonance [46]. Due to changing tip-sample forces, either the elongation of the cantilever or a change in the resonance frequency is measured.

Usually one distinguishes between two operating modes in AFM: the contact and the non-contact mode [47]. As the name suggests, in contact mode the probe is in contact with the surface. Here, usually the elongation of the cantilever is measured. In non-contact AFM the probe is positioned at a certain distance from the surface, while a feedback loop keeps the system in or close to resonance. Now, either the amplitude or the frequency is modulated. In the frequency modulation (FM) mode, the cantilever is driven to oscillate at its eigenfrequency at a constant oscillation amplitude. Varying tip-sample forces will result in a change of the eigenfrequency, which can be be related to the force gradient (see section 2.8). In the amplitude modulation (AM) mode, the system is driven at a constant amplitude close to its eigenfrequency. Here changes in the tip-sample force result in an in- or a decrease of the oscillation amplitude.

In this thesis we used non-contact frequency modulated AFM. The cantilever used is a quartz tuning fork. These have been proposed to enable very small oscillation amplitudes due to their high stiffness [46]. These small amplitudes of $100\,\mathrm{pm}$ or lower enable simultaneous STM and AFM measurements, as higher amplitudes are not convenient for STM due to its exponential current to tip-sample distance relation. In the next parts we introduce the
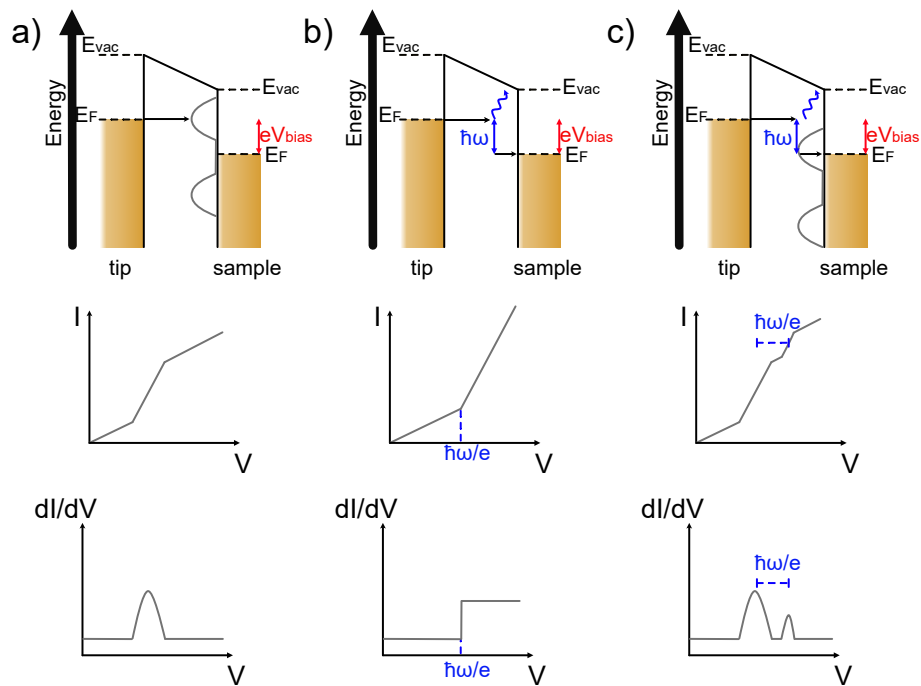
Figure 2.6: Illustration of elastic and inelastic tunnelling processes. a) Elastic tunnelling into an unoccupied state. b) When the bias voltage matches or surpasses the threshold voltage of an inelastic excitation, a second tunnelling path opens. c) If the unoccupied state is for example a molecular orbital, tunnelling into vibronic states is possible. Adapted from [27].

operation principle of the non-contact FM AFM and see, what complementary information can be gained with its spectroscopic methods.

2.8 The driven harmonic oscillator

Usually one can model the tuning fork as a damped harmonic oscillator, which is driven by an external force F_D at a frequency ω. Its equation of motion is given by:

$$m\ddot{x} - \frac{m\omega_0}{Q}\dot{x} + k_0 x = F_D cos(\omega t). \tag{2.12}$$

Here, m is the mass of the oscillator, ω_0 is connected to the resonance frequency f_0 via $2\pi f_0$ and Q is the quality factor of the oscillator. In textbooks, the term $\frac{\omega_0}{Q}$ is attributed to a damping constant. The solution of this equation is given by [48]:

$$z(t) = A(\omega)cos(\omega t - \phi(\omega)) \tag{2.13}$$

This describes an oscillator, which can move only in z-direction and which amplitude and phase shift depend on the driving frequency ω . The amplitude is given by:

$$A(w) = \frac{k_0}{m}\frac{A_D}{\sqrt{(\frac{\omega_0}{Q})^2\omega_0^2 + (\omega_0^2 - \omega^2)^2}}. \tag{2.14}$$

For $\omega = \omega_0$ equation 2.14 simplifies to just $A(\omega_0) = A_D Q$. We already mentioned that in FM AFM the amplitude is constant and changes in the resonance frequency are measured. The resonance frequency in this model is given by:

$$f_0 = \frac{1}{2\pi}\sqrt{\frac{k_0}{m}}. \tag{2.15}$$

When the oscillator is now brought closer to a substrate, it experiences forces, which change the effective stiffness of the oscillator by [48]:

$$k^* = k_0 - \frac{\delta F_{TS}}{\delta z}. \tag{2.16}$$

Therefore, the new resonance frequency is given by:

$$f^* = \frac{1}{2\pi}\sqrt{\frac{\frac{\delta F_{TS}}{\delta z}}{m}}. \tag{2.17}$$

As a result one can describe the frequency shift, which is the change in frequency from the original resonance frequency without tip-sample forces, for small oscillation amplitudes as :

$$\Delta f = -\frac{f_0}{2k_0}\frac{\delta F_{TS}}{\delta z}. \tag{2.18}$$

As a consequence the frequency shift is directly proportional to the tip-sample force gradient. Experimentally the frequency shift is very easily accessible by keeping the oscillator in resonance and recording the change in frequency. However, the force gradient is often a sum of several forces acting between tip and sample. We now want to present the most important ones and elaborate on how one can distinguish them in the experiment.

2.9 Forces in AFM

Chemical forces

Chemical forces in AFM are short-range forces. They are usually modelled with a Lennard-Jones potential, which is also used to describe the binding of atoms to molecules [49] and is shown in figure 2.7 a):

$$E_{LJ} = \epsilon[(\frac{z_m}{z})^{12} - 2(\frac{z_m}{z})^6]. \tag{2.19}$$

Here, ϵ is the binding energy and z_m is the binding distance. From equation 2.19 one can easily see, that the Lennard-Jones potential has two main terms, one with a positive sign that scales with the power to 12 and one with a negative sign that scales to the power of 6. The term which scales to the power of 12 is the repulsive part of the potential. It originates from the Pauli repulsion: when two atoms are brought into close proximity, their atomic orbitals will start to overlap. Eventually, two electrons would have to be in the same quantum state, which is strictly forbidden by the Pauli principle. Therefore, higher states of the atoms will be populated instead, resulting in an overall increase in energy. For us very short distances, at which a tunnelling current starts to flow, are especially interesting, as they allow for simultaneous STM/AFM measurements. Therefore for combined STM/AFM measurements the Lennard-Jones force plays an important role.

At larger distances the term with power to 6 is more relevant. It arises from van-der-Waals and dipole-dipole interactions, which are considered to stem from only one atom. As van-der-Waals forces are relatively long-ranged this assumption does not hold true completely and we will treat them separately in this section.

Chemical forces are the only forces with a repulsive character. Therefore, when accessing this regime one can get predominant contributions from the chemical force and learn about the chemical properties of atoms and molecules [50].

Van-der-Waals forces

Van-der-Waals forces arise from dipole-dipole interactions between single atoms and molecules. Typically, they are categorised in three interaction types: the Keesom force describes the interaction between two permanent dipoles [52]. The Debye force describes the case, where a permanent dipole acts on a polarizable atom or molecule and therefore induces a dipole [52]. The third case, the London dispersive force, categorises the spontaneous induction of a dipole moment in molecules, which do not exhibit a permanent dipole moment [53]. As mentioned above, considering the interactions between only two atoms or molecules, the total van-der-Waals forces are rather weak. However, parts of these are additive, so considering structures as the tip in our experiments can therefore lead to a substantial contribution to the total force. When the tip is modelled as a sphere of radius R, the total van-der-Waals forces is given by [54]:
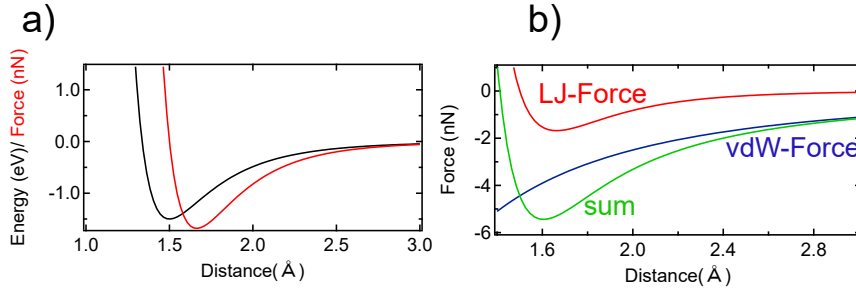
Figure 2.7: Chemical forces in AFM. a) Modelled Lennard-Jones potential and the corresponding force. The binding energy ϵ and distance z_m can be extracted from the potential minimum, which are in this case $\epsilon = 1.5 eV$ and $z_m = 1.5$ Å. b) Lennard-Jones force and a short range van-der-Waals force are shown, as explained in the text. The sum of both forces is shown in green. For short distances the sum resembles the shape of the Lennard Jones force reasonably well, even though the position of the potential minimum is slightly shifted. For larger distances the van-der-Waals forces dominate the spectrum. The Lennard-Jones force has the same parameters as given in a), the van-der-Waals force is modelled with $R = 20$ Å and $H = 3$ eV. Adapted from [51].

$$F_{vdW} = -\frac{HR}{6z^2}, \tag{2.20}$$

where H is the material dependent Hamaker constant. The contributions of these van-der-Waals forces are shown in figure 2.7 b) together with the Lennard-Jones force. One can see that for small distances the sum of the two forces resembles the shape of the Lennard-Jones force pretty well, even though the minimum is slightly shifted in distance. For larger distances however, the total force is almost entirely stemming from the van-der-Waals forces. So to minimize their contribution it is desirable to have a very sharp tip. The other way around, looking at the frequency shift at large tip-sample distances can give a first indication of the sharpness of the tip. Still, the model in equation 2.20 only holds, if the tip is of a round shape. For different tip shapes, other relations hold true [55]. To finish the description of the relative forces in AFM, we now want to look at the last relevant force, the electrostatic force.

Electrostatic forces

Electrostatic forces are the longest ranged forces in AFM. They manifest, if there is a potential difference between tip and sample, which can be intrinsically due to different work functions or induced by an applied bias voltage. Simplified, the force can be modelled as the electrostatic force of a capacitor [56]:

$$F_{el} = \frac{1}{2}\frac{\delta C}{\delta z}V^2. \tag{2.21}$$

Here, C is the capacitance of the capacitor. The voltage, which is effectively inside the capacitor is $V = V_b - V_{CPD}$, with V_{CPD} being the contact potential difference, which is the difference of the work functions of the two materials. Equation 2.21 is an inverted parabola, as $\dfrac{\delta C}{\delta z} < 0$, which maximum is at $V_b = V_{CPD}$. This point corresponds visually to the bias

voltage needed to compensate the contact potential difference between the two metals. This voltage can be determined experimentally and is the fundamental idea behind a technique called Kelvin probe force microscopy (KPFM), which will be introduced in the next section.

2.10 Kelvin probe force microscopy: probing local and non-local charges

Figure 2.8 a) illustrates the general case of two metals with different work functions, which are spatially separated from one another. If they are now brought closer together or are contacted, as shown in b), their Fermi levels will align. This happens by electron transfer to the metal with the higher work function. As a result space charges are formed at the interfaces, leading to an electrostatic force between the two metals. Now an external bias voltage can be applied to partially compensate for the electric field between the two metals. The bias voltage, which completely compensates for it, then gives the contact potential difference.

This concept can be used to determine the local electronic structure via Kelvin probe force microscopy. There, an additional ac voltage is applied to the dc voltage. The changing voltage will invoke a change in the frequency shift in the FM mode. Then, another feedback loop is employed to adjust the dc bias voltage such, that the response is minimal. Naturally, one gets this minimal response, if the dc bias voltage exactly matches the CPD, as can be seen here:

$$\Delta f \propto -\frac{1}{2}\frac{\delta^2 C}{\delta z^2}(V_{bias} - LCPD)^2. \tag{2.22}$$

To arrive at this expression we formed the derivative of equation 2.21 once more. Equation 2.22 is an inverted parabola, which curvature is given by the second derivative of the capacitance in z-direction. The maximum of the parabola is exactly at $V_{bias} = LCPD$. Usually other forces, like the chemical and van-der-Waals forces contribute to the offset of the parabola, but as they are not bias-dependent, they will not change during the measurements. This method has been shown to provide complementary information to the pure Δf measurements with an AFM [57]. Depending on the AFM used, this method can also yield a high spatial resolution and therefore often is referred to measure the local contact potential difference (LCPD).

The spatial resolution of this method was even further improved in 2009 by Gross and co-workers [58]. They used a qPlus [46] sensor design, which allows the usage of very small oscillation amplitudes. This is necessary for a higher contrast formation due to nature of the electrostatic force: it is long ranged. In the far field, AFM is sensitive to the effective electric field of all charges in a certain vicinity. To be able to probe the electric field of single atoms or molecules one has to therefore measure at smaller tip-sample distances. Gross and co-workers used $\Delta f - V$ spectroscopy to determine the charge states of single gold and silver atoms on sodium chloride layers grown on a copper substrate. Such spectra are then fitted with equation 2.22, from which the LCPD can be directly extracted. The parabolas shift for differently charged atoms, leading to different LCPD values. This method is slower
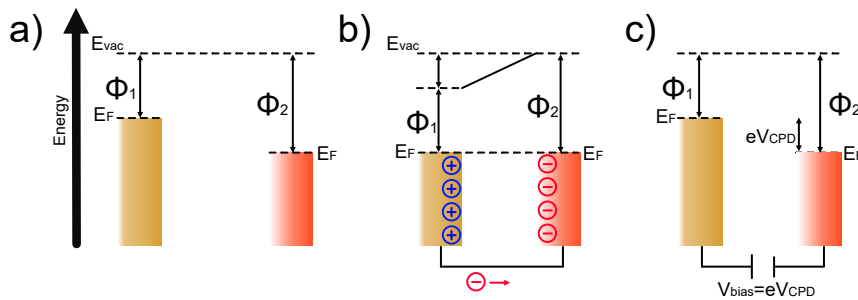
Figure 2.8: Contact potential difference between two metals. a) Two metals with different work functions are depicted. b) When the spacing between the two metals is short enough, electrons can tunnel into the metal with the higher work function. Alternatively the two metals can also be contacted, enabling the same process. This leads to a charge accumulation at the interfaces, which creates an electrostatic force between the two metals. c) This electrostatic force can be compensated by applying a bias voltage. The voltage necessary to compensate the CPD is $V_{bias} = \dfrac{\Delta \Phi}{e} = V_{\text{CPD}}$. Adapted from [51].

than the one described earlier, but gives a much higher, even intramolecular resolution of the charge distribution of nanostructures [59].

Still, the method exhibits two fundamental limits: first, it is not a quantitative measure for the electric charge. Second, when coming to very close tip-sample distances, where the electron cloud of atoms or molecules is penetrated, the background forces can also become bias dependent [60]. A first approach to overcome this limit was proposed by Albrecht and co-workers [60]. They recorded additional $\Delta f(z)$ spectra at different bias voltages to disentangle the electrostatic contributions from non-electrostatic contributions. With this they were able to make a first attempt to quantify the electronic charges within single molecules. Still, this method contains several uncertainties, which leads to high errors in the measurements. Therefore more adjustments have to be made before quantitative measurements are possible.

2.11 Specifications of the used scanning tunnelling microscopes

The experiments performed in this thesis were conducted with three different STMs, two Createc systems and one SPECS system. Their general functionality is identical, however some specifications differ. Here, we describe the design and working principle of the machines.

All experiments were performed under ultra-high vacuum conditions. For this several different types of pumps are used, namely turbomolecular pumps, ion-getter pumps, titanium sublimation pumps and cold traps. The vacuum chamber is divided in a preparation chamber and the actual STM chamber by a gate valve. The transfer between the two chambers is

done by a sample manipulator.

The preparation chamber is mainly used for the cleaning of samples by repeated cycles of sputtering and annealing as well as the growth of thin films and evaporation of atoms and molecules. Therefore it is equipped with a sputter ion gun, which is connected to a gas line via leak valve. We used neon gas for sputtering. Other leak valves and gas lines can be connected to the preparation chamber if needed. Moreover several ports for metal and molecular evaporators exist. The samples can be heated and cooled on the manipulator.

The STM chamber consists of the scanning head, which is thermally connected to a cryostat bath. The cryostat consists of two parts: an outer and inner part. The inner part is filled with liquid helium and determines the base temperature, which is about $4.6\,\text{K}$. The outer part is filled with liquid nitrogen, which reduces the helium consumption. Due to the low temperatures, the cryostat also serves as a cold trap, leading to even lower pressures in the STM chamber. These low temperatures lead to a higher energy resolution and less thermal drift of the STM tip and adsorbates on the surface. Moreover, the whole vacuum chamber is connected to pneumatic feet, which can decouple the chamber from the floor and thus reduce vibrations of the systems.

We said earlier that three different machines were used in this thesis. The two Createc systems provide identical tools for the purpose of this thesis. Their scanning head can be equipped with a qPlus sensor and therefore be used for simultaneous STM and AFM measurements. Moreover, the head is equipped with magnets for eddy current damping, which reduces the mechanical noise.

The SPECS STM is designed to reach even lower temperatures for a better energy resolution. Therefore, beside the helium cryostat, another bath exists, the 1 K pot. There, helium gas is pumped through a set of capillaries and precooled by the cryostat. It is then expanded into the 1 K pot by means of adiabatic gas expansion and can reach temperatures of about $1.1\,\text{K}$. The JT STM moreover has two superconducting coils, which can create an out-of-plane magnetic field, and a sample heater for variable temperature measurements. Also an evaporator port exist, which enables direct evaporation inside the STM head. This allows for lower sample temperatures during evaporation than in the preparation chamber, leading to less diffusion and therefore less clustering of the adsorbates.

The scanning head is electronically connected to a computer via a DSP board. The recorded data in this thesis was analysed with SpectraFox [61], WSxM [62] and IgorPro.

We described before the possibilities of sample preparation. In the following chapter we want to describe it in more details for the samples used in this thesis.

2.12 Samples

As mentioned earlier, we investigated different nanostructures on single layer MoS_2 in this thesis. We grew these on a Au(111) substrate. We now want to present the growth procedure and the most important electronic properties of both, MoS_2 and Au(111), as they will be important for reference later on.
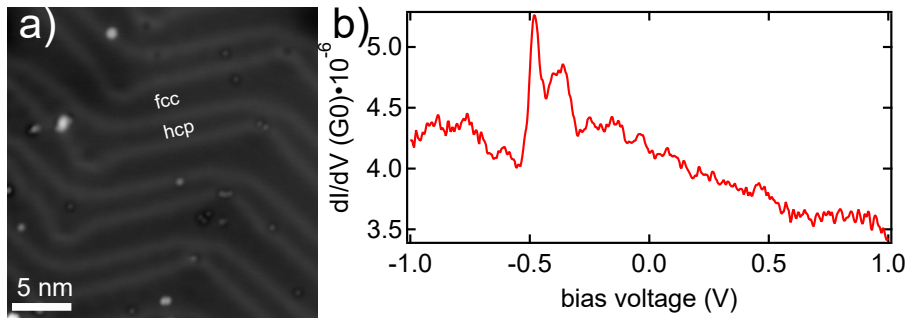
Figure 2.9: Au(111) surface. a) STM topography of the Au(111) substrate. The topography was recorded at a setpoint of $100\,\text{mV}$ and $100\,\text{pA}$ b) Typical dI/dV spectrum recorded on the Au(111) surface. One can see the surface state at around $-490\,\text{mV}$. The spectrum was recorded at a setpoint of $1\,\text{V}$ and $300\,\text{pA}$.

2.12.1 Au(111)

Gold is very common choice as a substrate in STM, as it is a very inert material and therefore easy cleanable. This especially holds true for crystals polished in the [111] direction. Figure 2.9 a) shows an example of a Au(111) surface. Darker appearing regions with different width are separated by bright lines. This stems from the well known surface reconstruction of the Au(111) surface: regions of face center cubic (fcc) and hexagonal closed packed (hcp) stacking orders alternate. They are separated by so called soliton lines, which appear brighter in the topography, as they are slightly stacking out of the surface. The soliton lines periodically rotate around $120°$, forming a zig-zag structure, which is referred to as herringbone reconstruction. Figure 2.9 b) shows a typical dI/dV spectrum recorded on the Au(111) substrate. Apart from a linear background a step-like feature around $-490\,\text{mV}$ can be seen, which arises from a surface state [63]. Verifying that these structural and electronic properties can be resolved is usually a good indication for the reliability of the STM tip's apex.

To clean the Au(111) substrate we applied repeated cycles (minimum of two) of sputtering and annealing to it. The sputtering was either done under static conditions (no pumps connected) at $1.5 \times 10^{-4}\,\text{mbar}$ or with the turbomolecular pump connected at $2 \times 10^{-6}\,\text{mbar}$ for about 15 minutes. The annealing was performed around $820\,\text{K}$ for about 10 minutes. This procedure usually gives reliably clean and large terraces, which is a necessity for the growth of single-layer MoS_2 islands.

2.12.2 (Single-layer) Molybdenum disulfide

Molybdenum disulfide belongs to the class of transition metal dichalcogenides (TMDCs), which recently has drawn a lot of attention due to its promising electronic and optical properties, which to some extent resemble those of graphene for device usage [64, 65]. As the name implies, the TMDC consist of a transition metal (for MoS_2 it is molybdenum), which is sandwiched between two chalcogenides (for MoS_2 it is sulfur), which is illustrated in figure 2.10 a) for a MoS_2 layer. In a bulk structure, the individual layers are only weakly coupled between each other via van-der-Waals interactions. Depending on the composition

of the TMDC, the electronic structure varies. For example, they have been reported to be superconductors [66], spin-liquids [67] or semiconductors with optical band gaps varying between 1 and 2 eV [68, 69]. Due to their weak interlayer binding, the TMDC crystals are easily exfoliated. This enables the study of single-layer TMDCs and heterostructures, which on top provides a huge tune-ability due to the vast selection of different materials [70].

It was found that the electronic structure of MoS_2 actually varies depending on the number of the layers. Whereas for bulk MoS_2 an indirect band gap of about $1.23\,eV$ was found in experiment, the band gap for a single-layer is about $1.9\,eV$ and direct at the K point of the Brillioun zone [71, 72]. This, for example, leads to an emerging photoluminescence in the single-layer, which was quasi absent for the bulk MoS_2 [73, 74].

While these properties are certainly intriguing to study, it is very challenging to study this samples with STM. Therefore attempts have been made to grow single-layer MoS_2 islands on metal substrate, such as Au or Ag. While at first only the growth of nanoclusters was achieved [75, 76], soon after also larger islands of several tenths of nanometers and more were grown successfully [77, 78].

The electronic structure of the MoS_2 layer on Au(111) is altered from the one of the freestanding single-layer due to hybridisation with the metal substrate [79]. Still, it provides several interesting optical and electrical properties [80, 81] and has been established as an excellent decoupling layer for molecules [43, 82–84]. We want to make use of both these properties in the course of this thesis and therefore describe the general properties of MoS_2 on Au(111) now in more detail.

We used two different methods to grow single-layer islands of MoS_2 on Au(111). The first method consists of evaporating molybdenum on a clean Au(111) sample in a H_2S atmosphere of about $2 \times 10^{-5}\,mbar$. Subsequently, the sample is annealed to $820\,K$ for about 20 minutes. This method yields coverages as can be seen in figure 2.10 b): several MoS_2 islands of sizes of tenths of nanometers can be seen. The other growing method combines both steps at the same time, the molybdenum is evaporated already on the hot sample in the H_2S atmosphere for about 40 minutes. This leads to larger island sizes, which is suggested to be promoted by the higher mobility of the Mo atoms on the hot Au substrate [85]. Figure 2.10 c) shows a zoom into one of the islands shown in b). One can clearly see a modulation in the topography, which is in the order of $3.3\,nm$ and therefore a magnitude bigger than the atomic spacing [86]. It results from a lattice missmatch between the Au(111) lattice and the MoS_2 lattice and is referred to as moiré superstructure [33]. Moreover, several dark spots and dark areas can be seen in the topography. These stem from point and areal defects and will be covered in more detail in section 4.

Figure 2.11 a) shows a representative constant-height dI/dV spectrum recorded on a MoS_2 island. One can see several resonances at positive bias, around $900\,mV$ (labelled Γ_1), around $1.4\,V$ (labelled Γ_2) and around $1.9\,V$. At negative bias only a resonance around $-2.1\,V$ is present. In b) a constant current spectrum is shown. The same peaks can be identified, with slightly shifted positions. In addition, a small peak at around $500\,mV$ can be seen. Krane and co-workers have identified it to arise from tunnelling into the conduction band minimum [33]. They found the electrical band gap of MoS_2 on Au(111) to be around $1.9\,eV$. To determine it, they had to use a novel method recently established in [87], where the tip height is modulated to gain enhanced sensitivity for states with $k_\parallel$.

We have mentioned before that the MoS_2 layer on Au(111) exhibits a moiré pattern. The STM topographies are always a convolution between topographic and electronic structure,
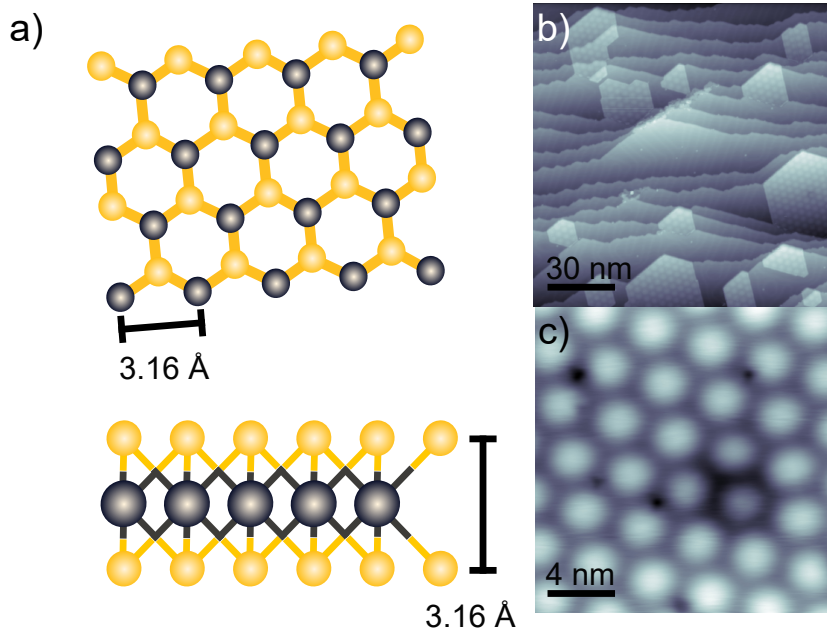
Figure 2.10: Structure of MoS$_2$. a) Stick and ball model of the MoS$_2$ lattice in the top view (upper) and side view (lower). The yellow balls represent the sulfur atoms and the black ones represent the molybdenum atoms. b) STM topography of MoS$_2$ islands grown on Au(111). c) Zoom into a MoS$_2$ island. The dark spots correspond to point and/or areal defects in the layer. The topographies were recorded at a setpoint of $100\,\text{mV}$, $500\,\text{pA}$ (b) and $900\,\text{mV}$, $100\,\text{pA}$ (c).

therefore its natural to ask, if the electronic structure varies along the moiré or if the corrugation is pure topographic. Figure 2.11 c) shows two constant-height dI/dV spectra, which were recorded on the spots shown in the topography in the inset, marked with the respective colours of the spectra. The black spectrum was recorded on a moiré maximum and the grey one on a moiré minimum. Comparing the two spectra, the most striking difference is the shift of the state at negative energies, which amounts to about $200\,\text{mV}$. It was proposed that it origins either due to a different hybridization with the Au bulk states or a more effective electronic screening [33]. Also the Γ_2 state shifts along the moiré, but not as much. All in all, it is apparent that the electronic structure varies locally along the moiré, which has been also recently supported by DFT calculations [88]. This finding will be important later on in this thesis.

It was reported previously that the apparent height of MoS$_2$ islands on Au(111) is around $2.3\,\text{Å}$ [77]. This value is smaller than the height of a freestanding MoS$_2$ layer, which is around $3.16\,\text{Å}$. We also looked at the apparent height of MoS$_2$ islands on Au(111), as shown in figure 2.12 a) and d). In a) a topography of a MoS$_2$ islands is shown. The red bar represents the line, the profile of which is shown in d). We find an apparent height difference between the Au(111) surface and the moiré dome of $2.4\,\text{Å}$, which is very similar to the previously reported value. As this apparent height is still a convolution between electronic structure and topography, we in addition performed $\Delta f - z$ spectra, to extract the deconvolved topography of the islands. Figure 2.12 b) shows two approach curves for
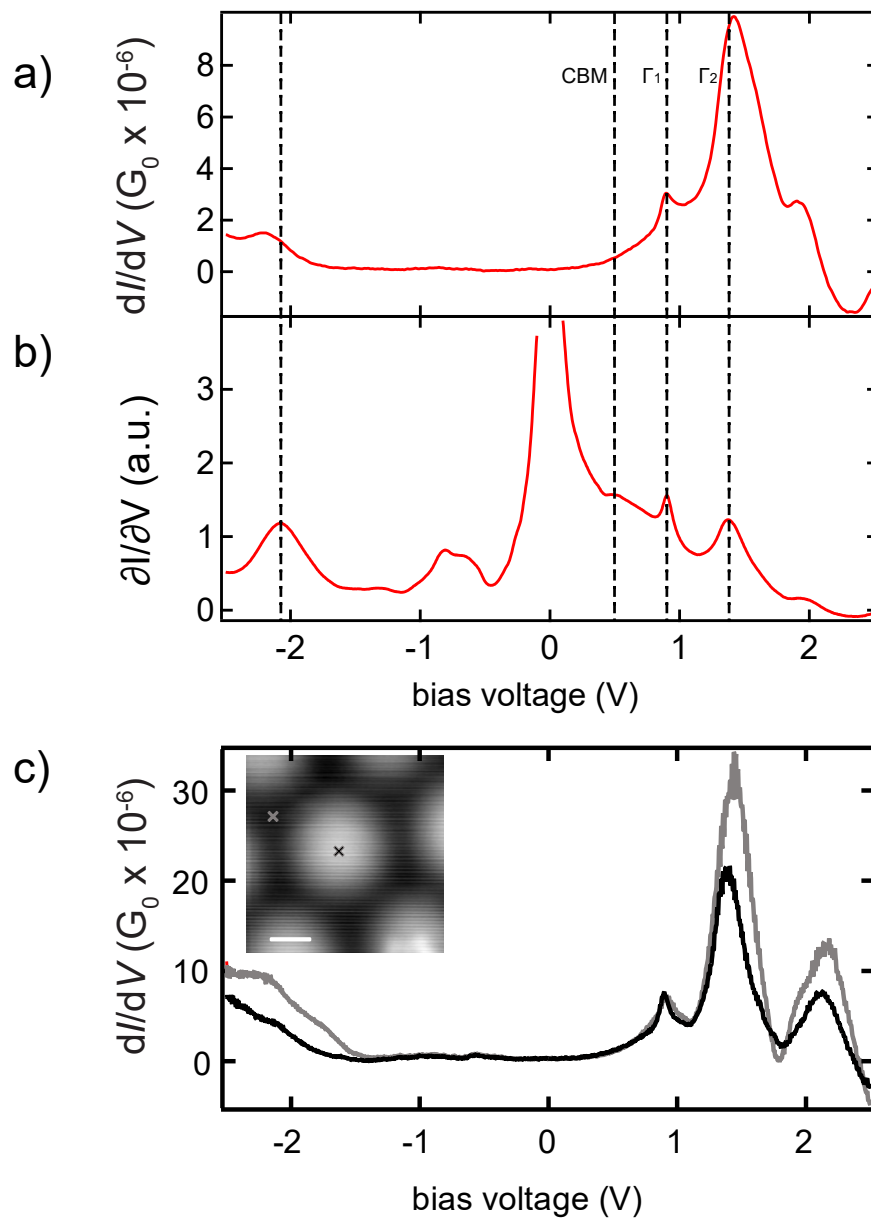
Figure 2.11: Electronic structure of MoS_2 on Au(111). a) Constant-height dI/dV spectrum. b) Constant-current dI/dV spectrum. The peak intensities and positions vary in comparison to the constant-height spectrum. A small additional peak around $500\,mV$ appears. c) Constant-height spectra recorded on the moiré dome and the valley, as indicated in the inset. The spectra were recorded at a setpoint of $2.5\,V$ and $500\,pA$ (a), at a constant current of $300\,pA$ (b) and at $10\,mV$ and $20\,pA$ with the tip additionally retracted by $220\,pm$ (c). The STM topography in the inset was recorded at $50\,mV$ and $100\,pA$, the scale bar amounts to $1\,nm$.

the MoS$_2$ island and for Au(111). To record those, the tip was positioned over the spot at the same setpoint at which the topography in a) was recorded. After that the feedback was switched off and the bias voltage was set to $50\,\mathrm{mV}$ to minimise background forces. Then the tip was approached towards the sample. From b) one can see that the curve recorded on the MoS$_2$ reaches the more repulsive region of the forces (the local minimum) around $0.35\,\text{\AA}$ earlier. Therefore the real height of the MoS$_2$ islands on Au(111) is $h_{STM} + h_{AFM} = 2.05\,\text{\AA}$. This is approximately two thirds of the height of the freestanding MoS$_2$ layer and suggests that the growth of the MoS$_2$ leads to a partial reconstruction of the Au(111) surface. This also manifests itself in an absence of the herringbone structure under the MoS$_2$ islands. Still, the determination of the height of the MoS$_2$ layer is not error free, as the background forces over the Au(111) substrate and the MoS$_2$ may vary. Therefore, to learn about the exact nature of the MoS$_2$/Au(111) interface, further investigations have to be performed.

The same experiment can also be done to extract the deconvolved height difference between the moiré minima and maxima. We find that the $\Delta f - z$ curves vary by roughly $10\,\mathrm{pm}$, leading to a total height difference of $32\,\mathrm{pm}$. So even though the difference between STM topography and the approach spectra is not huge in absolute values, still there is an electronic variation even at low bias voltages along the moiré structure. We will study those variations in more detail in their interplay with single atoms in sections 5 and 6. Moreover we will study the decoupling properties of the MoS$_2$ layer on high dipole molecules in section 7.

a) 2nm

b) frequency shift (Hz) / Δz (pm)
~0.35Å
MoS$_2$
Au(111)

c) STM: Δz= 2.4Å
AFM: Δz= -0.35Å

d) apparant height (Å) / distance (Å)
2.4Å
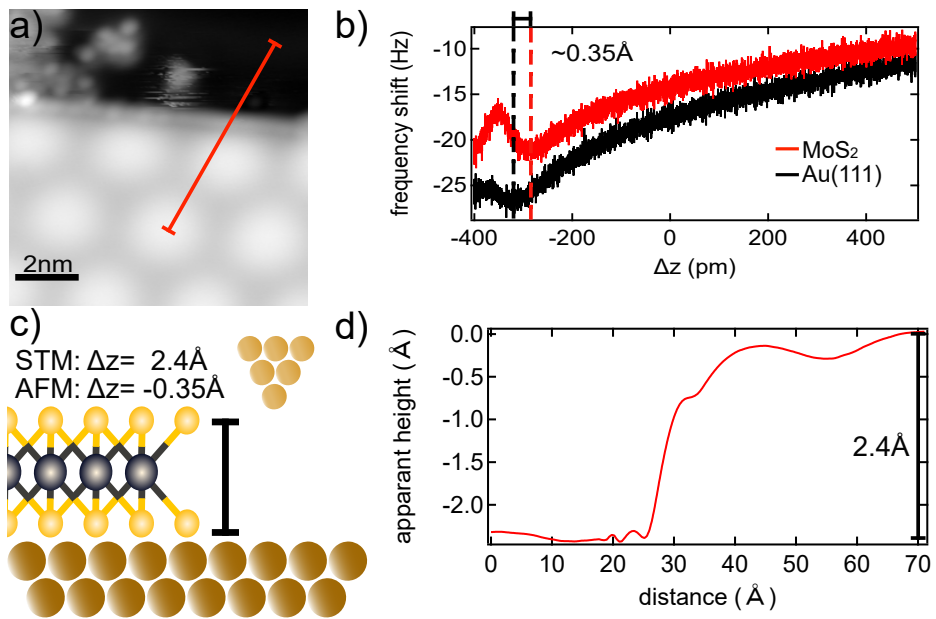
Figure 2.12: Determination of the height of the MoS$_2$ layers on Au(111). a) STM topography of a MoS$_2$ island on Au(111). The topography was recorded at a setpoint of $1\,V$ and $30\,pA$ b) $\Delta f - z$ spectra recorded on the bare Au(111) substrate and the MoS$_2$ island. The feedback was stabilised at the same parameters as the topography in a). After the feedback was switched off, the bias voltage was changed to $50\,mV$. c) Illustration of the MoS$_2$ island height in comparison to the Au(111) substrate. d) Topography along the red bar shown in a).

3 Single-atom magnetism on surfaces

In the course of this thesis we will study several cases of single-atom magnetism. For a proper description of the experimental findings, we therefore want to introduce the theoretical framework of the occurring processes in this section. At first we illustrate how magnetic anisotropy influences the excitation spectra of single atoms. Afterwards we have a look at the coupling mechanisms between single atoms, which will be important for the results in section 6. Following up we will introduce the Kondo effect, which describes the formation of a many-body state, which arises from exchange interaction of magnetic impurities with metal host electrons. Finally, we will illustrate how the Kondo effect and magnetic anisotropy can be detected with STS and how these two phenomena compete with each other at low energy scales, which will be important in section 5.

3.1 The effective spin Hamiltonian

The origin of magnetism in single atoms and molecules are unpaired spins, which lead to a non-zero spin state of the system. In gas phase the ground state configuration, from which one directly can see the spin state, can be purely determined by Hunds rules: first, the total spin **S** of the system is maximised, which is a direct consequence of the exchange interaction between the single electrons. Secondly, the total angular momentum **L** is maximised. At last, the coupling of **S** and **L** to the total angular momentum **J** is determined to be either parallel or anti-parallel, depending on the filling of the respective electron shell. Applying these rules for example for an iron atom would lead to an electron configuration as shown in figure 3.1 a), which leads to a total spin state of 2. This configuration may alter, if the atom is exposed to a crystal field, as illustrated in b). Avoiding Pauli repulsion due to wave function overlap of the d-orbitals with the crystal field may be now energetically more favourable than occupation of the orbitals via Hunds rules. Therefore an iron atom in a tetrahedral crystal field, as illustrated, would have a spin state of 1.

As one can see, we labelled the d-orbitals differently in figure 3.1 a) and b). While in a) the d-orbitals which solve the Schrödinger equation are shown, b) implies linear combinations of those orbitals, which are formed such that the orbital angular momentum of the respective orbitals is equal to zero. Therefore the total angular momentum of an atom in a crystal-field is usually quenched. However, via second order perturbation theory, the states split by the crystal field can be coupled to states lying at higher energies. This restores a finite orbital angular momentum and allows to couple it to the total spin momentum via spin-orbit coupling. This results in a sizeable magnetocrystalline anisotropy, which enforces a preferred direction of the spin in space [89]. It can usually be modelled in a new effective Hamiltonian, called Spin Hamiltonian, which treats the system in terms of its spin components. It can be written as:
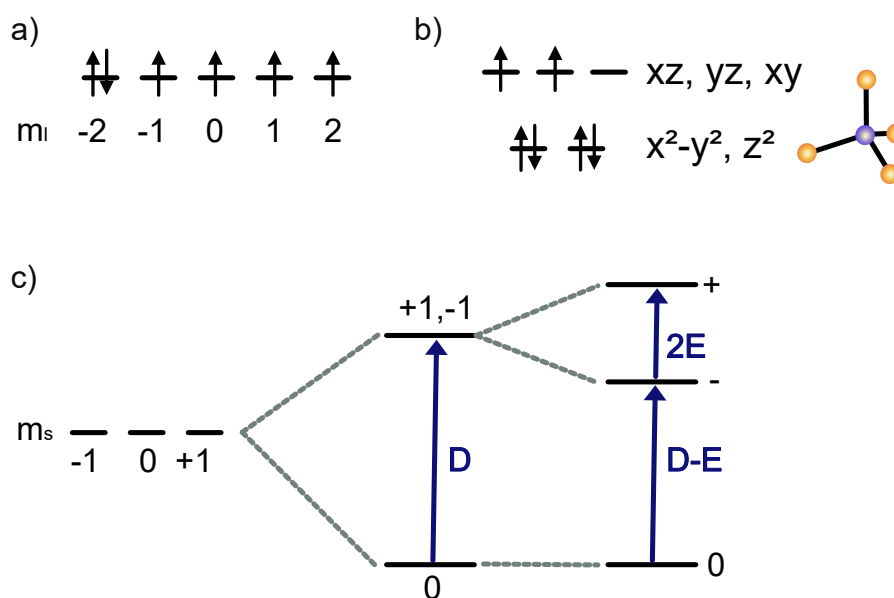
Figure 3.1: Effect of crystal-field splitting and magnetic anisotropy on the electronic config-
uration of an atom. a) Application of Hunds rules for an iron atom. This leads to
a gas phase spin state of **S**=2. b) In a crystal field (here tetrahedral) the d-orbitals
can become non-degenerate and the spin state of the system can change as a
result. In this case the crystal-field splitting would lead to a spin state of 1. c)
When no spin-orbit coupling is present, all levels of the spin projections m_S
are degenerate. When an axial anisotropy D is introduced to the system, the
degeneracy is lifted. If on top of that also a transverse anisotropy is introduced
into the system, the out-of-plane levels are also lifted, leading to a formation of
the $|+\rangle$ and $|-\rangle$ states. Adapted from [38].

$$\hat{H} = g\mu_B \mathbf{B} \cdot \hat{\mathbf{S}} + D\hat{S}_z^2 + E(\hat{S}_{x^2} - \hat{S}_y^2). \tag{3.1}$$

Here, g is the gyromagnetic factor, μ_B is Bohr's magneton, $\mathbf{B}$ is an externally applied magnetic field, $\hat{\mathbf{S}}$ is the total spin operator, D is the axial anisotropy and E the transverse anisotropy. The two latter are parametrised as $D = \lambda^2/2(\Lambda_{xx} + \Lambda_{yy}) - 2\Lambda_{zz}$ and $E = -\lambda^2/2(\Lambda_{xx} + \Lambda_{yy})$. Here, on the other hand, the Λ_{ii} terms represent the magnitude of the unquenched orbital angular momentum in ii direction [90]:

$$\Lambda_{ii} = \sum_n^{excited\ states} \frac{|\langle\phi_0|\hat{\mathbf{L}}_\mathbf{i}|\phi_n\rangle|^2}{E_n - E_0}. \tag{3.2}$$

From equation 3.1 it follows, that the different m_s eigenstates are now split in energy. This is also illustrated in figure 3.1 c) for a spin 1 system: when the transverse anisotropy is zero, the splitting is given by the axial anisotropy D and the $m_s = +1, -1$ states are degenerate. The sign of D determines, which state is the ground state. The example in c) shows the case for $D > 0$, which favours the lower spin projection, whereas the case of $D < 0$ favours the higher spin projection. An addition of a transverse anisotropy leads to a mixing of the former $m_s = +1, -1$ states to $|+\rangle = \frac{1}{\sqrt{2}}|+1\rangle + \frac{1}{\sqrt{2}}|-1\rangle$ and $|-\rangle = \frac{1}{\sqrt{2}}|+1\rangle - \frac{1}{\sqrt{2}}|-1\rangle$. Those two states are split by an energy of 2E.

One can determine the magnetic anisotropy of single atoms with IETS. The energy splitting of the spin projection levels now allows for spin-flip excitation into the energetically higher states for transitions ensuring $\Delta m_s = 1$. The energy of the excitation, detectable as a step in the $\mathrm{d}I/\mathrm{d}V$ signal as described earlier, is directly proportional to the axial and transverse anisotropy as we showed in this chapter.

The favourable spin direction, given by the anisotropy, can be perturbed and altered via coupling of the atom to other impurities and host electrons. We describe these processes and their impact on the anisotropy in the next sections.

3.2 Coupling between single magnetic atoms

There are several coupling mechanisms for pairing individual magnetic atoms, which are usually referred to as exchange interactions. They can be mediated directly via the overlap of atomic orbitals, through hopping processes with non-magnetic orbitals or by substrate electrons. Here, we want to describe these processes briefly and how one can distinguish them, as it will be important later on in this thesis in section 6.

3.2.1 (Direct) exchange interaction

The direct exchange interaction becomes relevant, when the wavefunctions of two magnetic impurities start to overlap. Depending on the strength of the overlap, this can lead to a ferromagnetic or anti-ferromagnetic alignment of the spins. As the wavefunctions of the two orbitals only overlap at very short interatomic distances, the direct exchange interaction is mostly only relevant at those short distances.
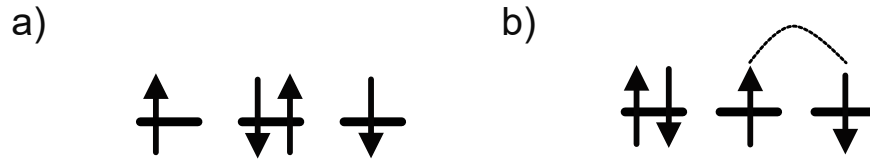
Figure 3.2: Illustration of the superexchange coupling. a) Two magnetic orbitals are occupied with one electron each, whereas the non-magnetic orbital is doubly occupied. b) In a virtual process, one electron can hop from the non-magnetic orbital to one of the magnetic orbitals, leading to an exchange coupling, as indicated with the dashed black line. Adapted from [95].

3.2.2 Superexchange interaction

Superexchange interaction was first introduced by Kramers [91] and later on refined by Anderson [92]. It basically describe a coupling mechanism between two spins, which is enabled by virtual hopping processes, mediated by bridging atoms, molecules or ions. The process is illustrated in figure 3.2: in a) the starting point is shown. Two singly occupied, magnetic orbitals coexist with a non-magnetic, doubly occupied orbital. The magnetic orbitals are spatially too far separated to be directly exchanged coupled. Now, via a virtual process, one electron of the non-magnetic orbital can hop into a magnetic orbital. As a result, the former non-magnetic orbital can now exchange couple with the other magnetic orbital, as illustrated in b) with the blue dashed line. This effectively links the two magnetic orbitals. Superexchange interaction has been observed experimentally for several phtalocyanines with magnetic centers [93–95]. In [95] the authors could determine the actual molecular orbitals involved in the superexchange interaction.

3.2.3 RKKY coupling

Another longer-ranged mediated mechanism, the so-called Ruderman-Kittel-Kasuya-Yosida (RKKY) coupling was introduced in the 1950s [96–98]. It describes the interaction between magnetic atoms on a metal surface. At sufficiently large distances the individual magnetic atoms can not interact with each other via direct exchange coupling. However, the conduction electrons in the close vicinity of the impurity get polarized. The preferred direction of the polarization oscillates with the distance between the two impurities, similar to an interference pattern [99]. The Hamiltonian for a RKKY interaction for two spins can be described as:

$$H = J_{\mathrm{RKKY}} S_1 S_2. \tag{3.3}$$

Here, J_{RKKY} is the exchange coupling term, which is proportional to [100]:

$$J_{\mathrm{RKKY}} \propto \frac{cos(2k_F d)}{(2k_F d)^2}. \tag{3.4}$$

This relation shows the above mentioned oscillatory behaviour of the RKKY coupling, a sign change in the coupling term leads to a change in the preferred coupling, from anti-

ferromagnetic to ferromagnetic or vice versa. The exponential dependence on the distance between the impurities in the denominator of equation 3.4 leads to an overall decreasing coupling strength, limiting the interaction range. Interaction ranges between 8 Å-15 Å have been reported [100,101], which are significantly higher than the ones for direct exchange coupling.

Interactions with the substrate electrons can not only lead to a coupling of impurity spins with each other, but also act as a relaxation mechanism for the respective spins or even enable an exchange coupling between the itinerant electrons and the impurity. This so-called Kondo exchange coupling is the fundamental requirement for a many-body phenomenon, called the Kondo effect, which will be discussed in the following section.

3.3 The Kondo effect

The Kondo effect describes an anomaly in the behaviour of the electrical resistance of metals with a small concentration of magnetic impurities at low temperatures. In general, the electrical resistance of metals decreases with decreasing temperature. One of the reasons for this is that at low temperatures fewer lattice vibrations are populated. As one of the main sources for electron scattering is phonons, this results in a larger overall conductivity of the metal. However, it was experimentally determined in 1934 that the resistivity of some metals started to increase again after passing a certain critical temperature [102]. Kondo provided the theoretical understanding of this effect [103,104]. He used a scattering model, which explicitly takes into account the interaction of the spins of the conduction electrons of the metal with the spin of the magnetic impurity. For this he treated the scattering as a perturbation in the s-d exchange Hamiltonian, proposed by Zener [105,106]:

$$H = \sum_{k,k'} J_{k,k'} (S^+ c^\dagger_{k,\downarrow} c_{k',\uparrow} + S^- c^\dagger_{k,\uparrow} c_{k',\downarrow} + S_z(c^\dagger_{k,\uparrow} c_{k',\uparrow} - c^\dagger_{k,\downarrow} c_{k',\downarrow})) + \sum_{k,k'} U_{k,k'} c^\dagger_{k,\sigma} c_{k',\sigma}. \quad (3.5)$$

Here, S_z and $S^\pm = S_x \pm iS_y$ are the spin operators of the spin of the d-level, $c_{i,n}$ and $c^\dagger_{i,n}$ are the annihilation and creation operators for conduction electrons with momentum i and spin n. J is the exchange coupling parameter and U is the potential scattering parameter. Those two parameters define the nature of the interaction of the impurity with the conduction electrons. One can immediately see that the first two terms in equation 3.5 represent a spin-flip process. The third term corresponds to a scattering process, where the spin of the impurity is conserved. Taking this perturbation to third order, Kondo found an additional contribution to the electric resistivity, which could explain the experimental findings.

Often, the mechanism behind this interaction is described in the so-called "Anderson single-impurity model" [107], which is illustrated in figure 3.3. The electronic structure of the impurity is simplified to one atomic orbital, usually a 3d or 4f orbital, which can be either singly, doubly or non-occupied [108]. The singly-occupied level is located at an energy ϵ_D below the Fermi energy and is separated from the doubly-occupied level by the Coulomb repulsion U_D. In general the Anderson model allows exchange processes to take place in two different ways: either the impurity level is emptied and then refilled again, as sketched in c) or it is doubly-occupied and then emptied again (b)). As shown in d),

these processes can result in an effective spin-flip of the impurity level. As discussed above, not all processes will actually flip the spin. However, taking several of these scattering events together leads to the formation of a many-body spin-excitation state, the Kondo resonance [108]. From figure 3.3 it is clear that these processes are not allowed in the classical framework. In quantum mechanics, however, they can arise as virtual processes for a short timeframe [109].

Until now we did not specify, how the Anderson model and the s-d exchange Hamiltonian used by Kondo relate to each other. These dependences were found by Schrieffer and Wolff as [110]:

$$
\begin{aligned}
J &= \frac{2}{\pi}\Delta^2(\frac{1}{\epsilon_D} - \frac{1}{\epsilon_D + U_D}) \\
U &= \frac{2}{\pi}\Delta^2(\frac{1}{\epsilon_D} + \frac{1}{\epsilon_D + U_D}).
\end{aligned}
\tag{3.6}
$$

Here, Δ is the level broadening of the d-states, which is given by $\Delta = \rho_0|V|^2$, where ρ_0 is the density of states at the Fermi level and V is the hybridization matrix element of the localized d state with the continuum of the band states of the host metal. For a spin $S = \frac{1}{2}$ the exchange coupling parameter J is always anti-ferromagnetic, which we define as positive values throughout this thesis. Moreover, we can see from equation 3.6, that the parameters in the Anderson impurity model determine the sign of the potential scattering parameter, as illustrated in figure 3.3 e)-g), at least for electron-hole symmetric systems.

Even though the above description of the Kondo-like interaction already reproduces the experimental results relatively well, it still exhibits a flaw, called the "Kondo problem". The additional term in the electrical resistivity diverges for temperatures very close to absolute zero, ultimately making the perturbative model fail at those temperatures [111]. To properly describe Kondo physics one has to differ between two different regimes, the weak coupling regime, where the above mentioned perturbative model is valid and the strong coupling regime, where different approaches have to be made [112–114].

In the next section, we want to discuss these two regimes and how they differ in STS experiments. At the end of the section we also want to discuss, how the Kondo-like exchange scattering and the magnetic anisotropy of a system scale with respect to each other.

3.3.1 The Kondo effect in STS

The Kondo effect manifests itself in STS as a resonance around zero bias [115]. The peak width is associated with a characteristic temperature, the so-called Kondo temperature T_K, which phenomenologically is the half-width at half-maximum at zero temperature [108]. For experimental temperatures lower than T_K usually the strong-coupling regime applies, whereas for the opposite case of higher temperatures than T_K, the weak coupling regimes is valid.

The strong coupling regime

The Kondo temperature in the strong coupling regime can be derived using the so-called poor person's scaling, proposed in [106, 112]. There the electron band width in the
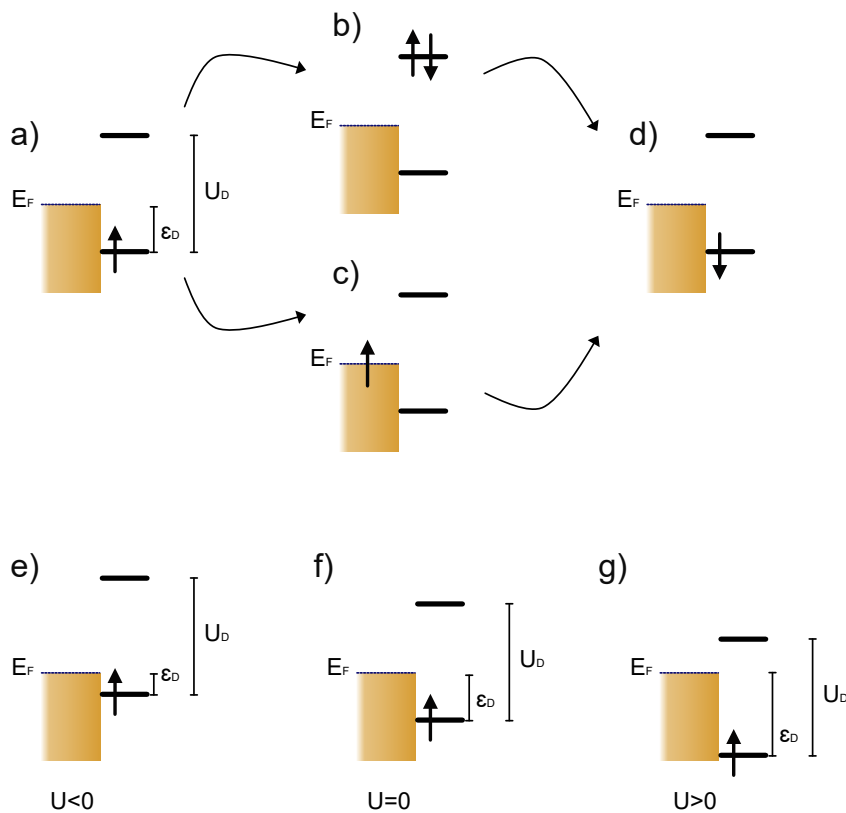
Figure 3.3: Illustration of the Anderson model to describe a single magnetic impurity on a metal substrate. a) At the start, an orbital is singly occupied and located at an energy ϵ_D below the Fermi energy. The doubly occupied level is separated from it by the Coulomb repulsion U_D. b) Scattering processes from conduction electrons at the magnetic impurity can lead to virtual excitations, which can result in a doubly occupied (b) or empty level (c). d) When relaxing into the ground state, in some of the cases the spin is effectively flipped in comparison to a). e), f), g) The energy level alignment of the singly and doubly occupied level has a direct influence of the potential scattering parameter U in the s-d orbital model. Adapted from [38].
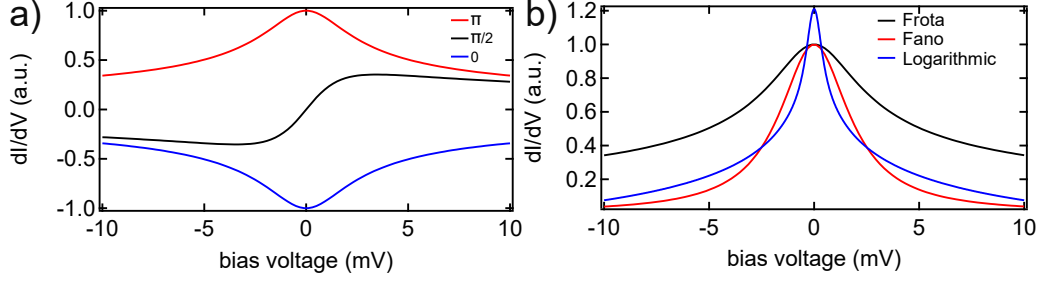
Figure 3.4: Lineshapes of the Kondo resonance in STS. a) Changes in the lineshape with varying phase factor ϕ. The resonance changes continuously from a dip-like structure ($\phi = 0$) to a peak ($\phi = \pi$). The variation in the lineshape is 2π periodic. b) Different lineshapes to describe Kondo resonances. Even though the parameter regime for the logarithmic function is different, one can still see that the width is heavily underestimated in comparison to a Fano or Frota function.

conduction band is progressively reduced, leading to a cancellation of virtual excitations. The resulting scaling equation of the exchange coupling takes the form:

$$\frac{dJ}{dlnD} = -2\rho J^2,$$ (3.7)

if the exchange coupling J is isotropic. Here, D is the electron bandwidth. Integrating equation 3.7 leads to:

$$De^{-1/2J\rho_0} \propto k_B T_K.$$ (3.8)

This scaling invariant defines the Kondo temperature T_K. It can also be expressed in terms of the parameters of the Anderson impurity model [108]:

$$k_B T_K \simeq \sqrt{2\Delta \frac{U}{\pi}} \exp\left[-\frac{\pi}{2\Delta} (|\frac{1}{\epsilon_F}| + |\frac{1}{\epsilon_F + U}|)^{-1} \right].$$ (3.9)

Note, that the above scaling equation holds true for a spin $S = \frac{1}{2}$ system. For different spin systems, equation 3.7 has to be modified slightly [116].

As mentioned above, the Kondo temperature is connected to the half-width at half-maximum Γ of an observed resonance. The energy position of such a resonance is located near the Fermi level, where the scattering processes take place, and is given by [108]:

$$E_K = \Gamma tan(\frac{\pi}{2}(1 - n_d)).$$ (3.10)

Here, n_d is the average occupation number of the d-orbital and is given by [117]:

$$n_d = -\frac{\epsilon_D}{U} + \frac{1}{2}.$$ (3.11)

Therefore, also the occupation number is related to the electron-hole symmetry in the system.

The first experiments performed on magnetic impurities on metals with STS revealed mostly asymmetric or dip-like lineshapes of the Kondo resonance [118–121]. Those lineshapes can be reproduced by the so-called Fano function [122]:

$$f(\epsilon) \propto \frac{(q + \epsilon)^2}{1 + \epsilon^2}. \tag{3.12}$$

Here, ϵ is the normalized energy defined as:

$$\epsilon = \frac{E - E_K}{\Gamma}. \tag{3.13}$$

The variable q in equation 3.12 is an interference factor, which describes the asymmetry of the lineshape. It results from different tunnelling channels available for an electron at these low bias voltages: either it can tunnel into the Kondo state or directly into the metal continuum. The ratio of those tunnelling channels effectively gives the asymmetry of the lineshape. A preferred tunnelling into the Kondo state gives a peak-like lineshape, whereas a tunnelling into the empty bulk states gives a dip-like feature. Note that recently it has been proposed that also the tunnelling channel into the spin-carrying orbital and the symmetry of this orbital can be relevant for the symmetry of the Kondo resonance [123, 124]. Therefore the exact mechanism behind the asymmetry of the resonance is still under debate.

Another lineshape to describe the Kondo resonance was introduced by Frota and Oliveira [125, 126] and has been shown to reproduce some experimental measured lineshapes better than the Fano function [127, 128]. It can be written as [123]:

$$f(\epsilon) = -A Re[e^{i\phi} \sqrt{\frac{i\Gamma_F}{E - E_K + i\Gamma_F}}]. \tag{3.14}$$

Here, the variable ϕ describes the interference between the different tunnelling channels and is connected to the Fano factor q by $q = tan(\phi/2)$. Figure 3.4 a) shows how the lineshape varies with ϕ. For $\phi = 0$ the resonance has a dip-like shape, whereas for $\phi = \pi$ the resonance is a peak. The parameter Γ_F is connected to the half-width of the resonance by $\Gamma \sim 2.54\Gamma_F$.

In figure 3.4 b) a comparison between the Frota and Fano lineshape is given. In a recent review [129], the Fano and Frota lineshape were extensively compared. Depending on the measurement parameters used and the different experimental broadenings present in the experiment, either function may reproduce the data better. Applying it to the conditions in this thesis, the Frota function is supposedly reproducing our results better. Therefore, unless otherwise specified, we will use it to fit our experimental data. In figure 3.5 b) another lineshape is shown, a temperature broadened logarithmic function. It described resonances in the weak coupling regime, which we will discuss in the following part.

The weak coupling regime

The weak coupling regime is usually best described by an perturbative approach, which was introduced by Appelbaum [131, 132] and Anderson [133] and later on modified for STM junctions by Ternes [111, 130]. It is usually used to describe Kondo correlations in the temperature regime $T \gg T_K$ or if the impurity is ferromagnetically coupled to the electron bath of the metal [134]. The model takes into account spin-flip scattering processes up to the 2nd order Born approximation and up to the third order in the exchange interaction J. The model is described in detail in the reviews by Ternes mentioned above, describing it in full detail here would go beyond the scope of this thesis. However, as the model will be
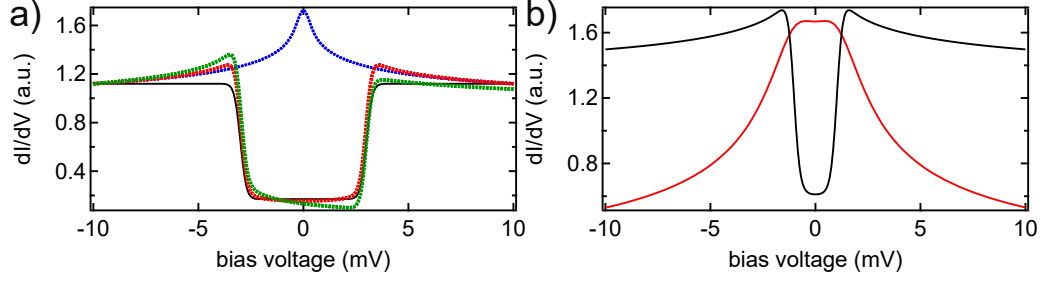
Figure 3.5: Parameter regime of a weak coupled Kondo resonance. a) Changes in the line-shape with varying parameters of U, $J\rho_0$ and D. The black curve corresponds to a 2nd order perturbation, where no intermediate states are considered. All other curves were calculated with 3rd order processes allowed. The parameters are respectively $D = 3\,\mathrm{mV}, J\rho_0 = -0.04, U = 0$ (red), $D = 3\,\mathrm{mV}, J\rho_0 = -0.04, U = 0.5$ (green), $D = 3\,\mathrm{mV}, J\rho_0 = -0.04, U = 0$ (blue). All spectra were calculated using the model in [130]. b) Behaviour of the Kondo resonances in a magnetic field. For a field of around $9\,\mathrm{T}$, the splitting of a weakly coupled Kondo resonance (black) is much more prominent than for an impurity in the strong coupled regime (red). For illustration purposed the Kondo temperature of the red curve was set comparably high ($T_K \sim 75\,\mathrm{K}$).

important later on, we want to highlight its results here. The transition probability in this model is given by:

$$W_{i\to f} \propto (|M_{i\to f}|^2 + J\rho_s \sum_m (\frac{M_{i\to m}M_{m\to f}M_{f\to i}}{\epsilon_i - \epsilon_m} + c.))\delta(\epsilon_i - \epsilon_f). \qquad (3.15)$$

Here, c is a constant and M is the scattering matrix element, which has the form of:

$$M_{i\to j} = \langle \psi_j, \sigma_i | \mathbf{S} * \sigma + U | \psi_i, \sigma_i \rangle. \qquad (3.16)$$

Here, $\mathbf{S} * \sigma$ describes the interaction of the tunnelling electrons with the spin, with σ being the Pauli matrix, $\psi_{i,j}$ is the eigenstate of the spin system and $\sigma_{i,j}$ is the wavevector of the interacting electron.

The first term in equation 3.15 arises without taking third-order contributions into account. It can phenomenologically describe inelastic excitations arising from magnetocrystalline anisotropy, as shown in figure 3.5 a) (black curve). Equation 3.16 shows that also potential scattering can be taken into account here, resulting in asymmetric lineshapes [130]. The second therm in equation 3.5 accounts for Kondo-like correlations. Calculating the conductivity gives rise to the previously mentioned temperature broadened logarithmic resonance [135]:

$$\sigma(E) = -(J\rho_0)^3 \int_{\omega_0}^{-\omega_0} \frac{f(\epsilon', T)}{\epsilon - \epsilon'} d\epsilon' * f'(\epsilon, T) + c. \qquad (3.17)$$

Here, the asterix represents a convolution, $f(x)$ ($f'(x)$) is the Fermi-Dirac distribution (its derivative) and ω represents a cut-off energy. Examples of the corresponding peaks are shown in the figures 3.4 b) and 3.5 a) as the blue curves. In comparison to the Fano

and Frota curves one can directly see that the width of the resonance differs significantly and the peak tends to be narrower for similar amplitudes. We stated before that the Kondo temperature is connected to the half-width of the corresponding resonance. This is not true anymore for the diverging function, as the peak width is not well-defined for it. Though one can still make estimations about the Kondo temperature, it usually is only indicative of the energy scale and prone to errors [135]. To describe the coupling strength in the weak coupling regime, usually the exchange coupling constant J or $J\rho_0$ is used.

Besides the characteristic lineshape, there are more ways to differ between the strong and weak coupling regime (and between Kondo resonances and other, non-magnetic resonances in general). First, the strongly coupled Kondo resonance has a special, intrinsic line width, which is given by [136]:

$$\Gamma = 2\sqrt{(\pi k_B T)^2 + 2(k_B T_K)^2}.$$
(3.18)

Note that the scaling factor of the temperature broadening of 2π was determined in the framework of the Fermi-liquid model. In different studies this factor is often parametrised as α and left as a parameter, while determining the Kondo temperature in a fit of temperature depending measurements (we will explain this in more detail in section 4). There, often smaller values for α have been found experimentally [137, 138]. For weakly coupled impurities the above described temperature scaling does not apply [135].

Another way to distinguish between the different regimes is to look at the behaviour of the resonance in an external magnetic field. The Kondo resonance is expected to experience a Zeeman like splitting in a magnetic field of [137, 139, 140]:

$$\Delta E = g\mu_B B,$$
(3.19)

where g is the gyromagnetic factor, μ_B is Bohrs magneton and B is the external magnetic field. This splitting can be most easily understood in the exemplary case of a spin $S = \frac{1}{2}$ system. Due to the magnetic field the degeneracy between the two spin projections $m_s \pm \frac{1}{2}$ is lifted. To still perform the spin-flip scattering process necessary for the Kondo resonance, an additional excitation has to be made, such that the process becomes inelastic. Another way to visualise it is to think of it as an additional magnetocrystalline anisotropy to be superimposed with the original Kondo resonance. Figure 3.5 b) shows exemplary simulated curves for an impurity in the weak-coupling regime (black) and one in the strong-coupling regime (red) in an external magnetic field of $9\,\mathrm{T}$. One can see that whereas the weakly coupled impurity shows a well pronounced splitting, the strongly coupled impurity has a barely visible splitting. It was found that it requires a magnetic field larger than the Kondo correlation energy $g\mu_B B > k_B T_K$ to cause a split of the strongly coupled impurity [111, 141]. So depending on the Kondo temperature of the impurity, the necessary fields to observe a splitting can become very large. Obviously, non-magnetic resonances do not split in an external magnetic field. Therefore, in this way Kondo resonances are distinguishable from other resonances experimentally.

The above described mechanism for the formation of the Kondo effect can be more complex in different cases. For example it has been proposed that not only the spin, but also the orbital moment can contribute to the formation of the Kondo state [142]. Moreover, the

Kondo state can experience other interesting features as a very strong spin polarization [143] and remains a topic of continuous interest.

We already showed in figure 3.5 a) that magnetocrystalline anisotropy and the Kondo effect can occur at the same time, which is understandable, as both effects deal with single spins on surfaces. In the next subsection we want to discuss the interplay of these two phenomena.

3.3.2 Competition between inelastic tunnelling and Kondo correlations

One of the first experiments to investigate the Kondo effect in presence of magnetic anisotropy was performed by Otte and co-workers in 2008 [137]. They looked at single Co atoms on Cu_2N patches grown on a Cu(100) substrate. They found that both, magnetic anisotropy and the Kondo effect were indeed present in the system. Moreover they have seen that the splitting of the Kondo resonance varied depending on the directionality of the applied magnetic field. As this effect did not occur for Ti atoms adsorbed on the same substrate, which were found to have a spin state of $S = \frac{1}{2}$, it is clearly correlated with the presence of a magnetic anisotropy (atoms with a spin state of $S = \frac{1}{2}$ can not experience a magnetic anisotropy due to Kramers degeneracy theorem [144]).

Co atoms were found to have a spin state of $S = \frac{3}{2}$. The formation of a Kondo peak in presence of a magnetic anisotropy requires a certain energy level alignment in this system, namely a hard-axis anisotropy, as can be seen in figure 3.6 a): here, the $m_s = \pm\frac{1}{2}$ levels are the ones lowest in energy. As a result, scattering events can occur between the two-fold degenerate ground state with $\Delta m_s = 1$ transitions, as indicated with the double headed black arrow. If the magnetic anisotropy would have promoted easy-axis anisotropy, one does not expect to observe a Kondo resonance, as scattering events then would require a $\Delta m_s = 3$ transition, which is prohibited by selection rules.

In 2014, Oberg and co-workers picked up the work on single Co atoms on Cu_2N [146]. In comparison to the previous described work, they grew larger patches of Cu_2N. They now found that the excitation energy and the amplitude of the Kondo resonance varied with the respective position of the Co atoms on the islands. Atoms on the edges of the islands showed larger resonance amplitudes and smaller excitation energies, whereas atoms in the center of the islands showed smaller resonance amplitudes and larger excitation energies. On a larger energy scale they also observed that the electronic band gap varied along the island, it grew larger towards the center of the island. The authors therefore explained the variation of the low-energy features with a changing single-electron broadening over the island, which stems from different tunnelling strength between the local orbitals and the substrate. This directly leads to a change of the tunnelling barrier, which also alters the Kondo exchange coupling $J\rho_0$. For the present case of a spin $S = 3/2$ system they ultimately found a relation between the excitations energy and the exchange coupling of:

$$\Delta = \Delta_0(1 - \frac{3}{16}(\rho J)^2 ln(\frac{2W}{\pi k_B T})), \tag{3.20}$$
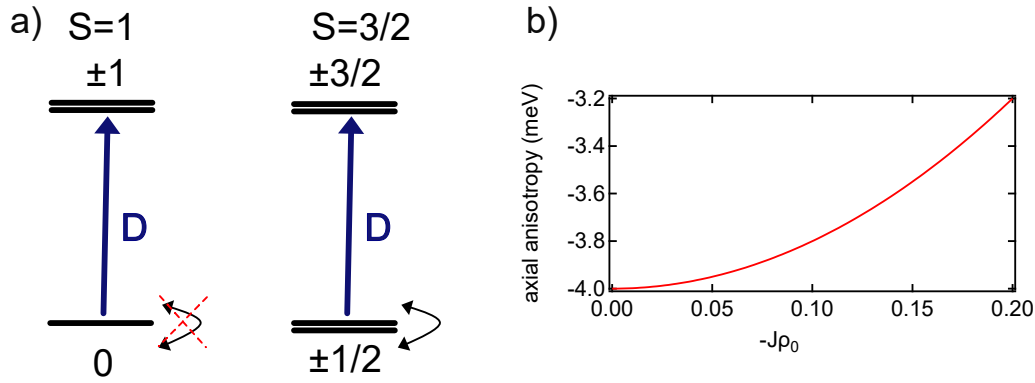
Figure 3.6: Visualisation of the Kondo effect in the presence of magnetocrystalline anisotropy. a) Energy-level diagram for a spin $S = 1$ and a spin $S = 3/2$ system with an axial anisotropy. For the $S = 1$ case, no (or very few) Kondo correlations take place, as the ground state does not allow the necessary spin-flip processes. In contrast, for the $S = 3/2$ case, the groundstate is degenerate with $m_s \pm 1/2$, which allows for spin-flip processes with the selection rule $\Delta m_s = 1$. b) Renormalisation of the anisotropy energy with increasing exchange coupling strength. The relation between those is given in [145]. Here, an exemplary value of $\alpha = 5$ was used.

where Δ is the excitation energy and W is the bandwidth of the substrate electrons. For systems with different spin states, this relation has to be altered [147].

A similar relation has also been found for a different system, CoH_x complexes $(x = 1, 2)$ adsorbed on a monolayer of hexagonal boron nitride (h-BN) grown on a Rh(111) surface [145]. Depending on the number of hydrogen atoms bound to the Co atom, the spin state changes between $S = 1(CoH_1)$ and $S = 1/2(CoH_2)$. Therefore, as explained above, for the CoH_2 molecule no magnetic anisotropy can be present. On the other hand, for the CoH_1 molecule, this is not the case. For an integer spin state the formation of a Kondo state is usually prohibited, when a sizable magnetic anisotropy is present, as can be seen exemplary for a spin of $S = 1$ in figure 3.6 a). Neither the ground, nor the exicted state exhibit degenerate energy levels, which enable a spin-flip event with $\Delta m_s = 1$. Therefore, it does not play a role for the formation of a Kondo resonance, which spin-direction is preferred by the anisotropy. However, Kondo correlation can still occur on a smaller scale and be treated perturbatively. Jacobsen and co-workers found that these correlation with a strength of $J\rho_0$ vary along the moiré structure of the substrate and can also lead to a renormalisation of the excitation energy with:

$$D(J\rho_s) \approx D_0(1 - \alpha(J\rho_0)^2), \qquad (3.21)$$

where α is a coefficient connected to the effective bandwidth [111]. An example of this relation is plotted in figure 3.6 b). For both introduced systems the general idea of the renormalisation of the excitation energy is the same: the more Kondo-like scattering processes occur, the less stabilised the anisotropy direction becomes. This leads to a reduction of the excitation energy. It is understood that at a certain threshold exchange interaction strength $J\rho_0$ even a $S = 1$ can be driven into a highly correlated Kondo state [111]. For this

the excitations energy has to drop below the Kondo energy scale $k_B T_K$. Ternes calculated that for the previous mentioned example of CoH_1 on h-BN, the critical anisotropy for this transition is $D \approx$ -1.5meV [111]. As the experimental measured value was above that, a treatment in the perturbative model is justified.

The example of the CoH_x molecules is intriguing, as it offers a system, which can be tuned in terms of spin state and exchange coupling to the substrate and therefore be switched from a Kondo regime into a regime, where the magnetic anisotropy is the more prominent effect. However, the transition between these two regimes is rather abrupt. In section 5 we want to introduce a system, where the transition between these two regimes can be tuned and studied smoothly.

In this chapter, we have introduced the most relevant single atom magnetism topics for this thesis. We have talked about the impact of magnetic anisotropy on the excitation spectra of single atoms, how coupling between single atoms can occur and about the different mechanics of the strong and weak coupling Kondo regime. At last, we have described the interplay between Kondo correlation and the magnetic anisotropy. All these mechanism will be more or less relevant for chapters 4-6.

4 Top-layer sulfur vacancies in a monolayer of MoS$_2$

As mentioned previously, a focus of this thesis is to investigate the interplay between adsorbates and the underlying MoS$_2$ layer. However, to be able to reliably study their properties, first we need to understand the impact of intrinsic defects on the properties of the TMDC, to be able to understand their interplay with adatoms and molecules on the surface. Intrinsic defects are known to form in TMDC layers during preparation with every established growing technique [148]. Defects in TMDC layers are known to significantly alter both the electronic [149] and optical properties of the material. For example, a strong photoluminescence enhancement has been reported due to an increased, engineered defect concentration in both single-layer and multilayer TMDC [150–154]. Also defects have been shown to effectively dope TMDC monolayers [155, 156] and even induce gate-tunable magnetism [157, 158]. In general, the impact and stability of defects varies between the monolayer and bulk limit [159, 160]. Depending on the desired functionality an increased defect concentration can be therefore beneficial or unfavourable and requires a good understanding of the interaction between the defects and the TMDC.

To reliably study defects it is beneficial to be able to control their concentration. Depending on the technique used, different types of defects can be intentionally created in the TMDC layers, ranging from point-like defect to larger, areal structures [161].

In this thesis we focus on the study of point defects, namely single chalcogen vacancies on the top of a single MoS$_2$ layer. Single chalcogen vacancies are of uttermost importance for understanding the properties of TMDC layers, as they have the lowest formation energy, are therefore often the most common defect type [149, 162, 163]. Understanding their properties on a local scale is very important for us to distinguish them from features of adatoms on the surface, which will be studied in the upcoming chapters. In this chapter we present first results on the local electronic structure of single sulfur vacancies in a monolayer of MoS$_2$ grown on a Au(111) substrate.

4.1 Preparation of sulfur vacancies

We prepared the MoS$_2$ islands according to the method described previously in section 2.12.2. As one can see in the previously shown STM topography in figure 2.10 c), this preparation method already leads to a certain concentration of intrinsic defects of different nature. To increase the concentration of top-layer sulfur vacancies after the initial preparation, we sputtered the sample for less than 10 seconds at an energy of $100\,\mathrm{eV}$ and under an incident angle of $55°$.

The result of this preparation after sputtering can be seen in figure 4.1 a): several bright spots appear on the MoS$_2$ layer. In the inset in b) and d) a zoom onto one of these structures

is shown, where a three-lobe structure becomes apparent. The brightness of these lobes varies along the MoS_2 island, the structures also vary in their apparent shape. To ensure that the observed three-fold symmetric shape stems from sulfur vacancies, we probed the Δf signal over the same spot as shown in a) at constant height. The resulting topography can be seen 4.1 c): the atomic lattice of the MoS_2 can be resolved clearly in the image. Moreover, several dark spots of the size of single atoms can be observed, indicating missing sulfur atoms. Comparing the two topographies in a) and c), one can see that most missing atoms in c) appear as bright protrusions in a) with the aforementioned three bright lobes, clarifying that they indeed originate from top-layer sulfur vacancies. One of these protrusions is exemplary highlighted with the blue circle. Vacancies, where several sulfur atoms are missing at next neighbour sites, deviate from this appearance. Some bright spots can not be assigned to missing top-layer sulfur atoms and probably stem from interstitials or bottom layer sulfur vacancies. In the following characterisation we focus our attention to single top-layer sulfur vacancies. Their threefold symmetry has also been experimentally observed for top-layer sulfur vacancies in WS_2 [164] and theoretically predicted for such vacancies on MoS_2 [163]. Note that in both aforementioned works, the top-layer vacancies can be clearly distinguished from bottom-layer sulfur vacancies not only from AFM measurements, but also by their appearance, where the three lobes of the bottom vacancy are rotated in comparison to the top-layer vacancy. One of these vacancies in encircled in green in a) and c). As the concentration of top-layer sulfur defects is much larger than the ones in the bottom-layer, we conclude that the sputtering of the sample actually yielded good results. If the concentration of defects is too high, we observed that annealing the sputtered sample in H_2S atmosphere leads to a reduction of defects again. In the next subsection we will proceed to describe the electronic structure of the top-layer sulfur vacancies. For convenience we will refer to them as just vacancies for the rest of the chapter.

4.2 Electronic structure of top-layer sulfur vacancies

Figure 4.1 b) shows dI/dV spectra recorded in the center (red) and one of the lobes of a vacancy. The red spectrum in the center of the defect looks very similar to a characteristic spectrum of the bare MoS_2, as shown for example in figure 2.11 a). Comparing this with the spectrum taken at one of the lobes one the vacancy, one can see two main differences: first, the Γ_1 and Γ_2 peaks of the MoS_2 appear to be shifted by some tenths of mV. Second, a small increase in differential conductance can be observed near the Fermi level for the spectrum on the lobe. To examine this closer, we recorded the same set of spectra in a smaller energy range, as shown in figure 4.1 d). There one can see that several broad resonances appear in the band gap of the MoS_2, one at positive bias around $300\,\mathrm{mV}$ and two at negative bias voltage around $-200\,\mathrm{mV}$ and $-800\,\mathrm{mV}$. In-gap states caused by sulfur vacancies in MoS_2 have been predicted for both a freestanding layer of MoS_2 [149, 159, 165], as well as MoS_2 on Au(111) [163]. In all these works, a state close to the VBM and two spin-degenerate in-gap states were found. The state close to the VBM could be the state we probe at $-800\,\mathrm{mV}$, the assignment of the other states is less clear. Possibly a hybridisation with the Au(111) states changes the character of the states or shifts it to different energies. We will come back and clarify the assignment of the in-gap states in section 4.4.

The most striking feature in the spectrum shown in figure 4.1 d) is the sharp resonance at
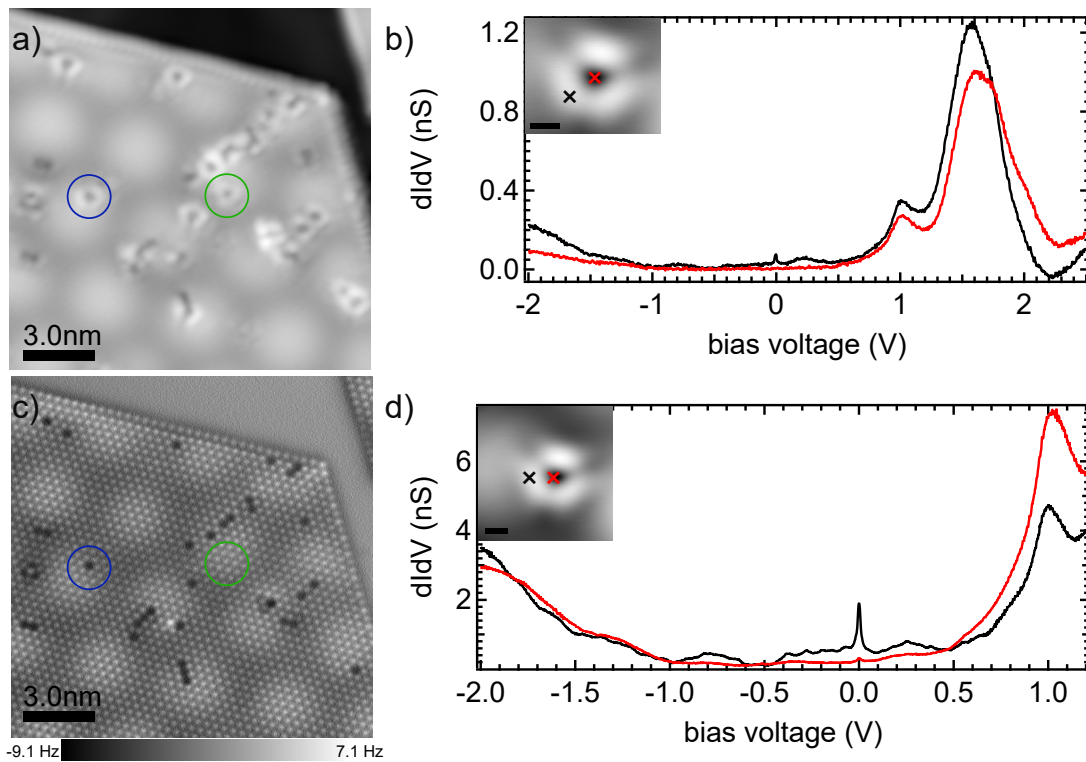
Figure 4.1: Characterisation of single top-layer sulfur vacancies in MoS$_2$. a) STM topography of a MoS$_2$ island after sputtering. Several bright spots appear around dark point defects. c) Constant-height Δf image. The bright spots from a) can clearly be assigned to stem from missing sulfur atoms in the top layer. b), d) dI/dV spectra recorded on the locations indicated in the insets. The STM topographies were recorded at a setpoint of $100\,\mathrm{mV}$ and $200\,\mathrm{pA}$ (a) and $300\,\mathrm{mV}$ and $200\,\mathrm{pA}$ (inset in b) and d). The Δf image was recorded at a setpoint of $1\,\mathrm{mV}$ and $200\,\mathrm{pA}$. The scale bars in the insets in b) and d) amount to $5\,\text{\AA}$. The dI/dV spectra were recorded at a setpoint of $2.5\,\mathrm{V}$ and $100\,\mathrm{pA}$ (b) and $-2\,\mathrm{V}$ and $200\,\mathrm{pA}$ (d).

or very close to zero bias. We have described in section 3.3.1 that such a resonance at zero bias can arise from Kondo exchange interactions of substrate electrons with a localised spin. Therefore, to give rise to a Kondo resonance, a sulfur vacancy would have to carry a net spin. However, even though a missing sulfur atom certainly leaves behind a dangling bond it is still under debate, if and under which conditions a charged sulfur vacancy is actually stable in a MoS_2 monolayer [159, 166]. In recent theoretical results by A. Akkoush and M. Rossi on a monolayer MoS_2 adsorbed on Au(111), provided to us in private communication, it is suggested that the vacancy is indeed negatively charged. Here, the metal underneath acts as a charge reservoir, helping to stabilise the negative charge. To check on this, we looked at the local charge distribution at a vacancy site with means of nc-AFM. Extracting the LCPD from $\Delta f - V$ spectra taken over a densely spaced grid in the area of interest is a common tool to assess the charge distribution on a local scale [59]. We took such a grid over the topography shown in figure 4.2 a), the extracted LCPD values are plotted in b) respectively. One can see that in the center of the grid, where the defect is located, there is an increase in positive LCPD values. Therefore in this region a more positive bias voltage has to be applied to compensate for a more negative charge. Even though this method does not yield a quantitative number of the exact charge it still hints towards a negatively charged vacancy.

We now look the spatial variation of the zero-bias peak. Therefore we recorded a constant-height dI/dV map at $1\,mV$, as shown in figure 4.2 c). The corresponding constant current topography at larger bias is shown on a). Surprisingly, the zero-bias peak does not resemble the triangular symmetry of the sulfur layer, but shows a two-fold symmetry. To investigate the origin of this, we looked at a larger region of a MoS_2 island at different bias voltages, as shown in the constant-current STM topographies in e) and f). The topography in f) was recorded at a voltage of $300\,mV$. At this energy all vacancies exhibit a three-fold symmetry. In contrast, the vacancies in e), which was recorded at $5\,mV$, all appear two-fold symmetric. Therefore, the resonance around zero bias seems to be associated to the observed two-fold symmetry around the Fermi level. Moreover, the two-fold symmetry of those vacancies occurs with different orientations with respect to each other. The lobes seem to be orientated towards the closest moiré maximum. This indicates that the moiré causes the symmetry breaking of the vacancies at these bias voltages. We would expect that this effect is less pronounced at the exact positions of the moiré minima and maxima, but lack the statistical evidence to proof this.

4.3 Characterisation of the zero-bias peak

We mentioned in section 3.3.1 that a Kondo resonance can be identified by two characteristic traits: a characteristic temperature broadening and a splitting of the resonance in a magnetic field. To obtain the necessary resolution for this analysis, we probed the dI/dV signal in a smaller energy area, as shown in figure 4.2 d). Besides the zero-bias peak, two bias symmetric peaks at around $\pm\,65\,mV$ arise, also the aforementioned broader resonance at $250\,mV$ can be resolved in more detail. While the latter probably stems from the neighbouring sulfur atoms, as scanning at voltages higher than this resonance restores the three-fold symmetry, the two peaks around the zero-bias peaks can be associated as Coulomb blockade peaks [167]. Such peaks have been observed before for magnetic molecular complexes and
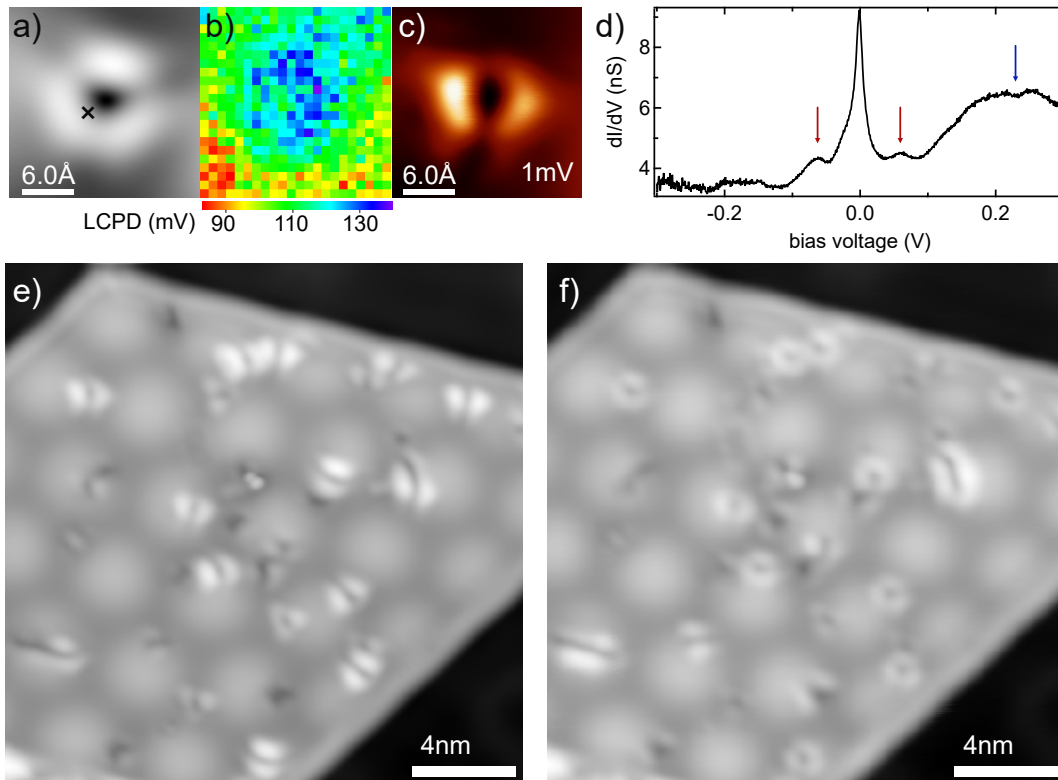
Figure 4.2: Properties of the zero-bias resonance. a) Close up STM topography of a sulfur vacancy. b) LCPD extracted from a densely spaced grid of $\Delta f - V$ spectra over the topography in a). c) Constant-height dI/dV map over the same area as shown in a). After adjustment of the tip-sample distance with the setpoint the feedback was switched off and the bias voltage was set to $1\,\text{mV}$, as indicated in the bottom right corner. d) dI/dV spectrum recorded on the location marked with the cross in a). Several resonances are highlighted with the arrows. e), f) STM topographies of several sulfur vacancies, recorded at different bias voltages. The STM topographies were recorded at a setpoint of $300\,\text{mV}$ and $200\,\text{pA}$ (a,c,f) and $5\,\text{mV}$ and $200\,\text{pA}$ e). The dI/dV spectra were recorded at a setpoint of $300\,\text{mV}$ and $200\,\text{pA}$ (b) and $300\,\text{mV}$ and $2\,\text{nA}$ (d).

further hint towards a Kondo resonance. After identifying all resonances in proximity to the zero-bias peak we can proceed to look at its temperature dependence.

4.3.1 Temperature dependence of the resonance

As shown in equation 3.18, the Kondo resonance has a characteristic temperature dependence. To check this for the zero-bias peak of the sulfur vacancies, we recorded several spectra in a small bias range at varying sample temperatures. For this the sample was heated inside the STM. For the analysis it is important to extract the intrinsic line width of the resonance, which is smeared out by temperature broadening and the lock-in modulation amplitude. First, the resonance width was extracted by fits with a Frota function [129]. As mentioned in section 3.3.1 in equation 3.14, to obtain the actual half-width of the resonance one has to multiply the fit value by 2.54 [123]. Then the intrinsic line width can be extracted by subtracting the temperature broadening and lock-in modulation V_m as [38]:

$$\Gamma_{intrinsic} = \Gamma_{Frota} - \sqrt{(2V_m)^2 + (3.5k_BT)^2}.$$ (4.1)

Figure 4.3 a) shows an exemplary graph of such extracted line widths plotted over the corresponding temperature. The probed defect is shown in the inset. The red dashed line corresponds to a fit with a slightly modified version of equation 3.18:

$$\Gamma_{intrinsic}(T) = 2\sqrt{(\alpha k_BT)^2 + 2(k_BT_K)^2},$$ (4.2)

where α is a phenomenological fit parameter. The fit matches the experimental data very well and yields values of $\alpha = 7.2 \pm 0.5$ and $T_K = 55 \pm 2K$. α gives the linear slope expected in the temperature dependence in regions of temperatures much larger than the Kondo temperature. While it is theoretically predicted to be 2π [136], experimental values of down to 5.4 have been found [137]. Our obtained value is larger. The Kondo temperature is determined from the intersection of the fit with the y-axis at zero temperature and is a measure of the coupling strength of the impurity to the conduction electron bath. Most defects probed had a Kondo temperature around $60\,K$, but we found impurities with Kondo temperatures in the range of 5-120 K. This is a rather large variance, which we would not intuitively expect for the same type of defect. There are a couple of explanations we propose for this: first, we have already seen that the moiré has an impact on the symmetry of the sulfur vacancies. Moreover, we previously explained that the local density of states varies along the moiré. As the coupling of the spin to the conduction electrons is crucial for the Kondo temperature, these variations along the moiré naturally should have an impact on it. In addition, sulfur vacancies are know to be highly reactive [161, 168] and for example bind oxygen. Such substitutional oxygen sites were found to be hardly distinguishable from the original defect sites in $MoSe_2$ [169]. There, sufficient contrast formation can only be achieved with functionalised tips at very small tip-sample distances. As we did not check for this, we can not exclude that some of our top defects have bound adsorbates to it. At last, single sulfur vacancies could theoretically couple with neighbouring defects. As mentioned before, we tried to exclude this by only probing single point defects, but it is not trivial to know, if for example the sulfur atom at the bottom layer could be missing at the same time as well. Therefore, to get a better idea about the variations in T_K a more detailed analysis has to be carried on in the future.
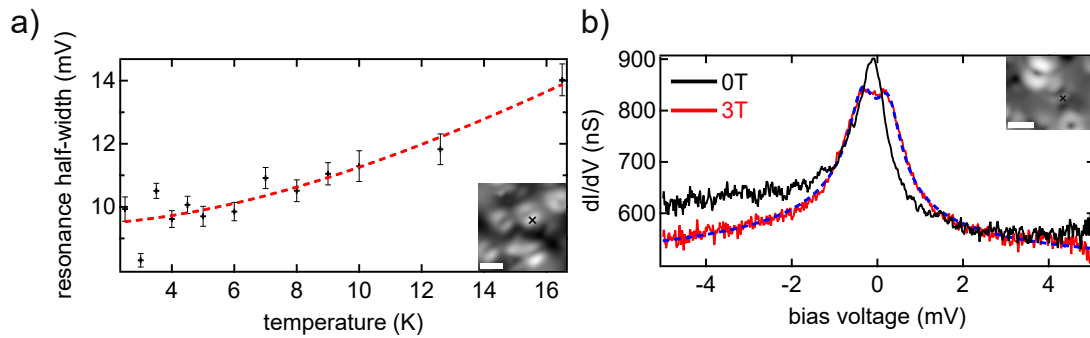
Figure 4.3: Identification of the zero-bias peak as a Kondo resonance. a) Extracted half-widths of a representative vacancy (shown in the inset), probed at different sample temperatures. The data was fitted with a characteristic function, stemming from a Fermi-liquid description of the Kondo problem [115, 171]. b) dI/dV spectra recorded on the vacancy indicated in the inset at zero magnetic field (black) and at an applied magnetic field of $3\,T$. The STM topographies in the insets were recorded at a setpoint of $50\,mV$ and $3\,nA$ (a) and $1\,mV$ and $100\,pA$ (b). The scalebars in the insets amount to $1\,nm$. The dI/dV spectra were recorded at a setpoint of $5\,mV$ and $3\,nA$.

4.3.2 Magnetic field dependence of the resonance

The last convenient proof for the Kondo resonance is its behaviour in a magnetic field. As our setup is limited to a field of $3\,T$, the defect shown in a) with a Kondo temperature of $T_K = 55 \pm 2K$ can not be split with such a field. We therefore tested the magnetic field dependence on the defect with the smallest Kondo temperature we found. The result is shown in figure 4.4: the black dI/dV spectrum shows the resonance at $0\,T$, whereas the red one was probed at $3\,T$. As expected, one can see a decrease of the Kondo amplitude and a small local minimum at zero energy, indicating a split of the resonance. To look at the magnitude of it, we fitted the red spectrum phenomenologically with two Frota functions. The fit is plotted as the blue dashed line over the red curve and shows a very good agreement with the data. The extracted splitting amounts to $622 \pm 12\mu V$, which also is in good agreement with the theoretically expected value of $695\mu V$ for a spin S=$\frac{1}{2}$ and g-factor of 2.

Therefore we conclude that the zero-bias peak observed on the vacancies indeed is a Kondo resonance. In the last section we looked at vacancies on so-called pit defects, which were found to have at least one Au(111) layer underneath missing [170]. Such areas of the MoS$_2$ islands consequently show much less effects of hybridisation and can be considered as quasi-freestanding.

4.4 Sulfur vacancies on free-standing MoS$_2$

Figure 4.4 a) shows a STM topography of several vacancies on a pit defect. These areal defects can hardly be scanned at voltages lower than $800\,mV$. The reason for this can be seen
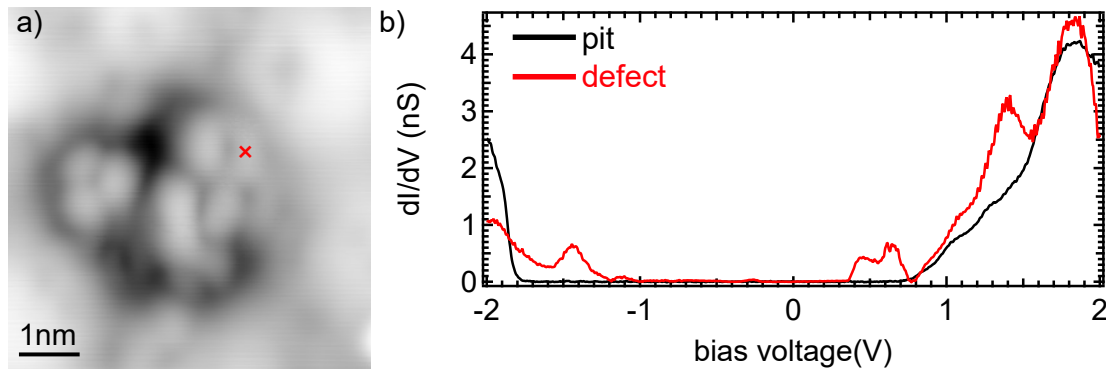
Figure 4.4: Sulfur vacancies on a pit defect. a) STM topography of point defects on a pit defect. b) dI/dV spectra recorded on a bare pit defect (black) and on a point defect, as marked with the red cross in the topography in a). The topography was taken at a setpoint of $800\,mV$ and $100\,pA$, the spectra were recorded at a setpoint of $2\,V$ and $3\,nA$ (red) and $800\,mV$ and $100\,pA$ (black).

in the dI/dV spectra shown in b): the black spectrum was recorded on a "clean" pit defect. In contrast to previously shown spectra on MoS_2, here zero conductance can be observed inside the band gap and the onsets at both the conduction and valence band are much sharper. Therefore, pit defects were also described as areas of quasi-freestanding MoS_2. The red spectrum in b) was recorded on a vacancy on a pit defect, as shown with the red cross in the topography in a). This spectrum differs from the previously shown ones in figure 4.1 b) and shows much more pronounced defect states. Moreover, the before observed Kondo resonance is absent. This is expected, as the spin of the defect can not be screened anymore, as the gold layer underneath is missing. It is also unclear, if the defect on the pit should be charged at all in the first place. The observed resonance can be again compared to theoretical results, as done in section 4.2. The resonance at $-1.4\,V$ can be assigned to the state close to the valence band maximum and the resonances at $450\,mV$ and $650\,mV$ are the expected in-gap states above the Fermi level. Even though theory predicts a degenerate state here, experimentally a lifted degeneracy due to spin-orbit coupling was found for the same type of defect on WS_2 [164]. The separation of the peak was found to be of $252\,mV$, which is close to our observed value of about $200\,mV$. If spin-orbit interactions are included into the simulations, the in-gap state is predicted to split [164]. We conclude that our measurements of vacancies on pit defects are in very good agreement with simulations of defect states in freestanding monolayer MoS_2.

4.5 Summary

In summary, in this chapter, we looked at single top-layer sulfur vacancies on MoS_2. It is possible to artificially control the defect concentration by sputtering the sample. The defects exhibit several in-gap states, one of which could be identified as a Kondo resonance. The symmetry of the resonance was unexpectedly two-fold, probably due to a symmetry breaking caused by the moiré superstructure. Large variations in the Kondo temperature

were observed, which have to be investigated further. Finally, the properties of vacancies on quasi-freestanding MoS_2 were investigated, which showed much more similarity with theoretical predictions. As sulfur vacancies are found to exhibit magnetic fingerprints, they have to be kept in mind while looking at magnetic properties of different adsorbates. In the next chapter we will look at one type of these magnetic adsorbabates, namely single iron atoms. Their properties and interaction with the substrate will be studied in detail.

5 Fe on MoS₂: Moiré tuning of spin excitations

The results presented in this chapter have been published as:

- *"Moiré Tuning of Spin Excitations: Individual Fe Atoms on MoS₂/Au(111)"* by Sergey Trishin, Christian Lotze, Nils Bogdanoff, Felix von Oppen and Katharina J. Franke, *Phys. Rev. Lett.* **127**, 236801 (2021)

The ultimate goal in magnetic storage is to controllably read and write a single magnetic atom. For this several challenges have to be met. For example, the quantum spin states have to be controlled coherently [172] and at the same time be protected against relaxation and spontaneous demagnetization, when adsorbed onto a substrate [173]. Even though some atoms can exhibit a sizable magnetic moment while adsorbed on a metallic lead [174, 175], usually decoupling layers are used to preserve the magnetic properties of single atoms and enhance the lifetimes of their excited states. One very famous example was presented in 2016 by Donati and co-workers. They studied single holmium atoms on thin layers of magnesium oxide and found traces of magnetic remanence up to $30\,\mathrm{K}$ and relaxation times of exited magnetic states of $1500\,\mathrm{seconds}$ at $30\,\mathrm{K}$, both being significantly higher than comparable experiments carried out before [14]. The symmetry of the magnesium oxide layer provoked an energy level alignment, which was protecting the spin states very efficiently against electron scattering processes and phonons. This system naturally draw more interest [176], leading ultimately in an experimental design, where the magnetization of the holmium atoms was read and written [177].

Moreover, also studies of magnetic atoms on two-dimensional materials have been promising in the past [178, 179]. These materials often exhibit a moiré superstructure when grown or exfoliated onto a substrate, due to a lattice mismatch. This can lead to a locally varying electronic structure, as we have discussed before in chapter 2.12.2 and as it was found in [145]. This enables a potential tuning of the magnetic states, as discussed in section. Taking this into account and additionally considering previous studies that found single layer MoS₂ grown on noble metal substrates to be a effective decoupling layer for molecules, we decided that it is a promising system to study single transition metal atoms.

In this chapter we will present our results on single iron atoms on MoS₂. First, we will describe the fundamental structural and electronic properties of the system. Afterwards we will discuss the magnetic fingerprints with respect to the atoms position in the moiré superstructure. Afterwards we will look at the effect of potential scattering on the appearance of the atoms. At the end, we will discuss the influence of defects and residuals on the electronic properties and give an outlook on open questions.

5.1 Adsorption structure of single Fe atoms on MoS$_2$

We performed most of the experiments in the JT-STM. There, a deposition of Mo on a hot sample in a H$_2$S atmosphere proved to give dissatisfying results, probably because of an unreliable temperature reading of the electron-beam sample heater. Therefore, after Mo deposition on a hot sample, we annealed the substrate at an additional preparation chamber, were a heating station was mounted with a more reproducible temperature control. After the growth, we evaporated a dilute amount of Fe atoms onto the sample. During that deposition, the sample temperature stayed under $10\,K$. The results of this preparation is shown in figure 5.1 a): several MoS$_2$ islands are visible on the Au(111), however their size was not as large as some of the previously shown islands before and more in the range of a few tenths of nanometers. The bright protrusions on the Au(111) and MoS$_2$ islands are single Fe atoms, which are roughly distributed equally over the whole sample. There is no evidence of cluster formation, indicating a low mobility of the atoms during the evaporation process.

Figure 5.1 b) shows a closer up look into one of the MoS$_2$ islands. Several round, bright protrusions can be identified, which can be identified as single iron atoms. Moreover, some point defects are present. Scanning the same image at bias energies of $100\,mV$ or lower leads to a drastically changed appearance, as shown in c): a vast majority of the atoms appear as triangular protrusions now. To the best of our knowledge, such shapes are only vary rarely observed for transition metals, as they do not resemble the symmetry of the d-orbitals. This appearance points to partially filled crystal-field split d-levels [180]. We will see later on in this chapter that the round appearing atoms are connected to impurities on the substrate. The orientation of the triangular atoms differs from island to island, as can be seen in d). The triangles may point upwards or downwards. Interestingly, all atoms of the left side of the island point downwards, whereas the ones on the right side point upwards. Noticeably, a zone boundary goes through the center of the island. Krane and co-workers have found that the orientation of MoS$_2$ islands on Au(111) depends on which domain of the herringbone reconstruction the respective islands are adsorbed [33]. So an island in a fcc site has a reversed orientation in comparison to an island on a hcp site. For atoms on a substrate the interaction with the top layer of the substrate is the strongest. It is therefore natural to assume that the triangular shape of the atoms resemble the symmetry of the top sulfur layer of the MoS$_2$. If now the orientation of an MoS$_2$ island is reversed as in d) also the direction of the triangle need to turn, assuming that all triangular atoms are adsorbed on the same lattice site. This assumption is supported by DFT calculations, which suggest that the S-hollow site with a Mo atom underneath is the preferred adsorption site [16, 17]. Later on in this section we will provide more evidence pointing towards a hybridisation of the Fe atoms with the S states.

Figure 5.1 e) shows the apparent height of along the three atoms marked with the lines in d). They have been set to the same background height for clarity. As one can see the round (blue line) and the triangular atom (red line) on the MoS$_2$ island appear with the same height, of roughly $180\,pm$. Their apparent width amounts to roughly $1\,nm$. The atom adsorbed on the Au(111) (green line) exhibits the same width, but a smaller height of about $120\,pm$. This could stem either from a suppressed, less spatially extended orbital in z-direction at that energy or that the Fe atom is adsorbed closer to the substrate on Au(111). Either way it could imply a stronger decoupling of the Fe atoms on the MoS$_2$ layer. However, only
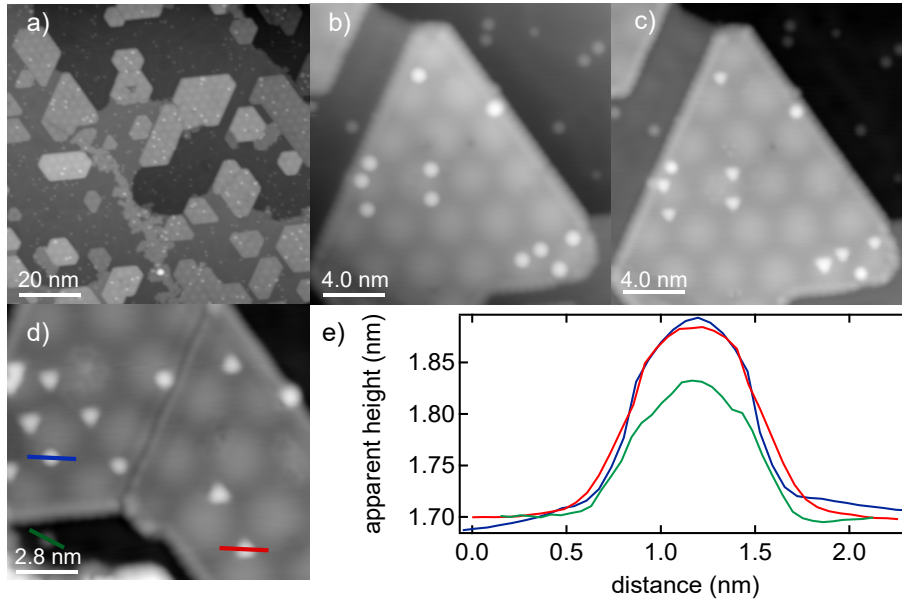
Figure 5.1: Appearance of single Fe atoms adsorped on MoS_2 islands. a) STM topography of several MoS_2 islands grown on Au(111). The bright, round protrusion are single iron atoms. One can see that the coverage on the Au(111) and the MoS_2 islands is similar. b) Closer up zoom into a MoS_2 island. Clearly several round protrusions can be seen. Also some point defects can be identified. c) The same scan area as in b) is shown, but recorded at a lower voltage. Now several atoms suddenly appear triangular. d) STM topography of a MoS_2 island, which is split by a zone boundary. On the left half the triangular atoms point downwards, whereas on the right half they point upwards. e) Apparent height profile of three different atoms, as indicated with the lines in d). Whereas the two atoms on the MoS_2 appear with the same apparent height, the atom on the Au(111) appears lower. The topographies were recorded at a setpoint of $816.1 \, mV$, $100 \, pA$ (a), $800 \, mV$, $100 \, pA$ (b) and $50 \, mV$, $100 \, pA$ (c),(d).

AFM measurements could clarify this for certain. In the next section we show how this adsorption affects the electronic structure of the iron atoms.

5.2 Electronic structure of single Fe atoms on MoS_2

Figure 5.2 a) shows a low-energy dI/dV spectrum recorded on the triangular shaped atom showed in the inset in b) (black). Two bias symmetric step-like features can be seen around $\pm 2.7 \, mV$. As we described before in chapter 3, step-like excitations in the differential conductance point towards inelastic excitations. The shown spectrum was smoothed, as the signal-to-noise ratio was suboptimal, as can be also seen in the reference spectrum on the bare substrate shown in red (the spectrum was faded out for better visibility). The overall increase in the conductance due to the opening of the inelastic channel is comparably small, in the order of 5%. We will see later on in section 5.4.1 why the contribution of the inelastic

channel is small on certain parts of the atoms. The spectrum can be modelled with the effective spin Hamiltonian from equation 3.1, which yields an axial anisotropy of $\pm 2.7\,\text{meV}$ (for a Spin S=1 system) and no transverse anisotropy. This anisotropy stems from the crystal field, which has a trigonal-pyramidal symmetry. This crystal field can either lead to a spin state of 1 or 2 for the Fe atoms, depending on the ratio of Hunds energy and the crystal-field splitting. Our measurements would be consistent with both spin states, density functional theory calculations also remain inconclusive about the spin state [16, 17]. Note that the results in this section do not qualitatively change, depending on if the actual spin state is S=1 or S=2.

Figure 5.2 b) shows a higher energy dI/dV spectrum recorded at the same locations as in a). One can see an onset at both, positive and negative voltages. The onset at positive voltage is also visible in the spectrum recorded on the bare MoS_2, but slightly shifted. This could stem from a partial hybridisation of the Fe atoms with the Γ_1 state of the MoS_2. The atoms became more and more unstable, the higher the applied bias voltages were, which often resulted in the movement of the atoms during the spectrum, if the applied bias voltages were higher than the ones used for the spectra in b). Therefore we can not show spectra recorded at higher energies than in b).

Theoretically, the inelastic excitation shown in a) could also arise from a vibration of the atom against the substrate, even though for a magnetic atom a spin-flip excitation is much more likely. To test the origin, we took a spectrum on a Fe atom at an externally applied magnetic fields of $3\,\text{T}$, which is the highest field we can instrumentally apply. The result is shown in figure 5.2 b) as the red curve. On top of the curve, a fit with the perturbative model proposed by Ternes [130] is shown, considering a magnetic field of $3\,\text{T}$ and an effective temperature of $1.1\,\text{K}$, which is our measurement temperature. As one can see no clear splitting at these conditions can be observed. Looking closely, on the left side two steps could be barely distinguished. The step on the right side appears broader due to the background slope and therefore smears out a possible second step even more. Therefore, our experimental resolution is not sufficient to confirm the magnetic origin of the inelastic excitations beyond doubt. In the next subsection we will see that we can prove it in a different way, with the scaling of the excitation energy in presence of exchange coupling.

In figure 5.2 d) the seen excitation is summarised. Assuming a spin state of S=1, the energy levels are split in a $m_s = 0$ groundstate and a degenerate $m_s = \pm 1$ excited state, considering an easy-axis anisotropy. The observation of only one step points to an absent or below our energy resolution transversal anisotropy. When applying a magnetic field perpendicular to the substrate, the degeneracy of the $m_s = \pm 1$ levels gets lifted. Then, in principle, two excitations should be observable. However, as the energy splitting goes Zeeman-like, for a magnetic field of $3\,\text{T}$ it is only around $350\mu V$, which is in the order of our energy resolution, especially considering the strong low-frequency noise in the setup. We already discussed the influence of the varying electronic structure along the moiré in the MoS_2 islands. In the next section we want to have a look, how this effects the observed inelastic excitations.
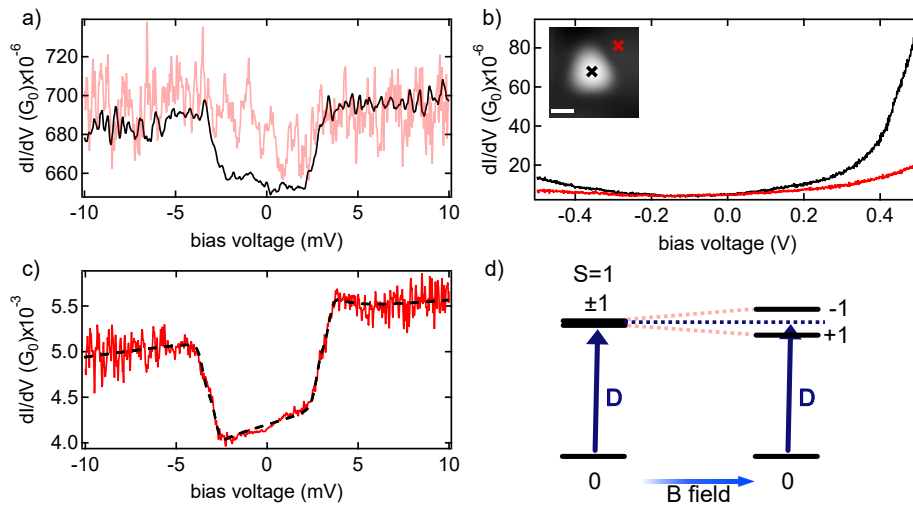
Figure 5.2: Electronic structure of single Fe atoms adsorbed on MoS_2 islands. a) dI/dV spectra performed on the locations marked in the inset in b). The background spectrum on the bare MoS_2 was faded out partially for clarity. b) dI/dV spectra performed at the same spots as in a), but at higher bias voltages. c) Representative spectrum of an Fe atom at a magnetic field of $3\,\mathrm{T}$. The black dashed line represents a fit performed with the method introduced in [130]. d) Illustration of the magnetic anisotropy related level splitting with and without a magnetic field. The topography in b) was recorded at a setpoint of $10\,\mathrm{mV}$, $100\,\mathrm{pA}$, the spectra were recorded at $10\,\mathrm{mV}$, $1\,\mathrm{nA}$ (a), $50\,\mathrm{mV}$, $20\,\mathrm{pA}$ with the tip additionally retracted by $80\,\mathrm{pm}$ (b) and $10\,\mathrm{mV}$, $4\,\mathrm{nA}$(c). The scalebar in the inset in b) amounts to $5\,\mathrm{\AA}$.

5.3 Moiré-dependent variations of the excitations spectra

Figure 5.3 shows dI/dV spectra in several different positions in the moiré superstructure, starting from the minimum in a) and ending on, or very close to the maximum in f), as indicated in the according insets. One can see that along the moiré the spectra undergo a qualitative drastic change: they range from pure inelastic excitations with no sign of any exchange interactions with the hosts electrons in the minimum (a)) until a fully emerged zero bias peak, which, as discussed in section 3.3.1, is a sign of significant Kondo-like exchange correlations. To properly explain this transition, we now want to describe it spectrum by spectrum.

The spectrum in a) is very similar to the one presented in figure 5.2 a). We can fit it with two temperature broadened Fermi Dirac distribution functions and extract step positions around $\pm 2.7\,\mathrm{mV}$. We find the widths of the steps to be $\pm 0.45\,\mathrm{meV}$, which is larger than the experimental broadening at $1.1\,\mathrm{K}$ and suggests a lower bound of the life time of the excitation to be $\approx 1\,\mathrm{ps}$. This value is significantly higher than other reports for Fe atoms, which were directly adsorbed onto metal substrates, thus demonstrating the decoupling properties of the MoS_2 layer [174, 175, 181, 182]. Note that the spectrum in a) could also have been reproduced using the perturbative model, without including any third order contributions in the exchange coupling, as we previously described in section 3.3.2.

The spectra in b)-d) were recorded on atoms lying between the moiré minimum and maximum. They all have very similar lineshapes, the inelastic excitation is still present, but also a clear asymmetry emerges in the spectrum. It is governed by a conductance overshoot at positive energies of the inelastic excitations and a conductance undershoot at negative energies of the inelastic excitations. The closer the atoms are located to the moiré maximum, the more pronounced this additional contributions to the conductance become. Moreover, the excitation energy decreases and the broadening of the step increases, pointing towards a more and more enhanced exchange coupling to the metal electrons. The spectra can be reproduced by using the perturbative approach established in [130], including third order perturbations in the exchange coupling constant $J\rho_0$, as shown as the overlayed black dashed lines in the spectra. The fit parameters are shown in the caption of figure 5.3. One can see that the extracted fit parameters indeed reproduce what we qualitatively saw in the evolution of the spectra: the exchange coupling constant $J\rho_0$ and the potential scattering parameter U increase towards the moiré dome, whereas the axial anisotropy D decreases.

Even though the fits reproduce the spectra very well, one can see that the fit accuracy is already significantly lowered for the spectrum in d). The spectrum in e) can not be captured at all with the perturbative framework, suggesting that a different description becomes necessary at the given interaction strength and the system has to be treated in the strong Kondo coupling regime. As described earlier, this can be done in a poor persons scaling approach. For the case of a spin state of S=1 and anisotropic exchange couplings $J_\perp$ and J_z it yields [116]:
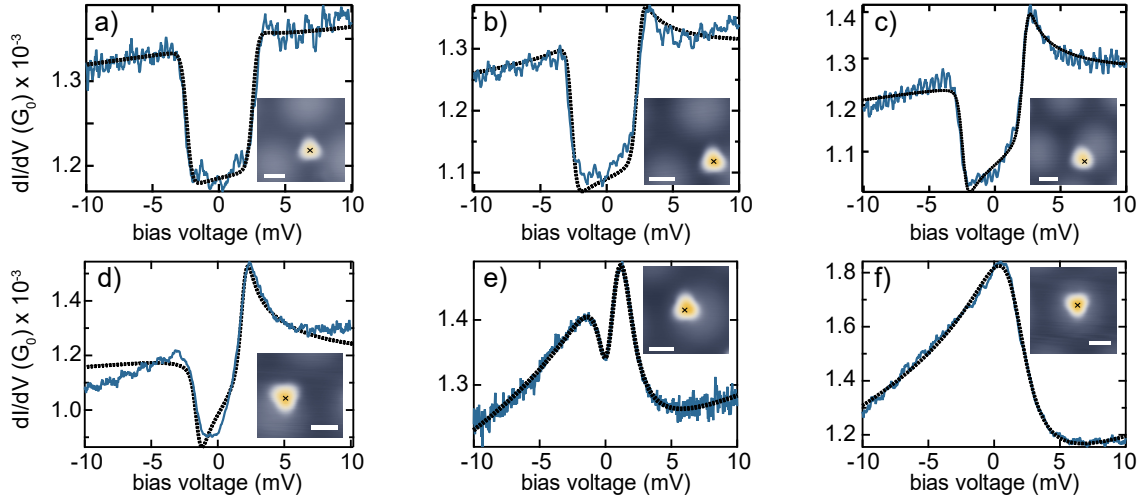
Figure 5.3: Moiré variation of spin excitations. a-f) dI/dV spectra recorded on different positions in the moiré superstructure. Fits of the spectra are shown as the black dashed lines. The spectrum in a) can be reproduced by temperature broadened Fermi-Dirac functions. The spectra in b-d) were fitted with the perturbative approach discussed previously. For e) and f) Frota peaks have been used, to accord for the dip feature in e) we additionally included a Lorentzian peak. The topographies were recorded at a setpoint of $50\,\text{mV}$, $100\,\text{pA}$, the spectra were recorded at $10\,\text{mV}$, $1\,\text{nA}$. Fit parameters are: a) Step position: $2.7\,\text{mV}$, step width: $0.45\,\text{mV}$ (error of the fit $\chi^2 = 7.4\times10^{-8}$), b) $J\rho_0 = -0.11$, $U = -0.32$, $D = 2.5\,\text{mV}$ ($\chi^2 = 3 \times 10^{-7}$) c), $J\rho_0 = -0.16$, $U = -0.71$, $D = 2.3\,\text{mV}$ ($\chi^2 = 4 \times 10^{-7}$) d), $J\rho_0 = -0.33$, $U = -1$, $D = 1.73\,\text{mV}$ ($\chi^2 = 1.9 \times 10^{-6}$), e) Frota phase $\phi = 3.87$, Frota width $\Gamma = 2.21\,\text{mV}$, Frota center $x_0 = 1.3\,\text{mV}$, Lorentz width $\Gamma_L = 0.79\,\text{mV}$ and Lorentz position $x_L = 0.11\,\text{mV}$ ($\chi^2 = 1.5 \times 10^{-7}$), f) $\phi = 4.12$, $\Gamma = 3.49\,\text{mV}$, $x_0 = 1.6\,\text{mV}$ ($\chi^2 = 9.1 \times 10^{-8}$).

$$\frac{dJ_z}{d\ell} = \frac{1}{1-\Delta}J_\perp^2 \tag{5.1}$$

$$\frac{dJ_\perp}{d\ell} = \frac{1}{2}(1 + \frac{1}{1+\Delta})J_\perp J_z \tag{5.2}$$

$$\frac{d\Delta}{d\ell} = \Delta - (J_z^2 - J_\perp^2)\ln 2. \tag{5.3}$$

Here, the exchange couplings are made dimensionless by means of the density of states ρ_0 of the conduction electrons, $\rho_0 J \rightarrow J$, ℓ is a scaling variable which parametrizes the bandwidth E_c, $\ell = \ln(E_{c0}/E_c)$, with initial bandwidth E_{c0}, and $\Delta = D/E_c$ measures the longitudinal anisotropy in units of the bandwidth [183].

We already mentioned that the increased DoS on the moiré maximum increases the exchange coupling, which manifest in a more and more developing Kondo peak. When the Kondo temperature, which as we have shown in proportional to $J\rho_0$, becomes larger than the axial anisotropy D, a fully developed Kondo peak will form. In addition, the exchange coupling not only increases towards the moiré maximum, but also provokes a renormalisation of D, as can be seen from the scaling equations. For $D > 0$ and $J_z > J_\perp$, which reflects easy axis anisotropy, as well as for $D < 0$ and $J_z < J_\perp$, which reflects easy-plane anisotropy the axial anisotropy gets reduced in magnitude by increased exchange coupling, which can be seen from equation 5.3. This decreases the level splitting even more, producing more and more degenerate energy levels of the spin projection m_s, which increase the likelihood of elastic spin flip processes, necessary for the formation of the many-body Kondo state. The renormalisation of the anisotropy has also been found in different works [184].

We see that with modelling parts of the spectra with the perturbative approach and then switching to a strong coupling description, we can explain all different encountered spectra. The spectra in figure 5.3 e) and f) were therefore fitted with a Frota functions, which is describing a Kondo resonance in the strong coupling regime (in e) and Lorentzian peak had to be included to phenomenologically account for a small anisotropy). To our knowledge such a continuous and complete transition from a complete absence of any Kondo correlations to a fully developed Kondo peak has not been observed before and proposed single Fe atoms on MoS_2 as a very promising system to tune quantum dynamics of the adatoms spin.

Still, we have not yet addressed the origin of the remarkable, triangular shape of the single iron atoms. In the following section, we want to look at it in more detail.

5.4 Origin of the triangular shape: potential scattering via a non-magnetic orbital

As mentioned above, the observed triangular shape for the iron atoms, when imaged at low bias voltages, was rarely observed for atoms on surfaces. It is safe to assume that certain electronic states in this energy region have to contribute to the appearance. We now want to present how the differential conductance varies spatially over a single atom. Due to

the large variations in the spectral fingerprints of atoms sitting on the moiré minima and maxima we want to discuss them separately.

5.4.1 Potential scattering in the moiré valley

Figure 5.4 a) shows a STM topography of a single Fe atom close to the moiré minimum. We now performed dI/dV spectroscopy at the center and at one of the vertices of the atom, as indicated with the crosses in the topography. The resulting spectra are presented in d): The spectrum in the center shows two symmetric steps, similar to the presented spectra in figure 5.3 a) and b). However, looking at the spectrum in 5.4 d) at one of the vertices of the triangular shape one sees a striking difference: first, the overall contribution of the inelastic channel is strongly enlarged, suggesting a much more efficient spin-electron-coupling. Secondly, the spectrum is suddenly asymmetric, which points towards a non-negligible potential scattering. Moreover, above the inelastic thresholds, one can see either an overshoot in the differential conductance (at positive bias) or a dip in the differential conductance (negative bias).

To see how this asymmetry in the excitation spectra maps out over the whole atom, we performed a grid of densely spaced spectra over it. In b) and c) the corresponding signal at the energies of the dip (b) and the overshoot (c) is shown, superimposed on STM topographies. One can clearly see that the triangular symmetry is also visible in the dI/dV spectra. The dip-like feature at negative bias is most prominent on the vertices of the atom (corresponding to a low differential conductance). Similarly, the conductance overshoot is also strongest developed at the vertices of the atom, which is reflected by the maxima of the differential conductance.

The shape of the red spectrum in figure 5.4 d) is similar to the ones presented in figure 5.3 c) and d). However, the latter ones were taken in the center of the respective atoms and at different sites of the moiré . We previously described the increasing peak width and overshoots with variation in the exchange coupling constant $J\rho_0$ along the moiré structure. For intraatomic variations of the asymmetry this explanation supposedly does not hold, as $J\rho_0$ should not change along the atom. Also, as mentioned before, if it where to change, we would expect to see a renormalisation of the magnetic anisotropy in the spectra, which we do not observe. Nevertheless, as we have seen from equation 3.15 and as described in literature [111, 130] also a varying potential scattering parameter U could cause this varying asymmetry in the spectra. To check, if we can reproduce the lineshapes at different parts of the atom, we fitted the spectra taken in b) and c) with the perturbative approach, while keeping the magnetic anisotropy and $J\rho_0$ fixed in the fit by constraint. In figure 5.4 e) a set of spectra are plotted, which were taken over the orange line shown in f). The fits are overlayed as the black dashed lines. Clearly, all spectra shown can be reproduced quite well while only changing the potential scattering parameter. Mapping the potential scattering over the whole atom yields the colour plot shown in f) (note that in comparison to b) and c) some points at the edges of the grid are left out, because the background spectra can not be fitted). In analogy to the signal shown in b) and c), the potential scattering also resembles the triangular symmetry, with being most dominant at the vertices of the triangles.

The contribution of the potential scattering can be understood as an interference effect, conceptionally close to the interference causing the Kondo resonance, as described in

section 3.3.1 and literature [117,185]. Whereas for the Frota-like interference the interference between tunnelling into the Kondo resonance and the bulk continuum states are believed to be the important contributions, recently it has been proposed that also tunnelling via atomic or molecular orbitals, which cross the Fermi level, can cause interference effects [123,186,187]. Then variations in the tunnelling amplitudes via the individual orbitals can cause such spatially varying lineshapes [124,188]. To justify this explanation of the varying intensities, we have to identify the contributing orbital. Therefore we performed dI/dV spectra spatially over a wider energy range. Figure 5.4 h) shows two spectra, performed on the same locations as the ones shown in d). For the spot in the center one can see a wide slope over the whole energy range, but no resonance is detectable. In contrast, looking at the spectrum at the right corner of the atom, one can observe a resonance around $150\,\mathrm{mV}$. This resonance is spatially mapped in g). Again, one can can see a triangular weight of the mapped signal, resembling the observed shape in the STM topography. This suggest that the detected resonance stems form a hybrid Fe-S state with concentrated weight on the S atoms, which leads to the triangular symmetry. This proposed hybrid orbital is consistent with DFT calculations [17].

Taking the Fe-S hybrid state in account we now can explain the asymmetry in the excitation spectra: at the center of the atom we observe a symmetric lineshape, which stems from co-tunnelling via the spin-carrying orbitals. The small weight of the Fe-S state here leads to a negligible potential scattering. Contrary, on the vertices of the triangle, the spectral weight of the Fe-S hybrid orbital is large. Therefore, the tunnelling paths through this orbital is strongly enhanced in comparison to the center of the atom, leading to a much more pronounced potential scattering.

In figure 5.5 a) we illustrate this trend once more: in a) a stacked plot of dI/dV spectra are shown, which are taken over the orange line in b) (half of the spectra were already shown in figure 5.4 e)). The stacked plot starts at the top of the line, at one of the vertex of the triangle. Here, the spectra show a very pronounced asymmetry. Towards the center of the atom the asymmetry gradually decreases, the spectra also generally have a lower signal. Towards the bottom of the line the asymmetry increases again partially, as the line passes the region between the bottom left and bottom right vertex of the triangle, where tunnelling through the Fe-S state is again more likely. After this point is passed, the signal intensity and asymmetry decreases again towards the bare MoS_2. In c) the potential scattering parameter is plotted along the orange line. It reflects the same trend: a gradual decrease from top to bottom with the exception of the area, where the line passes between two vertices.

So we have seen in this subsection that the Fe-S hybrid state was key for understanding the varying asymmetries of the excitation spectra along a single Fe atom. In section 2.12.2 we have seen that the electronic structure of the bare MoS_2 varies along the moiré. Therefore we now want to have a look if the above made observations are still valid for Fe atoms closer to the moiré maximum.

5.4.2 Potential scattering on the moiré dome

Figure 5.6 a) shows a STM topography of a single Fe atoms adsorbed on the edge of a moiré dome. We again performed spectra at the center and at one of the vertices of the atom, as indicated with the crosses in the topography. The resulting spectra are shown in
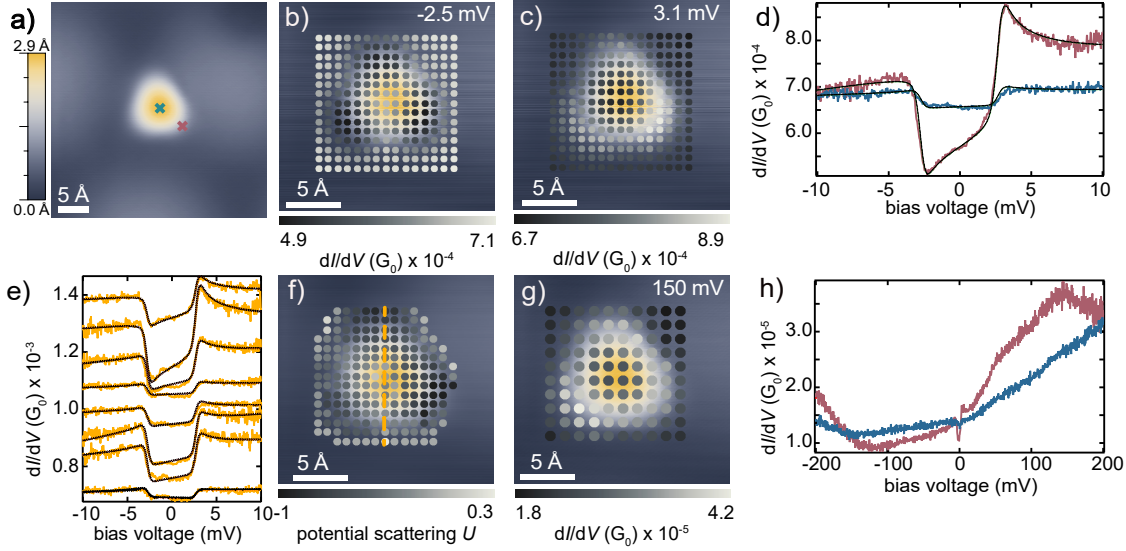
Figure 5.4: Intraatomic variations of the potential scattering. a) STM topography of an Fe atom located on a moiré minimum. b),c) STM topographies (blue-yellow, background) with superimposed dI/dV signal at the indicated bias voltages extracted from a densely spaced grid of spectra. (d) dI/dV spectra on the indicated positions in a) . Fits (black) with the perturbative model as described before [130] with $J\rho_0 = -0.13$, $U = -0.14$, $D = 2.75\,\text{mV}$ (center) and $J\rho_0 = -0.13$, $U = -0.78$, $D = 2.74\,\text{mV}$ (vertex). (e) dI/dV spectra recorded across the Fe–S complex along the orange line in (f) and fits (black) where $J\rho_0$ was kept constant in all fits, while U, the conductance offset and the effective tunnelling barrier of the junctions were adjusted. Spectra are offset for clarity. (f) STM topography with superimposed values of the potential scattering parameter U extracted from fits with the perturbative model of a grid of spectra. (g) STM topography with superimposed dI/dV signal at the indicated bias voltage extracted from a grid of spectra. (h) dI/dV spectra over a larger energy range at the same positions as in (b). Spectra in (b-f) were recorded at $V = 10\,\text{mV}$, $I = 1\,\text{nA}$ and tip retracted by $20\,\text{pm}$, lock-in frequency $f = 911\,\text{Hz}$ and modulation $V_{\text{rms}} = 50\,\mu\text{V}$; spectra in (g) and (h) at $V = 10\,\text{mV}$, $I = 20\,\text{pA}$ and tip retracted by $20\,\text{pm}$, lock-in modulation $V_{\text{rms}} = 1\,\text{mV}$. The topographies were recorded at $V = 10\,\text{mV}$, $I = 1\,\text{nA}$ (a),g)) and $V = 10\,\text{mV}$, $I = 1\,\text{nA}$ (b), c), f)). Grids were analyzed using SpectraFox [61].
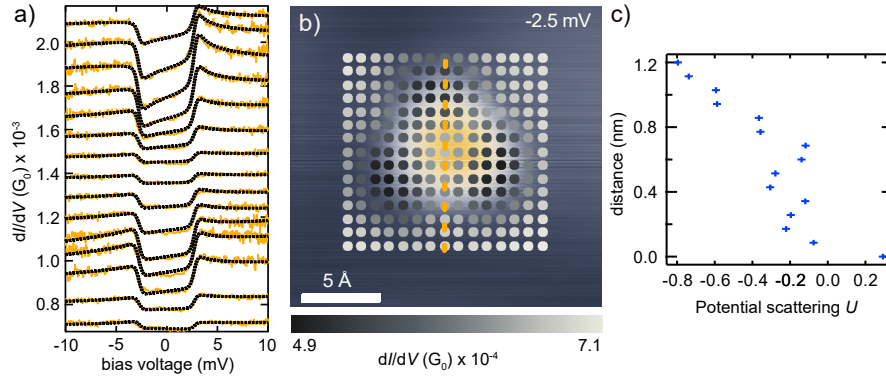
Figure 5.5: Lineprofile of the intraatomic variations of the potential scattering. a) dI/dV spectra recorded on the orange line shown in b), they are offset for clarity. b) STM topography with superimposed dI/dV signal at the indicated bias voltage extracted from a densely spaced grid of spectra. c) Extracted values for the potential scattering parameter from fits of the spectra in a) performed with the perturbative approach with $J\rho = -0.132$ and $D = 2.75$ meV kept constant. Grids were analyzed using SpectraFox [61]. The spectra in (a) and (b) were recorded at a setpoint of $V = 10$ mV, $I = 1$ nA. The topography in b) was recorded at $V = 10$ mV, $I = 100$ pA

.

in b): both spectra exhibit a similar asymmetry with an increased differential conductance at positive bias voltages around 1.6 mV and a decreased differential conductance around -0.9 mV. They foremost vary in their signal intensities. The shown spectra are comparable to the ones shown in figure 5.3 e). We now again want to look at the spatial variations of the excitation spectra. We therefore again took spectra over one of the symmetry axes of the Fe atom, which are shown in d). They were taken over the orange line shown in e). Again, we find that the signal intensity decreased towards the center of the atom. In e) and f) we additionally plot a densely-spaced grid of dI/dV spectra superimposed over a STM topography at 1.6 mV and -0.9 mV. As we have seen for the case of the atom in the moiré minimum, the signal intensities are again enhanced at the vertices of the triangular shape. However, the triangular symmetry in the dI/dV signal is broken by the superposition of the moiré modulation, as the top right vertex, which is the most far away from the moiré dome exhibits a lower signal intensity than the other two vertices.

Two correlate these changes with the higher-energy electronic structure, we performed dI/dV spectra at higher energies, which are shown in figure 5.6 c). Once again one can see that no resonance is present in the energy range of the spectrum taken at the center of the atom (blue curve). However, the spectrum at one of the vertices shows a small, but broad resonance at around 85 mV. Mapping this resonance out we can see that it follows the same symmetry as the the grids shown in e) and f): the intensity is lowest in the center of the atom and two of the three vertices have an increased intensity in comparison to the other one, breaking the threefold symmetry. We therefore also propose for Fe atoms closer towards the moiré dome that the variations in the signal intensity can be explained by different
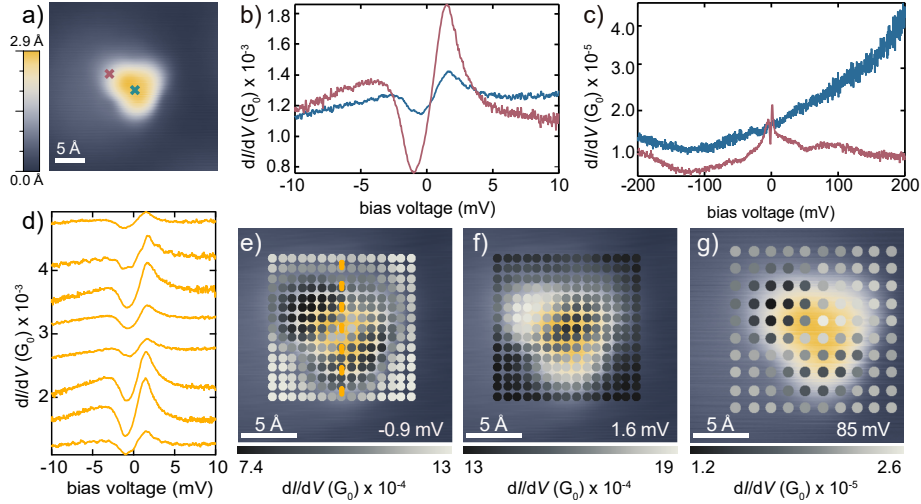
Figure 5.6: Intraatomic variations of the potential scattering. a) STM topography of an Fe atom located on a moiré maximum. a) STM topography image of an Fe atom close to a maximum of the moiré structure. (b),c)) Differential conductance spectra on the center (blue cross) and vertex (purple cross) of triangular shape of the Fe adatoms. d) Stacked plot of spectra (offset for clarity) along the orange dashed line indicated in (e). e)-g) STM topographies with superimposed differential conductance signal at the indicated bias voltage extracted from a densely spaced grid of spectra across the Fe atom at the indicated energies. The spectra in b), e) and f) were recorded at a setpoint of $V = 10\,\mathrm{mV}$, $I = 1\,\mathrm{nA}$, the spectra in c) and g) at $V = 10\,\mathrm{mV}$, $I = 20\,\mathrm{pA}$, with an additional retraction of the tip by $z = 20\,\mathrm{pm}$. The topographies were recorded at $V = 10\,\mathrm{mV}$, $I = 1\,\mathrm{nA}$. Grids were analyzed using SpectraFox [61].

contribution to the interfering tunnelling paths. However, for this present case we can not correlate the observed changes directly with the potential scattering parameter U, as the lineshapes can not be treated anymore in the perturbative model developed by Ternes.

5.5 Current dependence of the excitation spectra

Previously, we stated that from the lineshape of the spin excitation of the Fe atoms adsorbed on the moiré minimum we can deduce a lower bound of the lifetime of the excited states of about $1\,\mathrm{ps}$. This already illustrates the decoupling properties of the MoS_2 layer, as transition metal atoms on bare metal substrates usually show shorter lifetimes for their excited spin states, usually in the order of hundreds of femtoseconds [182]. Moreover, the spin-relaxation time of the system τ_1 is usually much larger than the spin-decoherence time τ_2 [182, 189]. Therefore the lifetime broadening seen in inelastic spectroscopy is most likely dominated by spin-decoherence processes, indicating that τ_1 might be sufficiently larger than $1\,\mathrm{ps}$ in our system. One way to determine which process determines the lifetime is to perform measurements at higher current setpoints. These measurements have an effect on both

τ_1 and τ_2. In regard to τ_1, larger currents may change the population of the excited state with respect to the ground state. This depends on the rate equations for the population of the energy levels: if electrons tunnel on average faster into the excited state than the lifetime of it and the electron induced de-excitation of the state allows for it, a second excited state can be populated. This effect is called spin pumping and would lead to the manifestation of a second step in the dI/dV channel, if the spin state of the atom allows for it [190] (for example, a spin state of S=1 is a two-level system and does not allow for that). On the other hand, if the lifetime broadening is limited by the decoherence time, the increased rate of electrons tunnelling into the excited state should promote a faster relaxation, which then would be visible in an increased step width. Figure 5.7 a) shows the extracted step width as a function of spectra taken at different setpoint currents. The current here varies between 3 and 23 nA. In this range no clear trend can be extracted from the changes in the widths of the excitations. Also, no additional step has been observed in the spectra. Therefore it remains inconclusive, which mechanism determines the lifetime of the excited spin states of the Fe atoms on MoS_2. Different experiments could help to resolve this question: electronic pump-probe schemes can measure τ_1, when it is in the order of nanoseconds or slower [191, 192]. If the lifetime would be in the order of picoseconds, not electrical, but optical pump-probe schemes would have to be applied. This could be done with a THz STM, which uses single short cycle terahertz pulses as ultrafast transient bias voltages [193, 194]. In contrast, a way to probe τ_2 can be achieved with an ESR STM [173].

Figure 5.7 b) shows measurements of the magnetic anisotropy energy with respect to the current setpoint. All measurements were performed on the atom shown in the inset, sitting in a position close to the moiré minimum. The anisotropy energies were extracted by fits with temperature broadened step functions. One can see that the anisotropy increases continuously with increasing current setpoint, e.g. smaller tip-sample distances. The origin of this relation is most likely non-electrical, but a structural one: The STM tip exhibits a force towards the Fe atoms. At sufficiently large distance this force is negligible, but at closer distances the force is attractive, pulling the atom slightly from the surface. At even closer distances the force starts to act repulsive, pushing the atom more towards the substrate. In this latter case one could expect larger anisotropy energies, as the atom experiences the crystal field of the sulfur atoms stronger the closer it get to the sulfur layer. Theoretically, also the coupling to the substrate electrons $J\rho_0$ could be tuned this way [195].

5.6 Fe atoms with a different appearance

In this section, we want to briefly cover the origin and properties of non-triangular shaped Fe atoms.

5.6.1 Hydrogenated iron atoms

Figure 5.8 a) shows a MoS_2 island scanned at a low bias voltage. In contrast to the previously shown STM topographies, only the minority of atoms appears triangular here, namely one atom at the right bottom edge of the island. In b) we show dI/dV spectra performed on two of the round atoms from the topography. The black atom, located close to the moiré maximum shows several broad step-like excitations, most noticeably around $\pm 0.3\,\mathrm{mV}$ and
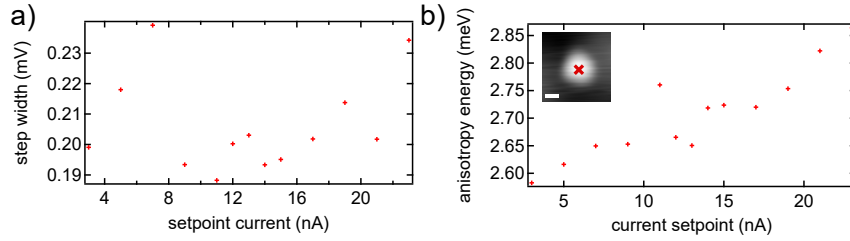
Figure 5.7: Tip-sample distance dependence of the excitation lineshape. a) Widths of the inelastic excitations of single Fe atoms at different current setpoints extracted from fits with Fermi-Dirac functions. The spectra were recorded at the spot indicated in the inset in b). b) Extracted energy of the axial anisotropy from the same fits as in a). The voltage setpoint of each spectrum was $V = 10\,\text{mV}$, the topography was recorded at $V = 50\,\text{mV}$, $I = 100\,\text{pA}$. The scalebar in the inset in b) amounts to $5\,\text{Å}$.

$\pm 3\,\text{mV}$. For the atom marked with the red cross two spectra are shown: the lower one of them shows one step-like excitation, very similar to the one observed on the triangular atoms, but at a slightly higher energy of $\pm 3\,\text{mV}$. The upper spectrum in contrast shows two step-like excitations around $\pm 1.7\,\text{mV}$ and $\pm 5\,\text{mV}$. The reason, why we show two different spectra of the red atom is that its spectrum actually changed over time. This is not typical, as the crystal field experienced by an atom is not supposed to change, while it sits on the same adsorption site. However it may change if the atom forms a bond with another, residual atom on the surface. A very likely candidate for this is the hydrogen atom/molecule. Due to its size and mobility hydrogen molecules are known to stick on samples at cryogenic temperatures. Moreover, transition atoms are know to dissociate hydrogen molecules and form metal-hydrogen complexes [196]. For Co atoms, CoH_n complexes of up to three hydrogen atoms have been observed [145, 178, 196]. The adsorption of hydrogen atoms can change the spin state of the transition metal atom, which has an immediate impact on the low-energy magnetic excitations and change the appearance of the atom [145, 178, 196].

Usually hydrogen atoms can also easily be desorbed from metal atoms, for example by applying voltage pulses in their proximity. We applied these to the round atoms shown in figure 5.8 a), the result can be seen in c): scanned at the same bias voltage, most of the atoms appear triangular again, indicating that indeed hydrogen atoms were removed from the Fe atoms. We have seen that the low-energy excitations for some of the hydrogenated Fe atoms are similar to the ones of the triangular atoms. To learn where the varying appearance comes from, we performed dI/dV spectra at higher energy ranges on the same atom before and after removing a hydrogen atom. The results are shown in d): The hydrogenated Fe atom (labelled as one, blue cross in a)) shows a resonance centred around $220\,\text{mV}$. In addition several equally spaced peaks are visible at the onset of the resonance, one of them marked with the black arrow. In contrast, the spectrum performed on the atom, while appearing triangular, shows no evidence of such a resonance, explaining the difference in appearance between.

A reason, why the red spectrum in b) changed over time could be that more hydrogen atoms adsorbed to the Fe atom, changing its spin state effectively. However, as the appearance of the atom did not change one can not say this with confidence. To learn more
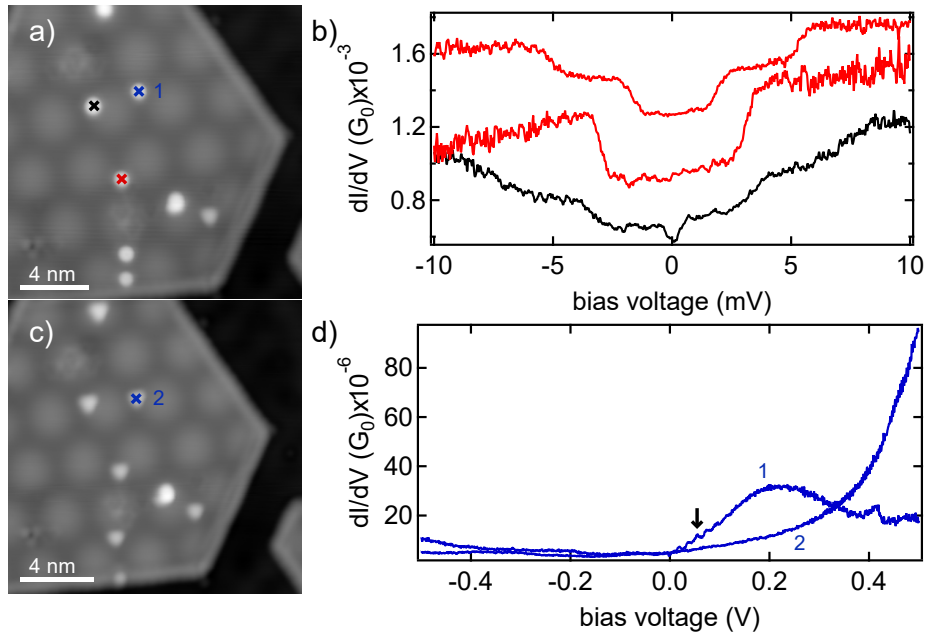
Figure 5.8: Influence of hydrogen adsorption on the iron atoms. a) STM topography of several single iron atoms at a low energy. Almost all atoms appear as round protrusions. b) dI/dV spectra recorded on the atoms marked in a) with the respective colours. c) STM topography at the same location and energy as in a) after a high bias voltage of $V = 1.5\,V$ has been applied to each atom. d) dI/dV spectra performed at the same atom before and after a high voltage was applied next to it. The setpoint of the spectra was $V = 10\,mV$, $I = 1\,nA$ and $V = 10\,mV$, $I = 20\,pA$ with an additional retraction of the tip by $80\,pm$, the topography was recorded at $V = 50\,mV$, $I = 20\,pA$.

about it, one either has to study the hydrogenated species further by for example controlled exposition of the atoms to hydrogen molecules or perform theoretical calculations. Also the variations of the spectra along the moiré superstructure could be an interesting aspect to study.

5.6.2 Fe atoms on point defects

We have seen in figure 5.1 that not all atoms appear triangular at low bias voltages. This holds true even for measurements performed soon after the preparation, where the hydrogen exposure of the sample is minimal. We show another example in figure 5.9. Here, in the top left and right corner two round atoms can be found, whereas the rest of the atoms appear triangular. We then performed spectra on both species of atoms in a wide bias range, as shown in b). The spectra were taken on the atoms, which are marked with crosses in a). One clearly can see a difference between the spectra of the round and the triangular atom: the triangular atom shows no resonances at negative bias voltages and two broad one at positive bias voltages. In contrast, the spectrum on the round atom shows two resonances at negative bias voltages, a zero bias peak and an onset of conductance

at positive bias voltages. We want to point out two observations here: first, the spectrum of the round atom differs significantly from the ones of the hydrogenated atoms shown in the previous section. Also, they are stable, when probed at higher bias voltages. This suggest that this type of round atoms is not hydrogenated. Moreover, the spectrum of the round atom has striking similarity with the ones of the sulfur vacancies presented in chapter 4. This suggests that the round atoms here could be adsorbed on point defects. To check this hypothesis we removed all atoms on a MoS_2 island after performing dI/dV spectra on them. To successfully remove all atoms on an island, we scanned the respective region at a very small tip-sample distance, which leads to a large van-der-Waals force between the tip and the Fe atoms. Figure 5.9 c) and d) show the island before (c)) and after (d)) the removal of the atoms. All round atoms before removal are marked with an orange circle. The same locations are still marked in the STM topography after the removal. One can see that all these spots now show point defects in the MoS_2. These defects can break the triangular symmetry of the sulfur layer and provide a different electronic environment for the atoms, which causes a different appearance in the STM topographies. As we observed this behaviour for all non-hydrogenated round atoms we can exclude that the magnetic properties of the triangular atoms are altered by defects in the MoS_2 layer. In this thesis we did not investigate the properties of the Fe atoms adsorbed on point defects further. Note though that theoretically this could be an interesting system to study, as the sulfur vacancies also exhibit a magnetic moment and therefore could couple magnetically to the Fe atoms.

5.7 Outlook: Fe dimers and single atoms on pit defects

We want to end this section with a small outlook to experiments, which could be performed in the future. One interesting system to study would be Fe atoms coupled to dimers. Here, besides the exchange coupling with the substrate electrons also interatomic exchange coupling would come into play. Figure 5.10 a) shows two Fe atoms in close proximity to each other. In c) low-energy dI/dV spectra performed on the two atoms are shown. One can see that now two spin excitations are visible, clearly indicating that the atoms influence each other. Performing several of such spectra with differing atom spacings and positions in the moiré superstructure could give more insights how the interatomic exchange coupling and the Kondo correlations scale with each other. This has been studied only vaguely in literature as usually Kondo correlation strength do not vary as drastically on atomic length scales as observed in our experiments.

Another future experiment could be the study of Fe atoms adsorbed on or close to pit defects, as shown in figure 5.10 b). As the Au(111) layer is missing below these areal defects, no exchange coupling with the substrate is present here. This should prolong the lifetime of the spin excitation of the Fe atoms, which is still present close to the pit defect, as can be seen from the spectrum shown in d). The energy level alignment itself seems to vary drastically for the atoms on the pit defects, as can be seen from the spectrum in e): here, two peaks inside the band gap emerge, at $-800\,mV$ and $250\,mV$. Of course, both experiments suggested could be also well combined by studying Fe dimers on pit defects. However the construction of such dimers is supposedly challenging, as the manipulation of Fe atoms only rarely worked on the MoS_2 layer. Therefore an evaporation of a higher coverage could be necessary to promote a formation of Fe dimers in general and on pit defects.
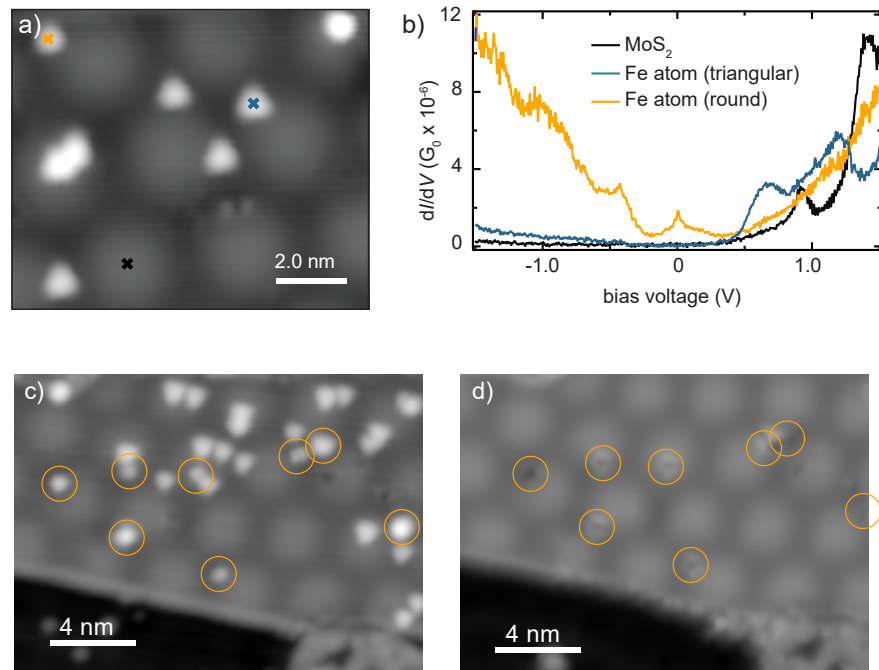
Figure 5.9: Fe atoms adsorbed on point defects in the MoS_2. a) STM topography of individual Fe atoms. The Fe atoms appear either triangular or circular shaped. b) dI/dV spectra recorded on a triangular (blue), circular (orange) shaped Fe atom and the bare MoS_2 (black). c) STM topography of several Fe atom on a MoS_2 island. Non-triangular appearing atoms are marked with orange circles. d) STM topography image of the same area as in c) taken after removing all Fe atoms. This has been achieved by scanning at a small bias voltage and large currents ($V = 4.7\,\mathrm{mV}$, $I = 25\,\mathrm{nA}$). The locations of the atoms which had been imaged with non-triangular shape are marked again by orange circles. The spectra were taken at a setpoint of $V = 1.5\,\mathrm{V}$, $I = 300\,\mathrm{pA}$. Topographies were recorded at a setpoint of $V = 50\,\mathrm{mV}$, $I = 100\,\mathrm{pA}$.

Figure 5.10: Fe dimers and single Fe atoms on pit defects. a-b) STM topography of several Fe atoms on MoS_2. In b) one atom is adsorbed close to a pit defect. c) dI/dV spectra performed on the two neighbouring atoms as indicated in a). d-e) dI/dV spectra performed on the atom marked in b). Spectra taken at a setpoint of $V = 10\,mV$, $I = 1\,nA$ (c)), $V = 50\,mV$, $I = 200\,pA$ (d)) and $V = 1\,V$, $I = 100\,pA$ (e)). Topographies were recorded at a setpoint of $V = 50\,mV$, $I = 100\,pA$ and $V = 500\,mV$, $I = 10\,pA$ (b)).

5.8 Summary

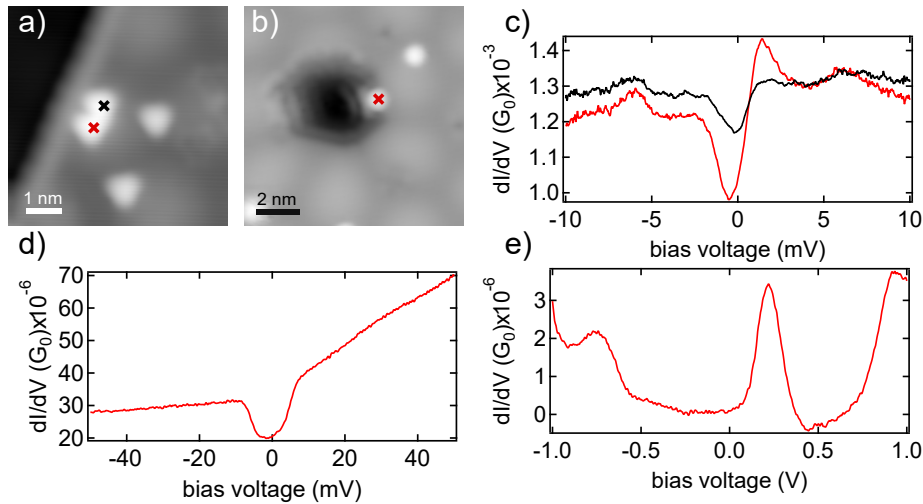To conclude, we investigated single Fe atoms on a layer of MoS_2 in this chapter. The Fe atoms show inelastic excitations, suggesting that their spin is still preserved after adsorption and the relaxation time of it is sufficiently long. Moreover we observed dramatic variations of the lineshapes of the single Fe atoms with respect to their positions in the moiré superstructure. Atoms on minima of the moiré did not exhibit signs of exchange coupling with the substrate electrons, whereas atoms on the maxima of the moiré showed full formed Kondo resonances, suggesting that their exchange interactions are the dominant processes. Moreover we found that the Fe atoms appear triangular at low bias voltages. We established that this appearance stems from tunnelling into a Fe-S hybrid orbital, which causes also an enhanced potential scattering at the vertices of the individual atoms. This then leads to asymmetric spin excitations, when probed off-center of the molecule. Finally we discussed the effects of defects and adsorbates on the electronic properties of the Fe atoms.

In the next chapter we want to study Mn atoms on MoS_2. As an non-integer spin system, Mn atoms are better suited to study Kondo physics. Also Mn atoms are known to easily couple to dimers, making it possible to study their interatomic exchange coupling.

6 Mn on MoS$_2$: Tuning a two-impurity Kondo system by a moiré superstructure

The results presented in this chapter have been published as:

- *"Tuning a two-impurity Kondo system by a moiré superstructure"* by Sergey Trishin, Christian Lotze, Friedemann Lohss, Giada Franceschi, Leonid I. Glazman, Felix von Oppen and Katharina J. Franke, *Phys. Rev. Lett.* **130**, 176201 (2023)

After discussing an integer spin atom in the previous chapter, we now want to focus our attention on a non-integer spin atom with manganese (Mn). Mn atoms on MoS$_2$ have been predicted to carry a substantial magnetic moment when adsorbed on the substrate [16,17]. In addition, the adsorption energy was found to be considerably smaller than for Fe atoms. As we found earlier on, the coupling to the substrate plays a crucial role for the quantum state of the atom, therefore it is intriguing to investigate Mn atoms under this circumstances.

As we have seen in section 3, spin $\frac{1}{2}$ systems exhibit the most efficient scattering with the substrate electrons, which leads to the formation of a Kondo state. For higher non-integer spin states, the efficiency of the scattering process can decrease, depending on the ground state of the system. For example, in previous works on Mn, a degenerate ground state of $m_s = \pm \frac{5}{2}$ was observed, which would require a $\Delta m = 5$ transition for a spin scattering and therefore does not lead immediately to the formation of strongly correlated Kondo state. In other works on cobalt (Co) atoms, which carry a spin of $3/2$ in gasphase, on Cu$_2$N the ground state was found to be $m_s = \pm \frac{1}{2}$, enabling an effective spin scattering [137]. Different studies on the same system suggest that the Kondo state can be suppressed by sufficiently large crystalline anisotropies, as we have also seen in section 5 [146]. Therefore non-integer spin systems also offer a wide range of Kondo physics and could provide intriguing and complementary information to our previous findings.

Moreover, we mentioned before that part of the motivation of studying magnetic adatoms on TMDCs was the theoretical prediction that in such systems the valley degeneracy of the TMDCs could be lifted with a large enough magnetic stray field. For this purpose larger atomic structures have to be build. Chains out of Mn atoms were one of the first larger systems to be constructed on an atomic scale with an STM and have been extensively studied since then [13]. For all these reasons Mn atoms seem to be a intriguing fit to learn more about single atom magnetism on MoS$_2$.
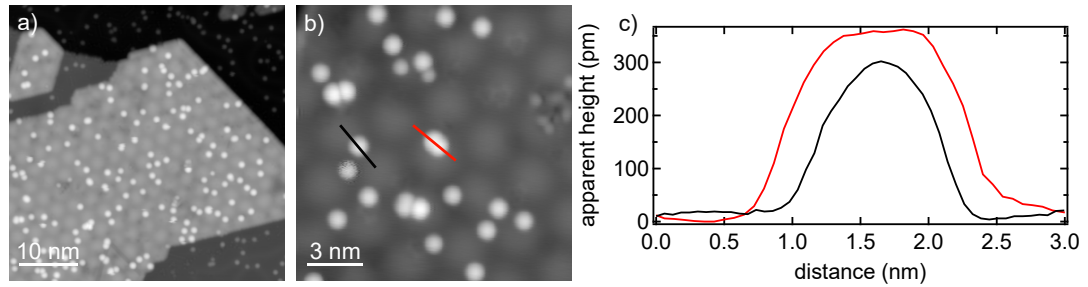
Figure 6.1: a) Appearance of Mn atoms adsorped on MoS$_2$ islands. a) STM topography of Mn atoms adsorped on MoS$_2$ islands on a Au(111) substrate. The atoms appear as round protrusions. Several atoms are unstable and appear to be moving during the scan. The topography was recorded at $1\,V$ and $100\,pA$. b) Smaller scale STM topography of Mn atoms on MoS$_2$. The topography was recorded at $100\,mV$ and $20\,pA$. At this smaller bias voltage the atoms appear to be more stable. Most of the atom appear as round protrusion, some as more elongated structures, probably stemming from Mn dimers. Several point defects can be observed in the MoS$_2$ layer. c) Apparent height profile of the black and red lines shown in b). The apparent widths differ between the round protrusion and the elongated one.

6.1 Adsorption structure of Mn atoms on MoS$_2$

We evaporated Mn atoms at a flux of 52 nA for 2 minutes on single-layer MoS$_2$ on Au(111), which was prepared following the steps given in section 2.12.2. The sample temperature was held under $12.5\,K$ to minimize diffusion of atoms, which could result in clustering of atoms. This was possible by directly evaporating into the STM chamber. All presented spectra in this chapter were measured at the JT-STM system at a base temperature of $1.1\,K$. Figure 6.1 a) shows an STM topography of two MoS$_2$ islands with several round protrusions, which we identify as Mn atoms. Even though larger clusters are visible, several single Mn atoms can be found. Some atoms are also adsorbed on the Au(111) surface and appear thinner.

In figure 6.1 b) a MoS$_2$ island is shown at a smaller scale. This image was recorded at a lower bias voltage of $100\,mV$. At such energies the Fe atoms, discussed in the previous section, appeared triangular. However, this does not seem to be the case for the Mn atoms, which still appear as round protrusions. This could be seen as a first evidence that the Mn atoms are coupled weaker to the MoS$_2$ than the Fe atoms, at least the hybridisation with the sulfur electronic states seems to be less relevant at such energies. Some structures appear ellipsoidal, hinting towards two atoms being adsorbed very close to one another. This dimer structures will be covered later on in this chapter. Figure 6.1 c) shows the profile of the black and red lines in b), which follows over a single Mn atom and a Mn dimer. Both, the apparent heights and widths of the two structures seems to vary. Whereas the variations in the height might at least partially stem from different adsorption sites in the moiré, the different widths indicate that the elongated structures indeed consist of two Mn atoms. As the lattice constant of MoS$_2$ is about $314\,pm$, the Mn atoms appear significantly bigger than

the sulfur atoms of the MoS_2 layer, making an exact determination of the adsorption site difficult, even when scanning with atomic resolution. We will later see that the movement of single Mn atoms and dimers during manipulation with the STM tip suggests that the atoms always sit on the same lattice site. As both the hollow site and the site over the molybdenum atom have been suggested in theory as the energetically lowest ones [16, 17] the exact adsorption site remains unclear at this point. In both figure 6.1 a) and b) several dark areas in the MoS_2 island are visible. In addition, in b), some point defect can be seen. This defects are formed during the growth process and can alter the electronic structure of the MoS_2 locally. We will discuss the influence of these defects in section 6.2.3. The spectra shown in all other sections were recorded on atoms sitting on non-defectious sites. We made sure of this by removing the atoms after the measurement set and inspecting the area.

6.2 Electronic structure of single Mn atoms

After discussing the adsorption structure of single Mn atoms on MoS_2, we now want to take a look at their electronic structure. For this, we performed dI/dV spectroscopy on several Mn atoms, exemplary results are shown in figure 6.2. In b) spectra recorded on the Mn atom, shown in the STM topography in a), (black) and the bare MoS_2 substrate in a range from $1\,V$ to $-1\,V$ are shown (red). The spectrum on the atom shows a resonance at negative bias around $-800\,mV$ and a resonance with a rising onset around $500\,mV$. These resonances most likely stem from tunnelling to or from d-orbitals of the Mn atom. However, especially the resonance at around $500\,mV$ could also be a new arising Mn-MoS_2 hybrid state, similar to the one we have seen for the iron atoms (even though there the appearance of the atoms made it much more evident). Unfortunately the Mn atoms were really unstable at higher bias voltages (e.g. higher electric fields), which made it impossible for us to record maps at those energies. Now, having seen the high voltage spectra, we want to take a look at our main interest: the magnetic fingerprints at lower energies. Figure 6.2 d) shows spectra recorded at the same position as the ones in b). Whereas for the MoS_2 only a linear background is visible, a small resonance at zero bias is apparent for the Mn atoms. In addition, no step-like features are seen in the given bias range. In c) an STM topography with superimposed dI/dV signal at the indicated bias voltage extracted from a densely spaced grid of spectra across the Mn atom is shown. The signal appears to be distributed uniformly over the whole atom. For a magnetic atom it is reasonable to assume that a zero bias peak stems from a Kondo resonance. However, in literature, different findings have been made for Mn on Cu_2N [197]. There, a small magnetic anisotropy was found, where the easy-axes was oriented out-of-plane. Therefore the ground state of the system is then $m_s = \pm\frac{5}{2}$ and spin-scattering events becomes less probable, as described before. Taking this back to the spectrum in 6.2 d), we conclude that absence of any magnetic anisotropy most likely results in degenerate energy eigenstates and allows Kondo correlations. The verification that the zero bias peak is indeed a Kondo resonance will be given in section 6.2.2, where measurements in a magnetic field will be presented. In the previous section we have found a significant magnetic anisotropy for the Fe atoms. Therefore, it is fair to asks ourselves, why it appears to be non-existing for the Mn atoms. Generally speaking, Mn has five half-filled d-levels. As a result, the orbital moment L equals zero. Consequently,

it is natural that Mn would exhibit a smaller spin-orbit coupling than iron and the absent magnetic anisotropy could be explained already like this. Another reason could be that the adsorption strength of the Mn atoms is indeed that low that the atoms have thus a larger distance to the surface than the Fe atoms, as predicted from DFT calculations [16,17]. As a result, the Mn atoms do not experience the crystal field, which most dominantly stems from the top sulfur layer of the MoS_2, the same way as the Fe atoms, even if they would be adsorbed at the exact same lattice site. Another possibility, describing another extreme and unlikely limit, would be a lifting of the degeneracy or occupation of the Mn d-levels (for example by electron transfer with the substrate), leading to an effective spin state of $S = \frac{1}{2}$. In this case, which requires very strong interaction with the substrate, no axial anisotropy can be present. However, even though a reduction of the spin state after adsorption is possible in general, most reports on magnetic atoms find best agreement with the initial spin state in gas phase [13,137,197]. The last possibility for the absence of any magnetic anisotropy we want to discuss at this point is the modification and suppression of the magnetic anisotropy by exchange coupling. We described this correlation in section 3.3.2 and it has been established in literature [146]. As we have seen, at large enough exchange coupling to the electron bath, the excitation energy basically becomes zero. To put this into perspective we first have to determine the exchange constant $J\rho_0$. This will be done in the following section.

6.2.1 Influence of the moiré superstructure on the spectral fingerprints

The determination of the exchange constant can be done in two ways: either we determine it directly via the perturbative approach established in [130] or determine the Kondo temperature and calculate the exchange constant via equation 3.8. Whereas the first approach is convenient for weakly coupled spins, the latter one is the more sophisticated approach for a strongly coupled impurity. Per default, we do not know in which regime the Mn atoms lie. And we have also seen previously for the Fe atoms that even some sort of intermediate regime exists. However, we can take an educated guess at the start: As the Kondo resonance in figure 6.2 d) appears relatively narrow (indicating a small T_K) and has a relatively low intensity (indicating a small $J\rho_0$) we first try to describe the Mn atoms with the perturbative model. Figure 6.3 a) shows two spectra, recorded on the atoms shown in the inset. Both show a Kondo resonance with different amplitudes. Two factors determine the amplitude of the Kondo resonance in the perturbative model: the exchange constant $J\rho_0$ and the tunnelling barrier constant T_0. Both values are not necessarily known quantities from the beginning. However T_0 should be similar for comparable junction resistances, so after obtaining the value ones we leave it fixed for spectra measured at the same setpoint. One reliable way to obtain T_0 is to fit spectra measured in a magnetic field, as the resulting splitting of the resonance can be reproduced by an unambiguous set of parameters of T_0 and $J\rho_0$. We find, for a setpoint of $15\,\text{mV}$ and $3\,\text{nA}$, a coupling constant of $4.1 \times 10^{-4} \pm 1.5 \times 10^{-4}$. We will use this coupling constant for the fits presented in this section.

Assuming a spin state of $S = \frac{5}{2}$, we get values of $J\rho_0$ = -0.080(red) and -0.049 (black) for the two spectra in figure 6.3 a). Values of $J\rho_0 \leq |-0.1|$ are usually considered to point to
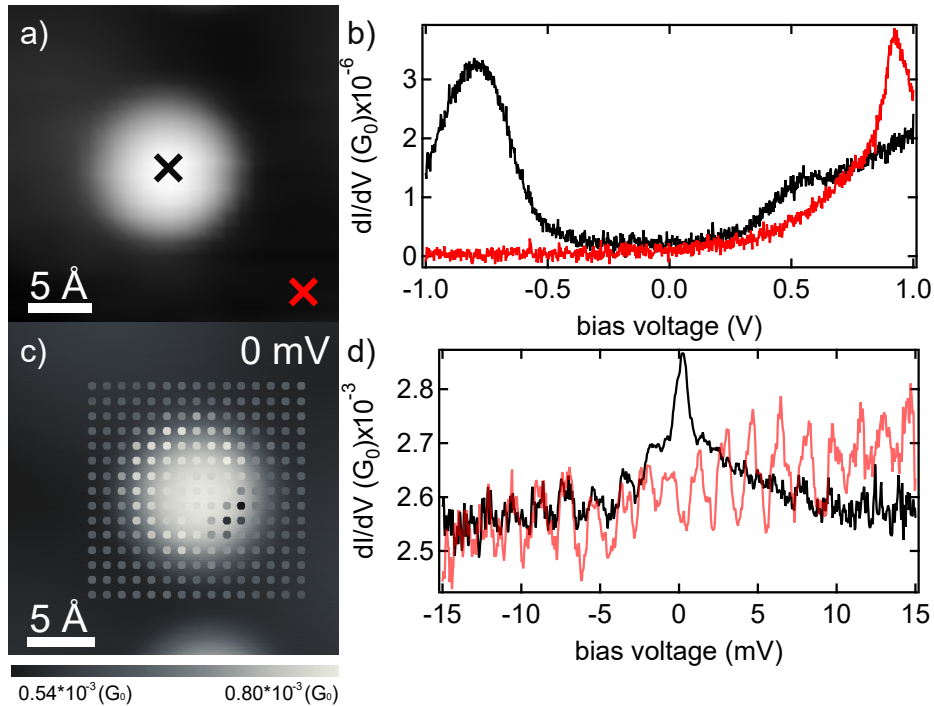
Figure 6.2: Electronic structure of single Mn atoms on MoS_2. a) STM topography of a Mn atom on MoS_2. The topography was recorded at $100\,mV$ and $20\,pA$. b) dI/dV spectra taken on the positions, indicated with the red and black crosses in a). The spectra on the Mn atom shows two resonances at $-0.8\,V$ and $0.55\,V$, which are absent on the bare MoS_2. These resonances can be attributed to excitation to/from the Mn d-levels. The spectra were recorded at a setpoint of $1\,V$ and $80\,pA$ and a modulation amplitude of $5\,mV$. c) STM topography with superimposed dI/dV signal at the indicated bias voltage extracted from a densely spaced grid of spectra across the Mn atom. The signal at zero bias has a similar strength across the whole atom, except at the bottom right of the atom. There, some instability during the stabilization of the setpoint led to a lower signal. The spectra were analysed using SpectraFox. The topography was recorded at $100\,mV$ and $20\,pA$. The spectra were recorded at a setpoint of $20\,mV$ and $1\,nA$ and a modulation amplitude of $200\,\mu V$. d) dI/dV spectra taken on the positions, indicated with the red and black crosses in a), but in a smaller bias range than in b). Whereas no excitation can be observed in this bias range on the bare MoS_2, on the Mn atom a zero bias peak can be seen. For better clarity, the spectrum on the bare MoS_2 has a reduced opacity. The spectra were recorded at a setpoint of $15\,mV$ and $3\,nA$ and a modulation amplitude of $167.5\,\mu V$.

relatively weakly coupled impurities and can be fitted consistently with the perturbative model [111, 130]. We note that the fits show an excellent agreement and yield an effective temperature T_{eff} of around $1.08\,K$, which is in very good agreement with our experimental temperature and indicates that there is no intrinsic broadening of the resonance at this temperature and the peak can still be reproduced by a temperature broadened logarithmic function. Relating this to our question raised earlier, if any potential magnetic anisotropy is just quenched by exchange interaction, we consider the determined coupling strength to be too small for this, as Kondo exchange interactions are only factoring in perturbatively here. We now want to discuss the differences in the two spectra in figure 6.3 a) further. The red spectrum was recorded on the upper inset image. There the atom was located close to the moiré maximum. In contrast, the black spectrum was recorded on the lower inset image, which was located closer to a moiré minimum. We established in the previous chapter for the Fe atoms that the exchange interaction is stronger on the moiré maxima than on the minima. Consequently, the higher value of $J\rho_0$ obtained from the fit of the red spectrum is in accordance with our previous results. To make this finding statistically more profound, we performed more fits for Mn atoms placed on several lattice sites. The result is shown in figure 6.3 b). Here, the coupling strength $J\rho_0$ is plotted against the distance of the Mn atoms from the moiré maximum. As the moiré superstructure is not rotationally symmetric (see section 2.12.2), the distances to the respective minima may vary slightly. However, as those variations are rather small, we determined the distances of the atoms from the moiré just by looking at the shortest path to the moiré dome. The different shapes of the markers represent different measurement sets with supposedly different tip apexes. We see that for each respective set of measurements the absolute value of the exchange coupling constant is highest close to the moiré maximum and smallest close to the moiré minimum. As mentioned previously, all fits were carried out by using the same tunnelling barrier constant. To account for its error, we included the red dashed lines into the figure, which represent the corresponding values of $J\rho_0$, if they would have been fitted with a different tunnelling barrier constant. For a better visualisation, we described the relation between the exchange coupling constant and the distance as a linear trend, even though it is not clear, if this has to be the case necessarily. In a linear model, the slope scales with $J\rho_0$, therefore leading to non parallel lines.

All sets of measurement show a change in coupling strength by a factor of 1.5-3. Still, no changes in lineshape, but the increased peak amplitude were observable. This relates to the factors we discussed above: as the Mn atoms do not experience a crystal field anisotropy, no inelastic excitations are expected to occur for high and low coupling strength. The width of the Kondo resonance could change though, when the system is driven from the weak coupling into the strong coupling regime. As a consequence the perturbative model would not be capable of fitting such lineshapes, as the width, resulting from the temperature broadening, will always be underestimated for a strongly coupled spin. We note that in our experiments the coupling never became sufficiently strong to provoke a transition into the strong coupling regime and the perturbative model was sufficient to reproduce all lineshapes.
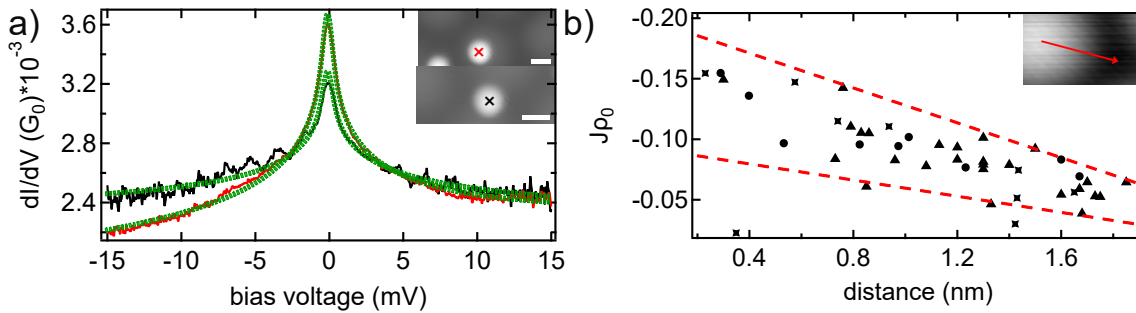
Figure 6.3: Moiré dependence of the Kondo scattering parameter. a) dI/dV spectra performed on the two Mn atoms shown in the inset. The upper atom (red) was adsorbed close to a moiré dome, the lower one close to a moirè minimum. The green dashed lines show fits according to the model proposed in [130], including third order processes. The fits yielded a $J\rho_0$ of -0.080(red) and -0.049 (black). The scale bar in the inset accords to $1\,nm$. b) Plot of the extracted $J\rho_0$ values from dI/dV spectra performed on atoms with differing position within the moiré superstructure as a function of the distance of the respective atoms from the moiré maximum. The different shapes of the markers represent different sets of measurements. The uncertainty in the coupling constant T_0 is accounted by the two red dashed lines. The red arrow in the STM topography in the inset indicates the defined start (moiré maximum) and end (moiré minimum) locations. The topographies were recorded at $100\,mV$ and $20\,pA$, the setpoint of the recorded spectra was $15\,mV$ and $3\,nA$.

6.2.2 Mn atoms in a magnetic field

Previously we stated that the zero bias peak shown before is a Kondo resonance. Even though this would not be uncommon for a magnetic atom, the final proof is still missing. This proof can be given by either looking at the temperature dependence of the resonance (for strong coupled impurities) or by taking spectra in a magnetic field. Figure 6.4 a) shows spectra taken at the same Mn atom without an applied magnetic field (black) and with an applied magnetic field of $3\,\mathrm{T}$ (red). Whereas the spectrum without field shows a zero bias peak, the spectrum measured at $3\,\mathrm{T}$ shows a resonance, which is split into two peaks, which are located symmetrically around zero bias. The blue dashed line represents a fit with the perturbative model [130], assuming the same essential parameters as for the spectrum without field, while additionally including the magnetic field of $3\,\mathrm{T}$. The fit shows a very good agreement with the measured data, assuming a Landé-factor of 2. Generally, two energy scales have to be surpassed by the magnetic field for a Kondo resonance to split: the Zeeman energy $\Delta E = g\mu_B B$ has to be higher than the thermal energy $k_B T$ and the Kondo correlation energy $k_B T_K$ [111]. Before those thresholds are exceeded the state is stable against the perturbation of the magnetic field or the splitting is not resolvable in experiment [137,196]. To put this into perspective, in our experiment, the thermal energy around $1.1\,\mathrm{K}$ is about three times smaller than the magnetic energy at $3\,\mathrm{T}$. Moreover, we mentioned before that we expect the Mn atoms to be in the weak coupled Kondo regime. For such impurities, which can be understood as nearly free, no real Kondo temperature can be defined. Still, it has been shown that the coupling strength $J\rho_0$, which as we have seen in the previous chapter differs from atom to atom, has an impact on the effective gyromagnetic factor [135]. It scales with $g_{\mathrm{eff}} = g_0(1 + J\rho_0)$. For an antiferromagnetically coupled impurity this would lead to a reduction of the gyromagnetic factor and therefore to a reduced splitting. Note that in the presented study the renormalization was found to be in the order of a few percent. For bigger deviations of 10 % or more the coupling strength would exceed values of -0.1 and therefore leave the weak coupled regime. To check if the varying coupling strengths along the moiré have an impact on the splitting of the Mn atoms in our system, we looked at Mn atoms on different moiré sites, which are exemplary presented in figure 6.4 b). Two spectra are shown, the red one was recorded on an atom at the moiré minimum and the black one on an atom very close to a moiré maximum. For clarification the red spectrum was offset in y-direction. As expected the amplitude of the two spectra is different. However, no visible difference can be seen in the splitting of the respective curves. We fitted both spectra with the above mentioned model and deduced that both spectra are well reproduced with a magnetic field of $3\,\mathrm{T}$. The fits are overlayed with the dashed lines on the spectra. Therefore we conclude that the observed modulations in $J\rho_0$ are too small to significantly impact the Zeeman splitting of the Kondo resonances of the Mn atoms.

6.2.3 Mn atoms on point defects

As mentioned above, not all spectra performed on single Mn atoms exhibit a Kondo resonance. One example is shown in figure 6.5 a). There two atoms can be seen with different apparent heights and widths. Taking a spectrum on the smaller atom leads to the spectrum shown in b): no signs of magnetic interactions can be seen. To investigate the
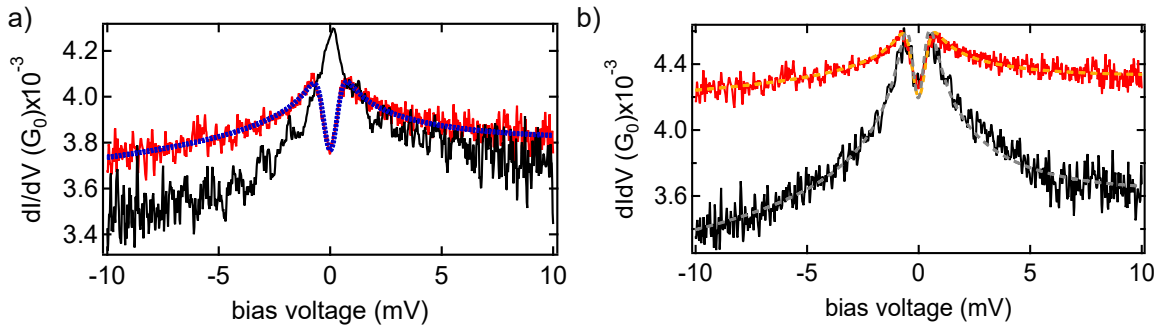
Figure 6.4: Spectral fingerprints of single Mn atoms in a magnetic field. a) dI/dV spectra performed on a Mn atom at $0\,T$ (black) and $3\,T$(red). While the zero-bias resonance at zero magnetic field is unperturbed, it clearly splits at $3\,T$. Fitting the red spectrum with the model established in [130] for a fixed magnetic field of $3\,T$ yields a very good agreement with the experimental data, visualised by the blue dashed line. b) dI/dV spectra taken at an applied magnetic field of $3\,T$ on different sites of the moiré superstructure. The dashed lines represent fits the the previously mentioned model. The red spectrum is offset by $0.5 \times 10^{-3} G_0$ for clarity. The spectra were recorded at a setpoint of $10\,mV$ and $3\,nA$.

origin of this, we removed the atom, as can be seen in c) and d). After removal, it becomes apparent that the atom was adsorbed on top of a point defect. Consequently, the adsorption structure is now different and major properties like the spin could be changed. Therefore it is not surprising that the Kondo resonance was absent for the atom. Several defects like the one shown in d) are present in our grown MoS_2 islands. They form during the CVD growth. For different TMDCs defects with similar appearance have been reported as substitutes of the transition metal atoms [198,199]. To make sure that they did not influence the previously shown data we therefore removed every atom after taking a spectrum on it to make sure that they were not adsorbed in close proximity to a defect. All atoms, which were adsorbed on a defect as shown in d), were not showing a Kondo resonance.

Sometimes, especially at higher bias voltages, Mn atoms became really unstable on the surface or even were completely vanished after taking a spectrum. This could be problematic, as Mn atoms on the tip could influence the spectra of the adsorbed Mn atoms on the substrate via exchange coupling [200]. To check this, we systematically picked up Mn atoms on the tip and performed spectra on other Mn atoms. The result is shown in figure 6.5 e): one still can see a resonance at zero bias, but now the symmetry is changed. Fitting the resonance with a Frota function gives a phase factor of $\phi = 1.76$. This suggest a strongly altered ratio between tunnelling via the Kondo state and directly tunnelling into the substrate. We have seen this change in lineshape several times after picking up a Mn atom, which allows us to differ between spectra with and without a Mn atom on the tip.
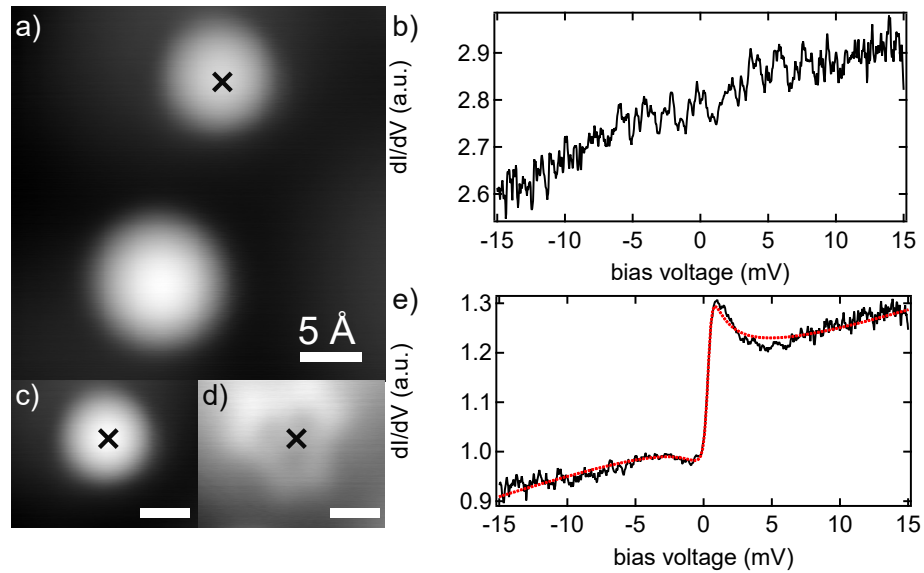
Figure 6.5: Mn atoms with atypical low-energy spectroscopic fingerprints. a) STM topography of two individual Mn atoms. Both atoms differ in their apparent heights and apparent widths. b) dI/dV spectrum recorded on the upper Mn atom (indicated with the black cross). The zero-bias resonance observed before is absent here. c,d) STM topographies of the upper atom shown in a), before (c)) and after (d)) atom manipulation. After the manipulation it becomes apparent that the atom was adsorbed directly underneath a point defect. As point defects are known to exhibit a drastically different electronic structure than bare MoS_2 it is plausible that this caused the change in appearance and electronic structure of the Mn atom. e) dI/dV spectrum recorded on a Mn atom after possible previous pick-up of a Mn atom. The Kondo resonance exhibits a changed lineshape compared to the previous discussed results. A fit with a Frota function yielded a Frota phase factor of $\phi = 1.76$, suggesting an altered ratio of the tunnelling channels. The topograpies were recorded at $100\,mV$ and $20\,pA$, the setpoint of the recorded spectra was $15\,mV$ and $3\,nA$. The scale bar in c) and d) amounts to $0.5\,nm$.

6.3 Coupling of Mn atoms

We already mentioned that the Mn atoms were weaker bound to the MoS_2 surface than the iron atoms. This could increase the likelihood of manipulating single Mn atoms into larger structures. Figure 6.6 shows several successful manipulation events: in a) two Mn atoms are clearly separated from one another. The according spectrum, recorded on the green cross, is shown in f). The atom exhibits a Kondo resonance, just like we established before as the general case for single atoms. To manipulate a single Mn atom, we placed the STM tip in close proximity of the atom and applied a bias voltage over $1.5\,V$ and turned the feedback controller off. After a certain time the detected current would decrease step like, indicating that the atom hopped to a different site. Note here that this kind of manipulation event suggests an interaction via the electrostatic force. Therefore the tip position and the applied bias voltage is critical to influence the direction in which the atom moves. We applied this technique to the lower atom in a), resulting in the topography shown in b): the lower atom moved closer to the upper atom and away from the tip. Still both atoms are clearly distinguishable. The corresponding red spectrum in f) however deviates from the spectrum of a single atom, as it shows a split Kondo resonance at zero field. By repeating the manipulation process one more time, one can push the atoms even closer together, resulting in the structure shown in c): here the lower atom moved even closer to the upper one. They are not well distinguishable between one another any more. Taking a spectrum on the atoms now gives a drastically changed spectrum, as shown as the blue curve in f): two bias symmetric steps around $11\,mV$ appear, indicating the opening of an inelastic tunnelling channel. Moreover, no additional Kondo correlations are present. In figure 6.6 d) and e) part of the manipulation process is shown for a different dimer, but in reversed order: in d) two Mn atoms are in close proximity to one another, but still separated by a nodal plane. The according spectrum in g) shows a split Kondo resonance. We now removed the right atom in the dimer structure, to see, if the single atom properties are recovered. The left atom shown in e) indeed exhibits an unperturbed Kondo resonance, which is shown in the green spectrum in g). This suggests that the change in spectra stems completely from the interaction of the individual atoms with one another. Such behaviour is most generally described by a Heisenberg model Hamiltonian [13]:

$$H = J_D \vec{S}_A \vec{S}_B, \tag{6.1}$$

where $\vec{S}_{A,B}$ are the spin operators of the individual atoms and J_D is the exchange coupling strength between the individual atoms. Figure 6.7 illustrates how our different dimer structures apply to the Heisenberg model: the clearly distinguishable atoms in b) show a Kondo resonance, as shown again in c). We propose that these atoms are separated by at least three atomic lattice sites, as shown in a), and are not exchanged coupled at all. Bringing the atoms now closer together, to a separation of two atomic lattice sites, like illustrated in d) and shown in e), leads to a change in the spectrum. We see the previously mentioned zero-field split Kondo resonance, which suggests a non-zero exchange coupling between the two atoms. We will show later on that the coupling is of anti-ferromagnetic nature (which we here define as positive J_D values). The atoms still can be brought even closer to one another, as seen in h) and illustrated in g). Here the atoms are spaced one lattice site from one another. The according spectrum in i) shows two bias symmetric steps and no signs of

Kondo correlations. This suggest a stronger coupling between the individual atoms. To sum up, we see two main interactions for Mn dimers: the exchange coupling of the individual spins with the substrate electrons and the exchange coupling between the two Mn spins.

As the Kondo exchange is not varying for the same respective sites in the moiré super-structure, the different exchange coupling strengths between the atoms is therefore the main factor behind the variations in the spectra. This leads to a different coupling mechanism for the individual dimers, the 3a dimers are in a single-impurity Kondo regime, the 2a dimer are coupled via anti-ferromagnetic RKKY interactions and the 1a dimers are coupled anti-ferromagnetically via direct exchange coupling. We will elaborate on this in more detail later in this section. First, we show proof that the nature of the coupling of the two Mn atoms is anti-ferromagnetic both for the 2a and the 1a dimer. The spectra in 6.7 f) and i) could in theory also result from ferromagnetic coupling. Though Mn atoms have been predicted to be coupled anti-ferromagnetically when coupled via direct exchange interaction [201], one needs to look at the excitation spectra in a magnetic field to ultimately see the nature of the coupling. Figure 6.8 shows the excitation spectra of the 1a dimer (a) and the 2a dimer (b) with and without an applied external magnetic field. For both dimers the qualitative lineshape is identical. To extract the influence of the magnetic field on the excitation spectra, we fitted the spectra with the sum of two step functions and a Frota function. The fits are shown as the blacked dashed lines in a) and b) respectively. The relevant parameter here is the broadening of the step functions: for the 1a dimer it increases for about 100 microvolts from the spectrum without field to the one measured at $3\,\mathrm{T}$. The difference is smaller for the 2a dimer, here it amounts to around three tenths of microvolts (exact numbers are given in the figure caption). As already mentioned in section 5.2, this broadening stems from the lifted degeneracy of the magnetic quantum numbers at non-zero fields via the Zeeman splitting. The energy level diagram for the 1a dimer is shown in figure 6.8 c): at zero field only one transition is possible, from the $|S_{\mathrm{tot}} = 0, m_s = 0\rangle$ singlet state to the $|S_{\mathrm{tot}} = 1, m_s\rangle$ triplet state, where $\mathrm{m}_s = 0$ and ± 1 are degenerate. With an external magnetic field present the degeneracy of these m_s values is lifted and three distinct excitations become possible. The highest magnetic field available in our setup is not sufficiently large compared to the thermal broadening, so instead of three distinct steps we observe a smearing out of those, resulting in an increased width of one step in the spectrum. A similar argument applies for the 2a dimer, only there the splitting is smaller. As mentioned earlier and shown in [202] and [203], the external field can counteract the exchange coupling of the two spins, when the field has the right directionality and can even completely suppress it at a certain critical field B_c. Therefore, if one would have access to strong enough fields, one could tune the two spins ground state in the phase diagram shown in figure 6.15.

Even though the quantitative changes of the spectra in the magnetic field is not enough to resolve distinct excitations, it still gives us information about the nature of the coupling between the two Mn spins. For a non-singlet ground state (e.g. for ferromagnetic coupling) we would see the emergence of a second step in the magnetic field measurements at lower energies, as the groundstate would become non-degenerate and an additional excitation would become possible. The absence of this proves that the Mn atoms indeed couple anti-ferromagnetically.

Until now we have seen that the differently spaced dimer exhibit different coupling strengths between the respective spins and different exchange coupling with the substrate electrons, suggesting different coupling mechanisms. In the next section we want to study
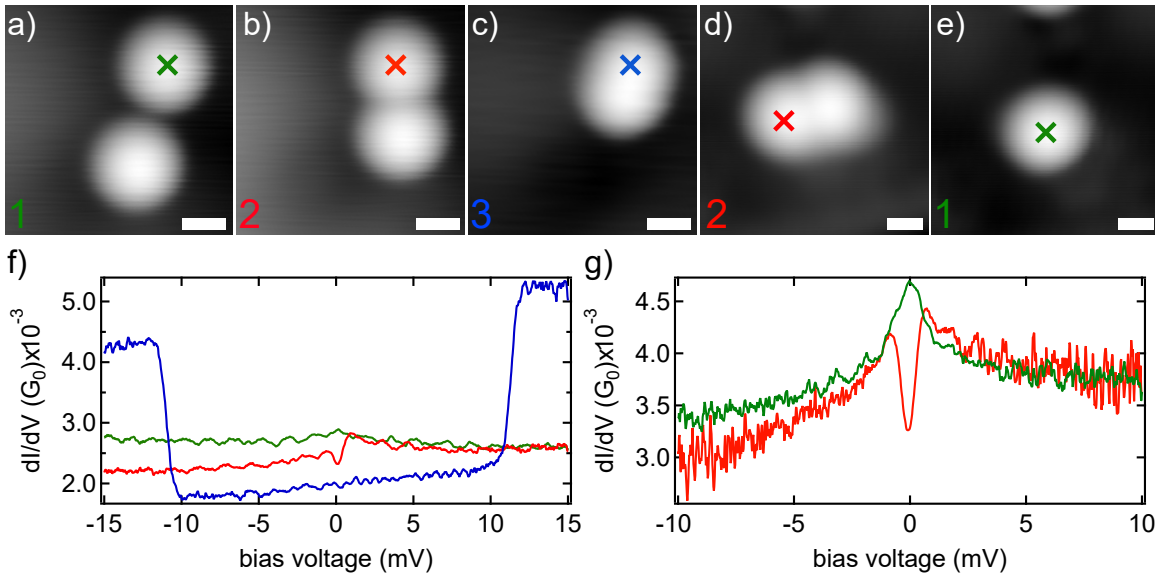
Figure 6.6: Manipulation of single Mn atoms into and out of dimer structures. a), b), c), d) and e) STM topographies of successive and successful manipulation events. The bottom atom in a) was pushed closer towards the other one, as seen in b). Here the atoms are still distinguishable. In c) the atom was pushed even closer to the upper atom, resulting in a dimer structure, were the atoms can not be distinguished. d) and e) show the reverse process, where one atom was pulled out of the dimer structure. f) dI/dV spectra performed on the upper atom in a), b) and c) respectively. g) dI/dV spectra performed on the left atom in d) and e). The topographies were recorded at $100\,mV$ and $20\,pA$, the setpoint of the recorded spectra was $15\,mV$ and $3\,nA$ (f) and $10\,mV$ and $3\,nA$ (g).

them individually and describe the coupling mechanism and its consequences in more detail.

6.4 Mn dimers - the direct exchange-coupling regime

To start with, we want to describe the 1a coupled dimers in more detail. Figure 6.9 a) shows two of such dimers, adsorbed in different direction with respect to the MoS$_2$ lattice. In c) a dI/dV spectrum, performed on the cross in a), is shown. Again we see two steps at around $\pm 10mV$. Steps in the dI/dV signal stem from inelastic tunnelling processes, which for magnetic atoms usually originate from spin-flip excitations. For this usually a sizeable magneto crystalline anisotropy has to be present to lift the degeneracy of the magnetic quantum numbers. However it would be very surprising if the dimer structure now suddenly sees a large anisotropy, as none has been seen for the monomers. Therefore, the observed inelastic process is resulting from a spin-changing transition, as mentioned earlier. The general mechanism is illustrated in figure 6.9 d) and e): the two atoms are coupled anti-ferromagnetically, which results in a singlet ground state of $S_{tot} = 0$. The strength of the coupling is directly proportional to the exchange coupling constant J_D, which one can
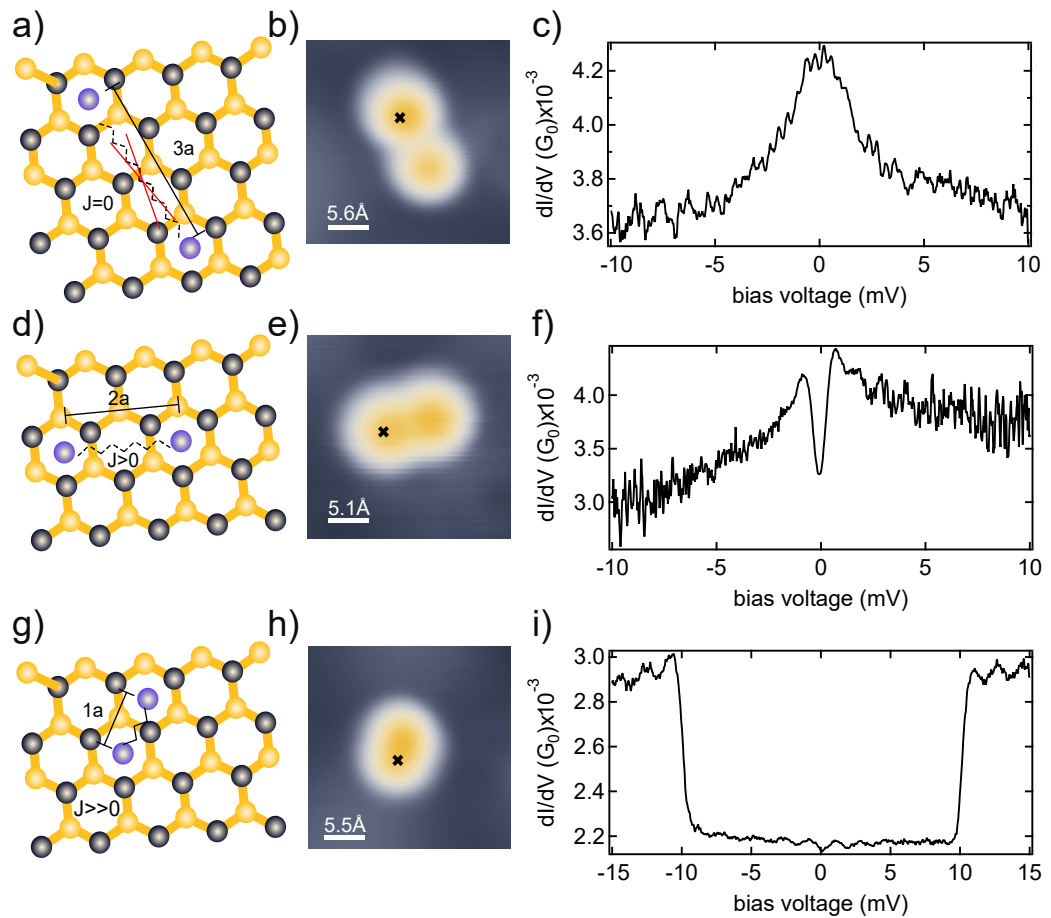
Figure 6.7: Visualisation of the different dimer structures. a), d), g) Visualisation of the likely adsorption sites of the Mn dimers. In a) the atoms are separated by three atomic lattice sites, showing no signs of exchange coupling. In d) the atoms are separated by two atomic lattice sites and coupled weakly via most likely RKKY like exchange coupling. In g) the atoms are separated by one atomic lattice site and experience the strongest coupling, which we assume to be direct exchange coupling. b), e), h) STM topographies of Mn dimer structures. c), f), i) dI/dV spectra recorded on the black crosses in b),e),h). The spectra vary drastically for the different dimer separations from a Kondo resonance c) to step-like increases in the differential conductance f), i). The topographies were recorded at $100\,mV$ and $20\,pA$, the setpoint of the recorded spectra was $15\,mV$ and $3\,nA$ c), f) and $10\,mV$ and $3\,nA$ i).
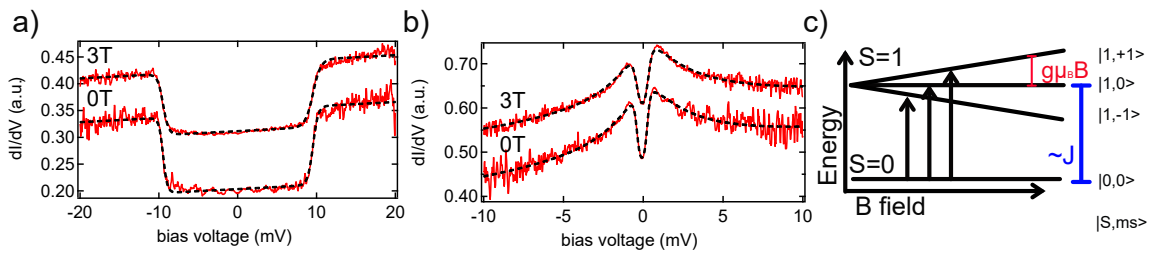
Figure 6.8: Spectroscopy on Mn dimers in a magnetic field. a), b) dI/dV spectra performed on Mn dimers. The spectra in a) show the previously established spin excitations at higher energies. At a magnetic field of $3\,\mathrm{T}$ a change in the width of the step-like excitation becomes evident. By fitting these curves with a phenomenological model of two step-functions one obtains a width of $292 \pm 18 \mu V$ ($0\,\mathrm{T}$) and $413 \pm 15 \mu V$ ($3\,\mathrm{T}$). In b) spectra on a dimer in the smaller coupling regime are shown. Here, a phenomenological fit of the sum of a Frota function and two step function was performed to determine width of the inelastic excitations. The results are: $95 \pm 17 \mu V$ ($0\,\mathrm{T}$) and $127 \pm 12 \mu V$ ($3\,\mathrm{T}$). c) Energy-level diagram of the observed spin-excitation: At zero magnetic field only one excitation from S=0 to S=1 is possible, as the states with the spin quantum numbers $m_S = 0, \pm 1$ are degenerate in energy. With an increasing magnetic field, those states start to split up, enabling three different excitations. At our measurement condition of $1.1\,\mathrm{K}$ and a maximum magnetic field of $3\,\mathrm{T}$ this split results in a broadening of the excitations, as seen in a) and b). For higher magnetic field one can distinguish the individual excitations.

see from equation 6.3 (the red dashed line in c) is a fit of the spectrum with equation 6.3). Therefore the spacing between the ground state and the first excited state is also directly given by J_D and the energy of the measured step in the dI/dV spectrum, which arises from the excitation of the $S_{tot} = 0$ ground state to the $S_{tot} = 1$ excited state, gives direct insight into the strength of the coupling. Comparing our results to previous measurements, our dimer structure exhibits a stronger coupling than Mn dimers on Cu_2N [13], but smaller than chains of CoPc molecules, which were decoupled from a Pb(111) by layers of CoPc molecules [95].

Figure 6.9 b) shows a STM topography with superimposed dI/dV signal at the indicated bias voltage extracted from a densely spaced grid of spectra across a Mn dimer. The signal intensity varies over the dimer and has a nodal plane at the center of the dimer, presumably in between the individual Mn atoms. This suggests that there is a different probability to excite the spin changing transition there, we will discuss this variation more in the next subsection. Ultimately, in f) a higher energy spectrum, performed on the black cross in a), is shown. In general, the dimers were really unstable at voltages of ± 500mV or higher, which required very small current setpoints to perform spectra at there energies or higher. The spectrum exhibits a resonance at around $400\,\mathrm{mV}$, similar to the one of the monomer, but no resonance in the negative bias regime is visible. As the coupling of the 1a dimers is mediated by direct exchange and therefore of a finite overlap of the atomic orbitals, it is not surprising that the orbitals can shift in energy. Due to the instability of the dimers, we could not probe them at higher voltages than ± 1V. Even at the voltages used in f), the atoms moved during a spectrum at around 30 % of the cases.

6.4.1 Potential scattering over the dimer structure

In the previous section we have seen that there is a slight variation of the signal intensity of the spin changing transition over the atom and now want to discuss this in more detail. Figure 6.10 a) shows a Mn 1a dimer adsorbed close to a moiré maximum. We performed spectra both on the center of the dimer and on the presumable center of one of the adatoms of the dimer. The results are shown in b): surprisingly the two spectra vary quite drastically. Whereas the spectrum on the atom (dark blue) shows a symmetric lineshape, the spectrum at the center of the dimer (teal) has an asymmetric lineshape, with an increased conductance at the negative bias side and an overshoot of decreased conductance at positive bias. On the first glance this result is contradicting the previously shown spectrum in figure 6.9 c), as there we saw a relatively symmetric lineshape in the center of the dimer. To elaborate on that, we took another set of spectra on a 1a dimer, positioned in the moiré minimum, as shown in figure 6.10 c). The corresponding spectra in d) show that at the center of one of the two atoms the spectra is again very symmetric and the spectrum at the center of the dimer is again asymmetric with an increased conductance at the negative bias side. However, in total, the asymmetry is much less enhanced and the conductance undershoot at positive bias is completely absent. As the dimer, on which the spectrum in 6.9 c) was measured, was also located close to the moiré minimum, this observation is consistent with the previously measured data.

We already observed and discussed a similar asymmetry in the tunnelling spectra across single iron atoms in section 5.4. It is natural to assume that the variations in the spectra in
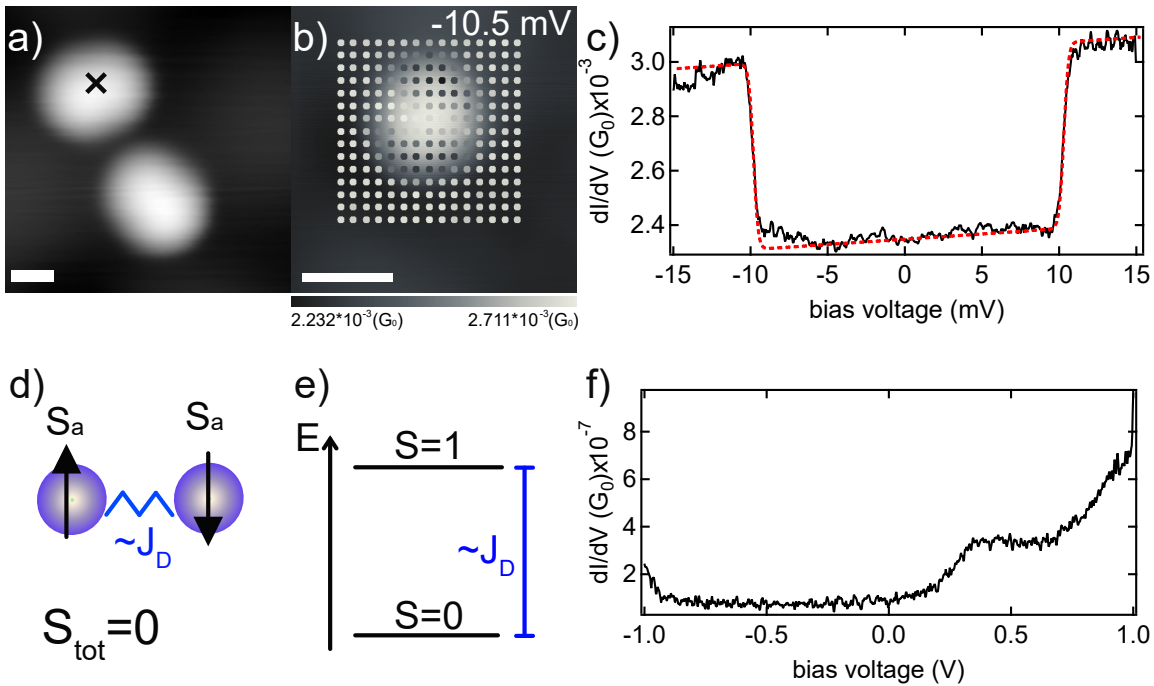
Figure 6.9: Mn atoms coupled to dimers. a) STM topography of two Mn atoms coupled to dimers. They can be clearly distinguished from an individual atom by their oval shape. b) STM topography with superimposed dI/dV signal at the indicated bias voltage extracted from a densely spaced grid of spectra across a Mn dimer. The spectra were analysed using SpectraFox [61]. c) dI/dV spectra performed on the location indicated by the black cross in a). It exhibits two step-like increases in the conductance symmetrically around $\pm 10\,\mathrm{mV}$. The red dashed line shows a fit performed with the model established in [130]. We assumed that the two atoms with the same spin $S_A = \dfrac{5}{2}$ are coupled via an antiferromagnetic Heisenberg like interaction model. The fit yields a coupling constant of $J_D = 10.05\,\mathrm{meV}$. d) Sketch of the interaction model. Two atoms with the same spin S_A are coupled antiferromagnetically to a total spin of zero. e) Sketch of the excitation process. An electron can be excited from the $S = 0$ ground state to the $S = 1$ state. The separation of these two energy levels is given by the coupling constant J_D. f) dI/dV spectra performed on the location indicated by the black cross in a). A resonance around $350\,\mathrm{mV}$, similar to the single atom case, can be seen. No states in the negative bias region can be found. The low signal intensity stems from the choice of the setpoint, as the tip had to be put sufficiently far away to not induce movement of the dimer. Overall the dimers were really unstable at voltages over $\pm 500\,\mathrm{mV}$ and no spectra above the here shown voltages could be recorded. The scale bar in b) amounts to 1 nm.

figure 6.10 b) and d) originate from a similar type of interference. Here, different tunnelling channels contribute to the signal, of which at least one exhibits a significant potential scattering. For the Fe atoms, we identified one tunnelling channel related to the d-orbitals and another one to co-tunnelling through a non-magnetic Fe-S hybrid state. The non-magnetic state exhibited a substantial potential scattering. For the Mn 1a dimers, the asymmetry is most pronounced in the center of the dimer structure. This suggests that the orbital, exposed to larger potential scattering, is localised between the two Mn atoms. To unambiguously prove this, one would need to look at eventual variations in the higher-energy spectra across the dimer.

Another striking feature is the difference in excitation energy between the spectra shown in c) and e): the dimer in the valley has the steps around $\pm\,10\,\mathrm{mV}$, whereas they are at a lower energy on the dimer on the dome, at around $\pm\,8\,\mathrm{mV}$. We previously discussed that the excitation energies depend purely on the coupling between the individual atoms of the dimer, which should be equivalent for same spacings and same adsorption sites. We will discuss these variations in the following subsection.

6.4.2 Renormalisation of the coupling energy

From the previous chapter we got the idea that the energy of the spin changing excitation may vary along the moiré structure. To get a better idea of it, we investigated more dimers on differing moiré sites, several examples are given in figure 6.11. There, in a), the dimer is located close to the moiré maximum. In b) the dimer is shifted slightly away from the moiré maximum. In c) it is almost at the minimum and finally in d) it is located at the moiré minimum. We performed spectra on all the dimers shown, which are presented in e). The colour of the crosses in the respective STM topographies correspond to the colours of the curves. The dimer in d) has the highest excitation energy at around $\pm\,10\,\mathrm{mV}$, similar to most of the other 1a dimers we described previously. For the dimer in c), which is closer to the moiré maximum, the excitation energy is reduced, to slightly under $\pm\,10\,\mathrm{mV}$. This trend continues for the dimer in b), which excitation energy is already significantly reduced to around $\pm 8\,\mathrm{mV}$. Finally, the dimer in a), which is the closest one we found to the moiré maximum, has the lowest excitation energy at around $7.5\,\mathrm{mV}$. To sum up, we really find a continuous change of the excitation energy along the moiré structure, which amounts to around 25%. Note that in contrast to the spectra shown in the previous subsection no asymmetry is present in the spectra, as we recorded them this time on the center of one of the individual Mn atom in the dimer structure, which showed a much lower contribution of potential scattering. This makes it easier to compare the excitation energies.

We now established on several occasions in this thesis that the moiré structure has a varying density of states. It is the highest on the moiré domes, which results in the strongest Kondo correlations through exchange coupling with the substrate electrons there. However, we also established that for the 1a dimer these correlations are absent in the spectra due to the non-magnetic S=0 singlet ground state. Therefore, to understand the variations in the singlet-triplet excitation energy Δ, we compute how it is affected by the hybridisation of the adatom d-orbitals with the substrate electrons. This hybridisation will lead to a shift of the energy levels of the singlet ground state and the triplet excited state and can then be related to the exchange interaction with the substrate electrons. This is schematically
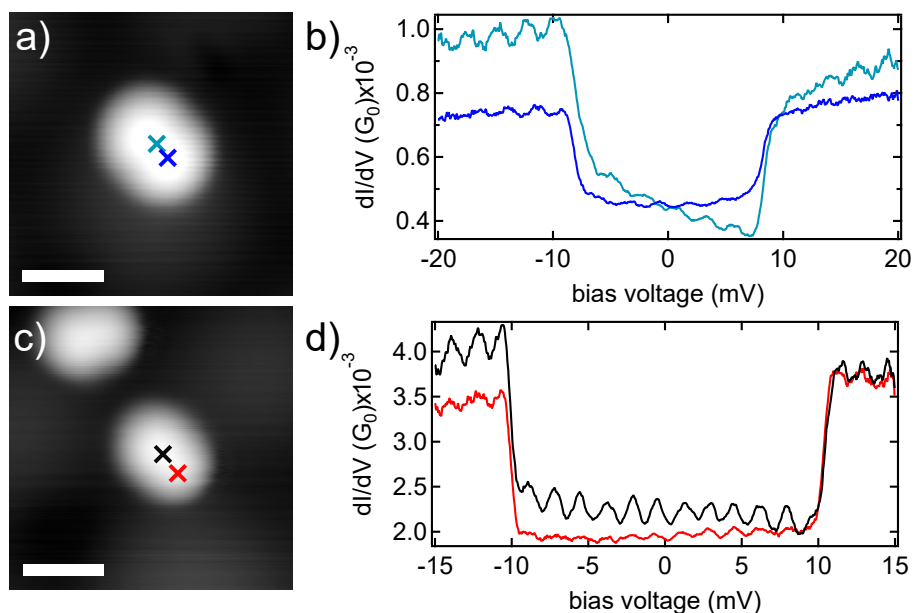
Figure 6.10: Lineshape differences along a single 1a dimer. a),c) STM topograhies of single dimers. Whereas in a) the dimer is adsorbed close to the moiré maximum, in c) the dimers are adsorbed in the moiré valley. b), d) dI/dV spectra performed at the crosses in a) (b)) and c) (d)). The observed spin excitation shows a significantly higher asymmetry in the center of the dimer in comparison to its edges. Note that the edges of the dimer correspond to the centers of the individual atoms. While this observation is present for all dimers, the effect becomes more pronounced the closer a dimer is adsorbed to the moiré maximum, as can be seen for example in the comparison of the spectra shown in b) and d). The scale bars in a) and c) amount to $1\,nm$. The topographies were recorded at $100\,mV$ and $20\,pA$, the setpoint of the recorded spectra was $20\,mV$, $1\,nA$(b) and $15\,mV$, $3\,nA$ (d).

illustrated in figure 6.11 g). We model the system as two anti-ferromagnetically coupled spins, which are coupled via the exchange coupling constant J_D. On the other hand, both atoms individually are exposed to exchange correlations with the substrate electrons, as indicated by the red arrows. The magnitude of these Kondo correlations, scaling with $J\rho_0$, can be related to the strength of the hybridisation. In the case of absent hybridisation, the states with a spin magnitude of S_{tot} will have a direct exchange energy of:

$$E_{ex}(S_A, S_B; S_{tot}) = \frac{J_D}{2}[S(S+1) - S_A(S_A+1) - S_B(S_B+1)]. \tag{6.2}$$

Here, S_A and S_B are the spins of the two respective adatoms. Assuming that the d shells of the two atoms remain half-filled during the hybridisation with the surface, the singlet-triplet transition energy is just:

$$\Delta = E_{ex}(\frac{5}{2}, \frac{5}{2}, 1) - E_{ex}(\frac{5}{2}, \frac{5}{2}, 0) = J_D. \tag{6.3}$$

Now we look, how this excitation energy is modified when taking hybridisation into account. The d orbitals can generally hybridise with five conduction electron channels [204]. As upon adsorption the symmetry of the d orbitals is broken, they will hybridise with different respective strength V_m, which will also depend on the conduction channel m. As a result, virtual excitation process become possible, which correspond to an electron either hopping out of the Mn atom into the substrate or a substrate electron hopping into a d-orbital of the Mn atom. Both processes will generally reduce the effective spin of the Mn atom, which will then lead also to a reduction of the direct exchange energy. We want to show this in more detail for the case of the singlet state following the calculation performed by our collaborators Felix von Oppen and Leonid Glazman in the publication mentioned at the start of the chapter [205]:

The virtual process of tunnelling in or out of one of the d-orbitals leaves the atom in an intermediate state, which can be denoted as : $|S_A, S_B; S_{tot}, m_s\rangle = |2, \frac{5}{2}; \frac{1}{2}, \pm\frac{1}{2}\rangle$. In this case atom A would be the one with an electron hopping in or out. The singlet and intermediate state have different exchange energies, being

$$E_{ex}(\frac{5}{2}, \frac{5}{2}; 0) = -\frac{35}{4}J_D \tag{6.4}$$

and

$$E_{ex}(2, \frac{5}{2}; \frac{1}{2}) = -7J_D \tag{6.5}$$

as it follows from equation 6.2. The total energy for the singlet state is then

$$E_s^{(0)} = 2E_{Mn} + E_{FS} + E_{ex}(\frac{5}{2}, \frac{5}{2}; 0), \tag{6.6}$$

where E_{Mn} is the energy of the uncoupled Mn atom and E_{FS} is the energy of the unperturbed Fermi sea. The intermediate state has an energy of:

$$E_{s,out}^{(0)} = 2E_{Mn} + |\epsilon_d| + E_{FS} + \xi_k + E_{ex}(2, \frac{5}{2}; \frac{1}{2}) \tag{6.7}$$

for an electron tunnelling out of the d-orbital and

$$E_{s,in}^{(0)} = 2E_{Mn} + \epsilon_d + U + E_{FS} - \xi_k + E_{ex}(2, \tfrac{5}{2}; \tfrac{1}{2}) \tag{6.8}$$

for an electron tunnelling into the d-orbital. Here, $-\epsilon_d > 0$ is the energy to remove an electron from the d-orbital and $\epsilon_d + U$ to add one electron to the d-orbital respectively. Now we can calculate the perturbative shift of the singlet state as:

$$\Delta E_s = 2|V_0|^2 \left\{ \sum_{\xi_k > 0} \frac{1}{[2E_{Mn} + E_{FS} + E_{ex}(\tfrac{5}{2}, \tfrac{5}{2}; 0)] - [2E_{Mn} + |\epsilon_d| + E_{FS} + \xi_k + E_{ex}(2, \tfrac{5}{2}; \tfrac{1}{2})]} \right.$$
$$\left. + \sum_{\xi_k < 0} \frac{1}{[2E_{Mn} + E_{FS} + E_{ex}(\tfrac{5}{2}, \tfrac{5}{2}; 0)] - [2E_{Mn} + \epsilon_d + U + E_{FS} - \xi_k + E_{ex}(2, \tfrac{5}{2}; \tfrac{1}{2})]} \right\}. \tag{6.9}$$

Both intermediate states $|2, \dfrac{5}{2}; \dfrac{1}{2}, \pm\dfrac{1}{2}\rangle$ give the same contribution here. Simplifying the equation leads to:

$$\Delta E_s = -2\rho_0|V_0|^2 \int_0^\infty d\xi \left\{ \frac{1}{|\epsilon_d| + \xi + \tfrac{7}{4}J_D} + \frac{1}{\epsilon_d + U + \xi + \tfrac{7}{4}J_D} \right\}. \tag{6.10}$$

Now, considering that the dimer coupling J_D is smaller than $|\epsilon_D|$ and U (which is reasonable, as both those latter quantities are usually in the order of electron volts), we can simplify equation 6.10 further to:

$$\Delta E_s = \text{const} + \frac{7J_D}{4} 2\rho_0|V_0|^2 \left\{ \frac{1}{|\epsilon_d|} + \frac{1}{\epsilon_d + U} \right\}. \tag{6.11}$$

Here the constant term results from the integration of equation 6.10, is independent of the exchange coupling and will later cancel out with the corresponding contribution of the triplet state. Repeating this whole procedure for the triplet state gives:

$$\Delta E_t = \text{const} + \frac{31J_D}{20} 2\rho_0|V_0|^2 \left\{ \frac{1}{|\epsilon_d|} + \frac{1}{\epsilon_d + U} \right\}. \tag{6.12}$$

Now we have all the ingredients to calculate the overall renormalised singlet-triplet transition energy. It is:

$$\Delta = J_D + \Delta E_t - \Delta E_s = J_D \left\{ 1 - \frac{1}{5} 2\rho_0|V_0|^2 \left[\frac{1}{|\epsilon_d|} + \frac{1}{\epsilon_d + U} \right] \right\}. \tag{6.13}$$

Applying the relation found by Schrieffer [204] between the exchange coupling constant $J\rho_0$ and the parameters used in the Anderson impurity model one can rewrite equation 6.13 as:

$$\Delta = J_D(1 - 2\rho_0 J). \tag{6.14}$$

Or, by considering all five conduction electron channels, one gets:

$$\Delta = J_D(1 - \sum_m 2\rho_0 J_m). \tag{6.15}$$

From equation 6.15 we can immediately see that indeed the Kondo-like exchange correlation lead to a reduction of the excitation energy and with increasing $J\rho_0$ this reduction also gets larger and larger. Now we want to compare the experimentally observed shift with the one theoretically predicted. As mentioned above, we observe a renormalisation of about 25 % for the examples shown in figure 6.11 e). To make this more statistically profound, we extracted the excitation energy of 39 different 1a dimers by fitting their respective spectra with a temperature broadened step function and plotting them with respect to the dimers position in the moiré superstructure. The distance of the dimers to the moiré maximum was determined the same way as for the monomers in plot 6.3 b). Hereby the center of the dimer structure was the reference point. The results are shown in figure 6.11 f): one can see that on average the excitation energy gradually increases from the moiré maximum towards the moiré minimum. The variation in excitation energy here is up to 40 %. To compare these variations to the theoretically predicted ones from equation 6.15 one now need to extract the variation of the Kondo exchange across the moiré. However, we established that this is not trivial for the dimer spectra. However, as shown previously in figure 6.3, we can extract them for the single atoms and assume that the variations are comparable. As discussed earlier, we extracted the $J\rho_0$ values from fits with the perturbative model described in [130]. The fit results for $J\rho_0$ strongly depend on the values used for the coupling constant T_0 and a range of values of those still gives acceptable fit results. Therefore the observed variations for the $J\rho_0$ values across the moiré vary between 4 (lower red dashed line in figure 6.3) and 10 % (upper red dashed line in figure 6.3), depending on the respective T_0 values. Plugging those into equation 6.15 one would expect a renormalisation in the excitation energy of 8 to 20 %. This is lower than the experimentally observed variation of 40 %. However, the fits from the perturbative model assume that the adatom-substrate exchange interactions are mediated by a single conduction channel. Therefore our finding of an theoretically underestimated renormalisation could hint to the fact that not one, but several conduction channels are involved in this renormalisation process. Then depending on the respective hybridisation strength of the individual conduction channels V_m and the symmetry of the associated orbital, every channel could contribute with a different magnitude to the renormalisation. Note also, that assuming all five channels to contribute equally in this process would overestimate the renormalisation. Moreover, we point out that the statistics in figure 6.11 f) lack points around the moiré maximum. As a result the exact magnitude of the experimental renormalisation is hard to estimate. Considering all deviations, the upper limit in figure 6.3 b) could still be compliant with a single channel model. Therefore, to improve the statement, a more detailed description, considering the symmetries of the involved channels has to be developed and more points around the moiré maximum have to be taken. Also, adatoms coupled to larger structures could help understand the fine details of the exchange coupling mediated renormalisation of the excitation energy.
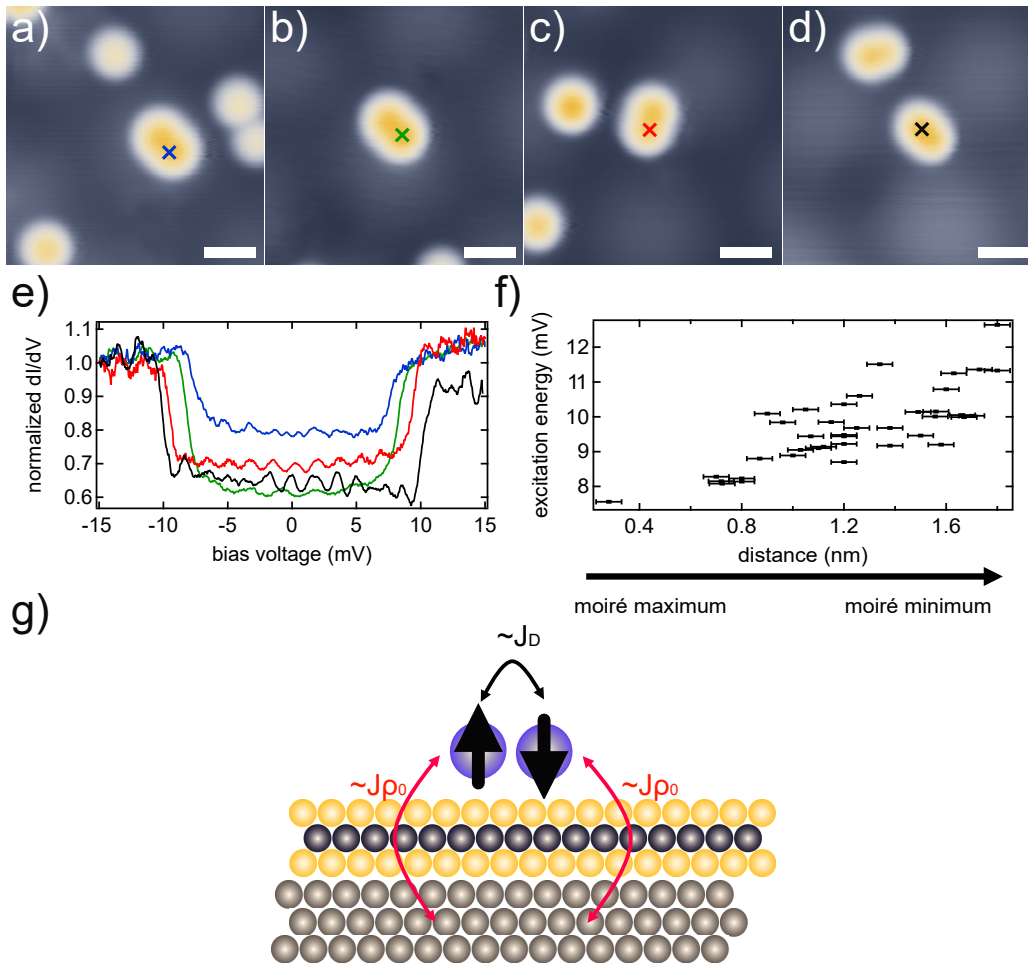
Figure 6.11: Moiré effect on anti-ferromagnetically coupled Mn dimers. a-d) STM topographies of Mn dimers on different moiré sites. e) dI/dV spectra acquired on the dimers shown in (a-d). The color of the crosses in (a-d) mark the correspondingly coloured spectra. f) Plot of the excitation energy of 39 different 1a dimers with respect to their adsorption position in the moiré superstructure. The excitation energy was extracted by fitting the individual dimers with a temperature broadened step function. g) Visualisation of the modelled interaction: the two Mn atoms are coupled via direct exchange coupling (with a magnitude proportional to J_D) to each other. Moreover, each atom is exposed to exchange coupling with the substrate electrons (with a magnitude of $J\rho_0$). The topographies were recorded at $100\,mV$ and $20\,pA$, the setpoints of the recorded spectra were $20\,mV$ and $1\,nA$ (b), $20\,mV$ and $3\,nA$ (a) and $15\,mV$ and $3\,nA$ (c), (d). The spectra were normalized for better clarity.

6.4.3 Adsorption position of the 1a dimer

In section 6.1 we described the adsorption structure of the monomer. From density functional calculations presented in literature and qualitatively similar dI/dV spectra for every monomer we concluded that the single atoms are most likely always adsorbed at the same hollow site of the MoS_2 layer, even though it remains unclear, which of the two hollow sites is the energetically preferred one. This applies in principle also to the dimer structures. Theoretically one could on the other hand also imagine, that the formation of a dimer could also energetically stabilise an atom on a different lattice site, if this promotes a favourable inter-atomic spacing. In figure 6.7 b), e) and h) we have already presented three dimer structures and discussed their probable adsorbtion structure in a), d) and g). What is striking is that the three dimers all are adsorbed along different directions of the top sulfur layer, all rotated by roughly $60°C$ from one another. This is already an indication that the atoms of these dimer structures are all adsorbed at the same lattice site. To gain more insight into it, we investigated more Mn 1a dimers and tried to manipulate them into different lattice sites. The results are shown in figure 6.12. In a), three 1a dimers are shown before manipulation. The angles drawn for every dimer correspond to $60°$. The dimers labelled 1 and 3 are adsorbed in parallel to one another, which already indicates that all atoms in those two dimers are adsorbed at the same lattice site. Atom 2 has a different rotation with respect to the bond of dimers 1 and 3, however it is different by an integer of $60°$ (rotated $60°$ clockwise with respect to 1 and 3), which makes it probable that this dimer is also adsorbed on the same site. We mentioned before that the dimers were really unstable at higher electric fields. To provoke a change in the adsorption position we positioned the STM tip close to all three dimers in a) and applied a voltage of $1.5\,V$. This enforced a change, as one can see in figure 6.12 b). Dimer 1 is now rotated by $60°$ clockwise and has the exact same configuration as dimer 2 had in a). Atom 2 is also rotated by $60°$ clockwise and atom 3 moved up by one lattice site, which is technically the same as a rotation by $180°$. In b) all three dimers have different orientations, all towards the three symmetry directions of the sulfur layer, as also seen previously in figure 6.7. We observed these orientation for the vast majority of 1a dimers, for about $> 95\%$ of the encountered dimers. Single deviations from this could result from partial adsorption on defects, which could provide energetically favourable adsorption positions. Such dimers usually also showed different features at low bias energies and were excluded from our studies.

From figure 6.12 we deduce that the adsorption energy of the preferred hollow site seems to be high enough to enforce a formation of dimers along the symmetry directions of the top sulfur layer. Therefore all arguments made above should also be valid for the 2a dimers. In the following section we want to take a closer look at the electronic properties of this type of dimer.

6.5 Mn dimers - the RKKY-coupling regime

We mentioned earlier that direct exchange coupling results from a partial overlap of the atomic orbitals. For an increased spacing between the two atoms this overlap is absent and the coupling of the two spins is taking place differently, which has immediate impact on the electronic structure of the atom. Figure 6.13 a) shows a Mn 2a dimer. It appears as an oval
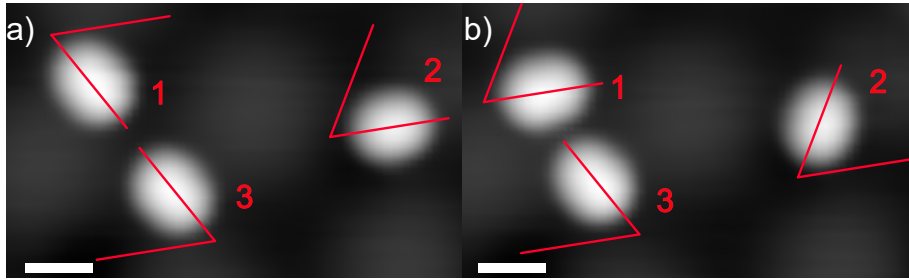
Figure 6.12: Rotation of Mn dimers. a),b) STM topograhies of single Mn dimers before (a) and after (b) applying a high bias voltage in their proximity. In a) the atoms 1 and 3 are adsorbed parallel to each other, whereas 2 is adsorbed roughly $120°$ clockwise rotated with respect to 1 and 3. After a bias voltage of $1.5\,\text{V}$ was applied to every atom in a), all atoms appear to have moved in b). Atom 1 rotated $120°$ counter clockwise, atom 2 rotated $60°$ counter clockwise and atom 3 rotated $180°$ (which can be also understood as a movement of the whole dimer of 1 lattice site). The scale bars in a) and b) amount to $1\,\text{nm}$. The topographies were recorded at $100\,\text{mV}$ and $20\,\text{pA}$.

structure, but both atoms can still be distinguished by a nodal plane. The dimer is oriented towards one of the symmetry directions also observed for the 1a dimers, as expected. Figure 6.13 b) shows a $\text{d}I/\text{d}V$ spectrum taken at the black cross in a). Two bias symmetric steps can be seen around zero bias, at much lower energies than the ones of the 1a dimer. We fitted the spectrum with the method established in [130], which makes use of equation 6.1. The fit yielded an exchange coupling constant of $J_D = 0.23\text{mV}$, which is around 50 times smaller than the one of the 1a dimer, indicating much weaker coupling between the two atoms. In figure 6.13 c) we mapped out the intensity of the probed excitation: as one can see it is distributed uniformly around the dimer. At last, we took a spectrum at higher bias voltages, again at the black cross in a), shown in d): the spectrum is dominated by the onset of a resonance at negative bias around $-400\,\text{pA}$, the resonance at positive bias previously seen for the 1a dimer is either absent or too small in intensity to be identified. An onset of a resonance at positive bias at around $400\,\text{mV}$ is visible. All in all, the high energy spectrum of the 2a dimer has more similarities with the one of the monomer presented in figure 6.2 b) and than with the one of the 1a dimer shown in figure 6.9 f).

The fit for the spectrum in figure 6.13 b) was performed without the addition of any Kondo correlation. That is surprising, as a different spectrum on a 2a dimer, which we presented in figure 6.7 f), had a clear indication of sizeable exchange interactions with the substrate electrons. To understand this differences, we looked at 2a dimers at different adsorption sites.

Figure 6.14 a) shows a 2a dimer adsorbed in the vicinity of the moiré valley. The spectrum taken on the right atom of the dimer is presented in figure 6.14 c) as the red curve: it again shows two step-like excitations at very low energies. No Kondo correlations are evident. We then wanted to compare the spectrum of the dimer to the one of a monomer adsorbed at the exact same lattice site. Therefore we removed one atom from the dimer structure, to get the isolated monomer, as seen in b). The spectrum of the monomer is also plotted in c) as the black curve: it shows a Kondo resonance, which is very small in
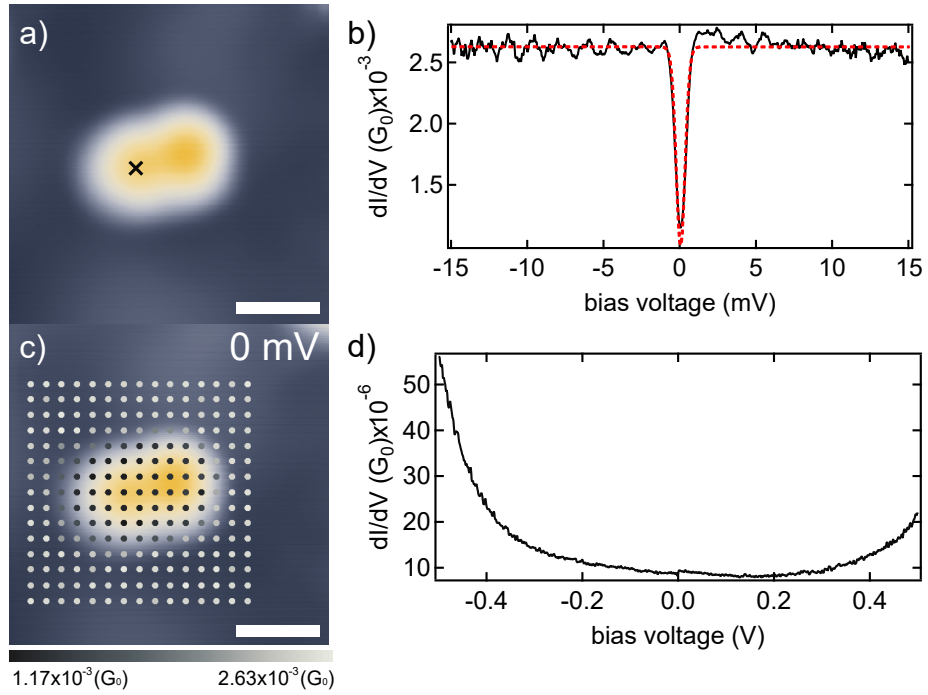
Figure 6.13: Electronic structure of the 2a dimer. a) STM topography of a Mn dimer. b), d) dI/dV spectra performed on the black cross in a). c) STM topography with superimposed dI/dV signal at the indicated bias voltage extracted from a densely spaced grid of spectra across a Mn dimer. The spectra were analysed using SpectraFox [61]. The scale bars in a) and c) amount to $1\,nm$. The topographies were recorded at $100\,mV$ and $20\,pA$, the setpoint of the recorded spectra was $15\,mV$ and $3\,nA$ (b) and $500\,mV$ and $500\,pA$ (d).

intensity in comparison to the spin excitation of the dimer. So even though for this dimer the exchange coupling between the spins is much bigger than the exchange coupling with the substrate electrons $J_D S_A S_B \gg J\rho_0 S_A S_B$, the spectrum can still be understood as the Kondo resonance of a monomer seeing the exchange field of a second atom. This becomes even more evident for a 2a dimer adsorbed close to a moiré dome: figure 6.14 d) shows such a dimer. The corresponding spectrum in f) (red) shows again two step-like excitations at bias voltages lower then $1\,\mathrm{mV}$, however a clear signature of a resonance at zero bias can be seen. Proceeding as before and removing one of the two atoms of the dimer reveals the spectrum of the monomer, which is shown as the black curve in f). The corresponding topography is shown in e). A Kondo resonance with a much higher intensity than the one of the monomer in the valley is present. So for the 2a dimer on the dome, the exchange energy between the two spins and the exchange energy with the substrate electrons are of a similar magnitude and signatures of both can be observed directly. As we can still observe the Kondo correlations, we conclude that the coupling mechanism of the 2a dimer is more RKKY-mediated, meaning indirect exchange interactions via the surface electrons. One of the first works to describe RKKY-like exchange interaction was made by Wahl et al. [101]. They studied the coupling of two cobalt atoms on a Cu(100) substrate. As the work was performed on a metal substrate, Kondo resonances with very high peak widths were seen. To obtain the magnitude of the exchange coupling between the two spins they therefore fitted the spectra with two Fano resonances, which are located at $\pm J/2$. They have seen that for dimers, which were spaced $2.56\,\text{Å}$ apart, which corresponds to a 1a spacing, no Kondo resonance could be seen. This is comparable to the case of the Mn 1a dimer. For a 2a spacing, which amounted to $5.12\,\text{Å}$ in their case, they found a sizeable RKKY-like exchange coupling. They managed to construct several dimers, which were spaced between two and three lattice constants apart. For those they also observe the classbook RKKY-like oscillatory behaviour of the exchange coupling. Finally, for a spacing of $8.1\,\text{Å}$, the properties of the Co monomer were almost restored, indicating the length scale of the RKKY-interaction. All in all, their findings fit exceptionally well with our results and strengthen our claim that the 2a dimer has a RKKY-like coupling. Usually it would be possible to investigate the periodicity of the RKKY-coupling, as it oscillates with the interatomic spacing. However, as we were not able to manipulate the atoms do different adsorption positions than the energetically preferred one, we could not construct differently spaced RKKY-coupled dimers. Another intriguing example of RKKY interactions between single magnetic adatoms was presented by Spinelli and co-workers [202], where they studied Co dimers adsorbed on a Cu_2N patch. With varying adatom spacings they could also reproduce the oscillatory behaviour of the interatomic exchange coupling. Moreover, they have shown that an external magnetic field can actually counteract the exchange coupling. Following up, they propose a phase digram, which is shown adapted in figure 6.15: it shows the different coupling configurations for two magnetic adatoms. The x-axis gives the exchange coupling strength between the two atoms normalised by the Kondo energy and the y-axis gives the magnitude of an applied external field normalised by the Kondo energy. For small x values the Kondo energy dominates the exchange coupling and Kondo correlations can be seen. As mentioned above, increasing RKKY mediated exchange coupling can be counteracted by a sufficiently large external magnetic field applied in the correct direction, leading to a linear change of the Kondo screening regime, marked as the rose area. Very large anti-ferromagnetic coupling in this diagram would represent the 1a dimers, which we described earlier.

The red spectrum in figure 6.14 f) shows a slight asymmetry. We saw something similar in section 6.4.1 for the 1a dimer. In the following section we want to discuss this in more detail.

6.5.1 Potential scattering over the 2a dimer

For the 1a dimer we have seen a difference in potential scattering over a single dimer and between dimers in different positions of the moiré superstructure. Figure 6.16 a) and c) show STM topographies of two distinct 2a Mn dimers, one absorbed close to a dome (a) and the other one in a valley of the moiré . We first want to describe the one adsorbed close to the moiré maximum: it's spectra are shown in b). The black curve was taken on the center of one of the atoms and the red spectrum was taken in the middle of the dimer. Both curves are qualitatively the same, however the red spectrum has a stronger asymmetry. This was also the case for the 1a dimer. Now looking at the spectra of the 2a dimer adsorbed in the valley, shown in d), we can see the same trend: the spectra at the center and the end of the dimer are very similar. Knowing the previous results one could also argue here that the asymmetry is higher for the spectrum taken on the center of the dimer. However, the difference is very small in comparison with the rest of the signal. So in general, the varying potential scattering of the 1a dimer can be also seen for the 2a dimer. Note only one significant difference: the spectrum of the 1a dimer shown in figure 6.10 c) shows a higher conductance at negative bias. For the spectra shown in this section, most pronounced for the one in 6.16 b), the signal is larger at positive bias, indicating a different sign of the potential scattering. The origin of this is not per se clear and needs to be investigated further.

At last we want to comment on the excitation energies of the 2a dimer. A fit of the black curve in b) gives an excitation energy of 0.59 ± 0.03mV, whereas the on in d) gives 0.76 ± 0.03mV. This variation is rather small and of a similar order as our experimental resolution. Therefore, if there even is a difference in excitation energy, it is much smaller than the variations observed for the 1a dimer.

6.6 Summary

To conclude, we investigated Mn single atoms and dimers on MoS_2. The results are summarised in the phase diagram shown in figure 6.17: single atoms show a Kondo resonance in the weak coupling regime, which varies in intensity, but not lineshape, within different positions of the atoms in the moiré superstructure. Here, the intensity increases towards the moiré maximum, as the adatom-substrate exchange interaction is largest there (left box in the phase diagram). Mn dimers can be partially controllable constructed. They do not interact for spacings of three atomic lattice sites or larger. Dimers, which are spaced two atomic lattice sites apart from one another show RKKY-like anti-ferromagnetic exchange interactions of a small magnitude, as shown in the center box in the phase diagram. Their spectra also vary along the moiré superstructure, as the ratio between the inelastic step and the Kondo resonance varies. Atoms, which are only one atomic lattice site apart can couple via direct exchange interaction, as seen in the right box of the phase diagram. The magnitude of their coupling is much larger than the one of the 2a spaced dimers. For the 1a dimers we also observe variations in the spectra across the moiré, however instead a
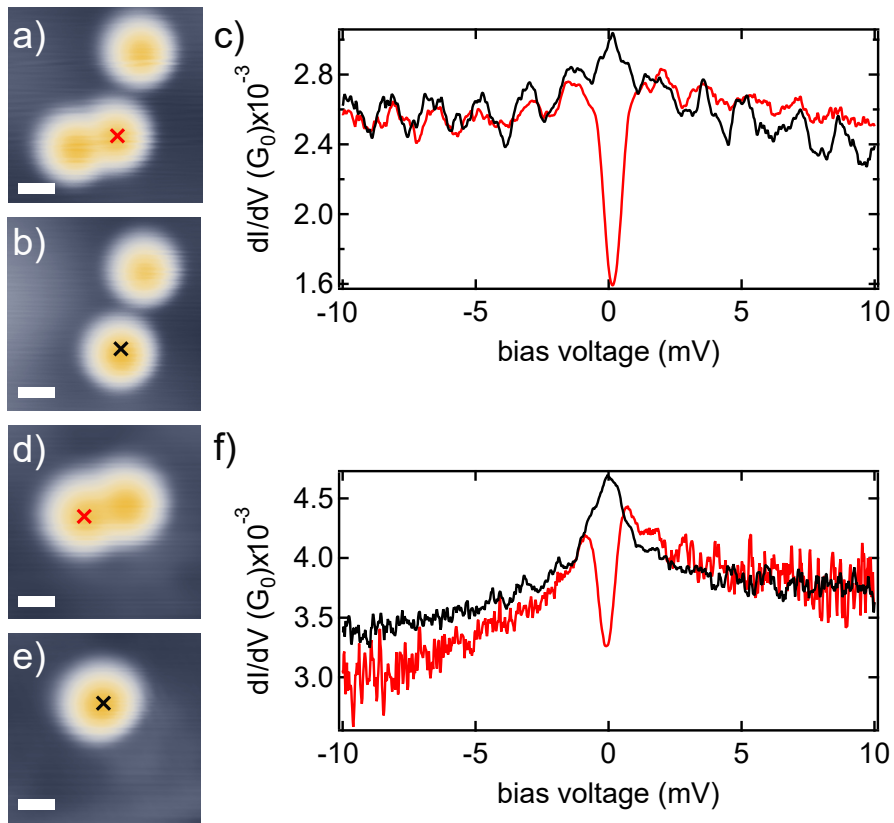
Figure 6.14: Influence of the moiré superstructure on RKKY-coupled Mn dimers. a), d) STM topographies of Mn dimers. Whereas in a) the dimer is adsorbed close to the moiré maximum, in d) the dimer is adsorbed in the moiré valley. c), f) dI/dV spectra performed at the crosses in a) and d)). b), e) show the same scan frame, after one atom has been removed from the dimer. The black spectra in c) and f) show the spectra of the respective monomer. The scale bars in a), b), d) and e) amount to $1\,\text{nm}$. The topographies were recorded at $100\,\text{mV}$ and $20\,\text{pA}$, the setpoint of the recorded spectra was $15\,\text{mV}$ and $3\,\text{nA}$ (c) and $10\,\text{mV}$ and $3\,\text{nA}$ (f).
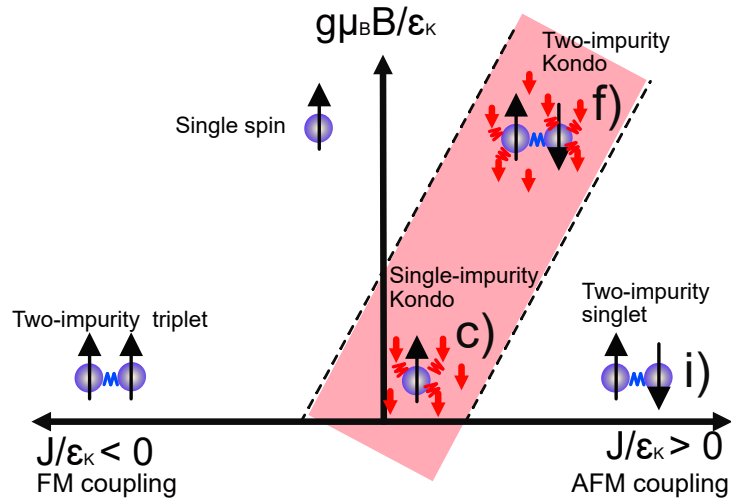
Figure 6.15: Visualization of the phase diagram of the two-impurity Kondo problem. Adapted from [202].

variation in the amplitude of the Kondo resonance we observe a renormalisation of the excitation energy. We assign this to arise from a hybridisation of the Mn d-levels with substrate states, which leads to a modification of the singlet and triplet energy levels. These arise from virtual hopping processes, which lead to a reduction of the adatom spin and therefore also to a reduction of the interdimer exchange coupling J_D. The hybridisation can be related to the adatom-substrate exchange coupling. A comparison between theoretical predictions and the experimental results suggest that the Mn d-orbitals are very likely coupled to the substrate bath via several conduction channels. However as these variation in the excitation energies seem to be absent or beyond our resolution limit for the 2a dimer, more research has to be done on the conditions for these renormalisations.
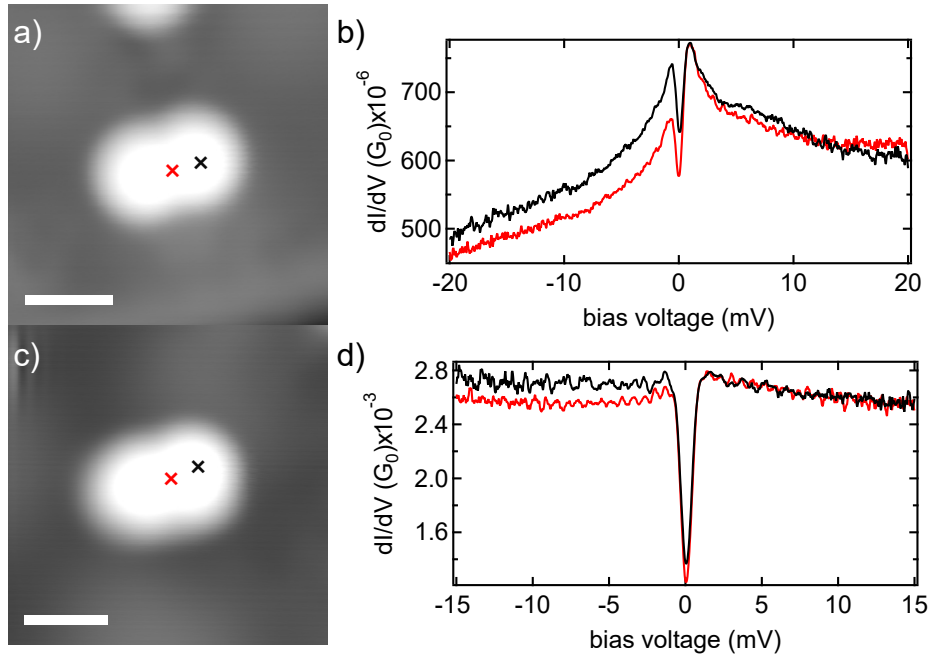
Figure 6.16: Varying interference effects for weak coupled Mn dimers. a),c) STM topograhies of single Mn dimers. Whereas in a) the dimer is adsorbed close to the moiré maximum, in b) the dimer is adsorbed in the moiré valley. b), d) dI/dV spectra performed at the crosses in a) (b)) and c) (d)). The spectra in b) show an exchange split zero-bias peak. Similar to the strongly coupled dimers shown in 6.11, the spectrum in the center of the dimer exhibit an asymmetry for the two bias sides. For the spectra in d) the previously seen zero-bias resonance is absent, while the asymmetry in the spectra is still slightly present. The scale bars in a) and c) amount to $1\,\mathrm{nm}$. The topographies were recorded at $100\,\mathrm{mV}$ and $20\,\mathrm{pA}$, the setpoint of the recorded spectra was $20\,\mathrm{mV}$ and $1\,\mathrm{nA}$(b)) and $15\,\mathrm{mV}$ and $3\,\mathrm{nA}$ (d)).

Figure 6.17: Phase diagram of Mn dimers on MoS_2/Au(111). Three distinct exchange coupling strengths J_D (x-axis) between Mn atoms were found, leading to a non-coupled single atom regime, a RKKY coupling regime (2a dimers) and a direct exchange coupling regime (1a dimers). In all three regimes the varying Kondo exchange interaction $J\rho_0$ (y-axis) leads to a change in the spectra.

7 Ethyl-DADQ: Resolving intramolecular variations of the local charge distribution and vibronic states
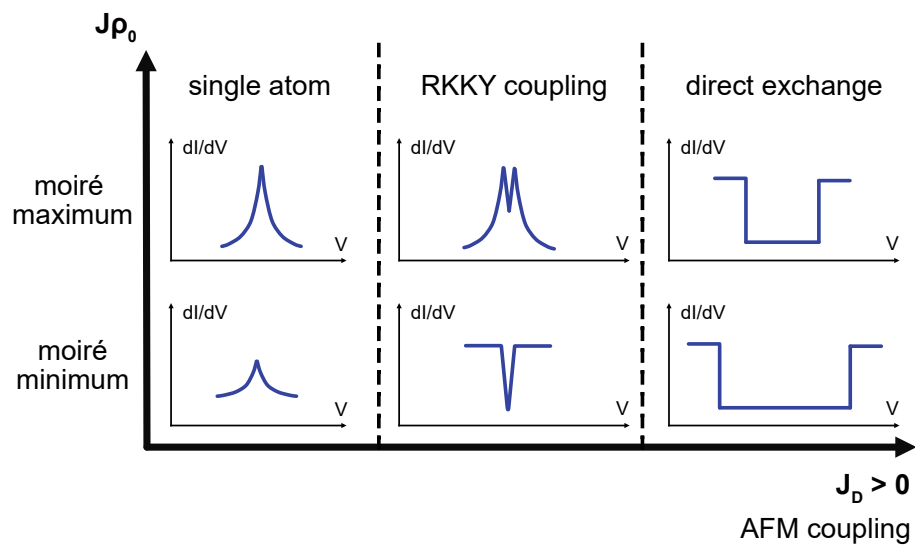
The results presented in this chapter have been published as:

- *"Resolution of Intramolecular Dipoles and a Push-Back Effect of Individual Molecules on a Metal Surface"* by Sergey Trishin, Tobias Müller, Daniela Rolf, Christian Lotze, Philipp Rietsch, Siegfried Eigler, Bernd Meyer and Katharina J. Franke, *J.* Phys. Chem. C 2022 **126**, 7667-7673

and

- *"Variation of vibronic states is densely-packed structures of molecules with intramolecular dipoles"* by Sergey Trishin, Christian Lotze, Johanna Richter, Gaël Reecht, Nils Krane, Philipp Rietsch, Siegfried Eigler and Katharina J. Franke, *p*hysica status solidi (a), 2023

In the previous sections, we covered the fundamental properties of single magnetic impurities on surfaces. In this chapter we want to extend our analysis towards organic molecules. Organic molecules have drawn interest in several surface science related topics, such as magnetism, chemical functionalization of substrates or molecular electronics and optics. Here we want to cover a molecule with a high intrinsic intramolecular dipole moment. This makes the molecules interesting for application in molecular based (opto)-electronic devices [206–208]. However, such applications in devices usually require an adsorption or contact to a metal substrate. Metal substrates are known for strong interactions with organic molecules via hybridisation or charge-transfer, which then often leads to an altering of the properties of the molecules [209–211]. To minimise this interaction, one can introduce a thin insulating layer for decoupling the molecule from the metal surface [33, 59, 212–215]. However, the decoupling efficiency of insulating layers varies. Ionic layers were found to lead to very high reorganization energies of adsorbed molecules due to their high electron-phonon coupling [216], which may be detrimental when studying for example vibronic fingerprints of excited molecular states. Here, covalently bound layers, most prominently MoS_2, where recently proposed to be better suited [43, 82–84]. Moreover, we have seen in the previous chapters than a monolayer of MoS_2 is a very intriguing surface to study single atoms. Note though that organic molecules were also predicted to impose variations on electronic and optical properties of TMDCs [217].

In this chapter, we want to look at Ethyl-Diaminodicyanoquinone (Ethyl-DADQ) molecules adsorbed on both a Au(111) substrate and a single-layer of MoS_2 on Au(111). The molecules were recently proposed to exhibit a large intrinsic dipole moment and shown to be highly fluorescent [218]. First, we have a look at the molecular structure on the Au(111) surface

and if the molecular dipole is preserved upon adsorption. In parts we will also show results from density functional theory simulations, which were carried out by our collaborators Tobias Müller and Bernd Meyer. Details of these are beyond the scope of this thesis and can be found in the aforementioned publication [219]. In the second part, we have a look at the molecular properties on MoS$_2$. The decoupling properties of the layer could give rise to an enhanced energy resolution and therefore allow the study of molecular properties in more detail.

7.1 Ethyl-DADQ on a Au(111) substrate

The experiments presented in this chapter were carried out in a STM, which was set up for combined STM/AFM measurements. The experiments were carried out at a base temperature of $4.8\,\mathrm{K}$. The Ethyl-DADQ molecules were evaporated at $500\,\mathrm{K}$ on a clean substrate held at room temperature.

7.1.1 Adsorption structure of the Ethyl-DADQ molecule

The inset in figure 7.1 a) shows the structure model of the Ethyl-DADQ molecule. It consists of a benzene ring (green) with a imidazolidine (red) and a dicyanomethylene (purple) moiety bound to it. The imidazolidine group has an electron-donor character, whereas the dicyanomethylene group is an electron acceptor, resulting in a dipole moment of 17.3 Debye in gas phase. Figure 7.1 a) shows a STM topography of Ethyl-DADQ molecules evaporated on a Au(111) substrate. The molecules align in chains with varying widths. We found that the widths of the chains can be enlarged by simply adding more molecules to the sample. Moreover, the chains do not assemble along a particular symmetry direction of the underlying substrate and do not modify the herringbone reconstruction, which points to a rather weak coupling to the substrate [220].

Figure 7.1 b) shows a zoom into one of the molecular chains. The individual molecules appear oval, with one termination of the molecule being slightly wider than the other. One can see that across a molecular row one molecule is always slightly sticking out of the chain, with every second molecule sticking out on the same side. The asymmetry in the oval shape is reversed for nearest neighbours within the row, which suggests an anti-parallel alignment of the molecules and a head to tail alignment of the molecules across a row. As indicated with the superimposed structure model, this alignment allows for energetically favourable hydrogen bonds, indicated with the red dashed lines, as well as for a compensation of the dipole moment of neighbouring molecules. In figure 7.1 c) a simulated STM topography is shown, which is based on the structure shown in d), obtained from density functional theory calculations. It resembles the STM topography in b) very well, as even slight details are reproduced. For example consecutive rows show a slight shift, which enforces that across a molecular row an imidazolidine group is closer to one of the neighbouring dicyanomethylene groups than the other, as marked with the red and green ellipses in b) and c).

It was found in the DFT calculations that shifting the molecules out of their preferred adsorption site is energetically not costly, also suggesting a rather weak interaction with the
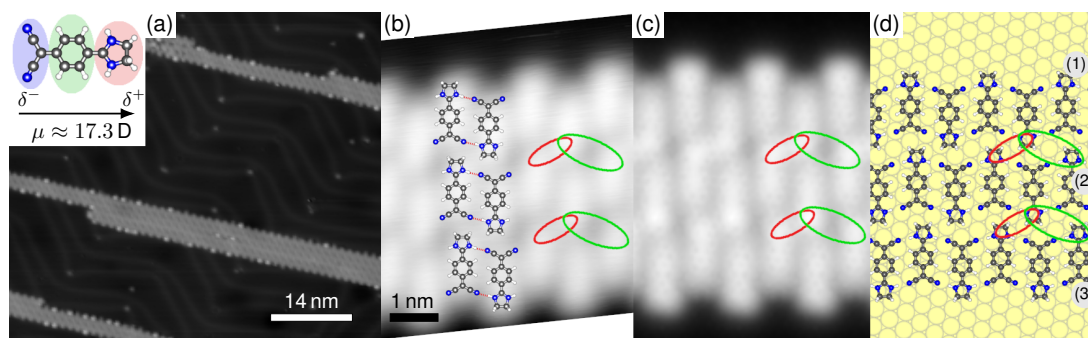
Figure 7.1: Adsorption structure of the Ethyl-DADQ molecule on the Au(111) substrate. a) STM topography of Ethyl-DADQ molecules on Au(111). The molecules assemble in chains with varying widths. The inset shows a structure model of the Ethyl-DADQ molecule: it consists of a benzene ring (green) with a dicyanomethylene (purple) and a imidazolidine (red) group bound to it. The end groups exhibit a different electron affinity as indicated, which leads to a large intrinsic dipole moment of 17.3 Debye in gas phase. b) STM topography at a lower scale, zoomed into a molecular chain. A molecular structure model is superimposed onto the topography and indicates the proposed molecular arrangement within the chain. The red dashed lines indicate hydrogen bonds. c) Simulated STM topography, where the structure in d) was taken as the according molecular arrangement. d) Relaxed molecular structure in a three-molecule-wide chain obtained from density functional theory calculation. See [219] for details. The STM topographies were taken at a setpoint of $1\,\mathrm{V}$ and $100\,\mathrm{pA}$ (a) and $2\,\mathrm{V}$ and $306\,\mathrm{pA}$ (b). The simulated topography was calculated for a bias voltage of $1\,\mathrm{V}$ and an isodensity of $2 \times 10^{-4} e/\text{Å}^3$.

substrate. In the next section we describe the electronic properties of the molecule and see, if this weak interaction has an impact on the intramolecular charge distribution.

7.1.2 Electronic structure of the Ethyl-DADQ molecule

We first look at the molecular resonances of the molecule in the above described structure. Figure 7.2 shows $\mathrm{d}I/\mathrm{d}V$ spectra at negative bias voltages (left) and positive bias voltages (right). One can see two resonances, one around $-1.1\,\mathrm{V}$ and one at $2.5\,\mathrm{V}$. We attribute them to the ionization and to the affinity level of the molecule, respectively. The affinity level could only be probed in the constant-current mode and small currents, as larger electric fields led to an instability of the molecules. The ionization level exhibits a width of about $160\,\mathrm{mV}$, which is narrower in comparison to resonances observed on other organic molecules on metal substrates and indicates a weak coupling to the substrate [221]. In contrast, the affinity level is broader and more asymmetric, which points to an excitation of vibronic levels [213] and vibrational-assisted tunnelling processes [222] associated with it. To look at this in more detail and learn about the intramolecular charge distribution, we measured the LCPD signal along several molecular chains.

Figure 7.3 b) shows a 2D plot of the extracted LCPD signal from a grid of densely spaced

spectra taken on the topography in a). One can see two main trends in the plot: first, the LCPD value seems to globally decrease towards the molecular chain and secondly, there seems to be some modulation of the LCPD along and across the chain. The superimposed structure model suggests that the LCPD value is lowest on the imidazolidine group and highest on the dicyanomethylene group. A similar trend is found in the calculated electrostatic potential shown in figure 7.3 c). Here also a modulation can be seen across and along the molecular plane. As the electrostatic field can be compared directly to the LCPD at the tip-sample distances used in the experiment [59], this is a good indication that an intramolecular dipole is preserved after the adsorption of the molecules to the substrate. This becomes even more clear when looking at the LCPD values and electrostatic potential taken along a line across a molecular chain, as shown in figure 7.4 a): here, the LCPD value is shown in blue, taken on the blue dashed line indicated in the STM topography below the graph. The electrostatic potential is plotted in red and was calculated across the red-dashed line shown in the molecular structure below the graph. One can see four local minima in the LCPD and electrostatic potential. The first three are highlighted with black dashed lines. Looking at the positions, where those spectra were probed on, one can see that those three minima all occurred on the imidazolidine group, as it was also the case in the LCPD grid shown in figure 7.2 b). This finding matches our expectation, as the imidazolidine group is the electron donor group and should therefore be more positively charged. In the LCPD measurements, a positive charge requires a more negative bias voltage to be compensated, which is in agreement with our findings. In contrast, one can see that local maxima can be found at the position of the dicyanomethylene group of the molecules, which require a more positive bias voltage to be compensated, due to their negative charge. As all three molecules probed show this intramolecular modulation of the LCPD signal and the electrostatic potential, we conclude that the intramolecular dipole moment is still preserved upon adsorption on the substrate.

The forth local minimum found can be explained by contributions from neighbouring molecules, sticking out of the molecular chain. Their contributions seem to deviate quantitatively between the measured LCPD and calculated electrostatic potential. This can be rationalised by two arguments: first, the LCPD is sensitive to the z-component of the electrostatic potential, therefore the tip-sample distance is a crucial parameter for an exact comparison. Moreover the shape of the STM tip also plays a role. An asymmetric tip could also lead to an asymmetry in the spectra. A very blunt tip is moreover also more sensitive to long-range electrostatic contributions than a sharp tip.

Until now we did not comment on the origin of the observed overall decrease of the LCPD and electrostatic potential over the molecular chain. Films of organic molecules were found to reduce the global workfunction of metals by compression of the electron density of the metal substrate leaking into the vacuum, for example in photo emission spectroscopy [223–225]. As this can be visualised as the molecule pushing the surface electron wave function back into the substrate, this effect was labelled as "push-back" effect. Sometimes also the term "pillow" effect is used. We observe this effect on a local scale, as the LCPD probed on the molecules is locally consistently lower than the one of the substrate.

Figure 7.4 b) illustrates the contribution to the electrostatic potential found: along the molecule, there is an oscillation, stemming from an intramolecular dipole moment (labelled $\delta-$ and $\delta+$). Additionally, the electrostatic potential is lowered over the molecules by a local scale push-back effect. In the next section we look at Ethyl-DADQ molecules adsorbed
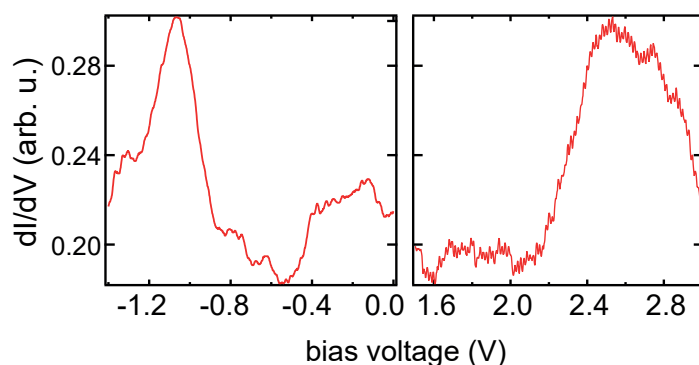
Figure 7.2: Electronic structure of the Ethyl-DADQ molecule. Two resonances can be seen at around -1.1 V and 2.5 V. The left spectrum was recorded at a setpoint of 1 V and 100 pA and the right one in the constant current mode at 100 pA.

on a layer of MoS$_2$. Here, we would expect that we can resolve the molecular resonances introduced in figure 7.2 better, possibly allowing us to study intermolecular variations.

7.2 Ethyl-DADQ on a single-layer of MoS$_2$/ Au(111)

We grew the MoS$_2$ islands as described in section 2.12.2. The Ethyl-DADQ molecules were evaporated at a temperature of 500 K on the as-prepared sample held at 230 K. This sample temperature is sufficiently low to ensure a satisfactory coverage of molecules on top of the MoS$_2$, but also sufficiently high to enable the growth of molecular chains. These are crucial for the experiment, as single molecules were found to be not stable enough to be probed. In the presentation of our results we will follow the structure of [226].

7.2.1 Adsorption structure of the Ethyl-DADQ molecule on MoS$_2$

Figure 7.5 a) shows a STM topography of Ethyl-DADQ molecules on MoS$_2$. Similar to the previously studied adsorption structure on Au(111), the molecules seem to adsorb in chains. Surprisingly, they seem to follow the three-fold symmetry of the moiré superstructure of the MoS$_2$ layer, which we did not observe for the molecules on the Au(111) substrate. In general, we find mostly single-stranded chains and never larger ones than triple-stranded. In the following analysis we focus on single and double-stranded chains. At first, we look at the adsorption structure of single-stranded chains. Figure 7.5 b) shows a STM topography of such a chain. One can see that the molecules assemble in a similar fashion as described before on Au(111), where next neighbours align anti-parallel to each other, to allow for the formation of hydrogen bonds and to compensate their dipole moments. This structure is even better resolved in the Δf image shown in figure 7.5 f). Here, the anti-parallel alignment of the molecules can be resolved without a doubt. Also one can clearly see that the imidazolidine group is the moiety sticking out of the molecular chain. Moreover, one can also see that there is a larger signal over the imidazolidine group, indicating a non-flat adsorption on the surface. For comparison, we simulated the expected signal with the probe-particle model [227] (see figure 7.5e)), which shows a very good agreement with the
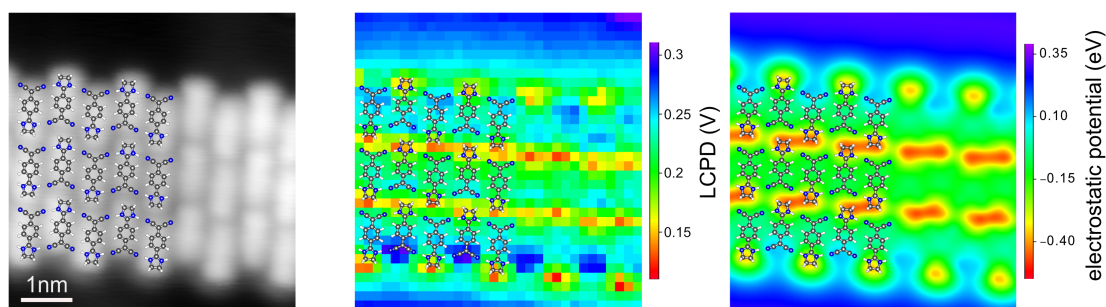
Figure 7.3: Local charge distribution within a chain of Ethyl-DADQ molecules. a) STM topography of a three molecule wide chain with a superimposed structure model. b) LCPD values extracted from a densely spaced grid of $\Delta f - V$ spectra across the area shown in a). c) Calculated electrostatic potential of a three-molecule-wide chain. The STM topography in a) and the spectra shown in b) were recorded at a setpoint of $1.5\,\mathrm{V}$ and $130\,\mathrm{pA}$. For recording the spectra the tip was additionally approached $0.8\,\mathrm{Å}$ towards the sample. The electrostatic potential in c) was simulated for a tip-sample distance of $7.1\,\mathrm{Å}$.

experimental contrast. We could identify that the increased contrast over the imidazolidine group stems from hydrogen atoms sticking out of the molecular plane.

A similar structure is also obtained for double-stranded chains, as can be seen in the STM topography in figure 7.5 c) and the corresponding Δf image in g). The zig-zag pattern of alternating molecules is still preserved, the second strand of molecules just assembles head-to-tail onto the first one. This structure on Au(111) resulted in a preserved dipole moment of the molecules. In the next subsection we check if this is also the case for single-stranded molecules on MoS$_2$ and how their energy-level alignment looks like with presumably less hybridisation with the substrate.

7.2.2 Electronic structure of single-stranded chains

Figure 7.6 a) shows the extracted LCPD values taken over the green-dashed line in the topography shown in b). The probed molecule lies at the edge of a single-stranded chain. As in the case for the molecules on Au(111), we can see an oscillation of the LCPD signal, where the lowest LCPD value is observed over the imidazolidine group and the highest one is seen over the dicyanomethylene group. That matches our expectations and previous results very well. Note also that in this case neither an effect of a local scale push-back effect was expected, nor seen and we therefore only observe a variation in signal due to the intramolecular dipole. We now focus on the description of the electronic structure of the Ethyl-DADQ molecules on MoS$_2$. Figure 7.7 a) shows $\mathrm{d}I/\mathrm{d}V$ spectra taken on the bare MoS$_2$(black), a molecule on the edge of a molecular chain (blue) and a molecule inside a molecular chain (green), as indicated in the inset topographies. The blue spectrum shows several resonances from $-900\,\mathrm{mV}$ onwards. No states can be seen at positive bias voltages, suggesting that the affinity level is located beyond the probed energy regime, as also seen for this state on Au(111). It is on first glance not exactly clear, why several resonances are observed inside the band gap. We have only observed one resonance for the molecules
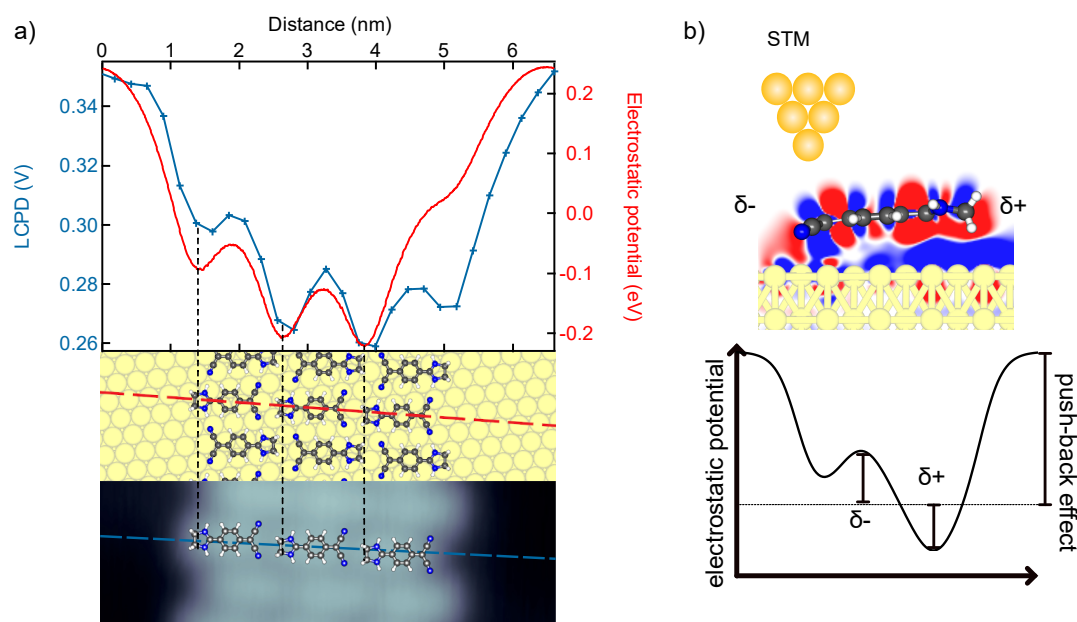
Figure 7.4: Influence of the local charge distribution and the push-back effect on the local electrostatic potential. a) Plot of the extracted LCPD value, (blue) taken on the blue-dashed line indicated in the STM topography below the line, and the electrostatic potential (red), calculated for the red-dashed line indicated in the structure model below the graph. The black dashed lines indicate the position of the imidazolidine groups of the respective molecules. The setpoint of the STM topography was $1\,V$ and $172\,pA$, the spectra were recorded at a setpoint of $2\,V$ and $300\,pA$ and the electrostatic potential was calculated for a tip-sample distance of $9.3\,Å$. b) Visualisation of the contributions to the varying electrostatic potential along a Ethyl-DADQ molecule. An overall reduction is obtained due to the push-back effect, whereas the observed oscillation stems from the varying charge distribution across the molecule.
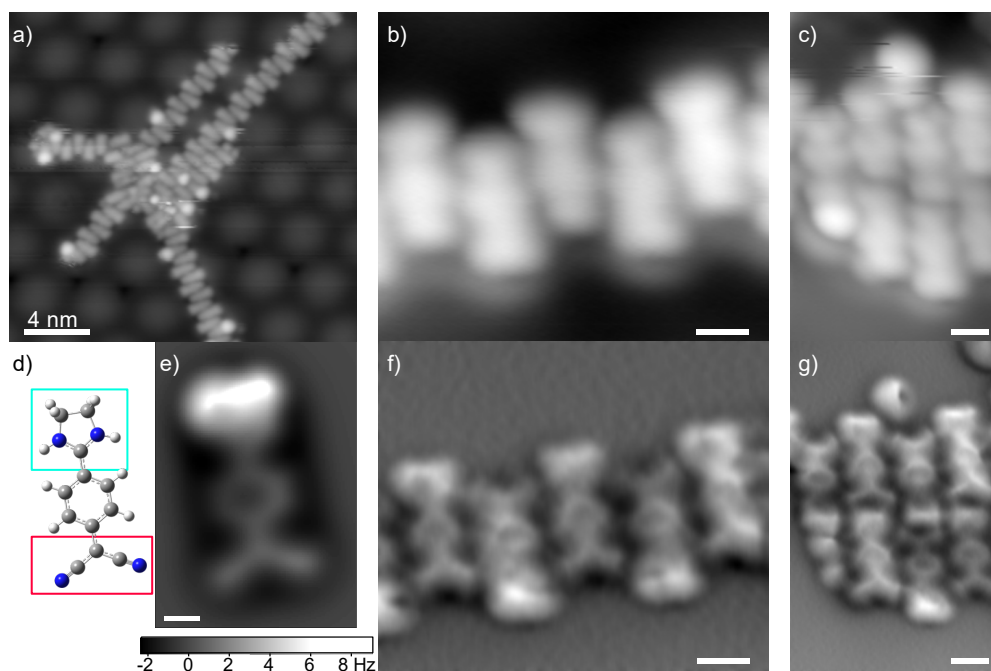
Figure 7.5: Adsorption structure of Ethyl-DADQ molecules on a single-layer of MoS_2. a) STM topography of chains of Ethyl-DADQ molecules. They exhibit a threefold symmetry, suggesting they might follow along the symmetry directions of the MoS_2 layer. b),c) Zoom into a single- (b) and double-stranded (c) chain. The topographies were taken with a Cl functionalised tip. d) Stick-and-ball structure model of the Ethyl-DADQ molecule. e) Simulated frequency shift signal of the Ethyl-DADQ molecule when probed at a tip-sample distance of $6.9\,\text{Å}$. The signal was calculated employing the probe-particle model [227, 228]. The structure fed into the simulation was relaxed before on a graphene sheet to mimic van-der-Waals interactions with the substrate. The map in e) is to scale with the model in d). f),g) Constant-height Δf images recorded on the areas shown in b) and c) respectively. The STM topographies in a) and c) were recorded at a setpoint of $1\,\text{V}$ and $30\,\text{pA}$ and the one in b) at a setpoint of $520\,\text{mV}$ and $30\,\text{pA}$. The constant-height images in f) and g) were recorded at a setpoint of $1\,\text{V}$ and $30\,\text{pA}$. After switching the feedback off, the bias voltage was set to $0\,\text{V}$ and the tip was approached by $0.1\,\text{Å}$ towards the substrate. The scalebars in b),c),f) and g) amount to $5\,\text{Å}$ and the one in e) amounts to $2\,\text{Å}$.

adsorbed on Au(111) and no other ionization level is predicted to lie that close in energy to the HOMO (the next molecular state is located 1.3 eV lower in energy). Therefore it is natural to assume that the resonances observed are sidebands of the lowest energy resonance and stem from the excitation of vibronic states [212, 213, 229–233]. The intensity of the individual observed vibronic satellite peaks depends here on the electron-phonon coupling of the associated vibrational mode, which is quantified by the Huang-Rhys factor. For the green spectrum in figure 7.7 a) these sidebands are much less pronounced. In contrast to the blue spectrum this spectrum was taken on a molecule inside a molecular chain, and not at one at the edge. We believe that here a strong damping of the affected vibrational excitations is taking place [216, 234]. As this behaviour was not observed for larger, extended molecules on MoS_2 [82], we speculate that this damping might arise due to the dipolar character of the molecules and affect especially the vibrational modes along the molecular axis.

To get a better understanding about the electronic structure of the molecules inside a chain, we recorded spectra in an energy window around the ionization level along a molecule, as indicted in the STM topography shown in figure 7.7 c). The corresponding spectra are presented in b). All spectra show asymmetric resonances, which suggest the presence of vibronic satellite peaks beyond our resolution limit. Interestingly, the weight of these peaks varies along the molecule: whereas at the imidazolidine group the peak has a higher intensity than the shoulder, in the center of the molecule and towards the dicyanomethylene group their intensities ratio switches. At the very edge of the molecule the intensities switch back. For a better visualisation of these variations in intensity, we mapped out the peaks in constant-height dI/dV maps. The maps are shown in figure 7.8 d)-g), they were taken at the same area as shown in the STM topography in a). The map in d) was taken around the onset of the peak at -900 mV. It shows a slight signal on the imidazolidine group. Going to a larger energy of -950 mV in e), one can see that the signal intensity increases on the imidazolidine group, but also some intensity around the dicyanomethylene group can be observed. This trend continues in the map in f) probed at -1 V, where the signal on the imidazolidine group is diminishing and additionally some signal between the molecules appears. Finally the map at -1.05 V in g) shows mostly only intensity between the molecules next to the dicyanomethylene group and the benzene ring.

This change in the spatial distribution of the intensity is surprising at first glance, as vibronic resonances arise from excitations of the ionization level and therefore should resemble the spatial extension of the according orbital. Therefore, to expound on these variation we compare them with the calculated shape of the HOMO of the molecule, which is shown in figure 7.8 b). As the wave function probed in the STM is always convolved with the probe wave function, we also simulated the Tersoff-Hamann image of the HOMO, which is shown in c). Here the orbital appears U-shaped. The signal is centred on the benzene ring and opens up towards the dicyanomethylene group. Comparing this with the dI/dV maps previously described one would not expect a large signal on the imidazolidine group of the molecule, as seen in d) and e). However, taking into account the Δf maps shown in figure 7.5 f) we assume that the signal observed there stems from the elevation of the hydrogen atoms and is more of a topographical than electronic nature. When excluding the signal on the imidazolidine group in the map at -950 mV, the map does resemble the Tersoff-Hamann image relatively well. This underlies that the first resonance probed in the dI/dV spectra indeed stems from tunnelling from the HOMO of the molecule. However, the symmetry of the higher energy maps in f) and g) does not really resemble the shape of the
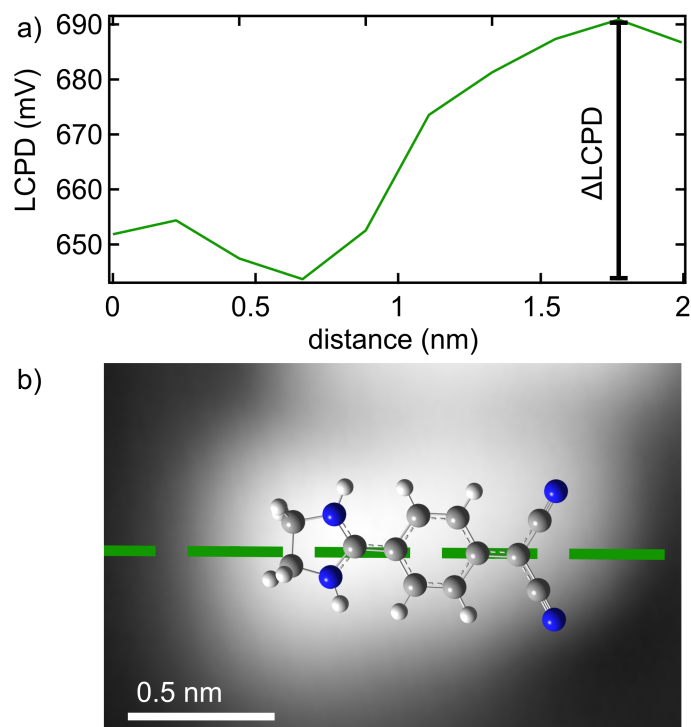
Figure 7.6: Intramolecular charge distribution. a) Extracted LCPD signal over a line of densely spaced spectra, as indicated with the green-dashed line in the STM topography below. b) STM topography of a Ethyl-DADQ molecule at the edge of a single-stranded molecular chain. A structure model was superimposed for clarity. The STM topography was taken at a setpoint of $1\,V$ and $30\,pA$, the spectra were taken at a setpoint of $-1.6\,V$ and $400\,pA$.

HOMO. We suggest that the additional resonances stem from vibration-assisted tunnelling processes. Here, the tunnelling matrix element can be perturbed by exciting an out-of-plane vibrational mode, which changes the wavefunction overlap and can create an increased intensity at a nodal plane of the molecular orbital [84, 222]. As tunnelling processes through the molecular orbital are unlikely at the nodal planes, the vibration assisted tunnelling is dominant there.

Until now we have seen that the electrostatic environment is crucial for the electronic structure of the Ethyl-DADQ. Therefore it is intriguing to look at the electronic structure of the double-stranded molecular chains as well, which we will do in the following subsection.

7.2.3 Electronic structure of double-stranded chains

Figure 7.9 c) shows a STM topography of a double-stranded chain. The two molecules across the chain do not encounter the same electronic environment: one of the molecules (exemplary marked with the blue box) is always sticking out of the molecular chain, whereas the other one (framed with the green box) is always embedded into the chain. To unravel
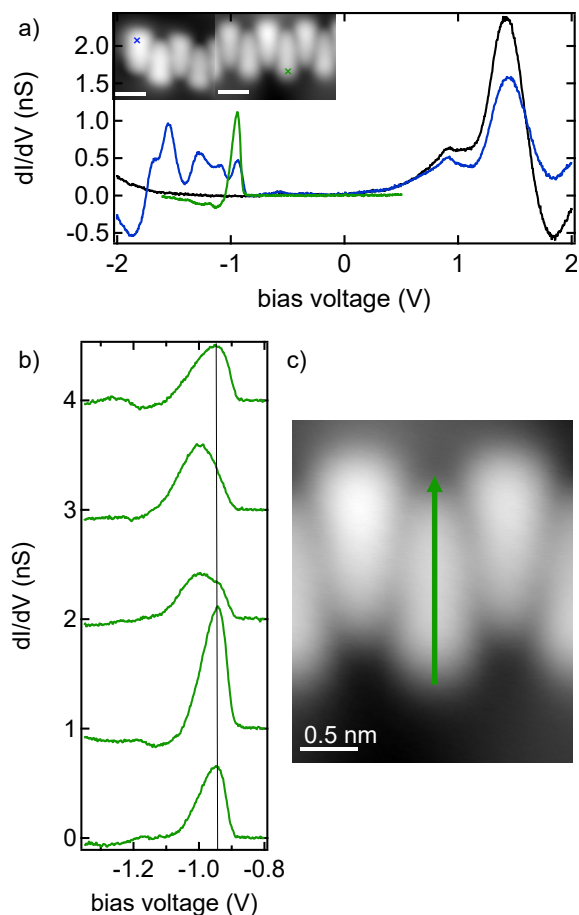
Figure 7.7: Electronic structure of single-stranded molecular chains. a) dI/dV spectra performed on bare MoS_2 (black), a molecule at the edge of a single-stranded chain (blue) and the middle of a single-stranded chain (green). The exact locations of the spectra are shown in the STM topographies in the inset. Several molecular resonances appear in the band gap of the MoS_2. b) dI/dV spectra taken along a single Ethyl-DADQ molecule, as shown in the green line in the topography in c). The apparent energy position and width of the resonance seem to vary. c) STM topography of a single-stranded chain. The STM topographies were recorded at a setpoint of $1\,V$ and $30\,pA$. The scale bars in the insets in a) amount to $1\,nm$. The didv spectra were taken at a setpoint of $2\,V$ and $1\,nA$ (a), black), $-1.6\,V$ and $400\,pA$ (a), blue) and $-1.6\,V$ and $50\,pA$ (a), green) and b). The spectra in b) are offset by $1\,nS$ for clarity.
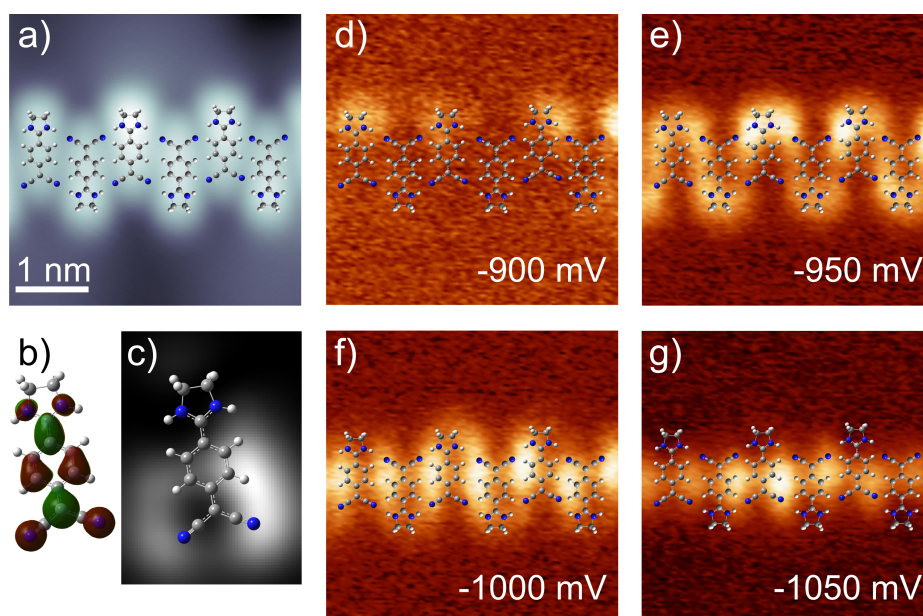
Figure 7.8: Spatial resolution of the dI/dV signal. a) STM topography of a single stranded molecular chain. A superimposed structure model was included for clarity. b) DFT simulation of the HOMO of the Ethyl-DADQ molecule. The molecule was relaxed on a sheet of graphene, see [226] for details. c) Simulated Tersoff-Hamann constant-height image of the simulated HOMO convolved with a s-wave tip at a tip-sample distance of $5\,\text{\AA}$. The highest signal intensity is located at the dicyanomethylene group and shows a u-like shape, which is typical for cyano-groups [167]. The asymmetry in the signal stems from a rotation of the imidazolidine group with respect to the phenyl-group. d)-g) Constant-height dI/dV maps recorded on the same area as shown in a). The energies of the respective maps are shown in the bottom right corners. The STM topographies were recorded at a setpoint of $1\,\text{V}$ and $30\,\text{pA}$. For the constant-height maps, the tip was approached additionally by $2\,\text{\AA}$ towards the sample, after the feedback was switched off.

the influence of these different electrostatic landscapes, we performed dI/dV spectra across the black line in in c). They are shown in a), the colour of the spectra represents on which molecule they were probed on. In addition the spectra were offset for clarity. The blue spectra show four resonances, which are located at $-900\,\mathrm{mV}, -980\,\mathrm{mV}, -1.1\,\mathrm{V}$ and $-1.27\,\mathrm{V}$. For a better visualisation we marked them with the blue arrows. Similar to the case of the single-stranded molecules, the intensity of the resonances varies drastically along the molecule. While the resonance at $-900\,\mathrm{mV}$ has a low intensity at the imidazolidine group and a high intensity at the center of the molecule, the resonance at $-980\,\mathrm{mV}$ is located at the center and dicyanomethylene group of the molecule. The resonances at $-1.1\,\mathrm{V}$ and $-1.27\,\mathrm{V}$ have their main contributions at the terminations of the molecules. In comparison, the spectra taken on the green boxed molecule do not look exactly alike. For example, the onset of the HOMO is shifted to higher energies by about $90\,\mathrm{mV}$, which is indicated by the black line in the graph. Still, we observe four resonances at energies of $-990\,\mathrm{mV}, -1.075\,\mathrm{V}, -1.22\,\mathrm{V}, -1.3\,\mathrm{V}$. All resonances are shifted towards larger energies in comparison to the blue boxed molecule, which can be explained by a different screening strength of the individual molecules due to their position in the moiré superstructure and their different electrostatic environment. However, as this shift is not rigid for all sidebands, these variations again point to a sizeable damping of some molecular vibrations due to a varying electrostatic environment.

To check how the electrostatic environment changes between the two molecules we probed the LCPD of the molecules along the same line as the spectra shown in figure 7.9 a). The result is shown in b): for both molecules the intramolecular oscillations observed previously are still present, again the lowest value is found on the imidazolidine group and the largest one at the dicyanomethylene group. Nevertheless, one can see that the size of the LCPD is different between the two molecules. This suggest that the environment of the molecules also leads to a different screening of the molecular dipole. As a consequence the different electrostatic potential probed in the LCPD might be correlated with the proposed damping of the vibronic resonances observed in the dI/dV spectra.

Finally, similar as for the single-stranded chain, we map out the spatial variations of the differential conductance in constant-height maps. The results are shown in figure 7.10 b) and c). These maps were probed on the same area as the STM topography shown in a). The map in b) resembles the crescent shaped structure, observed in the Tersoff-Hamann images, very well. As there is no significant signal on the imidazolidine group it might be that the molecules in the double-stranded chain are adsorbed flatter than the single-stranded ones. Moreover, only some molecules exhibit a signal at $-1.03\,\mathrm{V}$, whereas some remain completely dark. This is in accordance with the previous observation from the spectra shown in figure 7.9 a), where the onset of the molecular resonances varied between the molecules. The molecules exhibiting signal in the map in b) have the same position in the molecular chain as the green boxed ones in figure 7.9 c). The map in figure 7.10 c) was recorded at a higher voltage of $-1.17\,\mathrm{V}$ and shows a more pronounced intensity between the molecules. The crescent shaped signal only partially persists at this energy. From this we conclude that the vibration-assisted tunnelling processes start to dominate, similar to the case of the single-stranded chain, as shown in figure 7.8.

7.3 Summary

In summary, in this chapter we investigated Ethyl-DADQ molecules on a Au(111) substrate and a single-layer of MoS_2. The molecules assemble in chains of varying width after adsorption. For the molecules on Au(111) we found that the predicted intramolecular dipole is still preserved on the surface. Moreover we observed a local lowering of the LCPD signal over the molecules in comparison to the bare substrate, which we assigned to a local scale push-back effect. The intramolecular dipole was also preserved for the molecules studied on MoS_2. Moreover the increased energy-resolution allowed us to study the molecular resonances in more detail. We found that the HOMO of the molecule is located inside the band gap of the MoS_2, which allowed us to detect several vibronic satellite peaks. These varied drastically depending on the molecular environment, pointing towards a significant damping of some vibrational modes depending on their respective electrostatic environment. Moreover, also intramolecular variations in the excitation spectra were observed, which hints towards a non-negligible contribution of vibration-assisted tunnelling processes. The excitation spectra also varied across molecules in a double-stranded chain, furthermore indicating the crucial impact of the local electrostatic environment on the excitation spectra of the molecules. For further understanding, future experiments on single Ethyl-DADQ molecules on MoS_2 could be beneficial to disentangle the individual contributions to the excitation spectra. Also a more profound theoretical analysis of the eventual coupling of molecular vibrations could help to reproduce the individual excitation spectra. Therefore, as for now, it remains inconclusive how the damping mechanism of the vibrational modes and the associated selection rules work exactly.
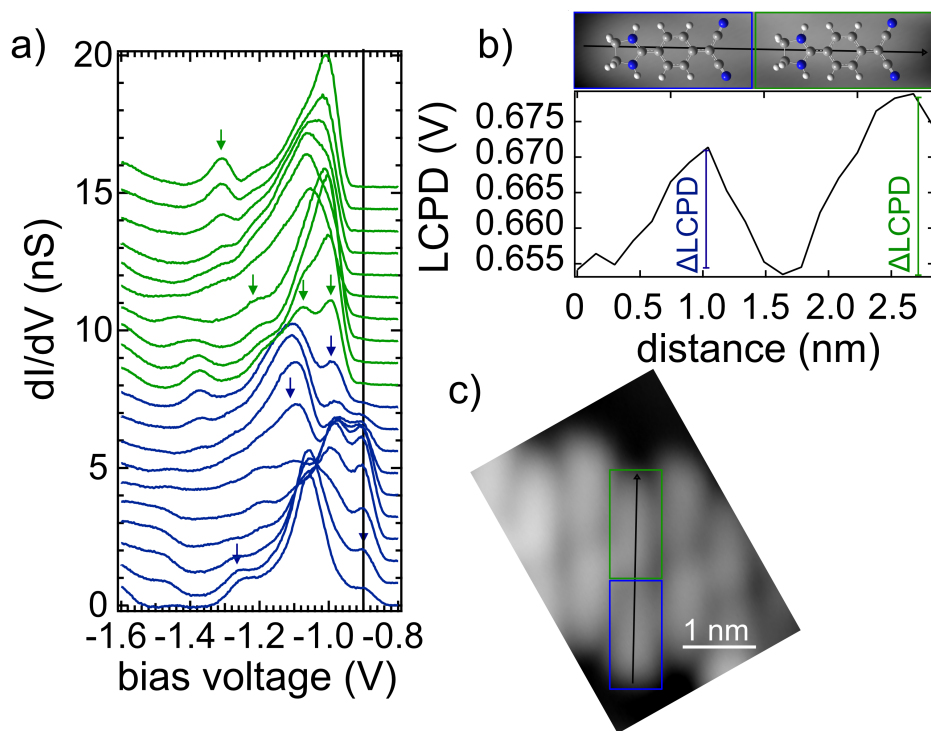
Figure 7.9: Electronic structure of a double-stranded chain. a) dI/dV spectra performed along the black line indicated in the STM topography in c). Several resonances appear, which seem to vary in their intensities across the molecules. The spectra are offset for clarity. The blue and green colour code of the spectra indicates, if the respective spectra were recorded on the blue or green boxed molecule in c). b) Extracted LCPD values across the same double-stranded molecular chain as in a), also as indicated in the STM topography on top of the plot. c) STM topography of a double-stranded molecular chain. The green and blue boxed molecule have a different electrostatic environment. The STM topographies were recorded at a setpoint of $1\,\mathrm{V}$ and $30\,\mathrm{pA}$, the spectra were recorded at a setpoint of $-1.6\,\mathrm{V}$ and $100\,\mathrm{pA}$ with the tip additionally approached by $0.6\,\mathrm{Å}$ towards the sample. The spectra in a) were offset by $0.8\,\mathrm{nS}$ for clarity.
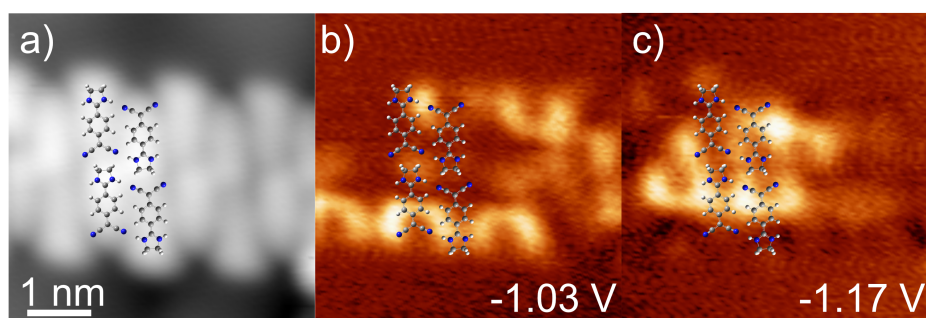
Figure 7.10: Spatial variation of the dI/dV signal in a double-stranded chain. a) STM topography of a double-stranded chain. A structure model was superimposed for clarity. b),c) Constant-height dI/dV maps taken at the same area as a). The energies of the maps are indicated in the bottom right corners. The STM topographies were recorded at a setpoint of $1\,V$ and $30\,pA$, for b) and c) the tip was additionally approached towards the sample by $2\,Å$ after switching the feedback off.

8 Conclusions and outlook

In this thesis, we investigated several different nanostructures on a single-layer of MoS_2, grown on a Au(111) substrate by means of STM and AFM. These nanostructures included single-point defects, magnetic adatoms and molecular chains. We investigated both their structure and their electronic and magnetic properties on the surface and how these can be tailored.

First, we focused on single top sulfur vacancies in the MoS_2 layer. The defects could be identified and distinguished from other defects by combined STM and AFM topographies. As predicted in theory and found for other TMDCs, the chalcogenide vacancies led to the formation of in-gap defect states. Most notably, a sharp resonance at zero bias was found, which could be traced back to Kondo-like exchange interaction by its characteristic temperature dependence and magnetic field behaviour. The formation of the Kondo resonance implies that the defect is charged. We also studied sulfur vacancies on pit defects, areas on the MoS_2, where some layers of the underlying gold are missing. There the defect states were more pronounced and located at different energies, but the Kondo resonance was absent. This shows that the hybridisation with the Au(111) layer has a crucial impact on the properties of the vacancies.

Second, we studied single iron atoms on MoS_2. Here, we found that the adsorption position of the atoms has a huge influence on their low-energy excitation spectra. Atoms adsorbed in minima of the moiré superstructure exhibit an inelastic excitation stemming from spin-flip excitations. This observation agrees with a spin state of S = 1, where the degeneracy of its spin-projections is lifted by magnetic anisotropy and confirms that a spin is preserved upon adsorption of the surface. Moreover, we also found that the lifetime of this excitation is at least $1\,ps$, indicating that the atoms are decoupled reasonably well from the substrate. However, iron atoms on the maxima of the moiré do not show any inelastic excitation, but a fully developed Kondo resonance. This points to a strong screening by the substrate electrons. We explained these variations by changes in the local density of states across the moiré : minima have a lower density of states around the Fermi level, which leads to weaker interactions with the iron atoms. In contrast, maxima have a higher density of states, which leads to stronger interactions. This explanation is supported by a theoretical scaling model for a spin S = 1 system, which explicitly shows the reduction of the magnetic anisotropy with increasing Kondo exchange interactions. Moreover, we found that this reduction happens continuously across the moiré: atoms, which are positioned somewhere between moiré minima and maxima showed fingerprints of both inelastic spin-flip excitations and Kondo exchange interactions. This allows for a remarkably high tunability of the system.

In addition, we observed an intriguing triangular shape of the iron atoms, when probed at low bias voltages. This comes along with an increased signal intensity and asymmetry of the above mentioned excitation spectra when probed at one of the vertices of the triangle.

We established that the triangular shape stems from a contribution of a higher-lying orbital, which is probably an iron-sulfur hybrid orbital. This non-magnetic orbital is also located at the triangular vertices. Due to its non-magnetic character it can lead to an increased potential scattering in its vicinity, explaining the increased asymmetry of the spectra. We also showed that the triangular shape is absent for atoms which are sitting on defective sites or are hydrogenated, which helps to distinguish them from one another.

After that, we studied single Mn atoms and dimers. We have seen that all distinct single Mn atoms exhibit a Kondo resonance in the weak-coupling regime. Even though the spectra are qualitatively equal over the moiré superstructure, we still have determined quantitative differences across the moiré by fitting the spectra. The fits revealed that the spectra differ in their respective amplitudes, which is correlated with the Kondo exchange coupling to the substrate in the weak-coupling regime. The exchange coupling was largest for the atoms on or close to the moiré maxima and smallest for the ones on the minima, in agreement with the previous results obtained on the iron atoms.

To study Mn dimers we first tested if we could successfully build such structures with the STM tip. Even though this process was challenging, we managed to construct some Mn dimers. Those constructed Mn dimers showed the same properties as dimers formed during adsorption, corroborating the assignment of as-adsorbed Mn dimers. We found three types of Mn dimers, based on their interatomic exchange interaction: dimers, which had an atom separation of at least 3 atomic lattice sites showed the same excitation spectra as single atoms. From this we concluded that these dimers show no interatomic exchange coupling at all. Dimers, which were separated by exactly two atomic lattice sites, showed a zero field splitting of the Kondo resonance. These observations can be interpreted such that the two atoms in the dimer interact with a sizeable RKKY like exchange interaction. The ratio of intensity between the amplitude of the Kondo resonance and the dip caused by the splitting of the resonance was also found to vary along the moiré. Finally, for atoms which were separated by one atomic lattice site, no Kondo correlations were observed. Instead, an inelastic excitation was seen, which results from an anti-ferromagnetic direct exchange interaction between the two atoms and can be modelled by a Heisenberg exchange Hamiltonian. On top, we observed that the energy of these inelastic, singlet-triplet excitations varied within the moiré superstructure. We observed lower excitation energies on the moiré maxima and larger excitation energies on the moiré minima. To unravel the origin of these variations, we looked at the effect of the hybridisation of the Mn d-levels with substrates states on the singlet and triplet energy level in a perturbative model. Here, a stronger hybridisation with the substrate leads to an increased probability of virtual hopping processes of electrons in or out of the Mn d-levels, reducing the effective spin of the atom. Accounting for all possible processes, we find that a renormalization of the singlet-triplet excitation energy does occur and can be related to the magnitude of the adatom-substrate exchange coupling. We compared the extracted experimental renormalizations to the theoretical predicted ones and have seen that the theoretical model underestimates the experimental variations. However, as we used values of the adatom-substrate exchange coupling obtained from a model considering only a single electron channel for our scaling equation we concluded that those differences arise from effects of multiple electron channels contributing. Here, for example, the symmetry of the respective d-orbitals could play a role in if and how strong the respective channels contribute to the renormalization.

Finally, we looked at Ethyl-DADQ molecules on both a bare Au(111) substrate and MoS_2.

We found that the molecules self-assemble in chains of varying width. The characterisation of the molecules on Au(111) showed that the intrinsic intramolecular dipole of the molecules is still preserved upon adsorption. Moreover, a local lowering of the LCPD was found over the molecules in comparison to the Au(111) substrate, which we assigned to a local scale push-back effect. The preservation of the intramolecular dipole was found also on the MoS_2. Moreover the improved energy resolution allowed the observation of several vibronic and vibration-assisted tunnelling processes related to the HOMO of the molecules. These satellite peaks and their intensity varied drastically depending on the electrostatic environment of the probed molecule, suggesting a significant damping of certain vibrations. We speculate that especially vibrations with a dipolar character are affected.

We have seen that the MoS_2/Au(111) interface is a very intriguing substrate to study. In case of the magnetic atoms, we have only scratched at certain parts of a very rich phase diagrams. For example, one could think of assembling circles of magnetic atoms on or around domes of the moiré or chains of atoms, which subsequently pass minima and maxima of the moiré. . There, it would not be clear how the interatomic exchange coupling or the observed renormalisation of the singlet-triplet excitation would look like. The high tunability of the iron atoms would make them also a prime candidate for temporal resolved measurements, as for example possible with a terahertz-STM [194, 235, 236]. Here the influence of the substrate on the lifetime of said excitations can be resolved directly. Also experiments involving the sulfur vacancies could be investigated with the aforementioned technique: in a pump-probe scheme an optical pulse could be used to heat the sample and perturb the Kondo state and a THz pulse could be than used to probe the reformation time of the many-body state. Defects with different Kondo temperatures could theoretically have different reformation times. For all this, besides its decoupling properties, the moiré superstructure of the MoS_2 layer is a very promising playground.

All in all, we found that fundamental properties of single atoms and molecules are extremely sensitive to their close environment. In certain cases this allows for a tunable control of those, but still more research has to be conducted to fully unravel the nature of the involved processes.

Bibliography

[1] G. Binnig, H. Rohrer, Ch. Gerber, and E. Weibel. Surface studies by scanning tunneling microscopy. *Phys. Rev. Lett.*, 49:57–61, 1982.

[2] G. Binnig, H. Rohrer, Ch. Gerber, and E. Weibel. Tunneling through a controllable vacuum gap. *Applied Physics Letters*, 40(2):178–180, 1982.

[3] G. Binnig, C. F. Quate, and Ch. Gerber. Atomic force microscope. *Physical Review Letters*, 56(9):930–933, 1986.

[4] V.V. Zhirnov, R.K. Cavin, J.A. Hutchby, and G.I. Bourianoff. Limits to binary logic switch scaling - a gedanken model. *Proceedings of the IEEE*, 91(11):1934–1939, 2003.

[5] J. Izydorczyk and M. Izydorczyk. Microprocessor scaling: What limits will hold? *Computer*, 43(8):20–26, 2010.

[6] M. Fuechsle, J. A. Miwa, S. Mahapatra, H. Ryu, S. Lee, O. Warschkow, L. C. L. Hollenberg, G. Klimeck, and M. Y. Simmons. A single-atom transistor. *Nature Nanotechnology*, 7(4):242–246, 2012.

[7] H. Song, Y. Kim, Y. H. Jang, H. Jeong, M. A. Reed, and T. Lee. Observation of molecular orbital gating. *Nature*, 462(7276):1039–1043, 2009.

[8] C. Schirm, M. Matt, F. Pauly, J. C. Cuevas, P. Nielaba, and E. Scheer. A current-driven single-atom memory. *Nature Nanotechnology*, 8(9):645–648, 2013.

[9] F. E. Kalff, M. P. Rebergen, E. Fahrenfort, J. Girovsky, R. Toskovic, J. L. Lado, J. Fernández-Rossier, and A. F. Otte. A kilobyte rewritable atomic memory. *Nature Nanotechnology*, 11(11):926–929, 2016.

[10] A. A. Khajetoorians, J. Wiebe, B. Chilian, and R. Wiesendanger. Realizing all-spin-based logic operations atom by atom. *Science*, 332(6033):1062–1064, 2011.

[11] S. Loth, S. Baumann, C. P. Lutz, D. M. Eigler, and A. J. Heinrich. Bistability in atomic-scale antiferromagnets. *Science*, 335(6065):196–199, 2012.

[12] S. Yan, D.-J. Choi, J. A. J. Burgess, S. Rolf-Pissarczyk, and S. Loth. Control of quantum magnets by atomic exchange bias. *Nature Nanotechnology*, 10(1):40–45, 2015.

[13] C. F. Hirjibehedin, C. P. Lutz, and A. J. Heinrich. Spin coupling in engineered atomic structures. *Science*, 312(5776):1021–1024, 2006.

[14] F. Donati, S. Rusponi, S. Stepanow, C. Wäckerlin, A. Singha, L. Persichetti, R. Baltic, K. Diller, F. Patthey, E. Fernandes, J. Dreiser, Ž. Šljivančanin, K. Kummer, C. Nistor, P. Gambardella, and H. Brune. Magnetic remanence in single atoms. *Science*, 352(6283):318–321, 2016.

[15] K. Greben, S. Arora, M. G. Harats, and K. I. Bolotin. Intrinsic and extrinsic defect-related excitons in TMDCs. *Nano Letters*, 20(4):2544–2550, 2020.

[16] X. Chen, L. Zhong, X. Li, and J. Qi. Valley splitting in the transition-metal dichalcogenide monolayer via atom adsorption. *Nanoscale*, 9:2188–2194, 2017.

[17] Y. Wang, B. Wang, R. Huang, B. Gao, F. Kong, and Q. Zhang. First-principles study of transition-metal atoms adsorption on MoS_2 monolayer. *Physica E: Low-dimensional Systems and Nanostructures*, 63:276–282, 2014.

[18] R. Wiesendanger, H.-J. Güntherodt, G. Güntherodt, R. J. Gambino, and R. Ruf. Observation of vacuum tunneling of spin-polarized electrons with the scanning tunneling microscope. *Phys. Rev. Lett.*, 65:247–250, 1990.

[19] R. M. Feenstra, Joseph A. Stroscio, J. Tersoff, and A. P. Fein. Atom-selective imaging of the GaAs(110) surface. *Phys. Rev. Lett.*, 58:1192–1195, 1987.

[20] L. J. Whitman, Joseph A. Stroscio, R. A. Dragoset, and R. J. Celotta. Scanning-tunneling-microscopy study of InSb(110). *Phys. Rev. B*, 42:7288–7291, 1990.

[21] N. D. Jäger, E. R. Weber, K. Urban, and Ph. Ebert. Importance of carrier dynamics and conservation of momentum in atom-selective stm imaging and band gap determination of GaAs(110). *Phys. Rev. B*, 67:165327, 2003.

[22] M. F. Crommie, C. P. Lutz, and D. M. Eigler. Imaging standing waves in a two-dimensional electron gas. *Nature*, 363(6429):524–527, 1993.

[23] M. F. Crommie, C. P. Lutz, and D. M. Eigler. Confinement of electrons to quantum corrals on a metal surface. *Science*, 262(5131):218–220, 1993.

[24] Ph. Avouris, I.-W. Lyo, and P. Molinàs-Mata. STM studies of the interaction of surface state electrons on metals with steps and adsorbates. *Chemical Physics Letters*, 240(5):423–428, 1995.

[25] B. C. Stipe, M. A. Rezaei, and W. Ho. Single-molecule vibrational spectroscopy and microscopy. *Science*, 280(5370):1732–1735, 1998.

[26] A. J. Heinrich, J. A. Gupta, C. P. Lutz, and D. M. Eigler. Single-atom spin-flip spectroscopy. *Science*, 306(5695):466–469, 2004.

[27] D. Rolf. *Fundamentals Properties of Atoms and Molecules on Surfaces: a combined STM and Shot-Noise Study*. PhD thesis, Freie Universitäet Berlin, 2018.

[28] I. Giaever and K. Megerle. Study of superconductors by electron tunneling. *Phys. Rev.*, 122:1101–1111, 1961.

[29] J. Bardeen. Tunnelling from a many-particle point of view. *Physical Review Letters*, 6(2):57–59, 1961.

[30] C. J. Chen. *Introduction to scanning tunneling microscopy*. Oxford University Press, 2007.

[31] J. Tersoff and D. R. Hamann. Theory and application for the scanning tunneling microscope. *Phys. Rev. Lett.*, 50:1998–2001, 1983.

[32] L. Gross, N. Moll, F. Mohn, A. Curioni, G. Meyer, F. Hanke, and M. Persson. High-resolution molecular orbital imaging using a π-wave STM tip. *Physical Review Letters*, 107(8):086101, 2011.

[33] N. Krane, C. Lotze, and K. J. Franke. Moiré structure of MoS_2 on Au(111): Local structural and electronic properties. *Surface Science*, 678:136–142, 2018. Surface Structure and Dynamics – in Honor of Karl-Heinz Rieder.

[34] M. Ziegler, N. Néel, A. Sperl, J. Kröger, and R. Berndt. Local density of states from constant-current tunneling spectra. *Phys. Rev. B*, 80:125402, 2009.

[35] Zurich Instruments. White paper: Principles of lock-in detection and state of the art, 2016.

[36] J. H. Scofield. Frequency-domain description of a lock-in amplifier. *American Journal of Physics*, 62(2):129–133, 1994.

[37] G. Reecht, B. W. Heinrich, H. Bulou, F. Scheurer, L. Limot, and G. Schull. Imaging isodensity contours of molecular states with STM. *New Journal of Physics*, 19(11):113033, 2017.

[38] L. Farinacci. *Tuning the Interactions of Magnetic Molecules on a Superconductor*. PhD thesis, Freie Universitäet Berlin, 2019.

[39] W. H. Weinberg. Inelastic electron tunneling spectroscopy: A probe of the vibrational structure of surface species. *Annual Review of Physical Chemistry*, 29(1):115–139, 1978.

[40] W. Ho. Single-molecule chemistry. *The Journal of Chemical Physics*, 117(24):11033–11061, 2002.

[41] N. Ohta, R. Arafune, N. Tsukahara, M. Kawai, and N. Takagi. Enhancement of inelastic electron tunneling conductance caused by electronic decoupling in iron phthalocyanine bilayer on Ag(111). *The Journal of Physical Chemistry C*, 117(42):21832–21837, 2013.

[42] D. Rolf, F. Maaß, C. Lotze, C. Czekelius, B. W. Heinrich, P. Tegeder, and K. J. Franke. Correlation of vibrational excitations and electronic structure with submolecular resolution. *The Journal of Physical Chemistry C*, 123(12):7425–7430, 2019.

[43] A.Yousofnejad, G. Reecht, N. Krane, C. Lotze, and K. J. Franke. Monolayers of MoS_2 on Ag(111) as decoupling layers for organic molecules: resolution of electronic and vibronic states of TCNQ. *Beilstein Journal of Nanotechnology*, 11:1062–1071, 2020.

[44] B. Verlhac, N. Bachellier, L. Garnier, M. Ormaza, P. Abufager, R. Robles, M.-L. Bocquet, M. Ternes, N. Lorente, and L. Limot. Atomic-scale spin sensing with a single molecule at the apex of a scanning tunneling microscope. *Science*, 366(6465):623–627, 2019.

[45] G. Czap, P. J. Wagner, F. Xue, L. Gu, J. Li, J. Yao, R. Wu, and W. Ho. Probing and imaging spin interactions with a magnetic single-molecule sensor. *Science*, 364(6441):670–673, 2019.

[46] F. J. Giessibl. Atomic resolution on Si(111)-(7×7) by noncontact atomic force microscopy with a force sensor based on a quartz tuning fork. *Applied Physics Letters*, 76(11):1470–1472, 2000.

[47] F. J. Giessibl. Advances in atomic force microscopy. *Rev. Mod. Phys.*, 75:949–983, 2003.

[48] F. J. Giessibl. Forces and frequency shifts in atomic-resolution dynamic-force microscopy. *Phys. Rev. B*, 56:16010–16015, 1997.

[49] J. E. Jones. On the determination of molecular fields. II. From the equation of state of a gas. *Proceedings of the Royal Society of London. Series A*, 106(738):463, 1924.

[50] L. Gross, F. Mohn, N. Moll, P. Liljeroth, and G. Meyer. The chemical structure of a molecule resolved by atomic force microscopy. *Science*, 325(5944):1110, 2009.

[51] C. Lotze. *Fundamental Processes in Single Molecule Juncions: Interplay of Forces and Electronic Effects*. PhD thesis, Freie Universitäet Berlin, 2013.

[52] J. N. Israelachvili. 5 - interactions involving the polarization of molecules. In *Intermolecular and Surface Forces (Third Edition)*, pages 91–106. Academic Press, Boston, third edition edition, 2011.

[53] J. N. Israelachvili. 6 - van der waals forces. In *Intermolecular and Surface Forces (Third Edition)*, pages 107–132. Academic Press, Boston, third edition edition, 2011.

[54] H.C. Hamaker. The London—van der Waals attraction between spherical particles. *Physica*, 4(10):1058–1072, 1937.

[55] C. Argento and R. H. French. Parametric tip model and force–distance relation for Hamaker constant determination from atomic force microscopy. *Journal of Applied Physics*, 80(11):6081–6090, 1996.

[56] J. Lü, M. Guggisberg, R. Lüthi, M. Kubon, L. Scandella, C. Gerber, E. Meyer, and H.-J. Güntherodt. Surface potential studies using Kelvin force spectroscopy. *Applied Physics A*, 66(1):S273–S275, 1998.

[57] S. A. Burke, J. M. LeDue, Y. Miyahara, J. M. Topple, S. Fostner, and P. Grütter. Determination of the local contact potential difference of PTCDA on NaCl: a comparison of techniques. *Nanotechnology*, 20(26):264012, 2009.

[58] L. Gross, F. Mohn, P. Liljeroth, J. Repp, F. J. Giessibl, and G. Meyer. Measuring the charge state of an adatom with noncontact atomic force microscopy. *Science*, 324(5933):1428–1431, 2009.

[59] F. Mohn, L. Gross, N. Moll, and G. Meyer. Imaging the charge distribution within a single molecule. *Nature Nanotechnology*, 7(4):227–231, 2012.

[60] F. Albrecht, J. Repp, M. Fleischmann, M. Scheer, M. Ondráček, and P. Jelínek. Probing charges on the atomic scale by means of atomic force microscopy. *Phys. Rev. Lett.*, 115:076101, 2015.

[61] M. Ruby. Spectrafox: A free open-source data management and analysis tool for scanning probe microscopy and spectroscopy. *SoftwareX*, 5:31–36, 2016.

[62] I. Horcas, R. Fernández, J. M. Gómez-Rodríguez, J. Colchero, J. Gómez-Herrero, and A. M. Baro. Wsxm: A software for scanning probe microscopy and a tool for nanotechnology. *Review of Scientific Instruments*, 78(1):013705, 2007.

[63] F. Reinert, G. Nicolay, S. Schmidt, D. Ehm, and S. Hüfner. Direct measurements of the l-gap surface states on the (111) face of noble metals by photoelectron spectroscopy. *Phys. Rev. B*, 63:115415, 2001.

[64] B. Radisavljevic, A. Radenovic, J. Brivio, V. Giacometti, and A. Kis. Single-layer MoS_2 transistors. *Nature Nanotechnology*, 6(3):147–150, 2011.

[65] C. Gong, L. Colombo, R. M. Wallace, and K. Cho. The unusual mechanism of partial Fermi level pinning at metal–MoS_2 interfaces. *Nano Letters*, 14(4):1714–1720, 2014.

[66] M. S. El-Bana, D. Wolverson, S. Russo, G. Balakrishnan, Don M. Paul, and S. J. Bending. Superconductivity in two-dimensional $NbSe_2$ field effect transistors. *Superconductor Science and Technology*, 26(12):125020, 2013.

[67] W. Ruan, Y. Chen, S. Tang, J. Hwang, H.-Z. Tsai, R. L. Lee, M. Wu, H. Ryu, S. Kahn, F. Liou, C. Jia, A. Aikawa, C. Hwang, F. Wang, Y. Choi, S. G. Louie, P. A. Lee, Z.-X. Shen, S.-K. Mo, and M. F. Crommie. Evidence for quantum spin liquid behaviour in single-layer 1T-$TaSe_2$ from scanning tunnelling microscopy. *Nature Physics*, 17(10):1154–1161, 2021.

[68] R. Coehoorn, C. Haas, J. Dijkstra, C. J. F. Flipse, R. A. de Groot, and A. Wold. Electronic structure of $MoSe_2$, MoS_2, and WSe_2. i. Band-structure calculations and photoelectron spectroscopy. *Phys. Rev. B*, 35:6195–6202, 1987.

[69] K. K. Kam and B. A. Parkinson. Detailed photocurrent spectroscopy of the semiconducting group vib transition metal dichalcogenides. *The Journal of Physical Chemistry*, 86(4):463–467, 1982.

[70] A. K. Geim and I. V. Grigorieva. Van-der-Waals heterostructures. *Nature*, 499(7459):419–425, 2013.

[71] X. Li and H. Zhu. Two-dimensional MoS_2: Properties, preparation, and applications. *Journal of Materiomics*, 1(1):33–44, 2015.

[72] T. Cheiwchanchamnangij and W. R. L. Lambrecht. Quasiparticle band structure calculation of monolayer, bilayer, and bulk MoS_2. *Phys. Rev. B*, 85:205302, 2012.

[73] A. Splendiani, L. Sun, Y. Zhang, T. Li, J. Kim, G. Chim, C.-Y.and Galli, and F. Wang. Emerging photoluminescence in monolayer MoS_2. *Nano Letters*, 10(4):1271–1275, 2010.

[74] K. F. Mak, C. Lee, J. Hone, J. Shan, and T. F. Heinz. Atomically thin MoS$_2$: A new direct-gap semiconductor. *Phys. Rev. Lett.*, 105:136805, 2010.

[75] M. V. Bollinger, J. V. Lauritsen, K. W. Jacobsen, J. K. Nørskov, S. Helveg, and F. Besenbacher. One-Dimensional Metallic Edge States in *MoS$_2$*. *Physical Review Letters*, 87(19):196803, 2001.

[76] S. Helveg, J. V. Lauritsen, E. Lægsgaard, I. Stensgaard, J. K. Nørskov, B. S. Clausen, H. Topsøe, and F. Besenbacher. Atomic-scale structure of single-layer MoS$_2$ nanoclusters. *Phys. Rev. Lett.*, 84:951–954, 2000.

[77] S. S. Grønborg, S. Ulstrup, M. Bianchi, M. Dendzik, C. E. Sanders, J. V. Lauritsen, P. Hofmann, and J. A. Miwa. Synthesis of epitaxial singl-layer MoS$_2$ on Au(111). *Langmuir*, 31(35):9700–9706, 2015.

[78] S. G. Sørensen, H. G. Füchtbauer, A. K. Tuxen, A. S. Walton, and J. V. Lauritsen. Structure and electronic properties of in situ synthesized single-layer MoS$_2$ on a gold surface. *ACS Nano*, 8(7):6788–6796, 2014.

[79] A. Bruix, J. A. Miwa, N. Hauptmann, D. Wegner, S. Ulstrup, S. S. Grønborg, C. E. Sanders, M. Dendzik, A. Grubišić Čabo, M. Bianchi, J. V. Lauritsen, A. A. Khajetoorians, B. Hammer, and P. Hofmann. Single-layer MoS$_2$ on Au(111): Band gap renormalization and substrate interaction. *Physical Review B*, 93(16):165422, 2016.

[80] J. A. Miwa, S. Ulstrup, S. G. Sørensen, M. Dendzik, A. Grubišić Čabo, M. Bianchi, J. V. Lauritsen, and P. Hofmann. Electronic structure of epitaxial single-layer MoS$_2$. *Phys. Rev. Lett.*, 114:046802, 2015.

[81] A. Grubišić Čabo, J. A. Miwa, S. S. Grønborg, J. M. Riley, J. C. Johannsen, C. Cacho, O. Alexander, R. T. Chapman, E. Springate, M. Grioni, J. V. Lauritsen, P. D. C. King, P. Hofmann, and S. Ulstrup. Observation of ultrafast free carrier dynamics in single layer MoS$_2$. *Nano Letters*, 15(9):5883–5887, 2015.

[82] N. Krane, C. Lotze, G. Reecht, L. Zhang, A. L. Briseno, and K. J. Franke. High-resolution vibronic spectra of molecules on molybdenum disulfide allow for rotamer identification. *ACS Nano*, 12(11):11698–11703, 2018.

[83] G. Reecht, N. Krane, C. Lotze, and K J. Franke. π-radical formation by pyrrolic h abstraction of phthalocyanine molecules on molybdenum disulfide. *ACS Nano*, 13(6):7031–7035, 2019.

[84] G. Reecht, N. Krane, C. Lotze, L. Zhang, A. L. Briseno, and K. J. Franke. Vibrational excitation mechanism in tunneling spectroscopy beyond the Franck-Condon model. *Phys. Rev. Lett.*, 124:116804, 2020.

[85] H. Bana, E. Travaglia, L. Bignardi, P. Lacovig, C. E. Sanders, M. Dendzik, M. Michiardi, M. Bianchi, D. Lizzit, F. Presel, D. De Angelis, N. Apostol, P. Kumar Das, J. Fujii, I. Vobornik, R. Larciprete, A. Baraldi, P. Hofmann, and S. Lizzit. Epitaxial growth of single-orientation high-quality MoS$_2$ monolayers. *2D Materials*, 5(3):035012, 2018.

[86] D. Yang, S. Jiménez Sandoval, W. M. R. Divigalpitiya, J. C. Irwin, and R. F. Frindt. Structure of single-molecular-layer MoS$_2$. *Phys. Rev. B*, 43:12053–12056, 1991.

[87] C. Zhang, Y. Chen, A. Johnson, M.-Y. Li, L.-J. Li, P. C. Mende, R. M. Feenstra, and C.-K. Shih. Probing critical point energies of transition metal dichalcogenides: Surprising indirect gap of single layer WSe$_2$. *Nano Letters*, 15(10):6494–6500, 2015.

[88] C. C. Silva, D. Dombrowski, N. Atodiresei, W. Jolie, F. F. zum Hagen, J. Cai, P. T. P. Ryan, P. K. Thakur, V. Caciuc, S. Blügel, D. A. Duncan, T. Michely, T.-L. Lee, and C. Busse. Spatial variation of geometry, binding, and electronic properties in the moiré superstructure of MoS$_2$ on au(111). *2D Materials*, 9(2):025003, 2022.

[89] Jean-Pierre Gauyacq, Nicolás Lorente, and Frederico Dutilh Novaes. Excitation of local magnetic moments by tunneling electrons. *Progress in Surface Science*, 87(5):63–107, 2012.

[90] D. Dai, H. Xiang, and M.-H. Whangbo. Effects of spin-orbit coupling on magnetic properties of discrete and extended magnetic systems. *Journal of Computational Chemistry*, 29(13):2187–2209, 2008.

[91] H.A Kramers. L'interaction entre les atomes magnétogènes dans un cristal paramagnétique. *Physica*, 1(1):182–192, 1934.

[92] P. W. Anderson. Antiferromagnetism. Theory of superexchange interaction. *Phys. Rev.*, 79:350–356, 1950.

[93] C. G. Barraclough, R. L. Martin, S. Mitra, and R. C. Sherwood. Paramagnetic anisotropy, electronic structure, and ferromagnetism in spin $SFIXME = 32$ manganese(II) phthalocyanine. *The Journal of Chemical Physics*, 53(5):1638–1642, 1970.

[94] H. Yamada, T. Shimada, and A. Koma. Preparation and magnetic properties of manganese(II) phthalocyanine thin films. *The Journal of Chemical Physics*, 108(24):10256–10261, 1998.

[95] X. Chen, Y.-S. Fu, S.-H. Ji, T. Zhang, P. Cheng, X.-C. Ma, X.-L. Zou, W.-H. Duan, J.-F. Jia, and Q.-K. Xue. Probing superexchange interaction in molecular magnets by spin-flip spectroscopy and microscopy. *Phys. Rev. Lett.*, 101:197208, 2008.

[96] M. A. Ruderman and C. Kittel. Indirect exchange coupling of nuclear magnetic moments by conduction electrons. *Phys. Rev.*, 96:99–102, 1954.

[97] T. Kasuya. A theory of metallic ferro- and antiferromagnetism on Zener's model. *Progress of Theoretical Physics*, 16(1):45–57, 1956.

[98] K. Yosida. Magnetic properties of Cu-Mn alloys. *Phys. Rev.*, 106:893–898, 1957.

[99] F. Delgado and J. Fernández-Rossier. RKKY oscillations in the spin relaxation rates of atomic-scale nanomagnets. *Phys. Rev. B*, 95:075413, 2017.

[100] L. Zhou, J. Wiebe, S. Lounis, E. Vedmedenko, F. Meier, S. Blügel, P. H. Dederichs, and R. Wiesendanger. Strength and directionality of surface Ruderman–Kittel–Kasuya–Yosida interaction mapped on the atomic scale. *Nature Physics*, 6(3):187–191, 2010.

[101] P. Wahl, P. Simon, L. Diekhöner, V. S. Stepanyuk, P. Bruno, M. A. Schneider, and K. Kern. Exchange interaction between single magnetic adatoms. *Phys. Rev. Lett.*, 98:056601, 2007.

[102] W.J. de Haas, J. de Boer, and G.J. van dën Berg. The electrical resistance of gold, copper and lead at low temperatures. *Physica*, 1(7):1115–1124, 1934.

[103] J. Kondo. Resistance minimum in dilute magnetic alloys. *Progress of Theoretical Physics*, 32(1):37–49, 1964.

[104] J. Kondo. Effect of ordinary scattering on exchange scattering from magnetic impurity in metals. *Phys. Rev.*, 169:437–440, 1968.

[105] C. Zener. Interaction between the d shells in the transition metals. *Phys. Rev.*, 81:440–444, 1951.

[106] A. C. Hewson. *Models of Magnetic Impurities*, page 1–28. Cambridge Studies in Magnetism. Cambridge University Press, 1993.

[107] P. W. Anderson. Localized magnetic states in metals. *Phys. Rev.*, 124:41–53, 1961.

[108] Markus Ternes, Andreas J Heinrich, and Wolf-Dieter Schneider. Spectroscopic manifestations of the kondo effect on single adatoms. *Journal of Physics: Condensed Matter*, 21(5):053001, 2008.

[109] L. Kouwenhoven and L. Glazman. Revival of the Kondo effect. *Physics World*, 14(1):33, 2001.

[110] J. R. Schrieffer and P. A. Wolff. Relation between the Anderson and Kondo hamiltonians. *Phys. Rev.*, 149:491–492, 1966.

[111] M. Ternes. Probing magnetic excitations and correlations in single and coupled spin systems with scanning tunneling spectroscopy. *Progress in Surface Science*, 92(1):83–115, 2017.

[112] P. W. Anderson. A poor man's derivation of scaling laws for the Kondo problem. *Journal of Physics C: Solid State Physics*, 3(12):2436, 1970.

[113] K. G. Wilson. The renormalization group: Critical phenomena and the Kondo problem. *Rev. Mod. Phys.*, 47:773–840, 1975.

[114] N. Andrei. Diagonalization of the Kondo Hamiltonian. *Phys. Rev. Lett.*, 45:379–382, 1980.

[115] V. Madhavan, W. Chen, T. Jamneala, M. F. Crommie, and N. S. Wingreen. Tunneling into a single magnetic atom: Spectroscopic evidence of the Kondo resonance. *Science*, 280(5363):567–569, 1998.

[116] R. Žitko, R. Peters, and Th. Pruschke. Properties of anisotropic magnetic impurities on surfaces. *Phys. Rev. B*, 78:224404, 2008.

[117] O. Újsághy, J. Kroha, L. Szunyogh, and A. Zawadowski. Theory of the Fano resonance in the STM tunneling density of states due to a single Kondo impurity. *Phys. Rev. Lett.*, 85:2557–2560, 2000.

[118] J. Li, W.-D. Schneider, R. Berndt, and B. Delley. Kondo scattering observed at a single magnetic impurity. *Phys. Rev. Lett.*, 80:2893–2896, 1998.

[119] H. C. Manoharan, C. P. Lutz, and D. M. Eigler. Quantum mirages formed by coherent projection of electronic structure. *Nature*, 403(6769):512–515, 2000.

[120] T. Jamneala, V. Madhavan, W. Chen, and M. F. Crommie. Scanning tunneling spectroscopy of transition-metal impurities at the surface of gold. *Phys. Rev. B*, 61:9990–9993, 2000.

[121] N. Knorr, M. A. Schneider, L. Diekhöner, P. Wahl, and K. Kern. Kondo effect of single Co adatoms on Cu surfaces. *Phys. Rev. Lett.*, 88:096804, 2002.

[122] U. Fano. Effects of configuration interaction on intensities and phase shifts. *Phys. Rev.*, 124:1866–1878, 1961.

[123] S. Frank and D. Jacob. Orbital signatures of Fano-Kondo line shapes in STM adatom spectroscopy. *Phys. Rev. B*, 92:235127, 2015.

[124] L. Farinacci, G. Ahmadi, M. Ruby, G. Reecht, B. W. Heinrich, C. Czekelius, F. von Oppen, and K. J. Franke. Interfering tunneling paths through magnetic molecules on superconductors: Asymmetries of Kondo and Yu-Shiba-Rusinov resonances. *Phys. Rev. Lett.*, 125:256805, 2020.

[125] H. O. Frota and L. N. Oliveira. Photoemission spectroscopy for the spin-degenerate anderson model. *Phys. Rev. B*, 33:7871–7874, 1986.

[126] H. O. Frota. Shape of the Kondo resonance. *Phys. Rev. B*, 45:1096–1099, 1992.

[127] H. Prüser, M. Wenderoth, P. E. Dargel, A. Weismann, R. Peters, T. Pruschke, and R. G. Ulbrich. Long-range Kondo signature of a single magnetic impurity. *Nature Physics*, 7(3):203–206, 2011.

[128] H. Prüser, M. Wenderoth, A. Weismann, and R. G. Ulbrich. Mapping itinerant electrons around Kondo impurities. *Phys. Rev. Lett.*, 108:166604, 2012.

[129] M. Gruber, A. Weismann, and R. Berndt. The Kondo resonance line shape in scanning tunnelling spectroscopy: instrumental aspects. *Journal of Physics: Condensed Matter*, 30(42):424001, 2018.

[130] M. Ternes. Spin excitations and correlations in scanning tunneling spectroscopy. *New Journal of Physics*, 17(6):063016, 2015.

[131] J. Appelbaum. "$s - d$" exchange model of zero-bias tunneling anomalies. *Phys. Rev. Lett.*, 17:91–95, 1966.

[132] J. A. Appelbaum. Exchange model of zero-bias tunneling anomalies. *Phys. Rev.*, 154:633–643, 1967.

[133] P. W. Anderson. Localized magnetic states and Fermi-surface anomalies in tunneling. *Phys. Rev. Lett.*, 17:95–97, 1966.

[134] P. Gentile, L. De Leo, M. Fabrizio, and E. Tosatti. Lack of Kondo screening at nanocontacts of nearly magnetic metals. *Europhysics Letters*, 87(2):27014, 2009.

[135] Y.-H. Zhang, S. Kahle, T. Herden, C. Stroh, M. Mayor, U. Schlickum, M. Ternes, P. Wahl, and K. Kern. Temperature and magnetic field dependence of a Kondo system in the weak coupling regime. *Nature Communications*, 4(1):2110, 2013.

[136] K. Nagaoka, T. Jamneala, M. Grobis, and M. F. Crommie. Temperature dependence of a single Kondo impurity. *Phys. Rev. Lett.*, 88:077205, 2002.

[137] Alexander F. Otte, Markus Ternes, Kirsten von Bergmann, Sebastian Loth, Harald Brune, Christopher P. Lutz, Cyrus F. Hirjibehedin, and Andreas J. Heinrich. The role of magnetic anisotropy in the Kondo effect. *Nature Physics*, 4(11):847–850, 2008.

[138] S. M. Cronenwett, T. H. Oosterkamp, and L. P. Kouwenhoven. A tunable Kondo effect in quantum dots. *Science*, 281(5376):540–544, 1998.

[139] R. Žitko, R. Peters, and Th. Pruschke. Splitting of the Kondo resonance in anisotropic magnetic impurities on surfaces. *New Journal of Physics*, 11(5):053003, 2009.

[140] L. Liu, K. Yang, Y. Jiang, B. Song, W. Xiao, S. Song, S. Du, M. Ouyang, W. A. Hofer, A. H. Castro Neto, and H.-J. Gao. Revealing the atomic site-dependent g factor within a single magnetic molecule via the extended Kondo effect. *Phys. Rev. Lett.*, 114:126601, 2015.

[141] T. A. Costi. Kondo effect in a magnetic field and the magnetoresistivity of Kondo alloys. *Phys. Rev. Lett.*, 85:1504–1507, 2000.

[142] T. O. Wehling, A. V. Balatsky, M. I. Katsnelson, A. I. Lichtenstein, and A. Rosch. Orbitally controlled Kondo effect of Co adatoms on graphene. *Phys. Rev. B*, 81:115427, 2010.

[143] K. von Bergmann, M. Ternes, S. Loth, C. P. Lutz, and A. J. Heinrich. Spin polarization of the split Kondo state. *Phys. Rev. Lett.*, 114:076601, 2015.

[144] A. F. Otte. *Magnetism of a Single Atom*. PhD thesis, Leiden University, 2008.

[145] P. Jacobson, T. Herden, M. Muenks, G. Laskin, O. Brovko, V. Stepanyuk, M. Ternes, and K. Kern. Quantum engineering of spin and anisotropy in magnetic molecular junctions. *Nature Communications*, 6(1):8536, 2015.

[146] J. C. Oberg, M. R. Calvo, F. Delgado, M. Moro-Lagares, D. Serrate, J. Fernandez-Rossier, and C. F. Hirjibehedin. Control of single-spin magnetic anisotropy by exchange coupling. *Nat. Nanotech.*, 9:64–68, 2014.

[147] F. Delgado, C.F. Hirjibehedin, and J. Fernández-Rossier. Consequences of Kondo exchange on quantum spins. *Surface Science*, 630:337–342, 2014.

[148] S. Ding, F. Lin, and C. Jin. Quantify point defects in monolayer tungsten diselenide. *Nanotechnology*, 32(25):255701, 2021.

[149] S. KC, R. C. Longo, R. Addou, R. M. Wallace, and K. Cho. Impact of intrinsic atomic defects on the electronic structure of MoS_2 monolayers. *Nanotechnology*, 25(37):375703, 2014.

[150] H. Nan, Z. Wang, W. Wang, Z. Liang, Y. Lu, Q. Chen, D. He, P. Tan, F. Miao, X. Wang, J. Wang, and Z. Ni. Strong photoluminescence enhancement of MoS_2 through defect engineering and oxygen bonding. *ACS Nano*, 8(6):5738–5745, 2014.

[151] P. K. Chow, R. B. Jacobs-Gedrim, J. Gao, T.-M. Lu, B. Yu, H. Terrones, and N. Koratkar. Defect-induced photoluminescence in monolayer semiconducting transition metal dichalcogenides. *ACS Nano*, 9(2):1520–1527, 2015.

[152] Y.-C. Lin, S. Li, H.-P. Komsa, L.-J. Chang, A. V. Krasheninnikov, G. Eda, and K. Suenaga. Revealing the atomic defects of WS_2 governing its distinct optical emissions. *Advanced Functional Materials*, 28(4):1704210, 2018.

[153] E. Mitterreiter, B. Schuler, A. Micevic, D. Hernangómez-Pérez, K. Barthelmi, K. A. Cochrane, J. Kiemle, F. Sigger, J. Klein, E. Wong, E. S. Barnard, K. Watanabe, T. Taniguchi, M. Lorke, F. Jahnke, J. J. Finley, A. M. Schwartzberg, D. Y. Qiu, S. Refaely-Abramson, A. W. Holleitner, A. Weber-Bargioni, and C. Kastl. The role of chalcogen vacancies for atomic defect emission in MoS_2 . *Nature Communications*, 12(1):3822, 2021.

[154] Y. Lin, E. Hathaway, F. Habis, Y. Wang, R. G. Rodriguez, K. Alnasser, N. Hurley, and J. Cui. Enhanced emission from defect levels in multilayer MoS_2. *Advanced Optical Materials*, 10(19):2201059, 2022.

[155] S.-S. Chee, W.-J. Lee, Y.-R. Jo, M. K. Cho, D. Chun, H. Baik, B.-J. Kim, M.-H. Yoon, K. Lee, and M.-H. Ham. Atomic vacancy control and elemental substitution in a monolayer molybdenum disulfide for high performance optoelectronic device arrays. *Advanced Functional Materials*, 30(11):1908147, 2020.

[156] J. Yang, F. Bussolotti, H. Kawai, and K. E. J. Goh. Tuning the conductivity type in monolayer WS_2 and MoS_2 by sulfur vacancies. *physica status solidi (RRL) – Rapid Research Letters*, 14(9):2000248, 2020.

[157] E. C. Ahn. 2D materials for spintronic devices. *npj 2D Materials and Applications*, 4(1):17, 2020.

[158] T. D. Nguyen, J. Jiang, B. Song, M. D. Tran, W. Choi, J. H. Kim, Y.-M. Kim, D. L. Duong, and Y. H. Lee. Gate-tunable magnetism via resonant Se-vacancy levels in WSe_2 . *Advanced Science*, 8(24):2102911, 2021.

[159] A. M. Z. Tan, C. Freysoldt, and R. G. Hennig. Stability of charged sulfur vacancies in 2d and bulk MoS_2 from plane-wave density functional theory with electrostatic corrections. *Phys. Rev. Mater.*, 4:064004, 2020.

[160] H.-P. Komsa and A. V. Krasheninnikov. Native defects in bulk and monolayer MoS_2 from first principles. *Phys. Rev. B*, 91:125304, 2015.

[161] J. A. Robinson and B. Schuler. Engineering and probing atomic quantum defects in 2D semiconductors: A perspective. *Applied Physics Letters*, 119(14):140501, 2021.

[162] W. Zhou, X. Zou, S. Najmaei, Z. Liu, Y. Shi, J. Kong, J. Lou, P. M. Ajayan, B. I. Yakobson, and J.-C. Idrobo. Intrinsic structural defects in monolayer molybdenum disulfide. *Nano Letters*, 13(6):2615–2622, 2013.

[163] F. Tumino, C. S. Casari, A. Li Bassi, and S. Tosoni. Nature of point defects in single-layer MoS_2 supported on Au(111). *The Journal of Physical Chemistry C*, 124(23):12424–12431, 2020.

[164] B. Schuler, D. Y. Qiu, S. Refaely-Abramson, C. Kastl, C. T. Chen, S. Barja, R. J. Koch, D. F. Ogletree, S. Aloni, A. M. Schwartzberg, J. B. Neaton, S. G. Louie, and A. Weber-Bargioni. Large spin-orbit splitting of deep in-gap defect states of engineered sulfur vacancies in monolayer WS_2. *Phys. Rev. Lett.*, 123:076801, 2019.

[165] P. Vancsó, G. Z. Magda, J. Pető, J.-Y. Noh, Y.-S. Kim, C. Hwang, L. P. Biró, and L. Tapasztó. The intrinsic defect structure of exfoliated MoS_2 single layers revealed by Scanning Tunneling Microscopy. *Scientific Reports*, 6(1):29726, 2016.

[166] D. Hernangómez-Pérez, A. Donarini, and S. Refaely-Abramson. Charge quenching at defect states in transition metal dichalcogenide–graphene van-der-waals heterobilayers. *Phys. Rev. B*, 107:075419, 2023.

[167] I. Fernández-Torrente, K. J. Franke, and J. I. Pascual. Vibrational Kondo effect in pure organic charge-transfer assemblies. *Phys. Rev. Lett.*, 101:217203, 2008.

[168] K. A. Cochrane, J.-H. Lee, C. Kastl, J. B. Haber, T. Zhang, A. Kozhakhmetov, J. A. Robinson, M. Terrones, J. Repp, J. B. Neaton, A. Weber-Bargioni, and B. Schuler. Spin-dependent vibronic response of a carbon radical ion in two-dimensional WS_2. *Nature Communications*, 12(1):7287, 2021.

[169] S. Barja, S. Refaely-Abramson, B. Schuler, D. Y. Qiu, A. Pulkin, S. Wickenburg, H. Ryu, M. M. Ugeda, C. Kastl, C. Chen, C. Hwang, A. Schwartzberg, S. Aloni, S.-K. Mo, D. Frank Ogletree, M. F. Crommie, O. V. Yazyev, S. G. Louie, J. B. Neaton, and A. Weber-Bargioni. Identifying substitutional oxygen as a prolific point defect in monolayer transition metal dichalcogenides. *Nature Communications*, 10(1):3382, 2019.

[170] N. Krane, C. Lotze, J. M. Läger, G. Reecht, and K. J Franke. Electronic structure and luminescence of quasi-freestanding MoS_2 nanopatches on Au(111). *Nano Letters*, 16(8):5163–5168, 2016.

[171] P. Nozières. A "fermi-liquid" description of the Kondo problem at low temperatures. *Journal of Low Temperature Physics*, 17(1):31–42, 1974.

[172] K. Yang, W. Paul, F. D. Natterer, J. L. Lado, Y. Bae, P. Willke, T. Choi, A. Ferrón, J. Fernández-Rossier, A. J. Heinrich, and C. P. Lutz. Tuning the exchange bias on a single atom from 1 mT to 10 T. *Phys. Rev. Lett.*, 122:227203, 2019.

[173] P. Willke, W. Paul, F. D. Natterer, K. Yang, Y. Bae, T. Choi, J. Fernández-Rossier, A. J. Heinrich, and C. P. Lutz. Probing quantum coherence in single-atom electron spin resonance. *Science Advances*, 4(2):eaaq1543, 2018.

[174] A. A. Khajetoorians, S. Lounis, B. Chilian, A. T. Costa, L. Zhou, D. L. Mills, J. Wiebe, and R. Wiesendanger. Itinerant nature of atom-magnetization excitation by tunneling electrons. *Phys. Rev. Lett.*, 106:037205, 2011.

[175] A. A. Khajetoorians, T. Schlenk, B. Schweflinghaus, M. dos Santos Dias, M. Steinbrecher, M. Bouhassoune, S. Lounis, J. Wiebe, and R. Wiesendanger. Spin excitations of individual Fe atoms on Pt(111): Impact of the site-dependent giant substrate polarization. *Phys. Rev. Lett.*, 111:157204, 2013.

[176] F. D. Natterer, F. Donati, F. Patthey, and H. Brune. Thermal and magnetic-field stability of holmium single-atom magnets. *Phys. Rev. Lett.*, 121:027201, 2018.

[177] Fabian D. Natterer, Kai Yang, William Paul, Philip Willke, Taeyoung Choi, Thomas Greber, Andreas J. Heinrich, and Christopher P. Lutz. Reading and writing single-atom magnets. *Nature*, 543(7644):226–228, 2017.

[178] F. Donati, Q. Dubout, G. Autès, F. Patthey, F. Calleja, P. Gambardella, O. V. Yazyev, and H. Brune. Magnetic moment and anisotropy of individual Co atoms on graphene. *Phys. Rev. Lett.*, 111:236801, 2013.

[179] R. Baltic, M. Pivetta, F. Donati, C. Wäckerlin, A. Singha, J. Dreiser, S. Rusponi, and H. Brune. Superlattice of single atom magnets on graphene. *Nano Letters*, 16(12):7610–7615, 2016.

[180] R. Turanský, K. Palotás, J. Brndiar, Y. J. Li, Y. Sugawara, and I. Štich. Subatomic-scale resolution with SPM: Co adatom on p(2 × 1)Cu(110):o. *Nanotechnology*, 30(9):095703, 2019.

[181] T. Balashov, T. Schuh, A. F. Takács, A. Ernst, S. Ostanin, J. Henk, I. Mertig, P. Bruno, T. Miyamachi, S. Suga, and W. Wulfhekel. Magnetic anisotropy and magnetization dynamics of individual atoms and clusters of Fe and Co on Pt(111). *Phys. Rev. Lett.*, 102:257203, 2009.

[182] J. Hermenau, M. Ternes, M. Steinbrecher, R. Wiesendanger, and J. Wiebe. Long spin-relaxation times in a transition-metal atom in direct contact to a metal substrate. *Nano Letters*, 18(3):1978–1983, 2018.

[183] S. Trishin, C. Lotze, N. Bogdanoff, F. von Oppen, and K. J. Franke. Moiré tuning of spin excitations: Individual Fe atoms on MoS_2 Au(111). *Phys. Rev. Lett.*, 127:236801, 2021.

[184] D. Jacob. Renormalization of single-ion magnetic anisotropy in the absence of the Kondo effect. *Phys. Rev. B*, 97:075428, 2018.

[185] A. Schiller and S. Hershfield. Theory of scanning tunneling spectroscopy of a magnetic adatom on a metallic surface. *Phys. Rev. B*, 61:9036–9046, 2000.

[186] J. Fernández, P. Roura-Bas, and A. A. Aligia. Theory of differential conductance of Co on Cu(111) including Co s and d orbitals, and surface and bulk Cu states. *Phys. Rev. Lett.*, 126:046801, 2021.

[187] M. S. Tacca, T. Jacob, and E. C. Goldberg. Influence of surface states on the conductance spectra for Co adsorbed on Cu(111). *Phys. Rev. B*, 103:245419, 2021.

[188] C. Rubio-Verdú, A. Sarasola, D.-J. Choi, Z. Majzik, R. Ebeling, M. R. Calvo, M. M. Ugeda, A. Garcia-Lekue, D. Sánchez-Portal, and J. I. Pascual. Orbital-selective spin excitation of a magnetic porphyrin. *Communications Physics*, 1(1):15, 2018.

[189] F. Delgado and J. Fernández-Rossier. Spin decoherence of magnetic atoms on surfaces. *Progress in Surface Science*, 92(1):40–82, 2017.

[190] S. Loth, K. von Bergmann, M. Ternes, A. F. Otte, C. P. Lutz, and A. J. Heinrich. Controlling the state of quantum spins with electric currents. *Nature Physics*, 6(5):340–344, 2010.

[191] S. Loth, M. Etzkorn, C. P. Lutz, D. M. Eigler, and A. J. Heinrich. Measurement of fast electron spin relaxation times with atomic resolution. *Science*, 329(5999):1628–1630, 2010.

[192] W. Paul, K. Yang, S. Baumann, N. Romming, T. Choi, C. P. Lutz, and A. J. Heinrich. Control of the millisecond spin lifetime of an electrically probed atom. *Nature Physics*, 13(4):403–407, 2017.

[193] T. L. Cocker, V. Jelic, M. Gupta, S. J. Molesky, J. A. J. Burgess, G. D. L. Reyes, L. V. Titova, Y. Y. Tsui, M. R. Freeman, and F. A. Hegmann. An ultrafast terahertz scanning tunnelling microscope. *Nature Photonics*, 7(8):620–625, 2013.

[194] T. L. Cocker, D. Peller, P. Yu, J. Repp, and R. Huber. Tracking the ultrafast motion of a single molecule by femtosecond orbital imaging. *Nature*, 539(7628):263–267.

[195] L. Farinacci, G. Ahmadi, G. Reecht, M. Ruby, N. Bogdanoff, O. Peters, B. W. Heinrich, F. von Oppen, and K. J. Franke. Tuning the coupling of an individual magnetic impurity to a superconductor: Quantum phase transition and transport. *Phys. Rev. Lett.*, 121:196803, 2018.

[196] Q. Dubout, F. Donati, C. Wäckerlin, F. Calleja, M. Etzkorn, A. Lehnert, L. Claude, P. Gambardella, and H. Brune. Controlling the spin of Co atoms on Pt(111) by hydrogen adsorption. *Phys. Rev. Lett.*, 114:106807, 2015.

[197] C. F. Hirjibehedin, C.-Y. Lin, A. F. Otte, M. Ternes, C. P. Lutz, B. A. Jones, and A. J. Heinrich. Large magnetic anisotropy of a single atomic spin embedded in a surface molecular network. *Science*, 317(5842):1199–1203, 2007.

[198] B. Schuler, J.-H. Lee, C. Kastl, K. A. Cochrane, C. T. Chen, S. Refaely-Abramson, S. Yuan, E. van Veen, R. Roldán, N. J. Borys, R. J. Koch, S. Aloni, A. M. Schwartzberg, D. F. Ogletree, J. B. Neaton, and A. Weber-Bargioni. How substitutional point defects in two-dimensional WS_2 induce charge localization, spin–orbit splitting, and strain. *ACS Nano*, 13(9):10520–10534, 2019.

[199] B. Schuler, K. A. Cochrane, C. Kastl, E. S. Barnard, E. Wong, N. J. Borys, A. M. Schwartzberg, D. F.Ogletree, F. J. G. de Abajo, and A. Weber-Bargioni. Electrically driven photon emission from individual atomic defects in monolayer WS_2 . *Science Advances*, 6(38):eabb5988, 2020.

[200] M. Muenks, P. Jacobson, M. Ternes, and K. Kern. Correlation-driven transport asymmetries through coupled spins in a tunnel junction. *Nature Communications*, 8(1):14119, 2017.

[201] Y. Mokrousov, G. Bihlmayer, S. Blügel, and S. Heinze. Magnetic order and exchange interactions in monoatomic $3d$ transition-metal chains. *Phys. Rev. B*, 75:104413, 2007.

[202] A. Spinelli, M. Gerrits, R. Toskovic, B. Bryant, M. Ternes, and A. F. Otte. Exploring the phase diagram of the two-impurity Kondo problem. *Nature Communications*, 6(1):10046, 2015.

[203] A. F. Otte, M. Ternes, S. Loth, C. P. Lutz, C. F. Hirjibehedin, and A. J. Heinrich. Spin excitations of a Kondo-screened atom coupled to a second magnetic atom. *Phys. Rev. Lett.*, 103:107203, 2009.

[204] J. R. Schrieffer. The Kondo effect—the link between magnetic and nonmagnetic impurities in metals? *Journal of Applied Physics*, 38(3):1143–1150, 1967.

[205] S. Trishin, C. Lotze, F. Lohss, G. Franceschi, L. I. Glazman, F. von Oppen, and K. J. Franke. Tuning a two-impurity Kondo system by a moiré superstructure. *Phys. Rev. Lett.*, 130:176201, 2023.

[206] A. Aviram and M. A. Ratner. Molecular rectifiers. *Chemical Physics Letters*, 29(2):277–283, 1974.

[207] R. M. Metzger. Unimolecular electrical rectifiers. *Chemical Reviews*, 103(9):3803–3834, 2003.

[208] J. J. Bergkamp, S. Decurtins, and S.-X. Liu. Current advances in fused tetrathiafulvalene donor–acceptor systems. *Chem. Soc. Rev.*, 44:863–874, 2015.

[209] T. Meier, R. Pawlak, S. Kawai, Y. Geng, X. Liu, S. Decurtins, P. Hapala, A. Baratoff, S.-X. Liu, P. Jelínek, E. Meyer, and T. Glatzel. Donor–acceptor properties of a single-molecule altered by on-surface complex formation. *ACS Nano*, 11(8):8413–8420, 2017.

[210] F. Queck, F. Albrecht, P. Mutombo, O. Krejci, P. Jelínek, A. McLean, and J. Repp. Interface dipoles of Ir(ppy)3 on Cu(111). *Nanoscale*, 11:12695–12703, 2019.

[211] H. Ishii, K. Sugiyama, E. Ito, and K. Seki. Energy level alignment and interfacial electronic structures at organic/metal and organic/organic interfaces. *Advanced Materials*, 11(8):605–625, 1999.

[212] J. Repp, G. Meyer, S. M. Stojković, A. Gourdon, and C. Joachim. Molecules on insulating films: Scanning-tunneling microscopy imaging of individual molecular orbitals. *Phys. Rev. Lett.*, 94:026803, 2005.

[213] X. H. Qiu, G. V. Nazin, and W. Ho. Vibronic states in single molecule electron transport. *Phys. Rev. Lett.*, 92:206102, 2004.

[214] S. Kahle, Z. Deng, N. Malinowski, C. Tonnoir, A. Forment-Aliaga, N. Thontasen, G. Rinke, D. Le, V. Turkowski, T. S. Rahman, S. Rauschenbach, M. Ternes, and K. Kern. The quantum magnetism of individual manganese-12-acetate molecular magnets anchored at surfaces. *Nano Letters*, 12(1):518–521, 2012.

[215] F. Schulz, R. Drost, S. K. Hämäläinen, and P. Liljeroth. Templated self-assembly and local doping of molecules on epitaxial hexagonal boron nitride. *ACS Nano*, 7(12):11121–11128, 2013.

[216] S. Fatayer, B. Schuler, W. Steurer, I. Scivetti, J. Repp, L. Gross, M. Persson, and G. Meyer. Reorganization energy upon charging a single molecule on an insulator measured by atomic force microscopy. *Nature Nanotechnology*, 13(5):376–380, 2018.

[217] Y. Jing, X. Tan, Z. Zhou, and P. Shen. Tuning electronic and optical properties of MoS_2 monolayer via molecular charge transfer. *J. Mater. Chem. A*, 2:16892–16897, 2014.

[218] P. Rietsch, F. Witte, S. Sobottka, G. Germer, A. Krappe, A. Güttler, B.t Sarkar, B. Paulus, U. Resch-Genger, and S. Eigler. Diaminodicyanoquinones: Fluorescent dyes with high dipole moments and electron-acceptor properties. *Angewandte Chemie International Edition*, 58(24):8235–8239, 2019.

[219] S. Trishin, T. Müller, D. Rolf, C. Lotze, P. Rietsch, S. Eigler, B. Meyer, and K. J. Franke. Resolution of intramolecular dipoles and a push-back effect of individual molecules on a metal surface. *The Journal of Physical Chemistry C*, 126(17):7667–7673, 2022.

[220] J. van der Lit, F.a Di Cicco, P. Hapala, P. Jelinek, and I. Swart. Submolecular resolution imaging of molecules by atomic force microscopy: The influence of the electrostatic force. *Physical Review Letters*, 116(9):096102, 2016.

[221] I. F. Torrente, K. J. Franke, and J. I. Pascual. Spectroscopy of C60 single molecules: the role of screening on energy level alignment. *Journal of Physics: Condensed Matter*, 20(18):184001, 2008.

[222] N. Pavliček, I. Swart, J. Niedenführ, G. Meyer, and J. Repp. Symmetry dependence of vibration-assisted tunneling. *Phys. Rev. Lett.*, 110:136101, 2013.

[223] N. Koch, A. Kahn, J. Ghijsen, J.-J. Pireaux, J. Schwartz, R. L. Johnson, and A. Elschner. Conjugated organic molecules on metal versus polymer electrodes: Demonstration of a key energy level alignment mechanism. *Applied Physics Letters*, 82(1):70–72, 2002.

[224] A. Kahn, N. Koch, and W. Gao. Electronic structure and electrical properties of interfaces between metals and π-conjugated molecular films. *Journal of Polymer Science Part B: Polymer Physics*, 41(21):2529–2548, 2003.

[225] G. Heimel, L. Romaner, E. Zojer, and J.-L. Bredas. The interface energetics of self-assembled monolayers on metals. *Accounts of Chemical Research*, 41(6):721–729, 2008.

[226] S. Trishin, C. Lotze, J. Richter, G. Reecht, N. Krane, P. Rietsch, S. Eigler, and K. J. Franke. Variations of vibronic states in densely-packed structures of molecules with intramolecular dipoles. *physica status solidi (a)*, n/a(n/a), 2023.

[227] P. Hapala, G. Kichin, C. Wagner, F. S. Tautz, R. Temirov, and P. Jelínek. Mechanism of high-resolution STM/AFM imaging with functionalized tips. *Phys. Rev. B*, 90:085421, 2014.

[228] O. Krejčí, P. Hapala, M. Ondráček, and P. Jelínek. Principles and simulations of high-resolution STM imaging with a flexible tip apex. *Phys. Rev. B*, 95:045407, 2017.

[229] N. A. Pradhan, N. Liu, and W. Ho. Vibronic spectroscopy of single $C60$ molecules and monolayers with the STM. *The Journal of Physical Chemistry B*, 109(17):8513–8518, 2005.

[230] N. Ogawa, G. Mikaelian, and W. Ho. Spatial variations in submolecular vibronic spectroscopy on a thin insulating film. *Phys. Rev. Lett.*, 98:166103, 2007.

[231] F. Matino, G. Schull, F. Köhler, S. Gabutti, M. Mayor, and R. Berndt. Electronic decoupling of a cyclophane from a metal surface. *Proceedings of the National Academy of Sciences*, 108(3):961–964, 2011.

[232] K. J. Franke and J. I. Pascual. Effects of electron–vibration coupling in transport through single molecules. *Journal of Physics: Condensed Matter*, 24(39):394002, 2012.

[233] A. Mehler, N. Néel, M.-L. Bocquet, and J. Kröger. Exciting vibrons in both frontier orbitals of a single hydrocarbon molecule on graphene. *Journal of Physics: Condensed Matter*, 31(6):065001, 2018.

[234] J. Repp, G. Meyer, S. Paavilainen, F. E. Olsson, and M. Persson. Scanning tunneling spectroscopy of Cl vacancies in NaCl films: Strong electron-phonon coupling in double-barrier tunneling junctions. *Phys. Rev. Lett.*, 95:225503, 2005.

[235] S. E. Ammerman, V. Jelic, Y. Wei, V. N. Breslin, M. Hassan, N. Everett, S. Lee, Q. Sun, C. A. Pignedoli, P. Ruffieux, R. Fasel, and T. L. Cocker. Lightwave-driven scanning tunnelling spectroscopy of atomically precise graphene nanoribbons. *Nature Communications*, 12(1):6794, 2021.

[236] L. Wang, Yu. Xia, and W. Ho. Atomic-scale quantum sensing based on the ultrafast coherence of an H_2 molecule in an STM cavity. *Science*, 376(6591):401–405, 2022.

Curriculum Vitae

The CV is not included in the online version for data protection reasons.

List of Publications

Sergey Trishin, Christian Lotze, Nils Bogdanoff, Felix von Oppen and Katharina J. Franke
Moiré Tuning of Spin Excitations: Individual Fe Atoms on MoS$_2$/Au(111)
Phys. Rev. Lett. **127**, 236801 (2021)

Sergey Trishin, Tobias Müller, Daniela Rolf, Christian Lotze, Philipp Rietsch, Siegfried Eigler, Bernd Meyer and Katharina J. Franke
Resolution of Intramolecular Dipoles and a Push-Back Effect of Individual Molecules on a Metal Surface
J. Phys. Chem. C 2022 **126**, 7667-7673 (2022)

Sergey Trishin, Christian Lotze, Johanna Richter, Gaël Reecht, Nils Krane, Philipp Rietsch, Siegfried Eigler and Katharina J. Franke
Variation of vibronic states is densely-packed structures of molecules with intramolecular dipoles
Phys. Status Solidi A. Accepted Author Manuscript (2023)

Sergey Trishin, Christian Lotze, Friedemann Lohss, Giada Franceschi, Leonid I. Glazman, Felix von Oppen and Katharina J. Franke
Tuning a two-impurity Kondo system by a moiré superstructure
Phys. Rev. Lett. **130**, 176201 (2023)

Conference Contributions

2018

- The 21st International Conference on Non-contact Atomic Force Microscopy, Porvoo, Finland 17.09 - 21.09.2018
  (Poster) *Charge distribution within molecular dipoles and their influence on the local work-function of the substrate*

2019

- PhD Winter School of the TRR 227, Usedom, Germany, 25.02 - 28.02.2019
  (Oral presentation) *Investigation of magnetic nanostructures on MoS$_2$ with STM/AFM*

- DPG Spring Meeting of the Condensed Matter Section, Regensburg, Germany, 31.03 - 05.04.2019
  (Oral presentation) *Charge distribution within molecular dipoles and its influence on the local work function*

- The 22nd International Conference on Non-contact Atomic Force Microscopy, Regensburg, Germany 29.07 - 02.08.2019
  (Poster) *Energy levels and charge distribution within dipolar molecule*

- 794th WE-Heraeus Seminar: Exploring the Limits of Nanoscience with SPM, Bad Honnef, Germany, 27.10 - 31.10.2019
  (Poster) *Energy levels and charge distribution within dipolar molecules*

2020

- Ultrafast Spintronic Phenomena and Materials, Tisá, Czech Republic, 02.03 - 05.03.2020
  (Poster) *THz Generation and Magnetic Adatoms on Single-Layer Molybdenum Disulfide on Au(111)*

2021

- Joint School on Spin Physics, Apolda, Germany, 25.10 - 28.10.2021
  (Poster) *Moiré Tuning of Spin Excitations: Individual Fe Atoms on MoS$_2$/Au(111)*

2022

- Retreat of the TRR 277, Berlin, Germany 19.09 - 21.09.2022
  (Poster) *Moiré dependent magnetic fingerprints of individual atoms and dimers on MoS$_2$/Au(111)*

2023

- Retreat of the TRR 277, Potsdam, Germany 01.03 - 03.03.2023
  (Poster) *Moiré tuning of exchange interactions of single atoms and dimers on MoS$_2$/Au(111)*

- Advanced Atomic Force Microscopy Techniques 06.03 - 07.03.2023
  (Poster) *Variation of vibronic states in densely-packed structures of molecules with intramolecular dipoles*

- DPG Spring Meeting of the Condensed Matter Section, Dresden, Germany, 26.03 - 31.03.2023
  (Oral presentation) *Moiré - induced renormalization of singlet-triplet excitations in coupled Mn atoms on MoS$_2$/Au(111)*

Acknowledgements

Obviously, all the projects presented in this thesis can not be carried out by just one person alone. Without the incredible help and guidance of several people I would have never been able to write this thesis. Here, I want to express my gratitude towards them.

First and foremost, I want to thank (Prof. Dr.) Katharina (Franke). I spend a large fraction of my studies in your group and not once regretted the decision to join your group. When I started studying physics I did not think about pursuing a career in science at all. So thank you for taking me in your group, for trusting me with several projects, for being always available for discussions and for never losing patience with me. You resemble a lot of the positive traits of the scientific community and create a joyful and productive work environment. And with you its always possible to find a reason, why a cake break can be productive :D So thank you for everything and I hope our path continue to cross!

Next, I want to thank my second supervisor Tobias Kampfrath. Even though I spent only a fraction of my time working on the THz project, it was always nice discussing physics with you and I hope we can continue this fruitful collaboration in the time I will stick around.

Thanks a lot to Felix von Oppen for a very fruitful collaboration! I remembered there were times, when I was not sure if we could solve all the puzzling data we had. You helped us tremendously!

A royalty, a bread-board-boy, part-time google review writer, tech-guru: so much can be said about Christian Lotze. How much effort has been made to keep you around as a permanent staff member says everything about your personal and scientific value for the group. We worked on literally every single of my projects together and I would not want to have it any other way. Thanks for all the time you took for helping me, thank you for all the funny moments, all the sweets we shared and all the guidance you gave me. Most importantly, after all the time, I am happy to call you my friend.

Huge thanks to Daniela Rolf for her supervision during my Master thesis. I know that you would downplay your role in my PhD. But you were the first person to encourage me to start my own project and left me all the freedom in the world to learn and make mistakes. I still rely on most of the small pieces of advice you gave me and am very happy that you continue to coach me in our boulder classes :D

Michael Ruby played a similar rolemodel for me, just on a smaller scale. Thanks for all the mentoring, I still am impressed by the efficiency you could display!

Thanks to the students, who dared to work with me in the lab, Johanna Richter and Friedemann Lohss! I believe that one only understands a certain matter, when one can explain it to someone else. I remember when Johanna asked me how the lock-in amplifier works and I could not give a satisfying explanation. 2 years later Friedemann asked me the same question and I still stumbled to answer it properly (this is not an invitation to ask me this question in my defence) :D I learned a lot while working with you and enjoyed the time and I hope you did as well, even though I could not answer all your questions!

Nils Bogdanoff, I do not need to say much here, you know that I love you! I will continue to bother you with questions about the laser, bread-board-boy is a title given for life, even

though it is not the same without you around in the lab ;)

A big reason, why I had such a wonderful time during my PhD are the lovely people in AG Franke, some of which I am vary happy to have as friends. Carmen Rubio-Verdu, even though you did not stay a long time in the group and also travelled a lot during that short time I am very happy that our paths crossed! You are a wonderful person and a great scientific role model for me. You helped me a lot during a rough time and I always enjoyed our small coffee breaks! Times were a little bit crazy in the end, we were flatmates for like an hour. I am very happy that you got a well deserved PI position and I wonder how it would be working with you... Gael Reecht, I always enjoy spending time with you! I learned a lot from you, especially in efficient measuring. I find it a little bit funny that we steadily became closer friends. I hope it will continue this way :D Thanks also to Laetitia Farinacci, I believe you are one of the most talented researchers I came around and it is a little bit sad that we did not work so much together, because I think I could learn a lot from you. You drive a lot of social activities with your easy-going and encouraging nature and you were truly missed after you left the group! Shout-out also to Giada Franceschi. You emit so much positive energy, sometimes I thought one could solve all problems in the world with this enthusiasm. Unfortunately you were not around for a long time and that time was even troubled with Covid... I hope we will see each other around for enough conferences to make up for that time lost :D In the group, there were always people up for a chat or offer a helping hand. Probably I will forget to mention some, shame on me, but still a huge shout out to Rika Simon, Marc Westig, Idan Tamir, Jenny Hartfiel, Nils Krane, Olof Peters, Eva Liebhaber-Rudisch and many more! I know that not all my habits are particularly enjoyable (even though my singing probably got better over time :D) and I am grateful to all of you for accepting me for the person I am.

Last but not least, thank you to my family and friends for the incredible support I received over the years. It is crazy to think of all the things which happened during this time and I do not know how I would have managed without you!

Selbstständigkeitserklärung

Name: Trishin
Vorname: Sergey

Ich erkläre gegenüber der Freien Universität Berlin, dass ich die vorliegende Dissertation selbstständig und ohne Benutzung anderer als der angegebenen Quellen und Hilfsmittel angefertigt habe. Die vorliegende Arbeit ist frei von Plagiaten. Alle Ausführungen, die wörtlich oder inhaltlich aus anderen Schriften entnommen sind, habe ich als solche kenntlich gemacht. Diese Dissertation wurde in gleicher oder ähnlicher Form noch in keinem früheren Promotionsverfahren eingereicht. Mit einer Prüfung meiner Arbeit durch ein Plagiatsprüfungsprogramm erkläre ich mich einverstanden.

Berlin, den 28.04.2023